eman ta zabal zazu

Universidad del País Vasco
Euskal Herriko Unibertsitatea

Departamento de Ingeniería de Comunicaciones

Desarrollo de un sensor de fibra óptica para la medida del tip clearance y tip timing en motores aeronáuticos

Iker García Esteban-Barcina

Director

Joseba Zubia Zaballa

Bilbao, 2017

A Ana y Naia,

AGRADECIMIENTOS

Me gustaría expresar mi agradecimiento por el apoyo y la confianza que me han prestado todas las personas e instituciones que han participado en este trabajo. En primer lugar quiero agradecer la confianza y libertad, que desde el inicio y durante toda la tesis, me ha dado mi director, Joseba Zubia. Así como el apoyo recibido por el resto de integrantes del Grupo de Fotónica Aplicada de la UPV/EHU.

También me gustaría agradecer las colaboraciones del Centro de Tecnologías Aeronáuticas y del Instituto Tecnológico de las Fuerzas Aéreas polacas, sin los cuales este proyecto no se podría haber llevado a cabo.

Gracias a mis padres por su esfuerzo para darme la oportunidad de hacer siempre lo que más me ha gustado y ser el mejor ejemplo a seguir. También a mis hermanos por aguantarme, especialmente a Vanessa por su ayuda con el inglés.

Finalmente quiero agradecer su paciencia, amor y apoyo a Ana y a Naia, ya que vosotras sois la razón de todo.

RESUMEN

Los sensores basados en fibra óptica son cada vez más utilizados en aeronáutica debido a las ventajas que presentan frente a sensores más tradicionales. En esta tesis se presenta el diseño y desarrollo de un sensor de fibra óptica para la medida del tip clearance y del tip timing en motores aeronáuticos. Este sensor está basado en la modulación de la luz reflejada por parte de los álabes de un motor aeronáutico en función de la distancia a la que se encuentran.

En el capítulo 1 se realiza una introducción a los sensores de fibra óptica dedicando especial atención a que utilizan la modulación de la intensidad como principio de funcionamiento, y se explican los parámetros que serán objeto de medida por el sensor desarrollado en la presente tesis.

En el segundo capítulo se presenta la metodología seguida en el diseño y desarrollo del sensor. Se definen los objetivos y requisitos iniciales que el sensor debe cumplir y los pasos seguidos hasta conseguirlo.

En el tercer capítulo se muestran los resultados obtenidos para aplicaciones reales de funcionamiento del sensor diseñado. Se presentan los resultados conseguidos en dos entornos reales de trabajo. Por un lado, el túnel de viento que el Centro de Tecnologías Aeronáuticas posee en sus instalaciones de Zamudio (Vizcaya), y por el otro, el banco de ensayos con el que cuenta el Instituto Tecnológico de las Fuerzas Aéreas polacas en Varsovia (Polonia).

Este documento concluye con un capítulo en el que se recogen las conclusiones del trabajo, así como las líneas futuras del mismo. También se enumeran los artículos (incluidos en un apéndice) en los que se basa la tesis, así como las conferencias y otras publicaciones realizadas durante este periodo.

ÍNDICE DE CONTENIDOS

Índice de Figuras

Índice de Tablas

Capítulo 1

Introducción

En este primer capítulo se realiza una presentación de los sensores basados en fibra óptica haciendo especial énfasis en aquellos basados en la modulación de la intensidad. Se exponen la estructura general de los sensores de fibra óptica y varias clasificaciones de los mismos en cuanto al parámetro de la luz modulado, magnitud física a medir o su distribución espacial. Además se introduce brevemente el funcionamiento de un motor aeronáutico, así como las vibraciones que se dan en los álabes del mismo, y los parámetros del tip clearance y tip timing que son el objeto de medida por parte del sensor desarrollado en la presente tesis.

1.1- Estructura de la tesis y contribuciones personales

En el siguiente documento se presenta el diseño, desarrollo y validación de un sensor de fibra óptica para la medida del tip clearance y de las vibraciones (mediante la técnica del tip timing) de los álabes de un turborreactor. El sensor resultante de este trabajo ha sido validado en dos entornos reales de funcionamiento: un túnel de viento para el estudio de turbinas de baja presión (Centro de Tecnologías Aeronáuticas) y un motor real (Instituto Tecnológico de las Fuerzas Aéreas Polacas).

La tesis se ha organizado como una compilación de los artículos publicados durante el desarrollo de la misma y el presente documento se ha estructurado en cuatro capítulos. En el primero de ellos se realiza una introducción a los sensores de fibra óptica en general y a los basados en la modulación de la intensidad en particular. También se dan unas nociones mínimas de los parámetros que son objeto de medida por parte del sensor desarrollado en la tesis, ya que no son de uso común al ser parámetros específicos de los turborreactores. En este apartado también se analiza el estado del arte de los sensores utilizados habitualmente para la cuantificación de dichos parámetros. La contribución que mejor recoge las ideas plasmadas en este capítulo es el **Artículo 1**, en él se hace una recapitulación de diversos proyectos llevados a cabo por el grupo de investigación APG (Applied Photonics Group) relacionados con los sensores de fibra óptica para la monitorización de estructuras y motores aeronáuticos.

En el segundo capítulo se describe el diseño y desarrollo del sensor. En él se detallan las pruebas preliminares en el laboratorio y en el túnel de viento, así como las diferentes alternativas consideradas para el desarrollo del sensor. Todo este trabajo dio origen a la publicación de los **Artículos 2, 3 y 4** en los que se describen los prototipos iniciales y los resultados obtenidos con ellos.

En el capítulo tercero se detalla el prototipo final del sensor y su validación en un compresor de un motor real. También se presenta la caracterización del mismo realizada en el laboratorio previa a las medidas en el motor. Todo ello queda plasmado en el **Artículo 5**.

Finalmente, el documento termina con las conclusiones principales del trabajo y con las líneas de trabajo futuras. Al final del capítulo se incluye un apartado con un listado de las publicaciones y conferencias realizadas durante el transcurso de la tesis.

1.2- Sensores de fibra óptica

1.2-1. Definición y características generales

El gran desarrollo de los sensores de fibra óptica tiene su origen en los grandes avances del sector de las comunicaciones ópticas. Estos sensores han permitido dar solución a varias de las limitaciones que presentan los sensores convencionales. Se puede definir un sensor de fibra óptica como aquel dispositivo que basado en fibra óptica es capaz de manifestar los cambios de una magnitud a medir mediante la modulación de al menos un parámetro de la luz que viaja por dicha fibra. Las ventajas que proporcionan este tipo de sensores son numerosas, y entre ellas podemos encontrar su ligero peso y pequeño tamaño, inmunidad frente a las radiaciones electromagnéticas, gran resolución y sensibilidad, y su idoneidad para ser multiplexados. Por el contrario, su mayor inconveniente sea seguramente su elevado coste comparado con sensores mejor establecidos en el mercado.

En función del parámetro modulado se podría hacer una primera clasificación de los sensores de fibra óptica [1]:

a) *Sensores basados en la modulación de la intensidad:* el valor de la intensidad de luz en la fibra varía debido a diferentes mecanismos (curvatura, atenuación,…) en función de la magnitud a medir. Son simples y de coste reducido lo que les confiere un gran potencial comercial.

b) *Sensores basados en la modulación de la longitud de onda:* probablemente los más utilizados dentro de esta categoría sean los basados en redes de Bragg. Entre sus grandes ventajas están la facilidad para ser multiplexados en una sola fibra e instalados en grandes estructuras (incluso embebidos en ellas) permitiendo la monitorización de su salud estructural.

c) *Sensores basados en la modulación de la fase*: el cambio de fase de la luz es detectado mediante métodos interferométricos en los que se hacen coincidir dos haces de luz, uno de referencia y otro expuesto a la magnitud a medir. Mach-Zehnder, Michelson, Fabry-Perot y Sagnac son los interferómetros más comúnmente utilizados. Su mayor ventaja es la gran sensibilidad que son capaces de proporcionar.

d) *Sensores basados en la modulación de la polarización:* cambios en la tensión de la fibra u otros efectos, como el efecto Faraday, modifican el estado de la polarización en el interior de la fibra, permitiendo la medida de magnitudes como la presión, corriente eléctrica,…

e) *Sensores basados en la modulación del espectro:* los sensores basados en espectroscopía analizan las variaciones del espectro transmitido para obtener la medida deseada.

f) *Sensores basados en la modulación de la luz dispersada:* la amplitud y la localización de la magnitud a medir puede ser determinada por el estudio de la luz dispersada por cualquier fenómeno de dispersión (Rayleigh, Raman o Brillouin).

Otra posible clasificación de los sensores de fibra óptica se puede realizar de acuerdo a la magnitud a medir. Así, encontramos sensores que miden magnitudes mecánicas, térmicas, electromagnéticas, radiación, composición química, flujos de fluidos o aquellas propias de ámbito biomédico [2].

Si se atiende a la distribución espacial de los sensores, estos se pueden clasificar en tres categorías diferentes. Los sensores de punto proporcionan la medida en un punto discreto. Los sensores distribuidos son capaces de proporcionar el valor de la magnitud a medir a lo largo de toda la fibra óptica. Entre ambos se encuentran los cuasi-distribuidos, que se obtienen por la multiplexación de varios sensores de punto a lo largo de la misma fibra.

La estructura general para un sistema de medición basado en un sensor de fibra óptica se encuentra representada en la Figura 1. Sus cinco elementos fundamentales serían la fuente luz (normalmente un láser o LED), la fibra óptica que sirve como canal de transmisión de la luz, el elemento transductor encargado de modular las propiedades de la luz, un detector óptico y finalmente toda la electrónica correspondiente al procesado de la información [3,4].

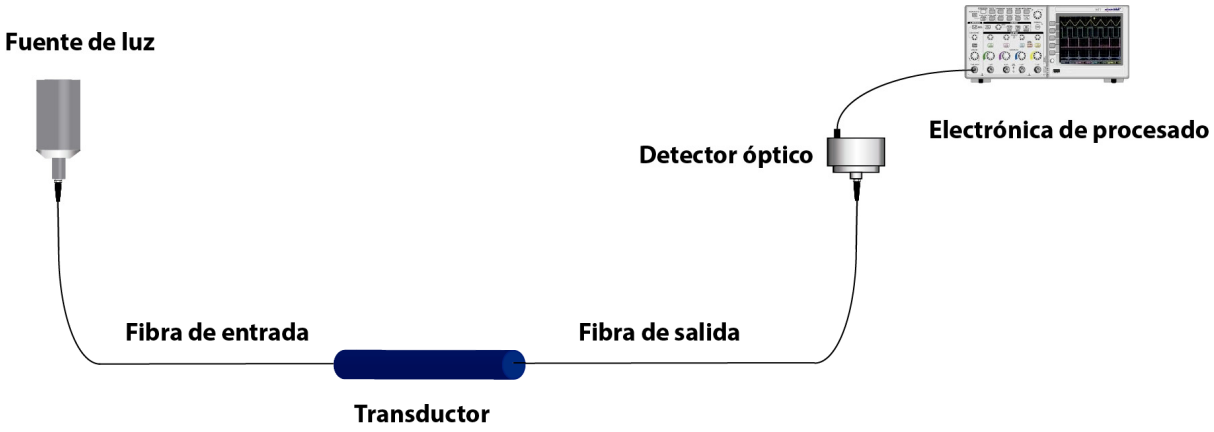

Figura 1. Estructura general de un sistema de medición basado en un sensor de fibra óptica.

1.2-2. Sensores basados en la modulación de la intensidad

Dado que en la presente tesis se ha desarrollado un sensor basado en la modulación de la intensidad, este apartado profundizará en los sensores de este tipo, en los que la intensidad de la luz es modulada por el efecto de la magnitud a medir sobre un transductor o bien directamente sobre la fibra. A pesar de que la exactitud que proporcionan estos sensores está lejos de aquellos basados en interferometría, esta es suficiente para cuantificar un gran número de propiedades físicas como el desplazamiento, temperatura, presión, tensión, rotación, vibración,...

En los sensores modulados en intensidad intrínsecos el proceso de modulación de la intensidad se debe a un efecto interno de la fibra óptica [5]. Los principales efectos que se dan en este tipo de sensores son la absorción, la dispersión o la fluorescencia [6]. En los extrínsecos, sin embargo, esta modulación se produce debido a un efecto externo a la fibra. Dentro de ellos los principales son:

a) *Sensores basados en la modulación de la luz transmitida por una fibra óptica.* La magnitud a medir provoca variaciones en la intensidad debidas a la atenuación producida por las curvaturas o deformaciones introducidas en la fibra. Se pueden provocar microcurvaturas mediante dispositivos dentados que provocan deformaciones en la fibra, o macrocurvaturas en las que la fibra se dispone en una determinada posición inicial (lazo, U,…) que es modificada por un elemento elástico que varía el radio de curvatura [7], y por lo tanto, la atenuación en función de la magnitud a medir (ver Figura 2).

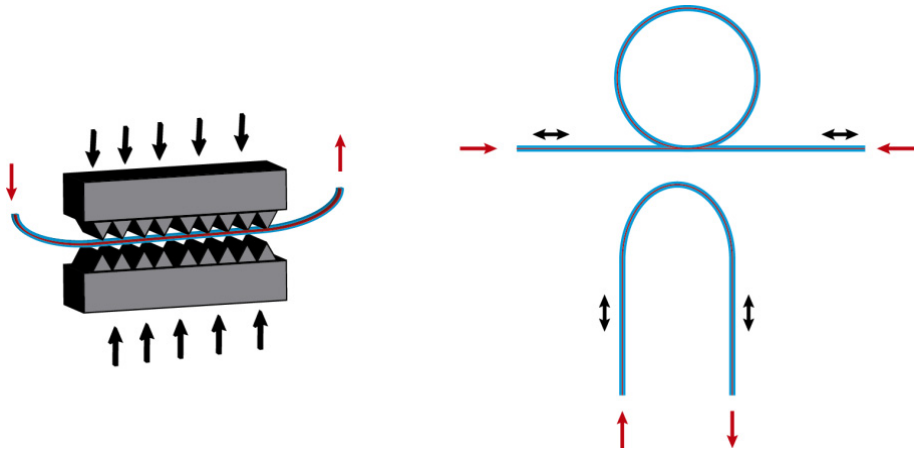

Figura 2. Ejemplos de disposiciones de la fibra óptica para ser utilizada en sensores basados en la modulación de la intensidad por microcurvaturas (izquierda) y macrocurvaturas (derecha).

b) *Sensores basados en la modulación de la luz transmitida entre dos fibras.* La variación de la posición relativa entre dos fibras enfrentadas debida a la magnitud a medir provoca cambios en la intensidad de la luz acoplada desde la fibra emisora a la receptora (ver Figura 3). El desalineamiento puede estar provocado por un desplazamiento axial o radial. Un dispositivo como por ejemplo una rejilla, cuyo movimiento obstaculiza el paso de luz también puede utilizarse como elemento transductor [8].

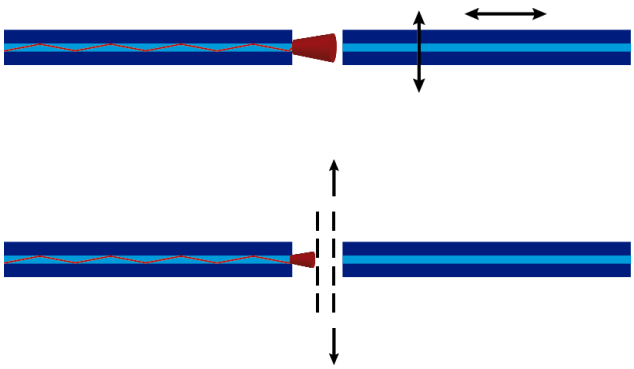

Figura 3. Fibras enfrentadas en las que la luz transmitida de una a otra se modula por un movimiento axial o radial (arriba), o mediante una rejilla móvil (abajo).

c) *Sensores basados en la modulación de la luz reflejada.* Este tipo de sensores están basados en dos conjuntos de fibras, emisoras y receptoras (también puede utilizarse una sola fibra de cada tipo e incluso una única fibra para emisión y transmisión con el empleo de un circulador o un divisor). Las fibras transmisoras van a enviar luz a un objetivo, mientras que la luz reflejada por el mismo será recogida por las fibras receptoras. Estas entregaran una intensidad luminosa a un fotodetector que es función de la distancia y las condiciones en las que se encuentra el objetivo. En la Figura 4 se pueden observar las curvas características de varias configuraciones para agrupaciones de haces de fibras bifurcados (un conjunto de fibras emisoras y otro de receptoras) y para el caso de una única fibra en emisión y recepción. Salvo en este último caso pueden observarse dos regiones diferenciadas; la primera con una pendiente positiva que denominaremos región I y la segunda con una pendiente negativa que llamaremos región II. La primera de ellas exhibe una mayor sensibilidad y linealidad, aunque su rango dinámico es sensiblemente menor que el de la región II. Las diferentes disposiciones de las fibras (coaxial,

semicircular, aleatoria, par de fibras o fibra única) junto con la posibilidad de elegir una de las dos regiones de funcionamiento permiten el diseño de sensores a medida para cada aplicación concreta [9].

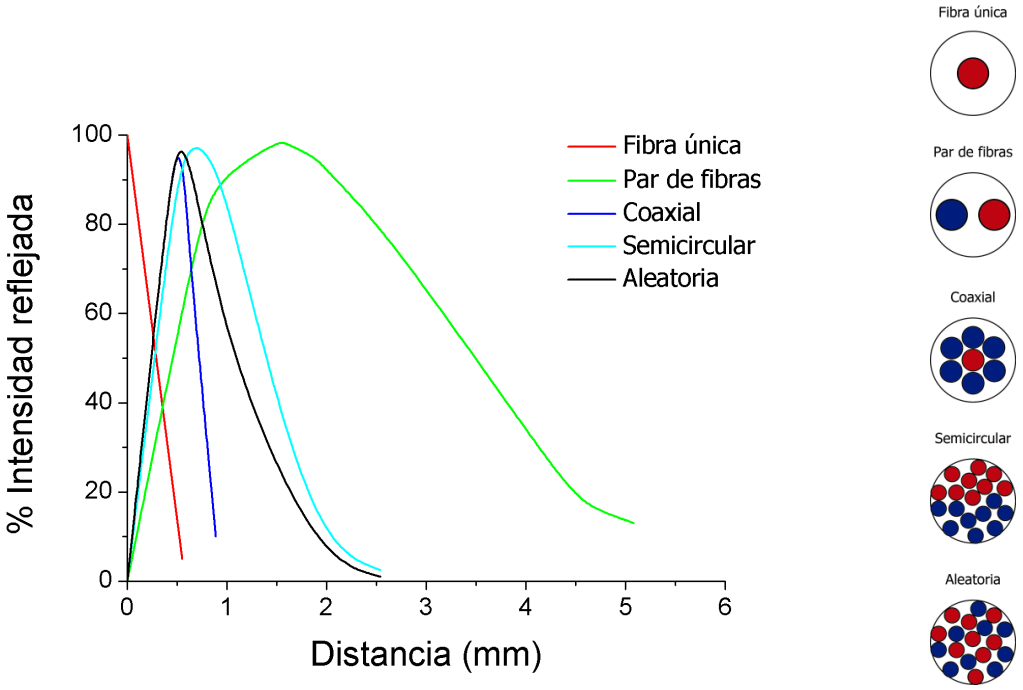

Figura 4. Curvas características para los sensores basados en la modulación de la luz reflejada para las configuraciones fibra única, par de fibras, coaxial, semicircular y aleatoria.

1.3- Tip clearance y tip timing

Debido a las importantes ventajas que presentan los sensores de fibra óptica, estos sensores son cada vez más utilizados para caracterizar componentes aeronáuticos, así como para verificar la salud estructural de los mismos. En esta industria los diferentes elementos se diseñan de forma que sean capaces de soportar cierto grado de deterioro sin que ello afecte seriamente a su rendimiento [10]. Esto hace que se requieran grandes esfuerzos en la inspección de los mismos para mantener esos posibles daños dentro de los márgenes de seguridad. Es aquí donde los sensores de fibra óptica encuentran su mayor campo de aplicación, ya que van a permitir reducir los tiempos de inspección/mantenimiento y por lo tanto, el tiempo que las aeronaves están en tierra. En el presente trabajo se ha diseñado un sensor para la evaluación de un componente muy concreto como es el motor, por lo que a continuación se describen brevemente sus componentes y características esenciales. En la Figura 5 aparecen representadas las partes principales de un motor aeronáutico, concretamente se trata del motor Trent 500 de Rolls-Royce. Si avanzamos en el sentido del flujo de aire, el primer elemento que nos encontramos es el ventilador. Este rotor, de mayor tamaño que el resto, va a introducir parte del aire impulsado por él en el núcleo del motor a través del compresor de baja presión. De aquí pasará al compresor de alta presión para llegar a la cámara de combustión. Finalmente, a la salida de la cámara de combustión se encuentran las turbinas de alta y baja presión que extraen la energía del flujo de aire para hacer girar el ventilador y el compresor.

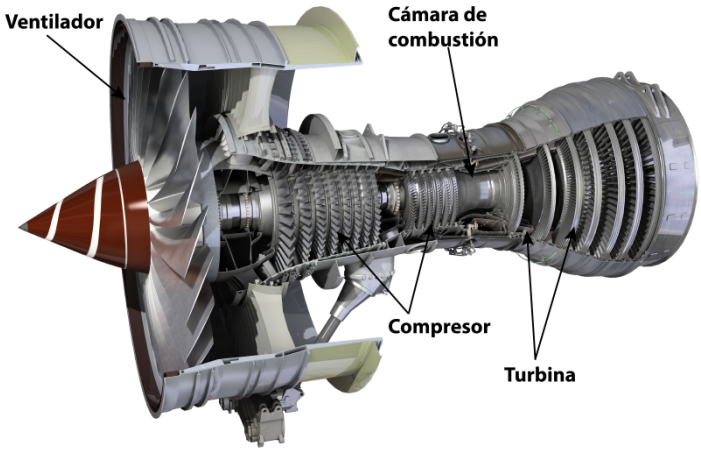

Figura 5. Motor Trent 500. Imagen cortesía de Rolls-Royce.

Se conoce con el nombre de blisk al rotor formado por el conjunto de un disco y una serie de álabes integrados en el mismo (blades + disk). Esta es la configuración más común para las diferentes etapas de los compresores y turbinas en los motores aeronáuticos. Durante la fase de desarrollo de estos motores son múltiples los parámetros que pueden ser medidos mediante el empleo de sensores de fibra óptica. Entre ellos están las vibraciones, la temperatura, la presión, la velocidad de rotación,… [11]. La caracterización de las vibraciones que se producen en los álabes de los blisks son de vital importancia en cuanto a la seguridad y la eficiencia del motor, y actualmente no existe ninguna tecnología que satisfaga completamente las necesidades de los fabricantes de motores. Es por ello que en esta área los sensores de fibra óptica pueden aportar soluciones a estas carencias.

Las vibraciones de los álabes pueden ser de tres tipos: radiales, axiales y tangenciales (ver Figura 6). El primer tipo de ellas va a producir cambios en la longitud total del álabe, que se acercará y alejará de la carcasa del motor debido a estas vibraciones. Se conoce como “tip clearance” al parámetro que proporciona la distancia existente entre el extremo de un álabe y la carcasa, por lo que este parámetro va a permitir determinar las vibraciones axiales. Las vibraciones tangenciales de los álabes se producen en el plano perpendicular al flujo de aire en el que se encuentra el rotor, y para caracterizarlas se emplea mayoritariamente la técnica conocida como “tip timing” [12]. Empleando este método es posible calcular las amplitudes y frecuencias de vibración de cada álabe. Para ello se emplean las diferencias entre los tiempos reales de llegada de cada uno de los álabes a un punto concreto y los calculados teóricamente. Por último, las vibraciones axiales son aquellas producidas en la misma dirección del flujo de aire, aunque no son menos importantes que las dos anteriores, quedan fuera del alcance del presente trabajo.

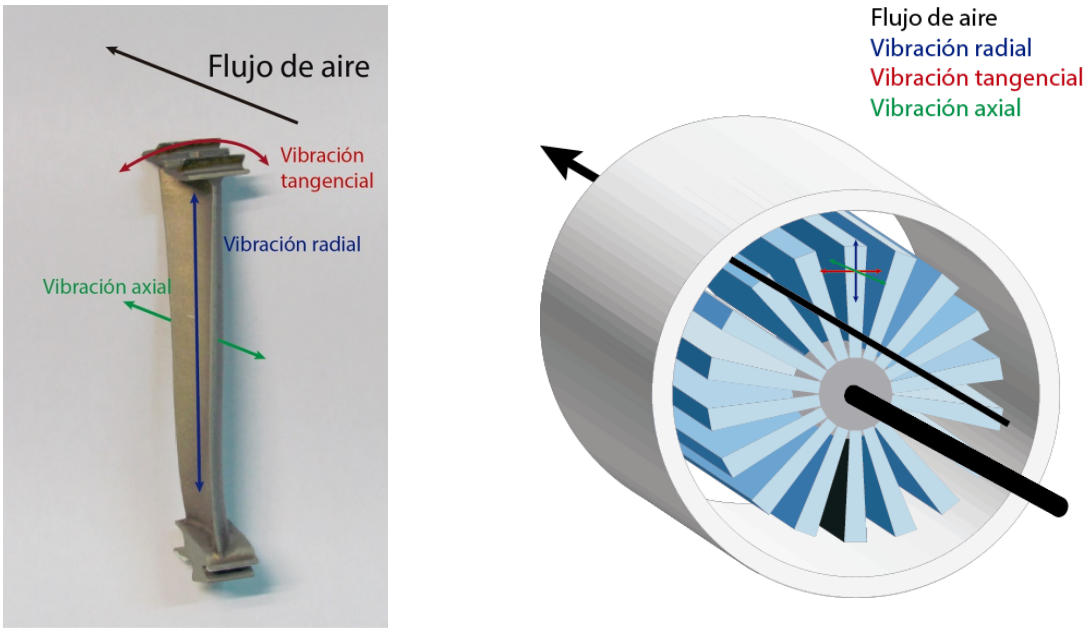

Figura 6. Álabe correspondiente a una turbina de baja presión con una representación de las posibles vibraciones que experimenta durante su funcionamiento (izquierda). Esquema de la turbina en la que se representan las diferentes vibraciones producidas en los álabes (derecha).

1.3-1. Tip clearance

Como se ha comentado en el aparatado anterior, el tip clearance correspondiente a un álabe de un blisk viene definido por la distancia entre el mismo y la carcasa del motor. Este hueco, representado en la Figura 7, permite el paso de un flujo de aire que no produce un trabajo útil y que por lo tanto, penaliza la eficiencia del motor [13]. Así, una reducción de 0,25 mm de esta distancia supone una disminución en el consumo del motor del 1% y de 10 °C en la temperatura de gases de escape [14]. Este descenso del consumo que puede parecer mínimo, si tenemos en cuenta el tráfico aéreo global podría producir una ahorro de más de 167 millones de dólares anuales [15]. Además de este beneficio económico, al trabajar el motor a menores temperaturas el ciclo de vida de sus componentes se alargaría. También se obtendrían ventajas medioambientales ya que las emisiones de gases y acústicas se reducirían. Por todo ello, resultaría enormemente interesante disponer de un sistema que mantuviera el tip clearance en un valor mínimo, lógicamente manteniendo siempre un intervalo de seguridad para evitar que un álabe tocara la carcasa y provocara una catástrofe. Estos sistemas se conocen con el nombre de sistemas de control activos del tip clearance, y permiten controlar el valor del tip clearance gobernando la expansión térmica de la carcasa. Para ello, redirigen hacia ella un flujo de aire mediante unas válvulas consiguiendo reducir el tip clearance y aumentar la eficiencia del motor.

Mientras que para las turbinas de generación de energía los valores típicos del tip clearance oscilan entre 2 y 8 mm, para los motores aeronáuticos rara vez se superan los 3 mm [16]. Al ser un parámetro tan crítico para la eficiencia y la seguridad, la precisión en su medida debe ser como mínimo de 25 µm. Los valores del tip clearance van a depender fundamentalmente del régimen de funcionamiento del motor (taxi, despegue, crucero y aterrizaje). Además influyen también otros factores, como por ejemplo el envejecimiento de los componentes del motor [17,18]. Como norma general deberemos considerar que el valor del tip clearance será menor cuanto mayor sea la velocidad de rotación del motor.

Existen diversas tecnologías que se pueden emplear para la medida del tip clearance, como por ejemplo sensores capacitivos, inductivos, basados en microondas o de descarga eléctrica. Los primeros son los más comúnmente utilizados ya que son robustos y relativamente baratos. Sin embargo tienen una pobre respuesta frecuencial (comparado con un sensor óptico), su mejor precisión es de 30 µm y requieren el uso de álabes conductores de la electricidad para poder realizar la medida [19,20]. Los sensores inductivos presentan una gran ventaja ya que no es necesario que tengan una vista directa con el álabe, aunque su calibración es dependiente de la forma del álabe y su velocidad de giro, lo que la hace muy complicada [21,22]. Los sensores basados en microondas requieren también de laboriosas calibraciones y de un avanzado sistema de procesado, siendo además una tecnología de elevado coste [23,24]. Los sensores de descarga eléctrica requieren también de álabes conductores y además solo proporcionan el tip clearance del álabe más cercano a la carcasa. Todas estas limitaciones se ven superadas con el empleo de sensores de fibra óptica, cuya mayor contrapartida es su sensibilidad a la contaminación debido a los residuos de combustión en el motor. Se han empleado diferentes técnicas para implementar sensores ópticos para la medida del tip clearance, pero teniendo en cuenta los requisitos en cuanto a precisión, ancho de banda, robustez y coste, los sensores basados en intensidad presentan ventajas frente a otras aproximaciones como los interferométricos y los basados en efecto Doppler [25,26].

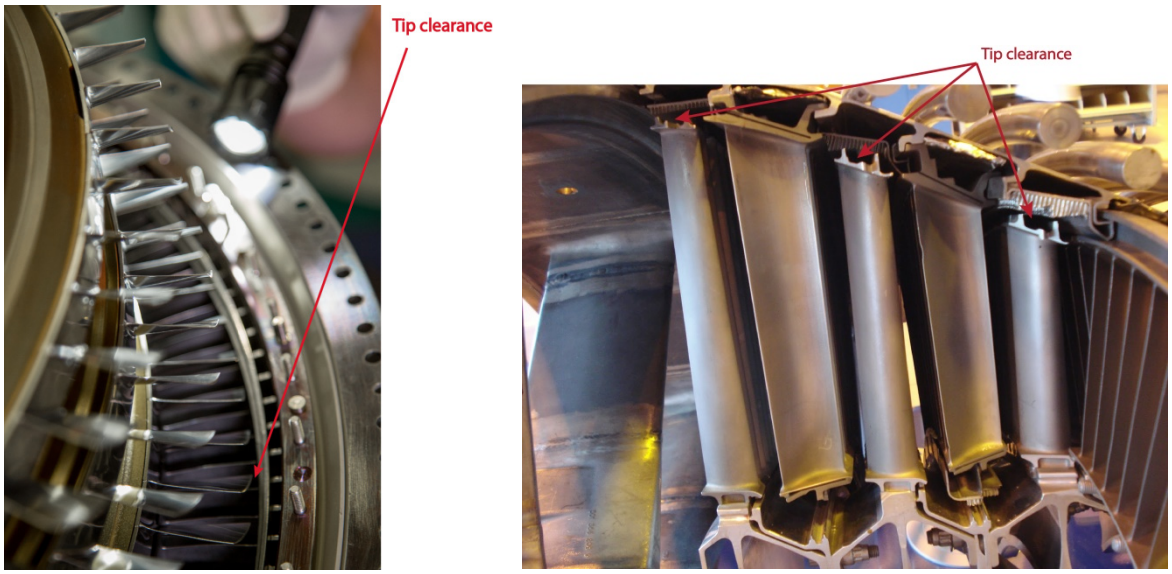

Figura 7. Detalle del tip clearance de un comprensor durante su montaje (izquierda). Imagen cortesía de Rolls-Royce. Tip clearance de la turbina de baja presión (derecha). Imagen cortesía de la revista "Ingenieros especialistas".

1.3-2. Tip timing

Mientras que la medida del tip clearance está más relacionada con la eficiencia del motor, la técnica conocida como tip timing va a proporcionar información relativa a la salud estructural del blisk. Para ello, mediante el tip timing se van a caracterizar las vibraciones tangenciales de los álabes, lo que va a permitir predecir fallos en los mismos debido a la fatiga [27], y como consecuencia la producción de motores más fiables y seguros. Esta técnica posibilita estimar la amplitud y la frecuencia de las deflexiones de los álabes mediante la determinación de los tiempos de llegada de los álabes al punto en el que se encuentra el sensor (ver Figura 8) [28-37]. Normalmente se instalarán varios sensores y los instantes de llegada se compararán con los instantes de llegada teóricos, aquellos que se producirían si el álabe no vibrara. Conocida la diferencia entre dichos instantes, la velocidad de rotación y el radio de la turbina, se puede obtener la amplitud de la vibración del álabe y procesando esta información la frecuencia de vibración del mismo, número de diámetros nodales del blisk,…

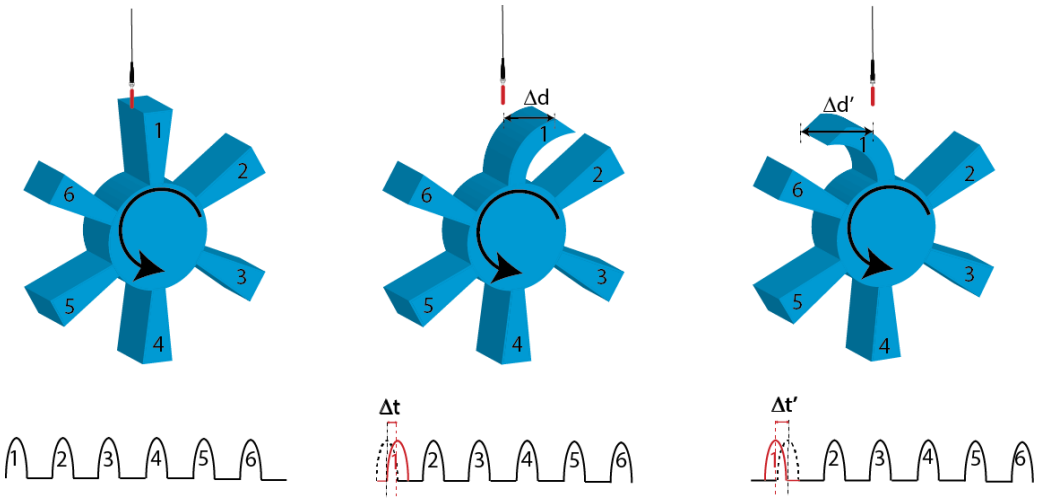

Figura 8. Representación de las vibraciones de los álabes y de las diferencias de tiempo en la llegada de los mismos a la posición del sensor. Estas diferencias se miden respecto al instante de llegada teórico (izquierda) y puede ocurrir que el álabe se retrase (centro) o se adelante (derecha) debido a su vibración.

Las vibraciones que aparecen en los álabes pueden deberse a diferentes causas. Por ejemplo, debido al estator o a los inyectores de la cámara de combustión pueden aparecer respuestas síncronas (su frecuencia es múltiplo de la frecuencia de rotación del motor). Estas vibraciones entran en resonancia, provocando grandes amplitudes en la vibración de los álabes, cuando la frecuencia natural de los álabes coincide con un múltiplo entero de la frecuencia de rotación del motor (engine order) [38]. Cuando se considera la vibración de todos los álabes del blisk, el modelo clásico de vibración para un solo álabe con modos de flexión y torsión se complica. El conjunto de todos los álabes se divide en subgrupos de álabes que vibran en fase. Debido a la naturaleza cíclica del blisk, estás vibraciones se propagan dando lugar a las ondas viajeras. Estas ondas viajeras se caracterizan a través del parámetro conocido como ángulo de fase entre álabes (σ) que nos proporciona la diferencia en la fase de la vibración de un álabe con el siguiente. Este parámetro a su vez está relacionado a través de la Ecuación 1 con el número de diámetros nodales (ND) presentes en el blisk, que se pueden definir como una línea de puntos estacionarios que separa partes del blisk que no vibran en fase [39]. El número de diámetros nodales puede variar desde 0 (cuando todos los álabes están en fase) hasta la mitad del número de álabes que componen el blisk (cuando todos vibran a contrafase) [40].

$$ND = \frac{\sigma \cdot N_{álabes}}{2\pi} \tag{1}$$

donde $N_{álabes}$ es el número de álabes del rotor.

En la Figura 9 se representa un rotor cuyos 24 álabes vibran con 4 diámetros nodales, por lo que σ = π/3. Los álabes pintados de azul se corresponden con una deflexión máxima positiva mientras los pintados de rojo con una deflexión máxima de sentido opuesto. Se ha representado también en amarillo la onda viajera.

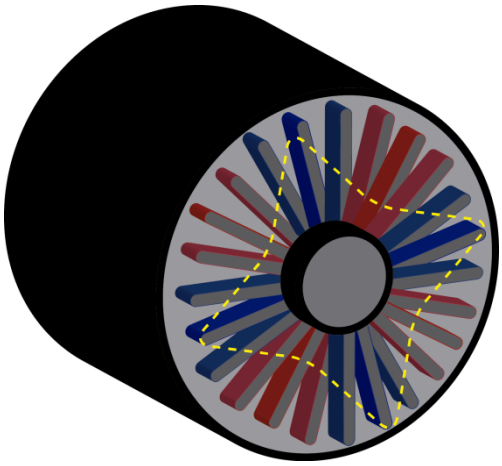

Figura 9. Rotor en el que sus álabes vibran con 4 ND. Se representa también la onda viajera (amarillo) que representa la vibración de un álabe en una vuelta completa debido a que está formando parte de un blisk.

Es importante destacar que un observador desde fuera del rotor va percibir la suma de los dos efectos, es decir, por un lado verá que el álabe vibra a una frecuencia determinada ($f_{álabe}$) y superpuesto a esta vibración observará la onda viajera que será igual a la frecuencia de rotación (f_r) multiplicada por ND [41]. Por lo tanto, la frecuencia percibida por ese observador (f_o) será:

$$f_o = f_{álabe} + f_r \cdot ND \tag{2}$$

Normalizando respecto a la frecuencia de rotación obtenemos que la frecuencia observada depende del engine order (EO) y del ND y es necesario conocer al menos uno de los dos para obtener la frecuencia de vibración del álabe:

$$f_o / f_r = f_{álabe} / f_r + ND = EO + ND \tag{3}$$

Volveremos a esta ecuación cuando desarrollemos el procesado de la información obtenida por tip timing.

Además de las respuestas síncronas, se pueden dar una serie de respuestas asíncronas debido a inestabilidades aerodinámicas como el desprendimiento (stall) y el flameo (flutter) de los álabes. Se dice que un flujo de aire se ha desprendido del álabe cuando este adquiere una velocidad cero debido a afectos viscosos del roce y a gradientes de presión adversos [42]. Esta inestabilidad provoca una perturbación local del flujo de aire que hace que el álabe adyacente al que ha sufrido el desprendimiento se sobrecargue, mientras el adyacente por el otro lado se descargue. Esto produce a su vez que el álabe sobrecargado entre en desprendimiento y el que estaba en desprendimiento pase a descarga, y así sucesivamente por lo que la inestabilidad se va desplazando por el rotor y termina afectando a todos los álabes del mismo. Como resultado de este fenómeno el rotor se desestabiliza y existe una pérdida de potencia debido a las fluctuaciones en la presión y en el flujo de aire. Se habla de desprendimiento cuando este fenómeno afecta de forma local a una serie de álabes. Si se generaliza el motor puede entrar en bombeo (surge). En esta situación se puede llegar a dar la inversión total del flujo de aire, lo que tendría consecuencias catastróficas para el motor si no se corrige a tiempo. Por su parte, el flameo se trata de una inestabilidad autoiniciada y automantenida en la que un álabe vibra a su frecuencia natural (o en sus cercanías). Se produce cuando la energía proporcionada por el fluido en movimiento es mayor que la que el amortiguamiento del álabe puede disipar [43].

Las vibraciones de los álabes son medidas normalmente mediante el empleo de galgas extensiométricas. Entre sus ventajas fundamentales está su robustez y su bajo coste, aunque presentan serios inconvenientes como la deriva de la señal a largo plazo, pero sobre todo, su cableado. Cada galga instrumentada en un álabe necesita dos cables para transmitir su señal que luego hay que desacoplar del movimiento del blisk mediante un anillo colector o un sistema de telemetría [44]. Ambas opciones requieren de un tiempo considerable para su puesta en marcha [45]. Otra alternativa al empleo de galgas es usar unos imanes permanentes fijados a la punta de los álabes, que inducen un voltaje en un cableado instalado en la carcasa del motor [46,47]. En cualquier caso este sistema presenta inconvenientes similares a los de las galgas. Por el contrario, la opción del tip timing es capaz de evitar todo ese tiempo de instrumentación debido a que es una técnica de medida sin contacto, que solo requiere la instalación de los sensores en la carcasa del motor. Además va a proporcionar datos de todos los álabes del blisk, no solo de aquellos instrumentados [48,49].

Respecto a los sensores empleados para el tip timing existen trabajos utilizando diferentes tipos como capacitivos [50], inductivos [51] o basados en microondas [52], pero ninguno de ellos proporciona una resolución comparable a la de los sensores ópticos. Como se ha comentado anteriormente, estos tienen la desventaja de ser sensibles a la contaminación, por lo que debe resolverse este obstáculo para que puedan ser utilizados en la turbina del motor durante largos periodos.

Capítulo 2

Diseño y desarrollo del sensor

En este capítulo se presentan los objetivos a cumplir durante el desarrollo del sensor, para que este proporcione unas propiedades que satisfagan las especificaciones mínimas que aseguren su aplicabilidad a un sistema real de medida. Por otro lado, se detallan todos los pasos en el diseño de los cinco prototipos del sensor desarrollado. Desde la estructura general del sistema, hasta su instalación en el blisk en el que se van a realizar las medidas, incluyendo una descripción completa de los componentes y de los resultados preliminares obtenidos en las pruebas de cada prototipo. En resumen, se presenta la trayectoria completa que se ha seguido en el diseño hasta conseguir la versión final del sensor.

2.1- Objetivos

El objetivo fundamental del presente trabajo es el desarrollo, validación y aplicación de un sensor de fibra óptica que permita determinar sin contacto el tip clearance y las vibraciones de los álabes de un blisk. Para conseguirlo se han de cumplir los siguientes objetivos parciales:

a) Diseño del sensor para la medida del tip clearance con una precisión de al menos 30 μm, que es el valor mínimo necesario para que el Centro de Tecnologías Aeronáuticas pueda obtener medidas significativas en su túnel de viento. Es deseable que el valor final de la precisión esté por debajo de 25 μm. Para facilitar este diseño se realizará un programa que sea capaz de simular la respuesta del sensor.

b) Desarrollo y caracterización de una "prueba de concepto" del sensor en el laboratorio previa a las medidas en entornos reales de funcionamiento.

c) Validación del sensor en condiciones reales de funcionamiento. Se validará el sensor en dos escenarios diferentes: un túnel de viento para la prueba y verificación de turbinas de baja presión y un compresor de un motor real.

d) Con respecto a la medida de las vibraciones de los álabes se empleará la técnica de tip timing. El mismo sensor empleado para la medida del tip clearance se diseñará de forma que sea capaz de proporcionar una señal con las características necesarias para la aplicación de dicha técnica.

e) Se realizará un pequeño programa, que si bien quedará lejos de un software comercial, permitirá procesar las señales obtenidas, obteniendo las vibraciones de cada álabe así como un análisis frecuencial mínimo de los resultados de la medida.

f) Para la validación de los resultados de las vibraciones de los álabes se compararán los resultados obtenidos mediante el sensor diseñado y aquellos proporcionados por otro de naturaleza inductiva, cuya validez para la medida del tip timing está previamente demostrada. Para la obtención de dichos resultados se empleará un software comercial al que se le suministrarán las señales de ambos sensores.

2.2- Diseño y desarrollo

Como se ha comentado en el apartado anterior el objetivo principal de la tesis es el desarrollo de un sensor basado en fibra óptica para la medida del tip clearance y las vibraciones de los álabes. Los requisitos que debe cumplir el sensor son los siguientes:

- Proporcionar una medida sin contacto, por simplicidad en su instrumentación y para no modificar el comportamiento mecánico de los álabes.
- Ancho de banda mínimo de 200 kHz. Este requisito es fundamental para recoger varios armónicos en la señal a procesar con el tip timing.
- Rango de medida mínimo de 2 mm sobre un offset inicial que va a depender de las características dimensionales del blisk concreto.
- Precisión mínima de 30 μm.
- Robustez para soportar el ambiente agresivo en el que se realizarán las medidas, sobre todo en cuanto a vibraciones.

- Económicamente viable para un futuro desarrollo de un producto comercial.

Teniendo en cuenta todos estos requisitos, la mejor solución es el empleo de un sensor basado en la modulación de la intensidad de la luz reflejada. En la literatura existen múltiples desarrollos de esto tipo de sensores para la medida de distancias [53-61]. El funcionamiento de la mayoría de estos sensores ha sido comprobado en un laboratorio y usando como blanco un espejo. Otros, se han demostrado como aplicación específica para la medida del tip clearance en simuladores de turbinas que funcionan también en un entorno controlado [22,62-65]. Sin embargo, ninguno de ellos ha demostrado su funcionamiento en condiciones de un motor real. Para el tip timing, aunque escasos, sí que existe algún trabajo previo de sensores similares aplicados a motores reales [45,46].

2.2-1. Primer prototipo

La estructura general del sensor diseñado y sus componentes principales puede observarse en la Figura 10. Se trata de un sensor basado en la modulación de la intensidad y que consta de una fuente de luz, un haz de fibras ópticas encargado de transportar la luz hasta los álabes del blisk y recoger la luz reflejada por los mismos, y unos fotodectectores encargados de realizar la conversión electro-óptica. Además también tendremos toda la electrónica para la adquisición de las señales y su almacenamiento, ya que estas serán post-procesadas.

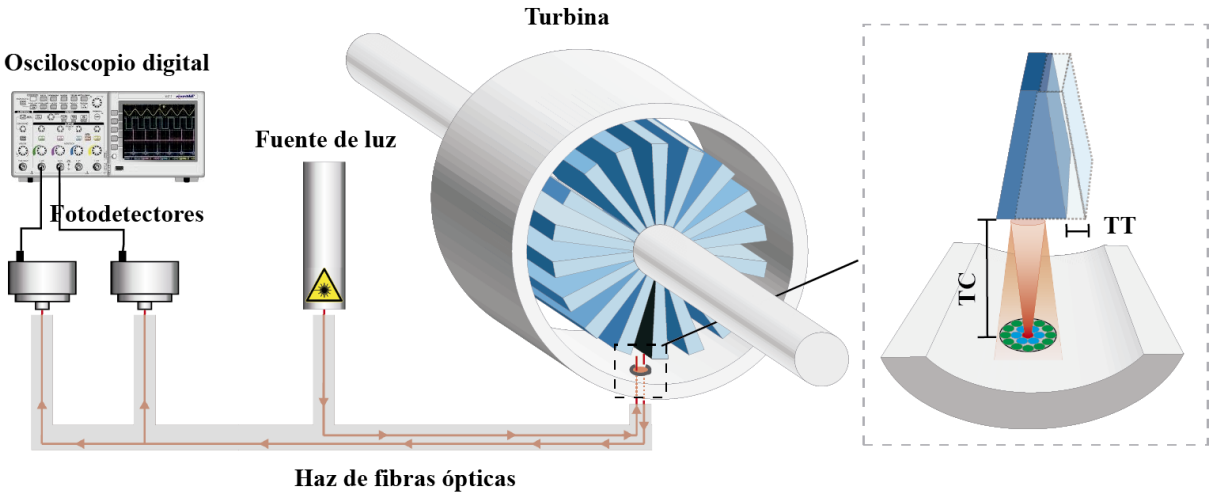

Figura 10. Componentes y estructura del sensor para la medida del tip clearance y tip timing.

El componente fundamental del sensor es el haz de fibras ópticas. Se decidió utilizar un haz de fibras con una distribución coaxial. Aunque no es la distribución que mejores prestaciones aporta respecto al rango de medición [66], debido a su simetría circular va a eliminar grandes problemas de alineamiento con el álabe que serán importantes cuando el sensor se instale en un motor. En este primer prototipo se utilizó un haz de fibras compuesto por 19 fibras ópticas de vidrio multimodo, todas iguales con una apertura numérica de 0,22 y un radio del núcleo de 100 µm. Su longitud total era de 3 metros y el rango de temperaturas para su utilización de -190 a 350 °C. Su estructura se puede observar en la Figura 11. Si nos fijamos en la sección transversal de la rama común del haz, podremos ver claramente la distribución coaxial del mismo. En el centro se encuentra la fibra transmisora (amarilla) que va a ser la encargada de llevar la luz desde la fuente hasta los álabes. Esta luz se reflejará en el álabe y será recogida por dos anillos de fibras receptoras que denominaremos como anillo 1, el más cercano a la fibra transmisora (6 fibras), y anillo 2, el más lejano de la fibra transmisora (12 fibras).

La fibra transmisora transporta la luz de la fuente conectada a la rama 1 del haz. En este prototipo se ha utilizado como fuente de luz un módulo láser, concretamente el módulo FP-65 7FE-SMA de Laser Components. Se trata de un láser de diodo que emite una potencia de 7 mW a una longitud de onda de 655 nm. Las fibras receptoras se van a agrupar en las ramas 2 (anillo 1) y 3 (anillo 2) del haz, y se conectarán a sendos fotodetectores. Se han empleado los PDA 100A-EC de Thorlabs que básicamente consisten en un diodo PIN inversamente polarizado y un amplificador de transimpedancia de ganancia configurable. Para adquirir y guardar las señales del fotodetector se empleó el osciloscopio Infinium MSO9104A de Keysight Technologies que dispone de una frecuencia de muestreo máxima de 20 GSa/s.

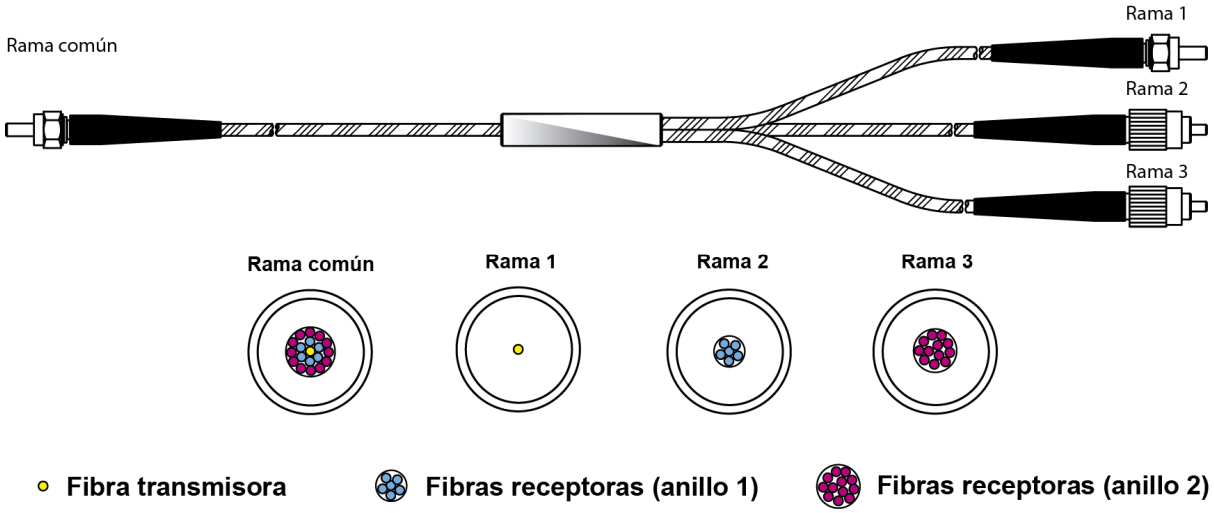

Figura 11. Haz de fibras utilizado en el primer prototipo.

Se ha elegido un haz de fibras trifurcado para poder obtener una señal diferencial que permita atenuar los efectos de las posibles variaciones en la reflectividad de los álabes, fluctuaciones de la fuente o pérdidas de potencia óptica. El utilizar un haz trifurcado en lugar de uno bifurcado permite calcular la distancia a los álabes en función del cociente de las tensiones de los fotodetectores conectados en las ramas 2 y 3. Vamos a denominar V_1 a la tensión obtenida en el fotodetector de la rama 2, debida a la irradiancia de la luz reflejada recogida por el anillo 1 de fibras receptoras. V_2 será la tensión obtenida debido a la luz recogida por el anillo 2. Ambas tensiones van a depender de la responsividad del fotodetector, de la ganancia del amplificador y de la irradiancia de la luz recogida por cada anillo. Estas tensiones proporcionadas por los fotodetectores pueden expresarse como:

$$V_1 = I_1 \cdot A_1 \cdot R_1 \cdot G_1 = K_0 \cdot K_1 \cdot F_1(d) \cdot R_{álabe} \cdot I_0 \cdot A_1 \cdot R_1 \cdot G_1 \quad (4)$$

$$V_2 = I_2 \cdot A_2 \cdot R_2 \cdot G_2 = K_0 \cdot K_2 \cdot F_2(d) \cdot R_{álabe} \cdot I_0 \cdot A_2 \cdot R_2 \cdot G_2 \quad (5)$$

donde,

V_i, es la tensión obtenida en el fotodetector *i*.

I_i, es la irradiancia de la luz que llega al fotodetector procedente del anillo *i*.

A_i, es el área iluminada sobre el fotodetector debido a la luz recogida por el anillo *i*.

R_i, es la responsividad del fotodetector *i*.

G_i, es la ganancia del fotodetector *i*.

K_0, es una constante que representa las posibles fluctuaciones de la fuente de luz.

K_i, es una constante que representa las posibles pérdidas en las fibras del anillo *i*.

$F_i(d)$, es una función que representa la irradiancia recogida por las fibras del anillo *i* en función de la distancia a la que se encuentra el álabe.

$R_{álabe}$, es la reflectividad del álabe.

I_0, es la irradiancia de la luz que sale de la fibra transmisora.

Dividiendo ambas ecuaciones obtenemos:

$$\frac{V_2}{V_1} = \frac{K_1 \cdot F_1(d) \cdot A_1 \cdot R_1 \cdot G_1}{K_2 \cdot F_2(d) \cdot A_2 \cdot R_2 \cdot G_2} = K \cdot F(d) \tag{6}$$

De la Ecuación 6 se obtiene que teóricamente el valor del cociente de las tensiones de los fotodetectores depende únicamente de un valor constante y de una función de la distancia a la que se encuentra el álabe. Por lo tanto no se vería afectado por las fluctuaciones del láser, ni por cambios en la reflectividad de los álabes, ni por las pérdidas en las fibras [22,67].

La curva proporcionada por el cociente de las tensiones en función de la distancia a la que se encuentra el álabe, va a ser la curva de calibración del sensor. Para obtenerla en el laboratorio se ha utilizado el montaje de la Figura 12. En primer lugar la rama común del haz de fibras se ha fijado a un poste mediante adaptador, de forma que la luz incida perpendicularmente sobre el álabe (Figura 13) que se ha instalado en una plataforma de desplazamiento lineal.

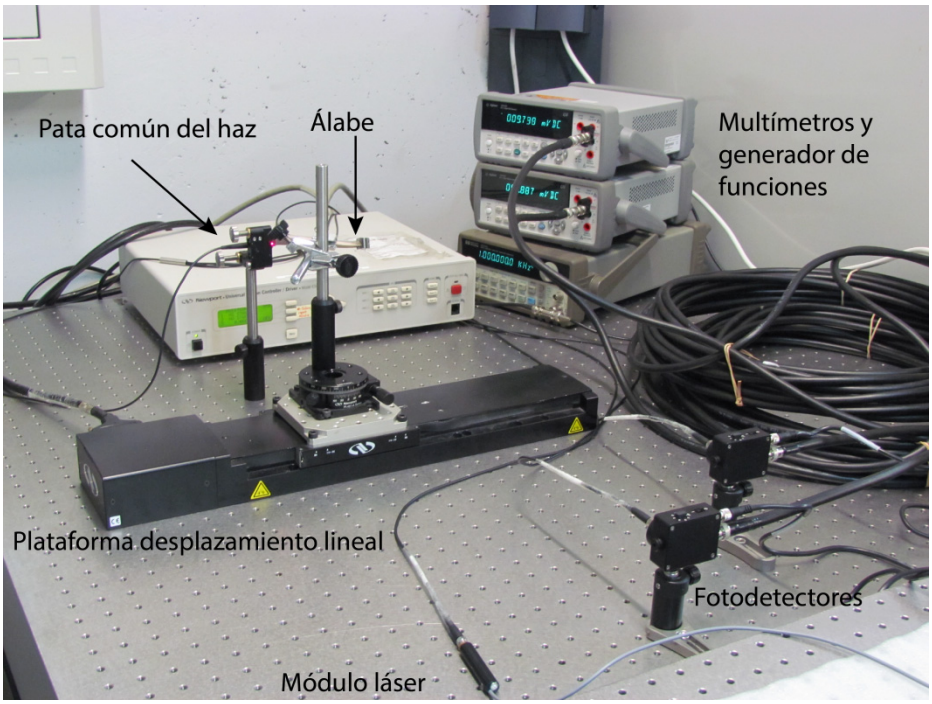

Figura 12. Montaje utilizado durante la calibración del sensor.

Para obtener la curva de calibración el álabe se fue alejando de la punta de la rama común en saltos de 10 µm y hasta una distancia total de 10 mm. En cada salto los multímetros obtienen la tensión de ambos fotodetectores. Debido a lo tedioso de este proceso se realizó un programa en LabVIEW para

automatizarlo. La pantalla principal de este programa puede observarse en la Figura 13. Este programa controla el movimiento de la plataforma, las lecturas de los dos multímetros que se producen en el mismo instante mediante una señal de disparo proporcionada por el generador de funciones (que también es controlado por el programa), el almacenamiento de los datos en archivos y su representación por pantalla.

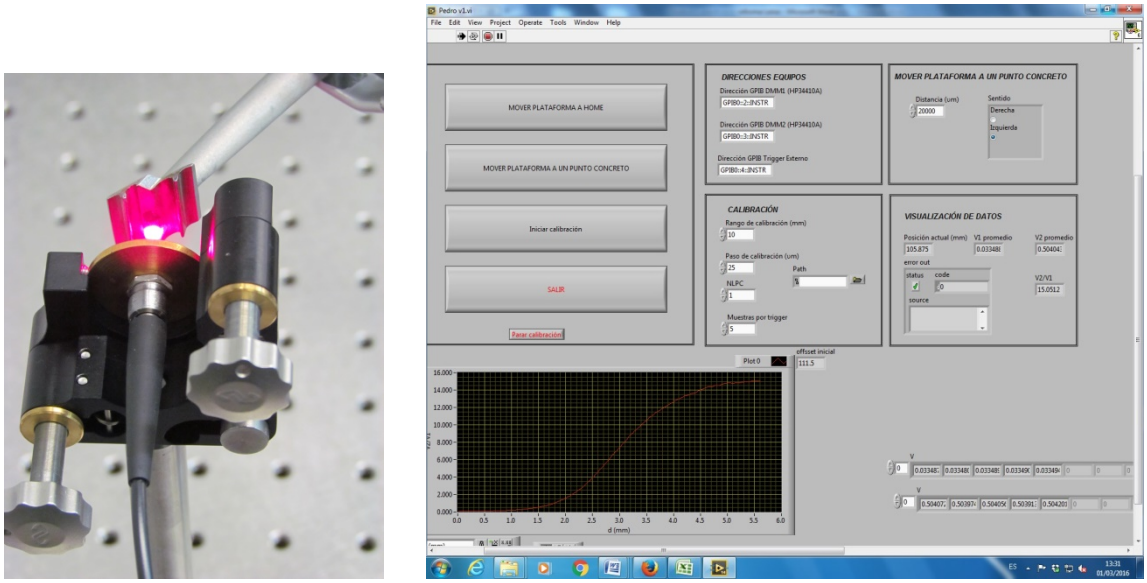

Figura 13. Detalle del álabe durante el proceso de calibración (izquierda). Imagen de la pantalla principal de programa desarrollado para la automatización de la calibración (derecha).

Una vez finalizado el proceso de calibración para el primer prototipo del sensor, la curva obtenida se ha representado en la Figura 14. En ella se pueden diferenciar claramente dos regiones de funcionamiento para dos rangos de medida. La región I que se caracteriza por su alta sensibilidad y bajo rango de medición, mientras que la región II es de menor sensibilidad pero mayor rango. Como veremos a continuación, los condicionantes del montaje del sensor en la carcasa del túnel de viento imponen el empleo de la región II. En dicha región se ha linearizado la curva obteniendo la expresión de la Ecuación 7 con un coeficiente de determinación $R^2 = 0.9945$.

$$V_2/V_1 = -0,0896 \cdot d + 1,8783 \tag{7}$$

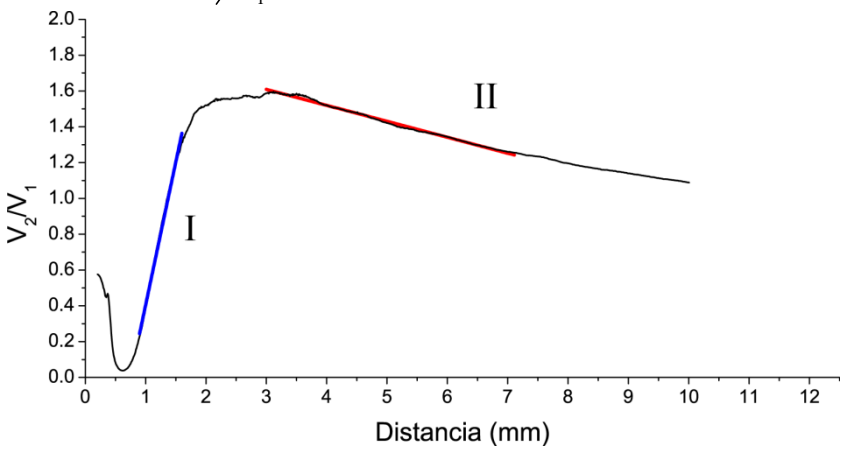

Figura 14. Curva de calibración para el prototipo 1. Se representan la región I en azul y la región II en rojo.

El funcionamiento de este sensor se comprobó en una turbina de baja presión con 146 álabes instalada en el túnel de viento que posee el Centro de Tecnologías Aeronáuticas en sus instalaciones de Zamudio. Se trata de un banco de pruebas transónico con un flujo de aire continuo. El nivel de presión, la temperatura y el flujo másico pueden ser controlados individualmente. De esta forma el número de Mach y de Reynolds pueden ser modificados de forma independiente. Para suministrar el aire en el túnel se emplean dos compresores eléctricos de potencias 3,7 MW y 5 MW, respectivamente, y que son capaces de aportar un flujo másico máximo de 18 kg/s a una presión máxima de 4,5 bar. La temperatura en el interior del túnel se puede regular desde temperatura ambiente hasta los 160 °C. Consta de un único eje capaz de girar hasta 7.800 rpm (revoluciones por minuto) y su sección es de un metro. También es importante destacar que se pueden adquirir hasta 800 señales de presión y 200 de temperatura [68].

Debido a las características geométricas del álabe (ver Figura 15), se decidió iluminar a la superficie plana situada entre los dos cuchillos. De esta forma se consigue obtener la mayor potencia de luz reflejada posible. En caso de iluminar en uno de los cuchillos cualquier posible vibración de los álabes haría que se iluminase otra zona del álabe, produciendo un error en la medida. En estas circunstancias para obtener el valor real del tip clearance se deberá restar a la distancia dada por el sensor los 1,3 mm correspondientes a la distancia entre la plataforma iluminada y el extremo del cuchillo.

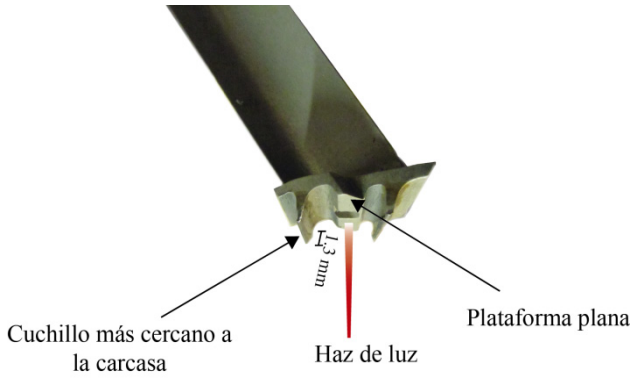

Figura 15. Geometría del álabe de la turbina utilizada para la evaluación del primer prototipo.

Para poder acoplar la rama común del haz de fibras a la carcasa del túnel se diseñó un adaptador especial que puede observarse en la Figura 16. Consta de dos partes, una cabeza roscada que se fija al conector SMA en la rama común del haz de fibras, y un armazón al que se fija esta cabeza roscada y que es atornillado a la carcasa del túnel.

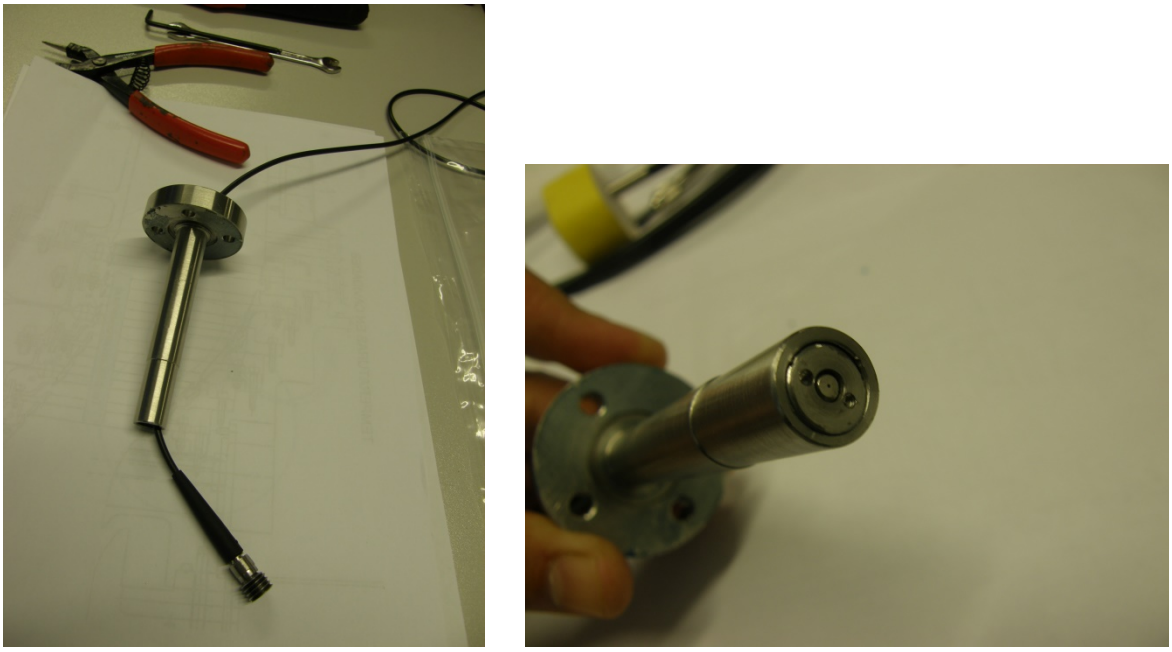

Figura 16. Adaptador diseñado para la fijación del sensor a la carcasa del túnel de viento.

Como puede observarse en la Figura 16, el extremo del conector SMA no queda a ras con el acoplador y existe un pequeño desplazamiento hacia adentro que habrá que tener en cuenta a la hora de calcular el valor del tip clearance real. Este desplazamiento es de 0,45 mm. Por lo tanto, para obtener el valor real del tip clearance habrá que restar esta distancia al valor dado por el sensor. Teniendo además en cuenta la diferencia entre la altura del cuchillo y la de la plataforma iluminada, habrá que restar un total de 1,75 mm a la distancia proporcionada por el sensor para obtener el valor real del tip clearance. Dado que este valor se esperaba que fuese alrededor de 3 mm, las distancias estimadas a medir durante los ensayos serán de unos 4,5-5 mm. Estas distancias nos obligan claramente a emplear la región II de la curva de calibración. En la Figura 17 puede observarse el sensor instalado en el túnel de viento durante los ensayos.

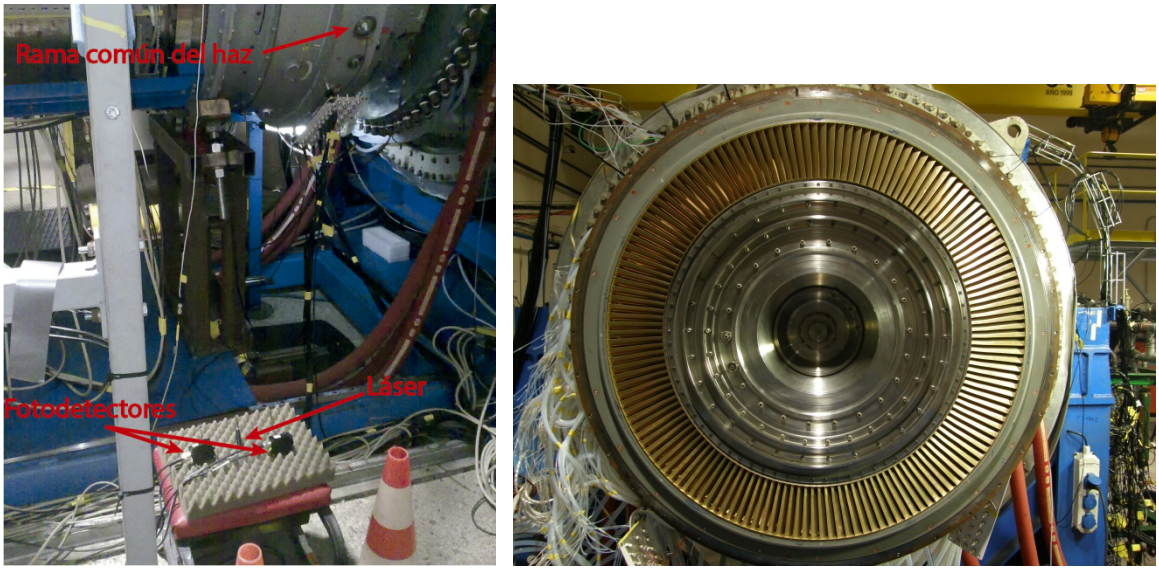

Figura 17. Sensor instalado en el túnel durante los ensayos (izquierda) y túnel abierto con la turbina a probar (derecha).

En estos ensayos se eligió una ganancia de 0,75 x10^4 V/A para ambos fotodetectores. En la Figura 18 pueden observarse las señales obtenidas. Para el caso del tip clearance los resultados obtenidos con el sensor fueron comparados con las medidas obtenidas mediante el empleo de un sensor de descarga eléctrica (Rotatip RCSM4 de Rotadata). Este sensor es el normalmente utilizado por el Centro de Tecnologías Aeronáuticas en sus ensayos. Los resultados muestran diferencias menores del 3%, aunque para conseguir estos valores además de un tedioso procesado, se debió promediar un gran número de mediciones y esto no va a ser siempre posible durante los ensayos, por lo que este método de procesado era inviable.

Para obtener el valor de la precisión del sensor en el laboratorio se empleó el mismo montaje que para la calibración, pero en este caso se recorrió todo el intervalo de medida en saltos de 25 µm. Se repitió el proceso tres veces y se calculó la deviación estándar del conjunto de las tres medidas para cada salto. Finalmente, se tomó como precisión del sensor la media de todas las desviaciones obtenidas y este valor fue de 141 µm. Este valor justifica la necesidad de promediar tantas medidas para la obtención de valores coherentes en las medidas, ya que las variaciones totales en el valor del tip clearance son aproximadamente unas 60 µm de un punto de trabajo a otro. La causa fundamental de esta pobre precisión era el ruido modal a la salida de la fibra transmisora [69] y para mejorarla se decidió reducirlo mediante diferentes métodos dando lugar a las siguientes versiones del sensor.

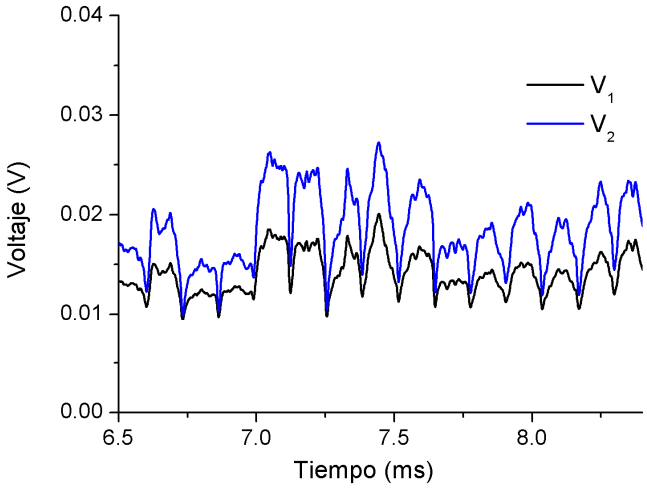

Figura 18. Señales obtenidas para ambos fotodetectores cuando la turbina está rotando a 3.148 rpm.

Los resultados obtenidos para el tip timing fueron bastante más satisfactorios. Para el procesado se utilizó la señal V_2 ya que proporcionaba una amplitud mayor. El primer paso para obtener las deflexiones de los álabes es decidir el método para determinar el instante de llegada de cada álabe. En este caso se empleó el método de la segunda derivada. Este procedimiento consiste en calcular la segunda derivada de V_2 y elegir un valor umbral que al ser sobrepasado por el valor de la segunda derivada determina el instante de llegada del álabe (ver Figura 19).

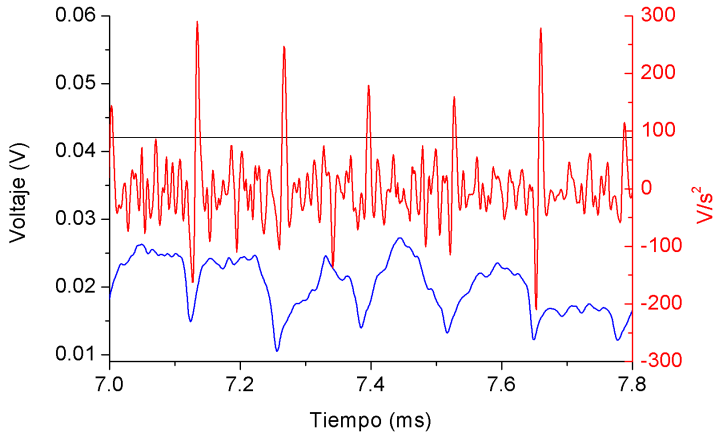

Figura 19. Señal V2 (azul), su segunda derivada (rojo) y valor umbral (negro) para determinar la llegada de cada álabe.

Una vez conocidos los instantes de llegada de los álabes a la posición en la que se encuentra el sensor, hay que calcular los instantes teóricos de llegada a partir de la velocidad de rotación y del número de álabes del blisk. Conocidos ambos, y el radio del blisk (R_b) se puede obtener la deflexión de cada álabe según la Ecuación 8.

$$d_i = \frac{2 \cdot \pi \cdot R_b}{T_r} \cdot \Delta t_i \tag{8}$$

donde Δt es la diferencia entre el tiempo de llegada real y teórico para cada álabe, y T_r es el periodo de rotación del blisk.

En la Figura 20 se pueden observar las deflexiones de cada uno de los 146 álabes que componen la turbina ensayada. Si se calcula la transformada de Fourier de estas deflexiones se obtiene el espectro de la onda viajera. Este espectro proporciona un valor medio de la amplitud de vibración de todos los álabes que componen la turbina para un EO y un ND determinados.

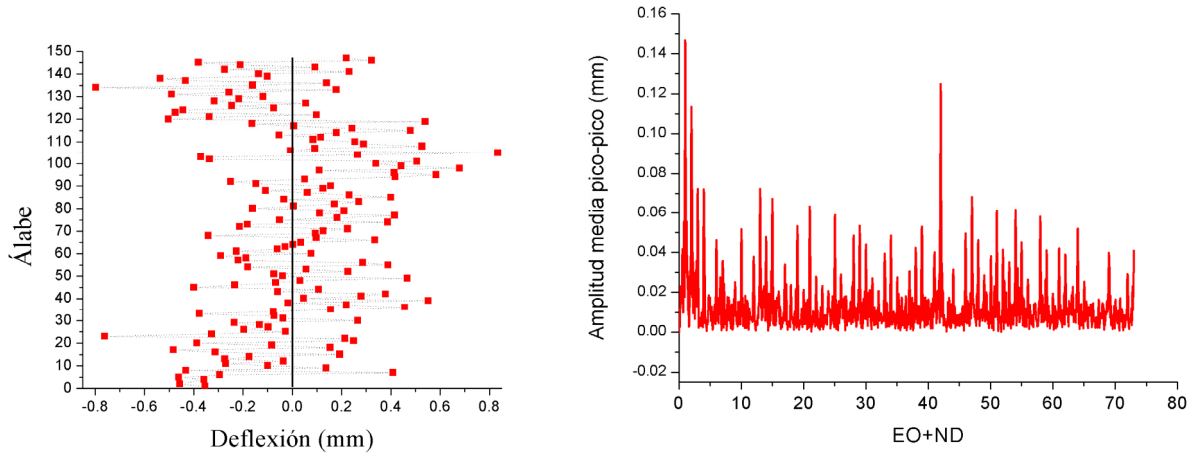

Figura 20. Deflexiones para cada uno de los álabes durante una vuelta (izquierda) y espectro de la onda viajera (derecha).

Una descripción más detallada del prototipo 1, así como de los resultados obtenidos, se puede encontrar en el **Artículo 2**.

2.2-2. Segundo prototipo

Como primera opción para disminuir el ruido modal que aparece en la fibra transmisora multimodo debido al empleo de un láser como fuente de luz [70-72], se decidió usar un mezclador de modos por su sencillez [73]. La fibra transmisora tiene una longitud aproximada de 3 metros por lo que los modos que se propagan por ella no van a alcanzar la distribución de equilibrio modal [74]. Para conseguir una mejor distribución de la potencia entre todos los modos se colocó el mezclador de la Figura 21 entre la fuente de luz y el haz de fibras. Este mezclador consta de dos cilindros de 42 mm de diámetro y separados 3 mm entre sí. Una fibra óptica de plástico se enrolló entre ambos cilindros siguiendo las directrices dadas en el estándar JIS C 6863 [75]. Las pérdidas de inserción del mezclador fueron compensadas aumentando la potencia del módulo láser empleado. Se utilizó el FP-SMA-650-30P que proporciona una potencia a su salida de 30 mW. Como fotodetectores se emplearon los mismos que en el caso anterior pero con una configuración de ganancias asimétrica (0,75 x 10^5 V/A para el primero y 2,38 x 10^5 V/A para el segundo). Esta configuración de ganancias va a permitir aumentar hasta en cuatro veces la sensibilidad del sensor.

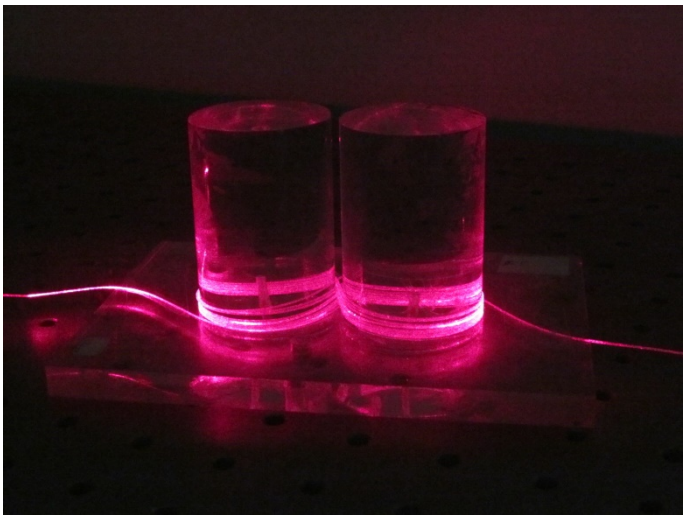

Figura 21. Mezclador de modos utilizado en el segundo prototipo.

Desafortunadamente cuando se fue a comprobar el funcionamiento de este prototipo la turbina inicial ya no se encontraba instalada en el túnel de viento. En su lugar se había instalado una turbina con 106 álabes con una geometría muy diferente a los de la turbina previa. Como se puede observar en la Figura 22 los cuchillos de los álabes son mucho mayores, lo que hace que la distancia a la plataforma también lo sea. Además, la superficie iluminada no es tan plana como en el caso anterior con lo que retornaba menos potencia al haz de fibras. Por todo esto las señales recibidas al girar la turbina eran demasiado pequeñas y el segundo prototipo no pudo ser evaluado en el túnel de viento.

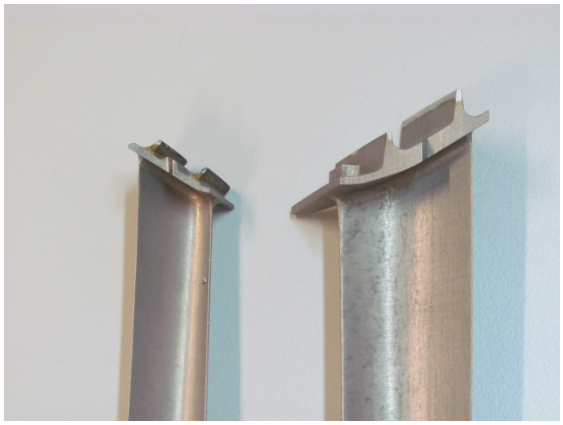

Figura 22. Álabes correspondientes a la primera (izquierda) y segunda (derecha) turbinas instaladas en el túnel de viento.

2.2-3. Tercer prototipo

Dado que en las fibras ópticas de plástico se va a alcanzar la distribución de equilibrio modal en una longitud de fibra menor [76,77], se decidió utilizar este tipo de fibras en el tercer prototipo del sensor. En este caso se empleó un haz de fibras de plástico cuyo núcleo tenía un diámetro de 240 µm y una apertura numérica de 0,5. Como fuente de luz se empleó el módulo láser comentado en el apartado anterior y también se repitió la configuración asimétrica de ganancia para los fotodetectores.

En el montaje para obtener la calibración el cuchillo del nuevo álabe no permite acercar el extremo de la rama común hasta que esté casi en contacto con la plataforma a iluminar, como ocurría en el primer prototipo. En este caso el soporte va a tocar en el cuchillo antes de que el extremo de la rama común del haz llegue a la plataforma. Por ello, con este nuevo montaje no vamos a tener que sustraer ninguna cantidad de la distancia medida para obtener el tip clearance, ya que se va obtener directamente la distancia entre el sensor y el cuchillo. La curva de calibración obtenida junto a la ecuación correspondiente a su linealización y el coeficiente de determinación se muestran en la Figura 23.

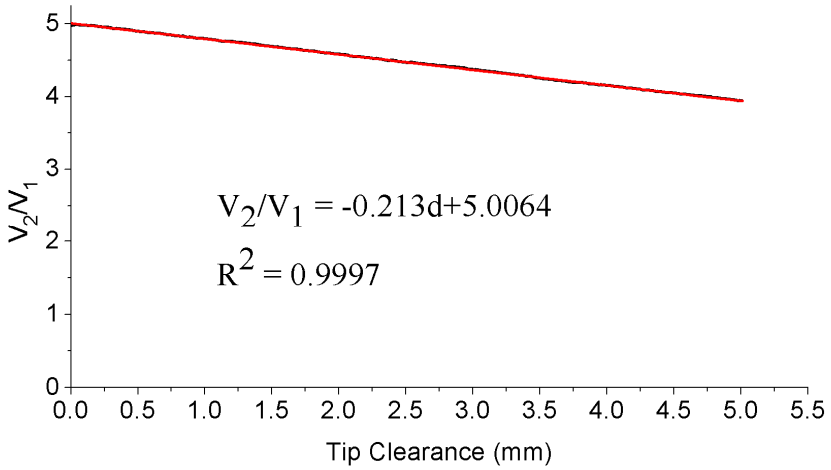

Figura 23. Curva de calibración obtenida para el tercer prototipo (negro) y su ajuste lineal (rojo) para el intervalo de 0-5 mm.

La precisión obtenida para este prototipo en el laboratorio y, siguiendo el mismo proceso que para el primer prototipo, fue de 33 µm. Durante los ensayos se midieron los valores de tip clearance para seis velocidades de rotación diferentes en dos sesiones separadas tres días. Para comparar la precisión obtenida en el laboratorio con la de las medidas en el túnel de viento se calculó la desviación estándar de

las dos medidas a cada velocidad de rotación. Posteriormente, se calculó la media de las seis desviaciones y este valor fue tomado como la precisión del sensor para los ensayos. El valor obtenido fue 25 µm, que es un valor dentro del objetivo inicial del sensor. Además hay que tener en cuenta que la distancia desde el extremo del haz de fibras hasta la plataforma del álabe en la que se refleja la luz en esta turbina era de unos 18 mm, cuando en el primer prototipo era de tan solo unos 5 mm, lo cual dificulta aún más la medida en la nueva turbina. En este caso el procesado también es menos laborioso. Se adquirieron las señales durante un minuto y se calculó el valor del tip clearance para cada una de las revoluciones de la adquisición, siendo el valor final la media de los tip clearance para cada una de las revoluciones analizadas. De esta forma se evita tener que volver a promediar más adquisiciones a la misma velocidad como ocurría en el procesado del primer prototipo.

El único inconveniente para este sensor es que su temperatura de trabajo máxima es de 60 °C, que es adecuada para ciertas pruebas realizadas a temperatura ambiente pero insuficiente para la mayoría de los ensayos en el túnel de viento. Este límite en la temperatura de trabajo no está impuesto por las fibras ópticas de plástico, sino por el adhesivo utilizado a la hora de fabricar el haz.

2.2-4. Cuarto prototipo

Ante las limitaciones del anterior prototipo se decidió utilizar una fibra monomodo como fibra transmisora para reducir el ruido modal a la salida del sensor [78], manteniendo las mismas fibras multimodo como receptoras. El diámetro del núcleo de la fibra transmisora elegida fue 4,3 µm y su apertura numérica 0,12. Como fuente de luz en esta versión del sensor se utilizó el módulo HSML-0660-20-FC de Frankfurt Components cuya potencia de salida era 20 mW y su longitud de onda 660 nm. Los fotodetectores y su configuración de ganancias fueron los mismos que para el caso anterior. La curva de calibración obtenida y la ecuación de su ajuste lineal al tramo 0-5 mm se representan en la Figura 24.

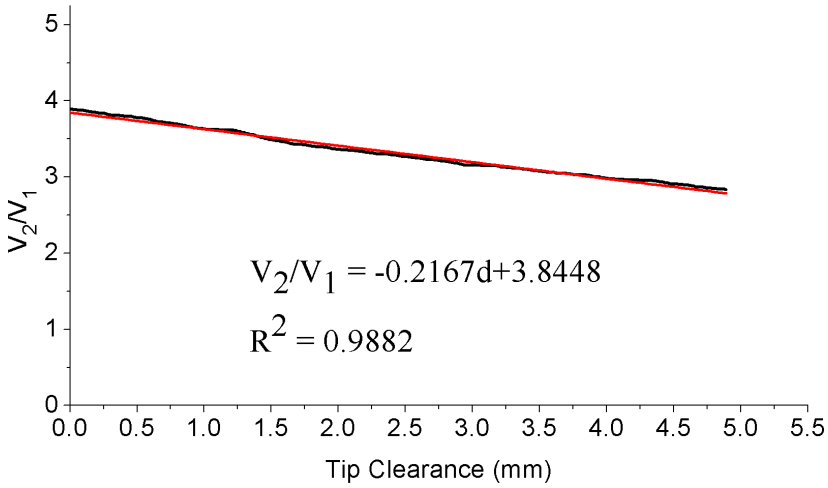

Figura 24. Curva de calibración obtenida para el cuarto prototipo (negro) y su ajuste lineal (rojo) para el intervalo de 0-5 mm.

Para comprobar el funcionamiento de este prototipo de nuevo se midió el tip clearance para seis velocidades diferentes. En este caso debido a que la turbina permaneció durante más tiempo girando a velocidad constante, se pudieron realizar dos medidas de cada velocidad en cada una de las dos sesiones. La precisión obtenida para estas medidas fue de 28 µm muy similar a la anterior versión, pero teniendo en cuenta que en este caso las velocidades de giro de la turbina eran sensiblemente mayores. Esta mayor velocidad va a producir mayores amplitudes de vibración en los álabes lo que se traduce en mayor

dispersión en las medidas. Todos los resultados obtenidos con estos prototipos, así como más detalles sobre su instalación en el túnel de viento se encuentran recogidos en el **Artículo 3**.

Con este prototipo se cumple el objetivo inicial en cuanto a la precisión del sensor, y además se supera la limitación de la anterior versión en cuanto a la temperatura de trabajo, permitiendo ensayos hasta los 350 °C. Sin embargo, el hecho de que se necesite adquirir un minuto para obtener información suficiente en las señales era un punto a mejorar. Por ello se diseñó la quinta versión del sensor en la que se utilizaría la región I de la curva de calibración para maximizar la relación señal a ruido, permitiendo una mayor precisión de las medidas y el poder diseñar un programa que permita obtener resultados en tiempo real sin necesidad de un procesado posterior.

2.2-5. Quinto prototipo

En la Tabla 1 se puede observar a modo de resumen las principales características de las versiones anteriores del sensor. Hasta este momento dos han sido las características de diseño que han mejorado el rendimiento del sensor. Por un lado se ha suprimido el ruido modal a la salida del haz de fibras mediante el empleo de una fibra transmisora monomodo, lo que ha redundado en una mejora de la precisión hasta llegar a valores que cumplen con el objetivo inicial de 30 μm. Por otro lado, el empleo de ganancia asimétrica para los fotodetectores ha proporcionado un aumento en la sensibilidad de más del doble respecto del valor del prototipo inicial. Sin embargo, para poder seguir mejorando las prestaciones del sensor había que abandonar el funcionamiento en la región II de la curva de calibración. Como claramente se observa en la Figura 14, la región I aporta una mayor sensibilidad y además una mejor relación señal a ruido ya que la potencia de la luz reflejada por los álabes que llega a los anillos receptores es mayor. Es por ello que en esta última versión del sensor se trabajó con la región I.

A finales del año 2015 surgió la posibilidad de una colaboración con el Instituto Tecnológico de las Fuerzas Aéreas Polacas (ITWL). Esta organización científica dependiente del Ministerio de Defensa polaco se ocupa de dar soporte y soluciones a todo tipo de problemas relacionados con la aeronáutica. En nuestro caso se realizó una cooperación con la sección dedicada al estudio de los motores, y que cuenta con un banco de ensayos en el que está instalado un motor SO-3. Este motor se emplea para propulsar el caza de entrenamiento TS-11 “Iskra” empleado por las fuerzas aérea polacas (entre otras) para el adiestramiento de sus pilotos (ver Figura 25 y 26).

Figura 25. Caza TS-11 “Iskra”. Fuente: www.airfoto.pl.

Prototipo	1	2	3	4
Módulo láser	λ = 655 nm Potencia = 7 mW	λ = 655 nm Potencia = 30 mW	λ = 655 nm Potencia = 30 mW	λ = 660 nm Potencia = 20 mW
Haz de fibras ópticas	Fibras transmisora y receptoras multimodo Ø $_{nucleo}$ = 100 µm NA = 0,22	Fibras transmisora y receptoras multimodo Ø $_{nucleo}$ = 100 µm NA = 0,22 Mezclador de modos	Fibras transmisora y receptoras POF Ø $_{nucleo}$ = 240 µm NA = 0,5	Fibras transmisora monomodo (Ø $_{nucleo}$ = 4,3 µm) NA = 0,12 y receptoras multimodo (Ø $_{nucleo}$ = 100 µm) NA = 0.22
Fotodetectores	Ganancia simétrica $G_1 = G_2 = 0{,}75 \times 10^4$ V/A	Ganancia asimétrica $G_1 = 0{,}75 \times 10^4$ V/A $G_2 = 2{,}38 \times 10^5$ V/A	Ganancia asimétrica $G_1 = 0{,}75 \times 10^4$ V/A $G_2 = 2{,}38 \times 10^5$ V/A	Ganancia asimétrica $G_1 = 0{,}75 \times 10^4$ V/A $G_2 = 2{,}38 \times 10^5$ V/A
Curva de calibración	$V_2/V_1 = -0{,}0896 \cdot d + 1{,}8783$	$V_2/V_1 = -0{,}2002 \cdot d + 2{,}4578$	$V_2/V_1 = -0{,}213 \cdot d + 5{,}006$	$V_2/V_1 = -0{,}2167 \cdot d + 3{,}8448$
Sección transversal de la salida del sensor			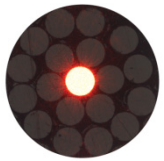	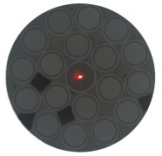
Precisión laboratorio	141 µm	51 µm	33 µm	24 µm
Precisión túnel de viento	24 µm	N.A.	25 µm	28 µm

Tabla 1. Resumen de las características y resultados obtenidos para las 4 prototipos previos.

Figura 26. Motor SO-3 en el banco de ensayos (izquierda) y sala de control (derecha). Imágenes cortesía del ITWL.

Se decidió realizar los ensayos en la primera de las siete etapas de las que consta el compresor, ya que es de fácil acceso y la temperatura de funcionamiento es mucho menor que en las etapas cercanas a la cámara de combustión. Esta etapa constaba de 28 álabes fabricados en acero y en los que la zona a iluminar tiene una anchura de 1,5 mm (ver Figura 27). Esta superficie es rugosa y frecuentemente presenta corrosión lo que dificulta su medida con métodos ópticos. Para acoplar el haz de fibras a la carcasa del motor se fabricó el adaptador mostrado en la Figura 27.

Una vez acoplado el sensor se estimó que el rango de distancias a medir sería de 2 a 4 mm. Luego para adaptar la región I al rango de medida del sensor son necesarias dos modificaciones en su diseño. En primer lugar la curva de calibración se tiene que desplazar de forma que la región I comience a una distancia de 2 mm. El comienzo de esta región viene determinado por la distancia del álabe a la cual la luz reflejada comienza a entrar en las fibras del segundo anillo. Es por ello que se debe aumentar la distancia entre la fibra transmisora y el anillo 2 para conseguir que la región I se desplace hacia la zona deseada. Para conseguirlo se podría haber introducido un gran número de agujas separadoras, pero lo que se hizo fue introducir otro anillo de fibras receptoras y solo una pequeña cantidad de estas agujas. Con lo que se obtuvo un haz de fibras tetrafurcado en lugar de los trifurcados de las versiones anteriores. La disposición final del haz se puede observar en la Figura 28. Este nuevo anillo de fibras receptoras va a permitir el tener una rama adicional con la cual poder realizar medidas de tip timing con una configuración de ganancia para el fotodetector independiente de la necesaria para las medidas del tip clearance. Respecto a los anteriores haces cabe destacar que la rama común tiene una cabeza roscada (M6) en lugar de un conector SMA, para así facilitar la fabricación del adaptador a la carcasa.

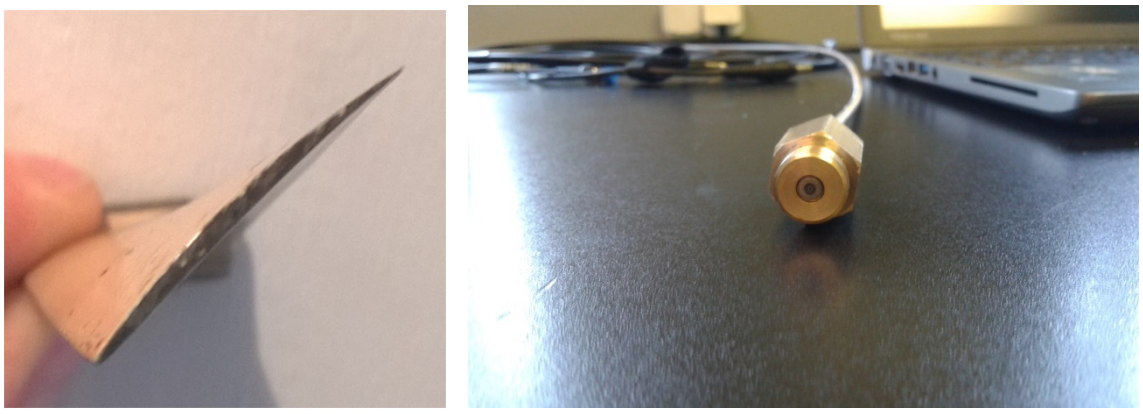

Figura 27. Superficie del álabe a iluminar (izquierda) y adaptador para acoplar el haz de fibras a la carcasa del motor (derecha).

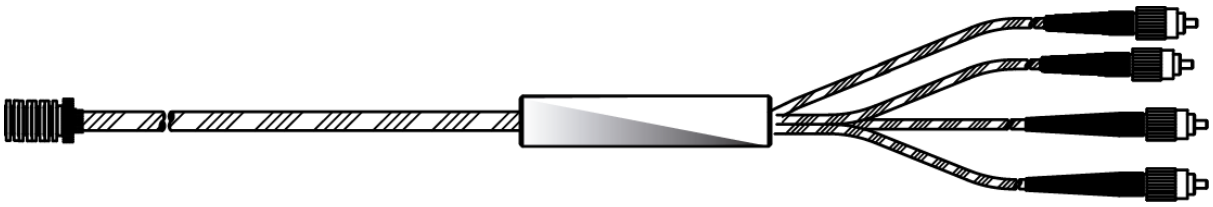

Figura 28. Disposición final del haz tetrafurcado utilizada en este prototipo.

La segunda modificación en el diseño del haz de fibras debe proporcionar un aumento en el rango de la medida del sensor. La región I va a terminar en la distancia del álabe para la cual la luz reflejada por el mismo cubre completamente el anillo 2 de las fibras receptoras. Esta distancia se puede aumentar disminuyendo la apertura numérica de la fibra transmisora o aumentando el diámetro del núcleo de las fibras receptoras. En este caso se decidió utilizar la segunda opción y el resultado final puede observarse en la Figura 29. En esta figura también se detallan los tipos de fibra utilizados en cada uno de los anillos receptores, así como el tipo de fibra transmisora. En el diseño inicial las distancias mostradas en la Figura 29 eran R1 = 300 µm, R2 = 700 µm y R3 = 1.070 µm. Las distancias resultantes en el haz fabricado fueron R1 = 324 µm, R2 = 686 µm y R3 = 1.125 µm, ligeramente diferentes a las anteriores.

Previamente a la fabricación del haz se realizó un programa en Matlab para simular el comportamiento que tendría el sensor. Este programa se basó en los desarrollos teóricos descritos en diferentes artículos para la caracterización de sensores de desplazamiento basados en la modulación de la luz reflejada [57,66,79,80]. Estos artículos utilizan como blanco un espejo. Para que nuestro programa produjera resultados más cercanos a la realidad cuando se ilumina un álabe, se modificaran los parámetros que gobiernan la luz reflejada por el mismo. Para la obtención de esos parámetros se realizaron una serie de medidas con los haces trifurcados empleados en los prototipos anteriores. En la Figura 30 se representan la curva de calibración obtenida con el sensor y la simulada por el programa para la región I.

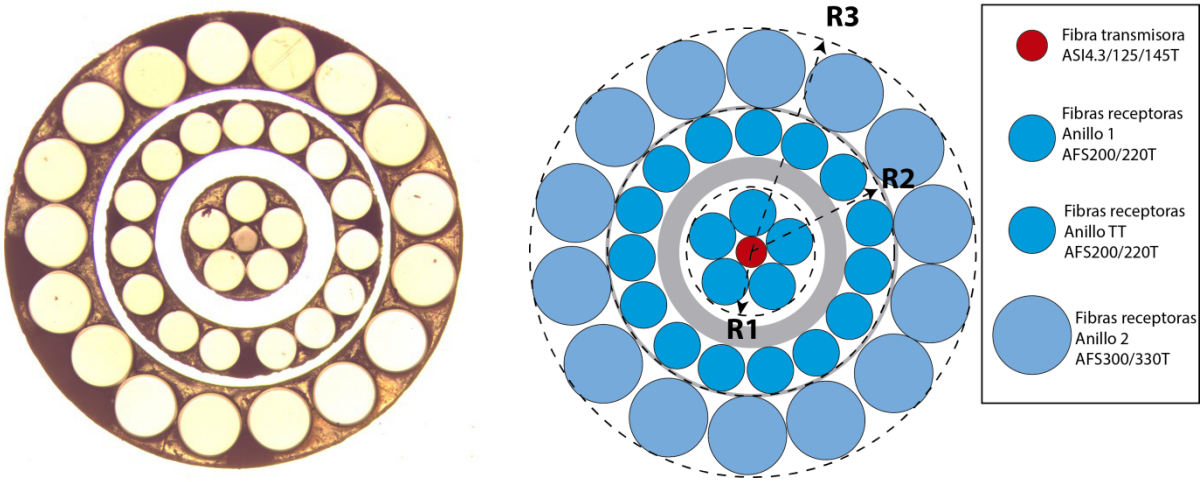

Figura 29. Imagen de la sección transversal del haz tetrafurcado fabricado (izquierda) y su diseño inicial (derecha).

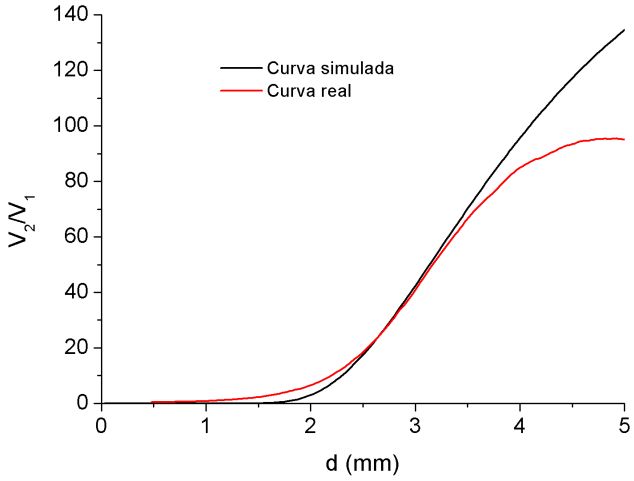

Figura 30. Curvas de calibración simulada y real para el intervalo de medida.

El módulo láser utilizado en este prototipo es idéntico al empleado en la anterior versión. Los fotodetectores también son los mismos, solo que ahora se tienen tres, uno por cada anillo. El anillo 1 (rama 2) y el 2 (rama 4) se emplearon para la medida del tip clearance y fueron los encargados de proporcionar las señales V_1 y V_2. Se configuraron con unas ganancias de 1,51 x 10^3 V/A y 1,51 x 10^5 V/A, respectivamente. El anillo TT (rama 3) proporcionó la señal para la medida del tip timing y su fotodetector se configuró con una ganancia de 4,75 x 10^4 V/A. Al configurarlo con esta ganancia el fotodetector proporciona el mínimo ancho de banda requerido que era de 200 kHz. Además cabe destacar que en este nuevo prototipo se introdujo un nuevo elemento. Entre el módulo láser y el haz de fibras se insertó un aislador óptico (IO-F-660 de Thorlabs) para evitar que posibles reflexiones llegaran hasta la fuente de luz y la desestabilizaran. En la Figura 31 aparecen representados todos los elementos correspondientes a esta versión del sensor.

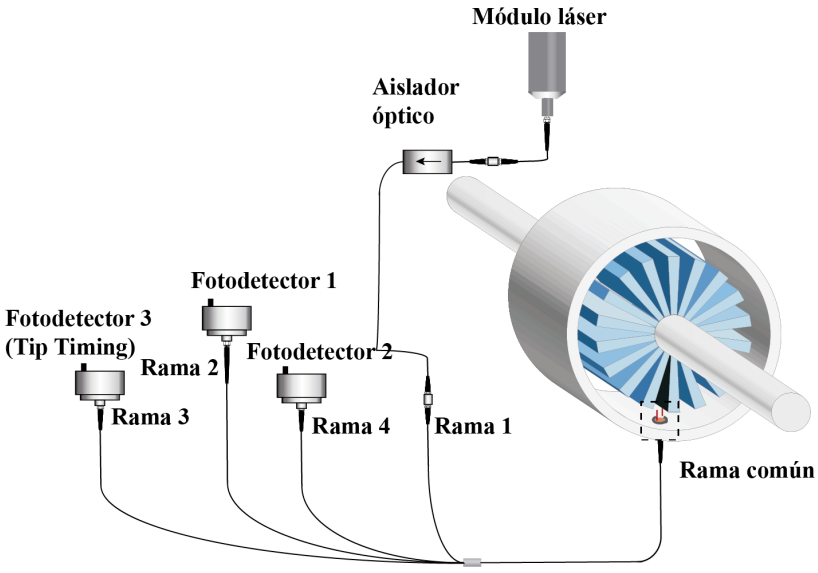

Figura 31. Componentes y estructura para el quinto prototipo.

Unos de los aspectos importantes a considerar durante los ensayos en el banco de pruebas del ITWL fue la baja temperatura ambiente que se esperaba. El banco de pruebas se encontraba en un recinto cerrado

pero debe disponer de la ventilación suficiente para eliminar los gases procedentes de la combustión. En este caso se trata de una ventilación natural y sin ningún tratamiento térmico, como los ensayos se realizaron en octubre (en Varsovia) se esperaban temperaturas entre 5-10 °C. Para comprobar el efecto que tiene la temperatura sobre el sensor se introdujeron todos los componentes en una cámara climática (ver Figura 32) y se obtuvo la curva de calibración para una temperatura de 10 y 20 °C (ver Figura 33). Las diferencias entre ambas fueron pequeñas en casi todo el intervalo de medida, salvo en el último tramo donde las diferencias llegaron a 100 µm. Por ello se empleó la obtenida a 10 °C.

Figura 32. Calibración del sensor en la cámara climática.

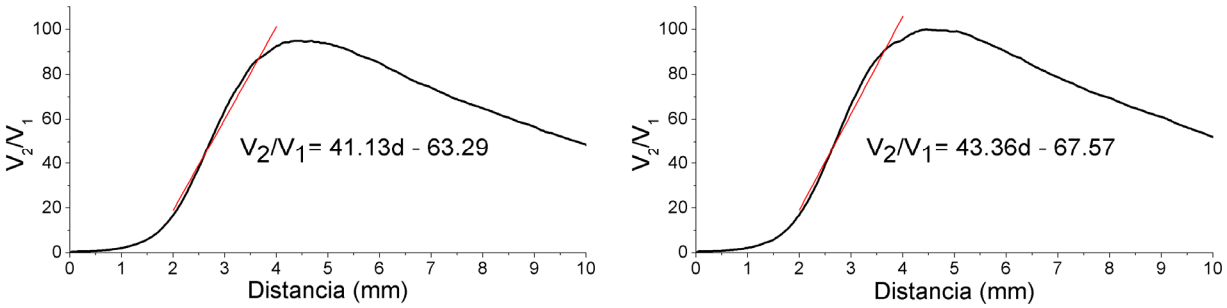

Figura 33. Curvas de calibración obtenidas a 20 °C (izquierda) y 10 °C (derecha), respectivamente.

Otro aspecto a tener en cuenta es el efecto que el posible cabeceo del álabe pudiera tener en la medida. Para medir este efecto en el laboratorio se hizo uso de una plataforma (APY001/M de Thorlabs) como la mostrada en la Figura 34 que nos permitió girar el álabe en sentido vertical y horizontal. El cabeceo esperado de los álabes era aproximadamente de 1º. En la Figura 34 se ha representado la curva de calibración para el caso de que no exista cabeceo y cuando este es ±2º en sentido horizontal y vertical. Se observa claramente que la región I es bastante insensible al cabeceo del álabe, dando los peores resultados en la parte final del rango de medida donde se llega a errores de máximos de 170 µm. Para el caso de que el cabeceo sea el esperado de 1º como máximo, los errores proporcionados por el sensor serían menores de 50 µm.

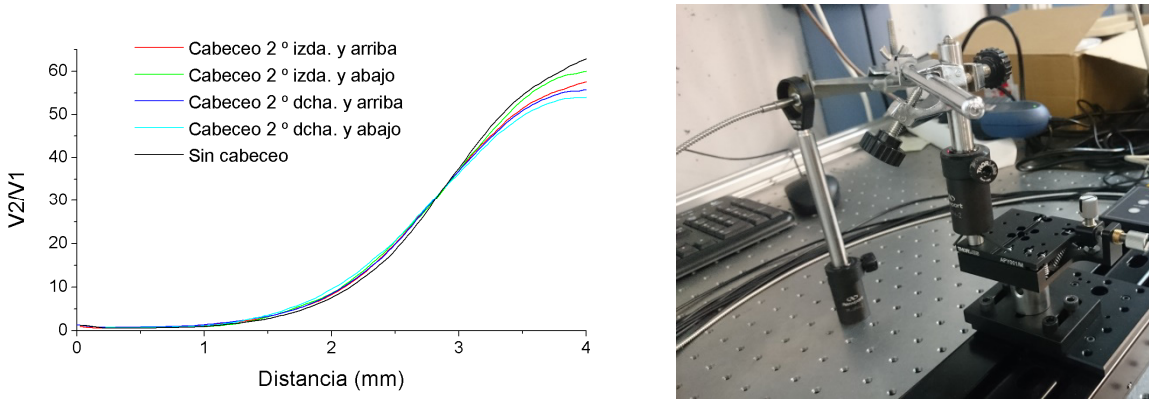

Figura 34. Curvas de calibración en función del cabeceo del álabe y montaje para la obtención de las curvas.

Las señales proporcionadas por los álabes del compresor van a presentar picos mucho más pronunciados que para el caso de una turbina, tal y como puede apreciarse en la Figura 35. Además existe una gran diferencia en sus amplitudes. Mientras V_1 presentaba una amplitud en torno a los 100 mV, V_2 alcanzaba varios voltios de amplitud. Esto obligó a tener que utilizar dos módulos de adquisición (PXIe-6358 de National Instruments) diferentes para poder sacar partido a los 16 bits de resolución que proporcionaban.

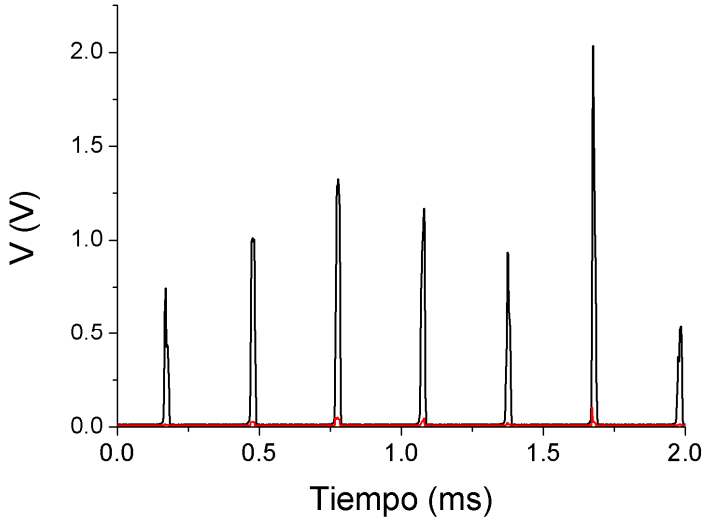

Figura 35. Señales V_1 (rojo) y V_2 (negro) proporcionadas por los fotodetectores cuando el motor está al ralentí.

Capítulo 3

Resultados

En este capítulo se muestran los resultados obtenidos con las diferentes versiones del sensor de fibra óptica. Se trata de aplicaciones específicas independientes de las pruebas preliminares para la comprobación del funcionamiento de cada uno de los prototipos. En la primera de ellas se caracteriza el comportamiento frecuencial de un disco rotativo mediante la medida del tip clearance en tres puntos diferentes del mismo. La segunda y la tercera consisten en la medida del tip clearance y del tip timing en el compresor de un motor real. La última aplicación consiste en la medida del tip clearance en una turbina de baja presión instalada en el túnel de viento empleando tres sensores.

3.1- Evaluación del comportamiento vibracional de un disco rotativo

En los motores aeronáuticos aparte de los blisk existen una serie de componentes rotativos con forma de disco encargados de separar zonas de diferente presión. La caracterización de las vibraciones en estos discos es de vital importancia para garantizar su rendimiento y alargar su tiempo de servicio [81], ya que los fallos debido a la fatiga producida por las vibraciones podrían desembocar en situaciones catastróficas. Justo después de evaluar el comportamiento del prototipo número 4 en el túnel de viento surgió la posibilidad de evaluar el comportamiento de uno de estos discos.

El disco a ensayar tenía un diámetro algo superior al medio metro y fue instalado en el túnel de viento de forma que se simularan sus condiciones reales de funcionamiento. Se creó un diferencial de presión entre ambas caras del disco, que a su vez creó un flujo de aire por el hueco existente entre el extremo del disco y la carcasa del túnel, es decir, por el tip clearance del disco. Bajo ciertas condiciones, este flujo de aire causaba la aparición de flameo en el disco. Como se ha explicado en el primer capítulo, esta inestabilidad aeroelástica provoca vibraciones autoiniciadas y automantenidas. El objetivo fundamental de los ensayos fue la caracterización del comportamiento vibracional del disco, es decir, al fabricante del disco le interesaba saber a qué frecuencias se producía el flameo y el número de diámetros nodales (ND) con los que el disco vibraba. Conocidos estos datos podría diseñar otra versión del disco en la que las vibraciones estarían atenuadas. La amplitud de las vibraciones también iba a ser interesante para comparar el grado de amortiguamiento conseguido.

Normalmente para realizar este tipo de estudios se utilizan galgas extensiométricas. Estos dispositivos presentan varios inconvenientes (analizados en el capítulo 1) y se decidió utilizar tres sensores ópticos que proporcionarían una medida sin contacto. Dado que al vibrar el disco iba a variar la distancia entre el mismo y la carcasa, se decidió caracterizar las vibraciones del disco mediante la medida del tip clearance del disco en tres puntos. Además, esta medida nos iba a permitir calcular la excentricidad del disco. Finalmente los sensores se colocaron formando un ángulo de 120º como se muestra en la Figura 36 y la distancia desde el extremo de cada haz de fibras a la zona iluminada del disco fue de 4,75 mm. La amplitud estimada para las vibraciones del disco era de 0,25 mm como máximo, por lo que la distancia a medir oscilaría entre 4,5 y 5 mm. Durante los ensayos la diferencia de presión entre ambos lados del disco osciló entre 2 y 3 bar, y se ensayaron cuatro velocidades de rotación diferentes: 0, $RPM_{nominal}$, 1,5 x $RPM_{nominal}$ y 2 x $RPM_{nominal}$, siendo $RPM_{nominal}$ la velocidad de rotación nominal para el disco.

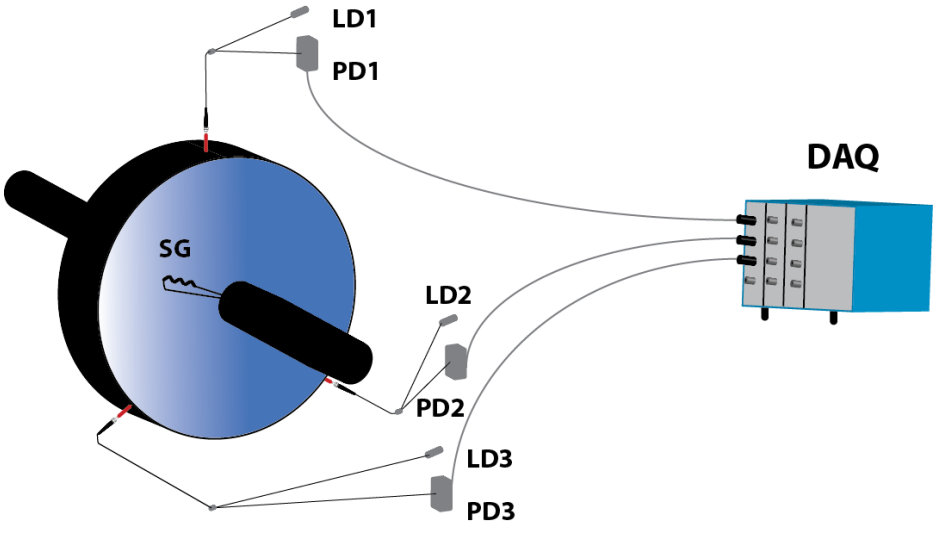

Figura 36. Montaje experimental para la medida del tip clearance en el disco rotativo.

Como se puede apreciar en la Figura 36, además de los sensores de fibra óptica se instaló una galga extensiómetrica para confirmar la detección de la frecuencia de vibración por parte de los sensores ópticos, y para determinar el ND del disco. Durante la instalación de los sensores surgió un problema con el número de canales disponibles para la adquisición de las señales. Debido al gran número de sensores para la medida de la presión y temperatura en diferentes puntos del túnel, solamente tres entradas del sistema de adquisición quedaron libres. Ante esta situación solo había dos alternativas: o se utilizaba un único sensor adquiriendo las señales de los dos fotodetectores, o se utilizaban tres sensores adquiriendo la señal de un solo fotodetector. Después de comprobar en el laboratorio que la pérdida de precisión debido a utilizar un único fotodetector era del ±8%, nos decidimos por utilizar la segunda opción. Esta pérdida de precisión no iba a influir en la detección de la frecuencia de vibración del disco, que es el objetivo fundamental de los ensayos. Solamente va a tener influencia en el cálculo de la amplitud, parámetro que se iba a usar como referencia de la mejora obtenida en un segundo prototipo. Además el uso de un único sensor óptico no iba a permitir calcular la excentricidad del disco.

En la Figura 37 puede observarse la zona a iluminar en el disco durante el proceso de calibración. Se decidió iluminar en la zona plana anterior al primer cuchillo. Este cuchillo tiene una longitud de 4,57 mm, por lo que para obtener el tip clearance real del disco hay que restar esta cantidad del valor proporcionado por el sensor. Respecto al proceso de calibración, se siguió el mismo procedimiento descrito en el capítulo 2 sólo que utilizando la tensión de un solo fotodetector. La curva obtenida se linealizó para el rango de medida esperado (4,5-5 mm).

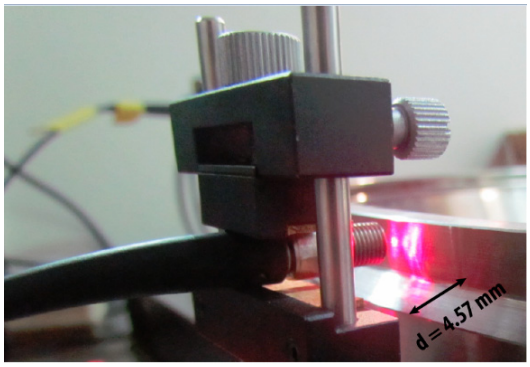

Figura 37. Disco iluminado durante el proceso de calibración.

Las señales fueron adquiridas a una frecuencia de muestreo de 25 kHz mediante un módulo PXI-4472 de National Instruments. Cada adquisición tuvo una duración de 5 segundos. La señal de la galga fue procesada por el programa que normalmente usa el Centro de Tecnologías Aeronáuticas (resolución en frecuencia 2 Hz), mientras que las señales del sensor óptico fueron procesadas por un programa basado en MATLAB desarrollado específicamente para estos ensayos (resolución en frecuencia 0.2 Hz). En la Figura 38 se muestran las señales obtenidas por el sensor en la posición del eje vertical, cuando la diferencia de presión entre ambas caras del disco es 2,5 bar y este está estático, o bien girando a $RPM_{nominal}$. En el primero de los casos la señal de la vibración del disco es muy clara, mientras que esta señal se complica cuando el disco comienza a girar. Esto es debido a que tal y como se observa claramente en sus transformadas de Fourier (ver Figura 39) se añaden muchas más componentes frecuenciales a la vibración. Una vez que la frecuencia de vibración se ha identificado es fácil obtener el número de diámetros nodales usando la Ecuación 9, que es una versión adaptada al disco de la Ecuación 2, donde f_o es la frecuencia proporcionada por el sensor óptico, f_{disco} es la proporcionada por la galga, f_r es la frecuencia de rotación y *ND* es el número de diámetros nodales del disco.

$$f_o = f_{disco} + f_r \cdot ND \tag{9}$$

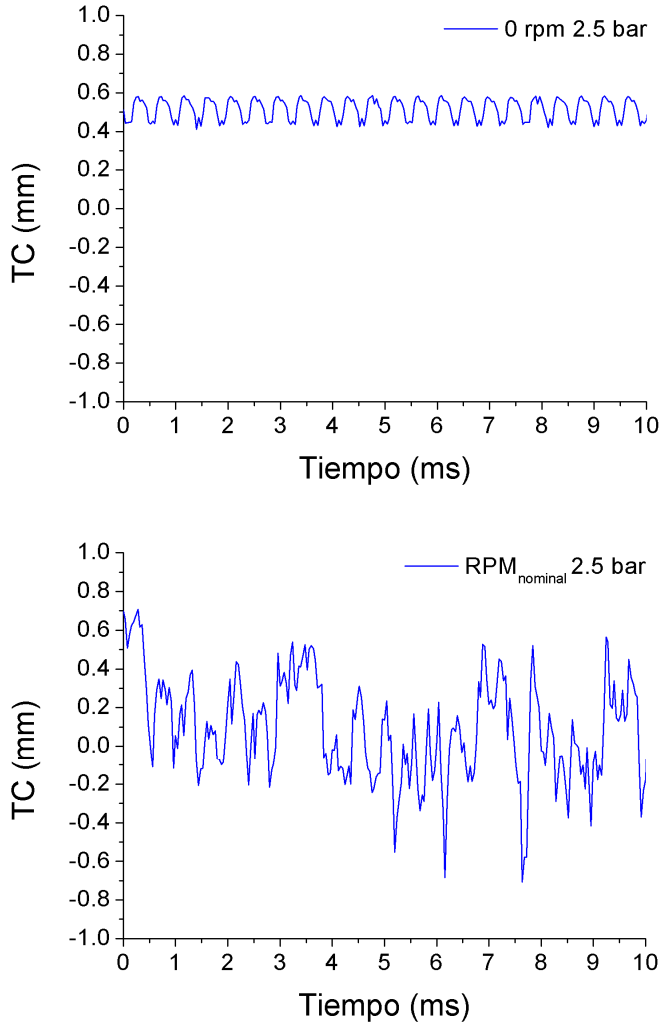

Figura 38. Señales para la medida del tip clearance obtenidas por el sensor en posición vertical.

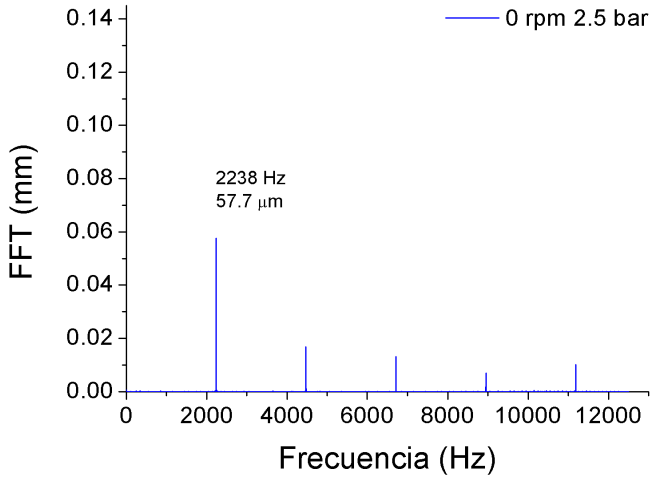

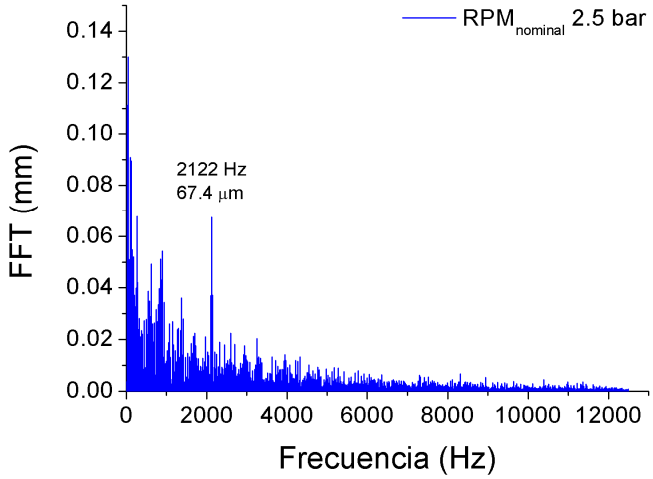

Figura 39. FFTs de las señales mostradas en la Figura 38.

Las frecuencias de vibración de los tres sensores coincidieron para todos los casos estudiados. Conocida la frecuencia de vibración dada por la galga se calculó correctamente el ND para cada caso. Es importante tener en cuenta que las frecuencias de vibración aportadas por la galga y el sensor óptico son las mismas, y coinciden una vez que la de este último ha sido demodulada utilizando la Ecuación 9 con el correcto ND, es decir, una vez que se ha desacoplado el efecto de ND. Toda esta información fue empleada por el fabricante del disco para producir una segunda versión del mismo en el que las vibraciones detectadas quedasen atenuadas. Se procedió a una caracterización similar con el nuevo disco, y en la Tabla 2 se muestran las reducciones en frecuencia y amplitud observadas por los tres sensores para cuatro puntos de trabajo del disco. Se puede comprobar que tanto la amplitud como la frecuencia de vibración se han reducido para todos los casos, salvo para la amplitud del sensor 2 (120º respecto la vertical) cuando el disco gira a 2 x $RPM_{nominal}$ y la diferencia de presión es 2,3 bar. Otra importante mejora en el comportamiento del segundo disco es que el ND de la vibración se mantiene constante para cada velocidad de rotación, mientras que el primero variaba el ND en función de la diferencia de presión entre sus lados.

Por último, en la Figura 40 se han representado los valores obtenidos para el cálculo del centro del disco en tres posiciones diferentes. Para obtener los diferentes centros se midió el tip clearance correspondiente a los tres sensores cuando el disco estaba estático y con una diferencia de presión de 2,3 bares entre sus caras. Este es el caso en el que las vibraciones son menores, y por lo tanto, menos van a afectar a la medida. Conocidas estas tres distancias tendremos tres puntos de la circunferencia del disco, con los que se calculó fácilmente su ecuación y a partir de ella su centro. Este proceso se repitió para tres posiciones del disco a 0º (posición inicial) y girando 90º y 202,5º respecto de esta posición, obteniendo una diferencia máxima de 0,65 mm respecto de la posición teórica del centro del disco.

Una versión más extendida con los resultados de todos los casos ensayados se presenta en el **Artículo 4.**

Punto de trabajo	SENSOR 1		SENSOR 2		SENSOR 3	
	Amplitud (%)	Frecuencia (%)	Amplitud (%)	Frecuencia (%)	Amplitud (%)	Frecuencia (%)
0 rpm 2.7 bar	98.6	9.48	99.6	9.48	99.8	9.48
$RPM_{nominal}$ 2.6 bar	53.6	24.3	40.4	24.3	63.5	24.3
$1.5xRPM_{nominal}$ 2.5 bar	24.5	24.3	35.8	24.3	41	24.3
$2xRPM_{nominal}$ 2.3 bar	20.7	23.9	-47.6	24	6.95	24

Tabla 2. Reducción en la amplitud y frecuencia de vibración para la segunda versión del disco en cuatro puntos del trabajo diferentes.

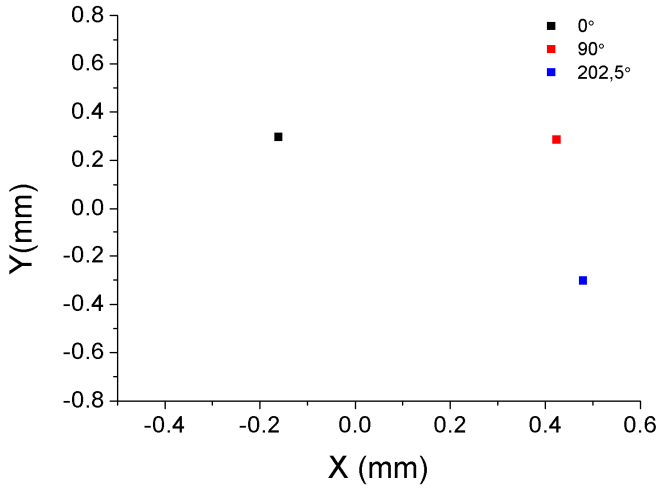

Figura 40. Representación de los centros del disco obtenidos para las posiciones de giro 0º, 90º y 202,5º.

3.2- Medidas del tip clearance en el compresor de un motor aeronáutico

Como se ha comentado en el capítulo 2, el funcionamiento de la última versión del sensor fue comprobado en un motor real (SO-3) en el banco de pruebas que el ITWL posee en Varsovia. En este sensor se empleó un haz de fibras tetrafurcado que permitió realizar medidas de tip clearance y tip timing de forma simultánea e independiente. En este apartado nos centraremos en las medidas de tip clearance dejando el tip timing para el siguiente.

Antes de realizar los ensayos en el motor se realizaron una serie pruebas en dos simuladores de turbinas que el ITWL disponía en sus instalaciones. Estas pruebas permitieron asegurar de forma previa a la instalación del sensor que la calidad de la señal proporcionada iba a ser aceptable. En la Figura 41 pueden observarse los dos simuladores empleados en esta fase previa, y en la Figura 42 se muestra el sensor ya instalado en el compresor del motor junto a una serie de sensores inductivos para la medida del tip timing.

Figura 41. Simuladores de turbina en los que se realizaron las pruebas preliminares del sensor.

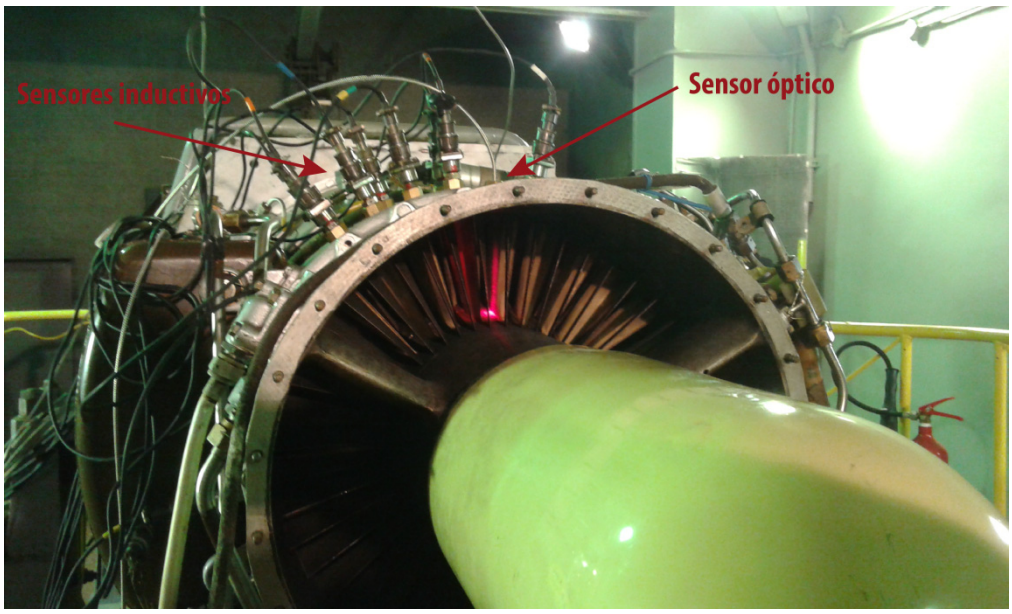

Figura 42. Motor SO-3 instrumentado con varios sensores inductivos y el sensor de fibra óptica.

Los ensayos constaron de 4 ciclos completos en los que el motor pasó de estar a ralentí a velocidad máxima (despegue) para volver a ralentí. La velocidad de partida del motor eran unas 7000 rpm para llegar a un valor máximo de aproximadamente 15600 rpm. Para el primer y el tercer ciclo la velocidad se fue incrementando y decrementando de forma lineal. Sin embargo, para el segundo y cuarto se fue aumentando la velocidad en saltos aproximados de 1000 rpm, para así conseguir mayores intervalos en los que la velocidad fuera constante, y por lo tanto lo fuera el tip clearance. La deceleración fue igual que para los otros ciclos. En la Figura 43 pueden observarse los perfiles de vuelo que siguió el motor para los ciclos 1 y 2.

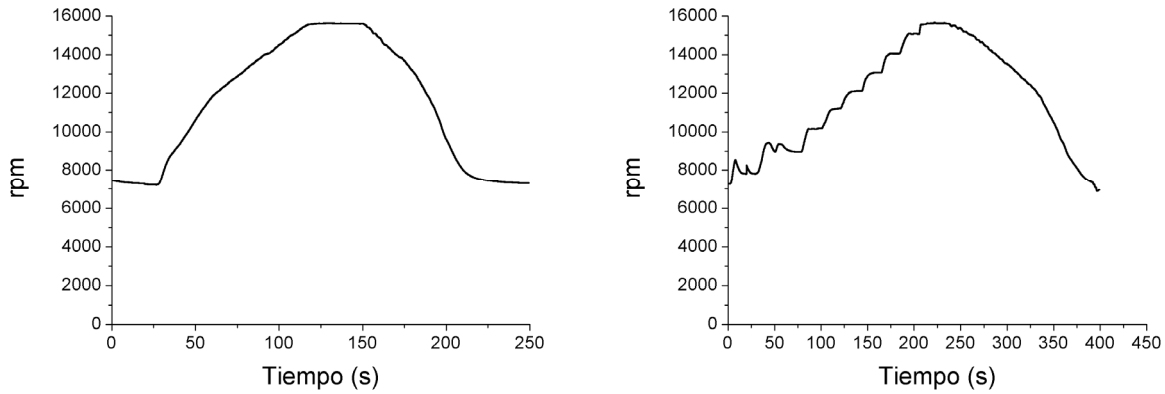

Figura 43. Perfiles de vuelo para el ciclo 1 (izquierda) y ciclo 2 (derecha).

Para el cálculo del tip clearance se adquirieron las señales V_1, V_2 y OPR (señal que produce un pulso por cada vuelta completa del motor) mostradas en la Figura 44. La frecuencia de muestreo fue de 500 kHz y las señales fueron post-procesadas mediante un programa desarrollado en LabVIEW. Este programa divide la adquisición completa en vueltas haciendo uso de la señal OPR. Para cada revolución evalúa el cociente V_2/V_1 y obtiene el valor del tip clearance para cada uno de los 28 álabes del compresor mediante la curva de calibración. Finalmente, el menor valor de los tip clearance de los álabes de esa vuelta se considera el valor del tip clearance en la vuelta correspondiente.

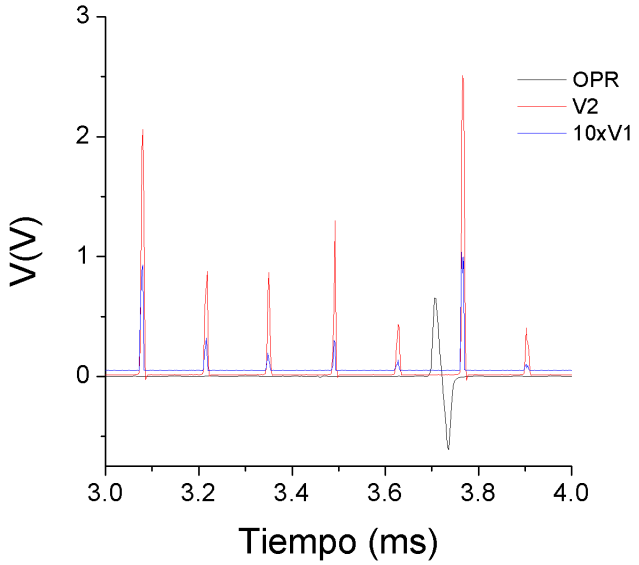

Figura 44. Señales OPR, V_1 (x10) y V_2 adquiridas cuando el motor gira a una velocidad de 15.600 rpm.

En la Figura 45 pueden observarse los resultados obtenidos para la medida del tip clearance en los cuatro ciclos durante la aceleración del motor. Se observa el comportamiento esperado ya que el tip clearance va disminuyendo al aumentar la velocidad de rotación del motor. Excepto para el caso del primer ciclo los valores obtenidos muestran una gran similitud. Para el caso de la deceleración este fenómeno no ocurre y el comportamiento de las medidas para los cuatro ciclos es muy similar. Se intentó buscar una explicación a esta desviación junto con los ingenieros y técnicos del ITWL pero no se pudo dar con una explicación que justificara este comportamiento que sólo se produjo en el primer ciclo.

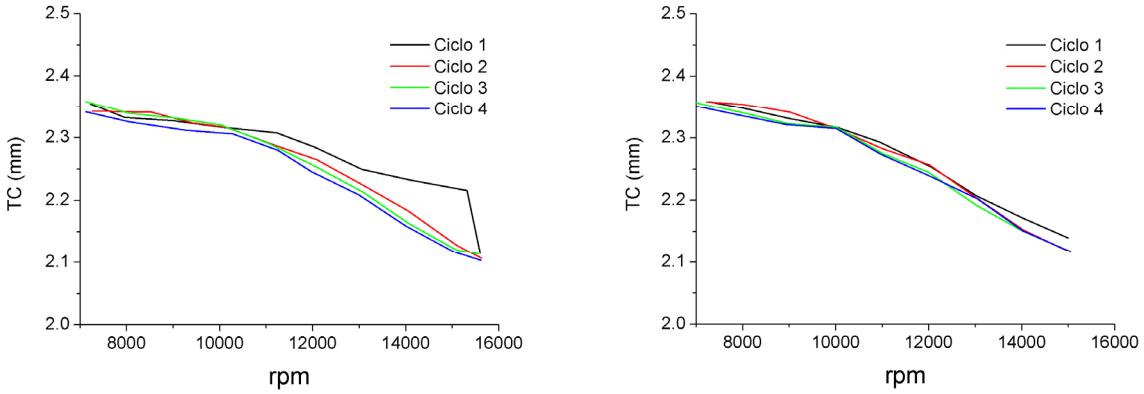

Figura 45. Medidas del tip clearance obtenidas para la aceleración (izquierda) y la deceleración (derecha).

Los sensores inductivos instalados se utilizaron únicamente para la medida del tip timing. La calibración de los mismos para la medida del tip clearance es muy complicada, ya que la amplitud de la señal que proporcionan es dependiente, además de la distancia a la que se encuentra el álabe, de la velocidad a la que gira el motor. Por lo tanto, no se pudo contar con ninguna referencia para comprobar la exactitud de las medidas en este ambiente real de funcionamiento. Las pruebas realizadas en el laboratorio proporcionaron errores menores que el 1% para todo el rango de medida y una precisión de 2 µm. Si tenemos en cuenta los cuatro ciclos de medidas la precisión resultante para el sensor es de 34 µm. Sin embargo, si descartamos el ciclo 1 debido a su comportamiento anómalo, esta precisión cae hasta las 12 µm, que es un valor excelente teniendo en cuenta que las medidas se realizan en un motor funcionando en condiciones reales. En la Tabla 3 se muestran los valores medios y la precisión de la medida tip clearance para cada velocidad, considerando y sin considerar el primer ciclo.

rpm	TC medio (mm)	TC medio (mm)*	Precisión (µm)	Precisión (µm)*
7000	2.353	2.351	7	8
8000	2.339	2.339	9	9
9000	2.326	2.325	9	10
10000	2.315	2.315	4	5
11000	2.286	2.281	11	7
12000	2.255	2.251	14	9
13000	2.212	2.207	18	11
14000	2.170	2.160	27	12
15000	2.134	2.119	34	5
15600	2.110	2.108	6	6

Tabla 3. Valores medios obtenidos para el tip clearance y precisión del sensor para el conjunto de medidas realizadas. Las columnas marcadas con * muestran los valores obtenidos al excluir el ciclo 1.

Una versión completa del procesado, así como todos de los resultados obtenidos en estos ensayos se encuentran en el **Artículo 5**.

3.3- Medidas del tip timing en el compresor de un motor aeronáutico

Como ya se comentó en capítulo 2, el haz de fibras tetrafurcado utilizado en las medidas para el motor SO-3 tiene una rama específica para la medida del tip timing. En este apartado presentaremos los resultados obtenidos para las medidas que se realizaron simultáneamente a las mostradas en el anterior apartado. En la Figura 42 pueden observarse los sensores inductivos que se utilizaron como referencia para evaluar el comportamiento del sensor de fibra óptica. Estos sensores forman parte del sistema SNDL-1b/SPL-2b, que es un sistema integral para la monitorización de la salud estructural del motor SO-3 desarrollado por las fuerzas aéreas polacas a principios de los 90 [82]. El funcionamiento de este sensor se basa en la creación de un campo magnético, por medio de un imán permanente, que es distorsionado con el paso de los álabes del blisk y que se manifiesta en la fuerza electromotriz generada en una bobina. [51,83].

Las señales de ambos sensores fueron adquiridas a una frecuencia de muestreo de 500 kHz. El propio programa diseñado para la adquisición de las señales hace un pequeño procesado para comprobar que las señales obtenidas tienen la calidad suficiente para ser utilizadas con la técnica del tip timing. En la Figura 46 se muestra el motor durante las pruebas de calidad de la señal para ambos tipos de sensor previas a los ensayos.

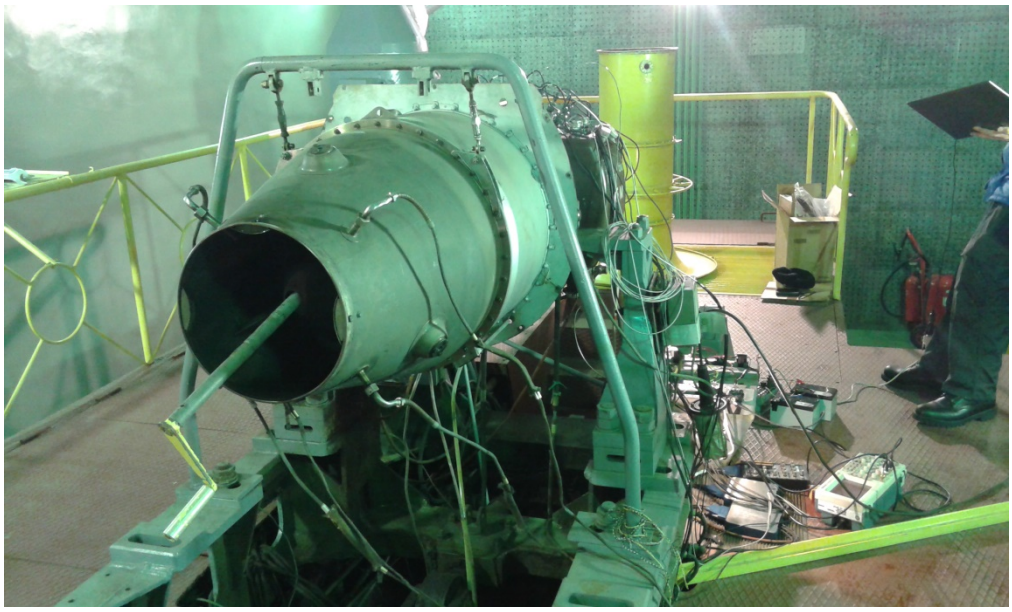

Figura 46. Pruebas de calidad de las señales para los sensores inductivos y para el sensor de fibra óptica previas a los ensayos.

Una vez adquiridas las señales fueron post-procesadas por un programa comercial. Este programa está optimizado para trabajar con las señales producidas por los sensores inductivos (ver Figura 47) y utiliza el paso por cero como forma de determinar la llegada del álabe. Este método de detección de la llegada del álabe es muy eficaz para este tipo de sensores, pero no lo es tanto a la hora de trabajar con las señales producidas por el sensor de fibra óptica.

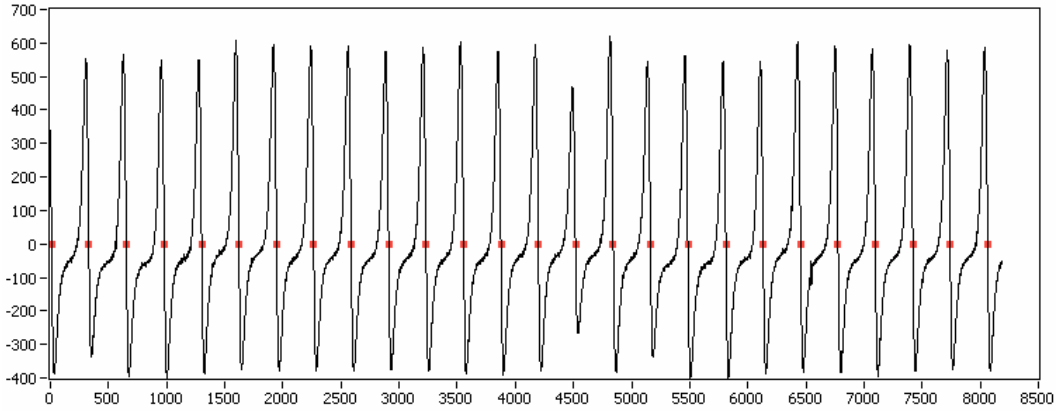

Figura 47. Señal obtenida para el sensor inductivo que sirve como referencia para las medidas de tip timing. En el eje de abscisas aparece representado el número de la muestra adquirida, y en el de ordenadas el valor de la tensión proporcionado por el sensor inductivo en mV.

Una vez que se han determinado los instantes de llegada reales para cada álabe se pueden obtener las deflexiones de cada uno de ellos siguiendo el método explicado en el apartado 2.2-1. En la Figura 48 se muestran estas deflexiones obtenidas cuando el compresor está girando a 11300 rpm. Los valores obtenidos para el sensor inductivo y el óptico son bastante similares, siendo las de este último ligeramente superiores. A la hora de comparar estas amplitudes hay que tener en cuenta que si bien los sensores se encuentran cerca, están midiendo vibraciones en diferentes puntos del compresor.

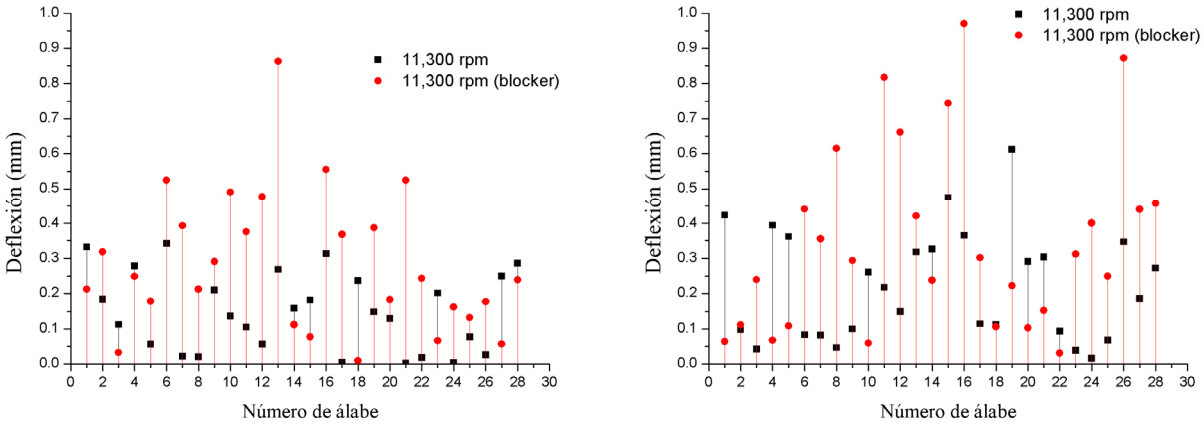

Figura 48. Deflexiones de los álabes obtenidas para el sensor inductivo (izquierda) y para el sensor de fibra óptica (derecha). Los cuadrados negros representan las deflexiones cuando el motor trabaja en condiciones normales y los círculos rojos cuando un blocker simula un FOD.

Se han representado las amplitudes de vibración cuando el motor trabaja en condiciones normales, pero también cuando se simula un daño producido por un objeto extraño (esta circunstancia se conoce como FOD, por sus siglas en inglés Foreign Object Damage) [84]. Este objeto puede ser hielo o un ave que impacta en el motor y sus consecuencias en el motor se simulan mediante la colocación de "blockers" como el mostrado en la Figura 49. Se puede apreciar como claramente la introducción del blocker produce un incremento en las amplitudes de vibración de los álabes. Así, se podría implementar un sistema para la monitorización de la salud estructural de los álabes mediante la definición de un valor umbral en sus deflexiones, que hiciera saltar una alarma cuando sea sobrepasado, ya que se habría

producido un daño en los álabes del compresor. Un buen valor podría ser 0,7 mm para el sensor inductivo y 0,8 mm para el caso del sensor de fibra óptica.

Figura 49. Blocker utilizado para simular un FOD antes (izquierda) y después (derecha) de montar la entrada de aire del motor.

Si se representan estas deflexiones para todos los álabes y en todo el rango de velocidades del motor se obtienen los denominados diagramas en cascada. En la Figura 50 puede observarse este diagrama para ambos sensores. Una vez más se aprecia la gran similitud en los resultados obtenidos. En este caso las vibraciones de cada álabe tienen fase diferente para cada sensor debido a la diferente posición circunferencial que ocupan cada uno de ellos en el compresor. Ambos sensores reflejan claramente las respuestas síncronas (8000 y 15500 rpm) y asíncronas (11500) de los álabes del compresor.

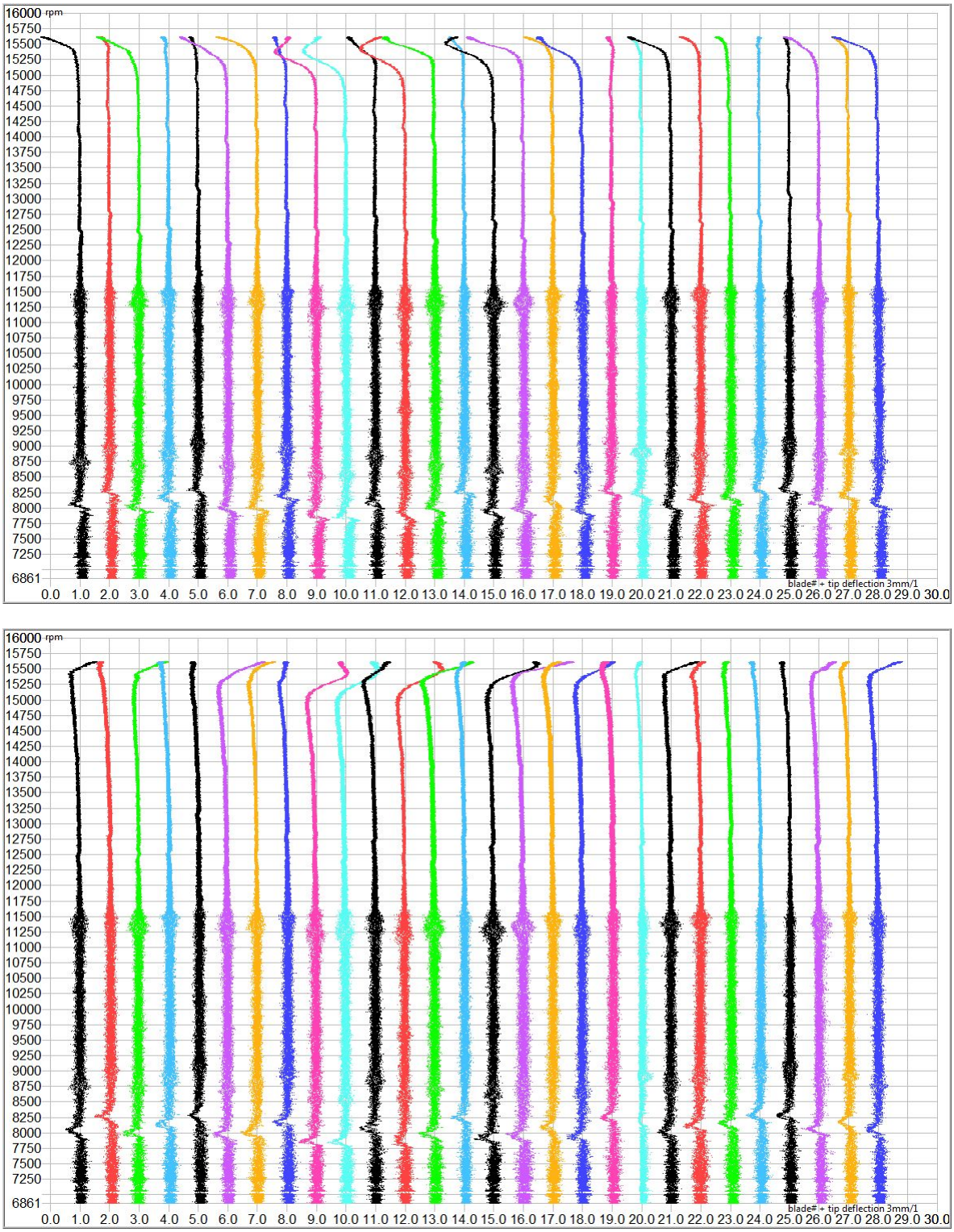

Figura 50. Diagramas en cascada para las deflexiones de los álabes obtenidos mediante el sensor inductivo (arriba) y el óptico (abajo).

Se puede realizar un análisis similar en el dominio de la frecuencia si se hace la FFT de las deflexiones de cada uno de los álabes para todas las velocidades del motor. La representación de esta FFT se conoce como espectro de todos los álabes y se representa en la Figura 51 para ambos sensores. En este caso el espectro del sensor de fibra óptica es un poco más ruidoso que el obtenido mediante el sensor inductivo.

Esto es debido a que el programa utilizado en este análisis esta optimizado para trabajar con las señales del sensor inductivo, y a que estamos comparando un prototipo frente a un sistema completamente desarrollado, como es el basado en sensores inductivos.

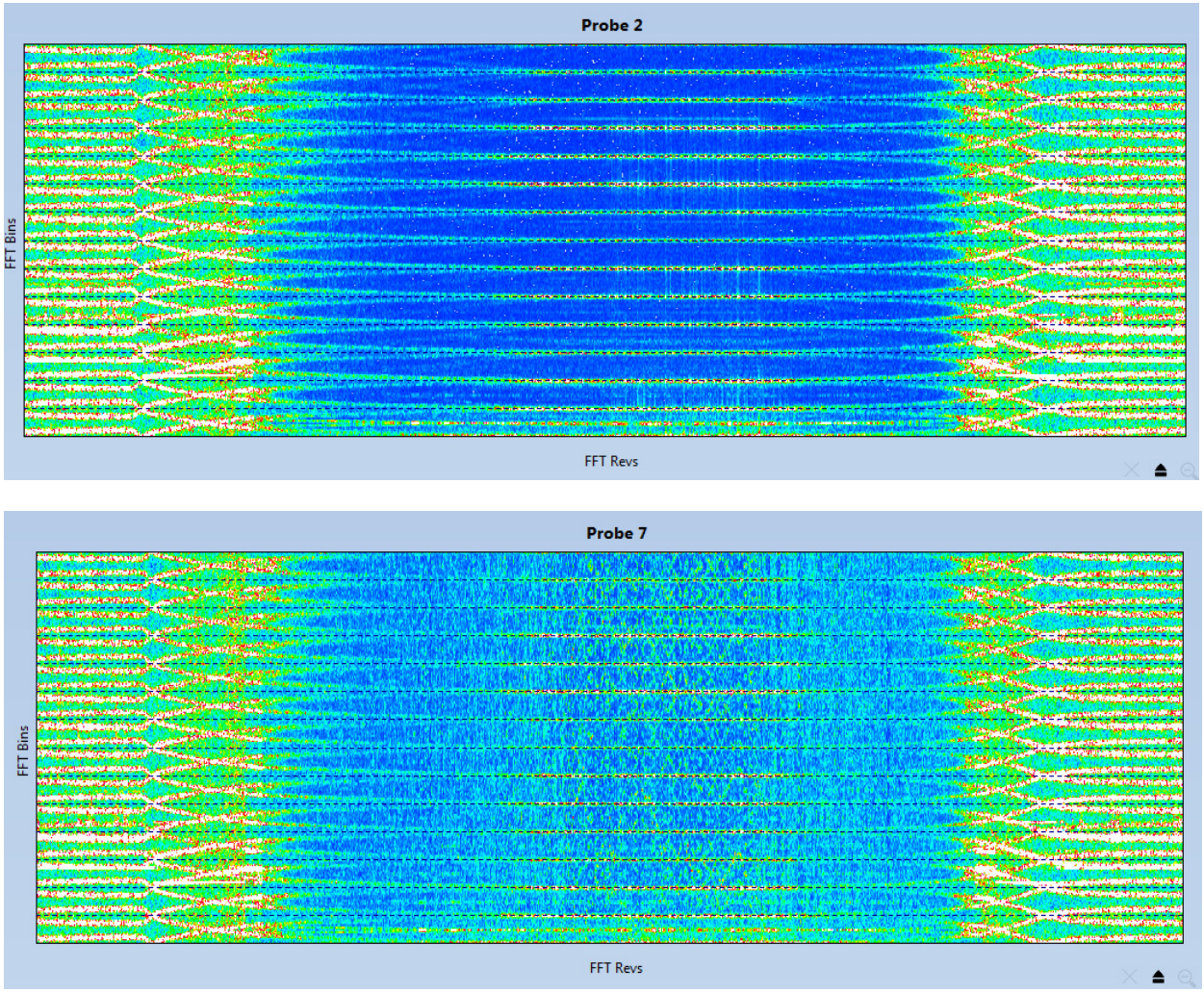

Figura 51. Espectro de todos los álabes obtenidos mediante el sensor inductivo (arriba) y el óptico (abajo).

3.4- Medidas de tip timing utilizando tres sensores

Los últimos resultados que se van a presentar en este capítulo son los correspondientes a las medidas de tip timing realizadas con tres sensores de fibra óptica para una turbina de baja presión con 81 álabes instalada en el túnel de viento. El objetivo de estas medidas era avanzar en el procesado de esta técnica al contar con tres señales en diferentes puntos de la turbina. Concretamente se instaló un sensor en el eje vertical del túnel y otros dos situados a ±120º respecto del primero. En estas medidas se utilizaron dos prototipos diferentes, un sensor del primer prototipo (sensor C) y dos sensores del cuarto prototipo (sensores A y B). Con ello se podría conseguir un objetivo secundario que era estudiar la influencia de la iluminación utilizando una fibra monomodo o multimodo en las señales obtenidas para el tip timing. Al realizar únicamente medidas de tip timing solo nos interesa una rama de salida de los haces de fibra, por lo que a pesar de ser trifurcados se emplearon como si fuesen bifuracados (por eso solo aparece una rama en los sensores representados en la Figura 52). Para adquirir las señales de cada sensor y la señal OPR se utilizó el mismo osciloscopio que para las medidas de los primeros prototipos del sensor. La frecuencia de adquisición fue de 4 MHz, que utilizada sin interpolación para la deteción de la llegada de los álabes,

proporciona una resolución de 77,5 µm para el cálculo de las deflexiones de los mismos. En la Figura 53 se muestran las señales adquiridas y se puede apreciar claramente que son bastante ruidosas. Esto se puede apreciar más todavía en la señal del sensor A debido a su menor amplitud (durante la realización de las medidas se dañó su módulo láser y pasó a emitir solamente un cuarto de su potencia nominal). Por ello, se les aplicó un filtrado paso paso bajo con una frecuencia de corte de 120 kHz (nos quedaríamos con la información correspondiente a los 12 primeros armónicos de las señales, que es más que suficiente para el análisis de esta turbina).

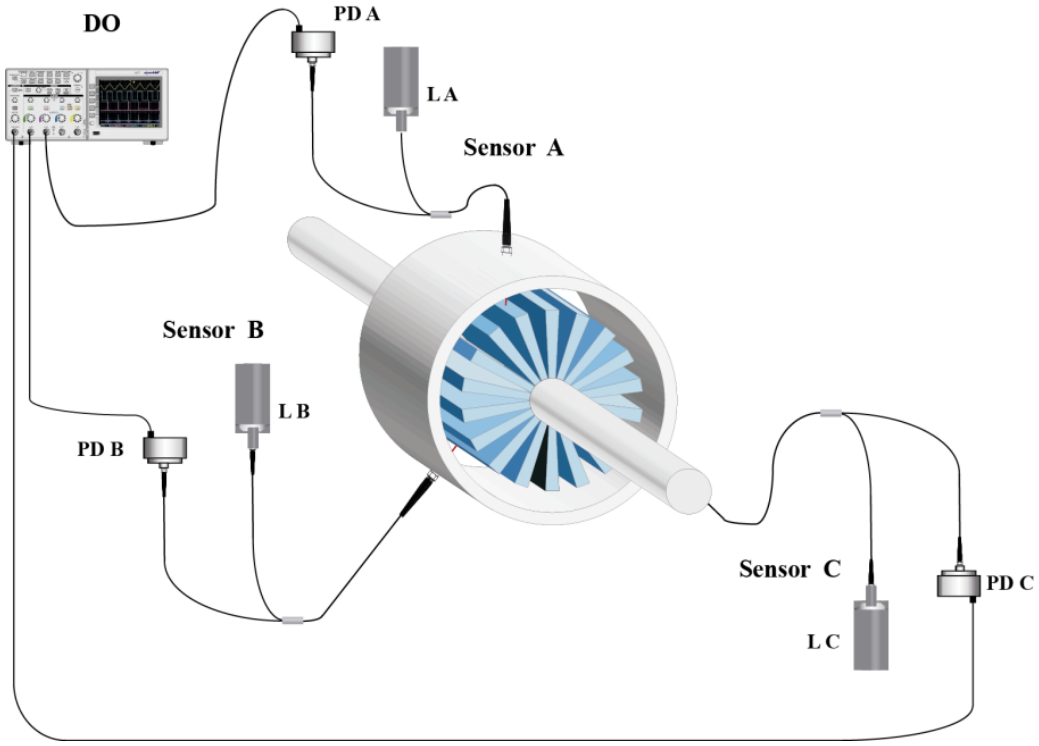

Figura 52. Montaje de los tres sensores para las medidas de tip timing en el túnel de viento. Se ha denominado LX a los módulos láser, PDx a los fotodetectores de cada sensor y DO al osciloscopio para la adquisición de las señales.

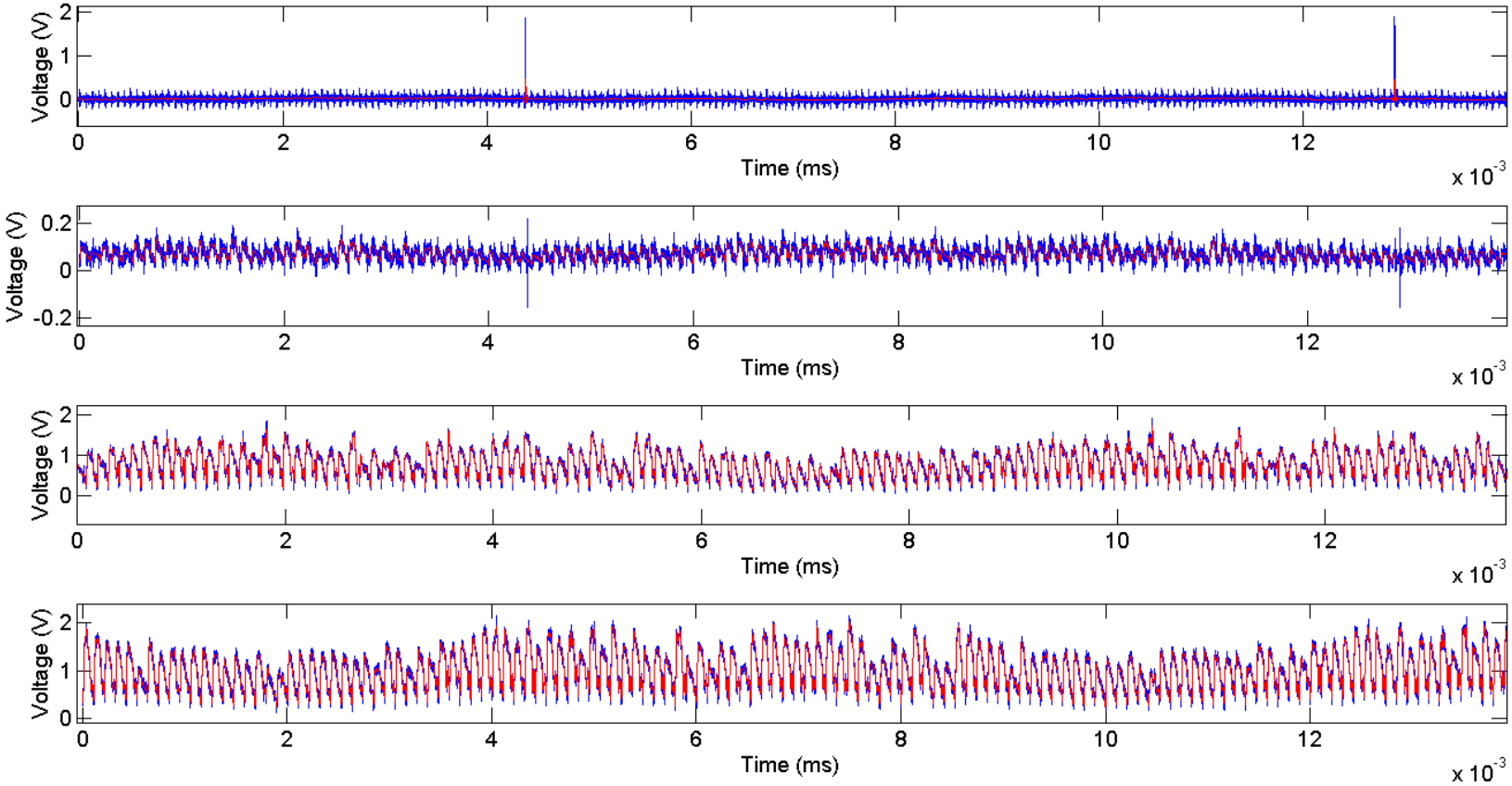

Figura 53. Señales OPR y del sensor A, B y C antes (azul) y después (rojo) del filtrado paso bajo.

En el procesado de estas señales se decidió utilizar para la detección de la llegada del álabe el método de la primera derivada. Este método consiste en considerar como instante de llegada el punto en el que la señal correspondiente a un álabe cambia de cóncava a convexa, es decir, su punto de inflexión. Se desarrolló un programa en MATLAB que con la ayuda de la señal OPR separó las señales de cada sensor en tramos correspondientes a una vuelta, calculó la derivada de cada una de la señales y estimó como instante de llegada de cada álabe el punto donde la primera derivada era máximo (segunda derivada nula). En la Figura 54 se han representado las derivadas de las señales con los instantes de llegada para cada álabe. También se han representado las señales de cada sensor para que sirvan de referencia. Se han representado los mismos álabes para los tres sensores y puede comprobarse que no existe una gran diferencia entre iluminar con un tipo de fibra u otro.

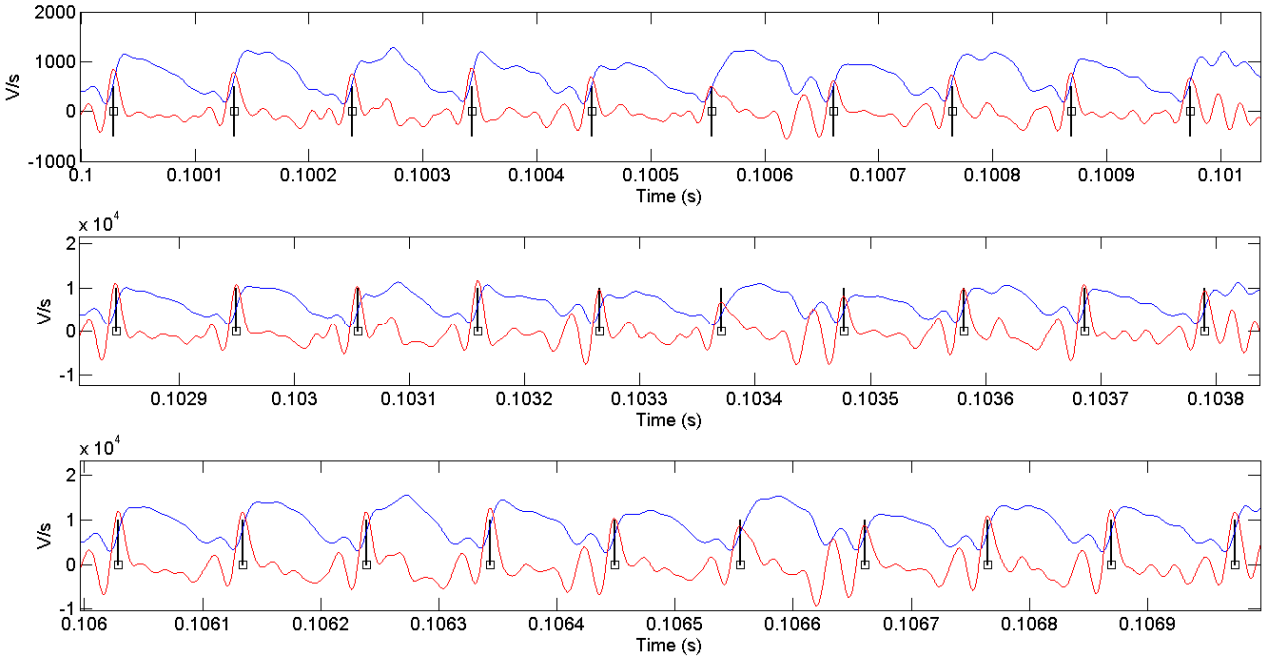

Figura 54. Derivada de la señal de los sensores A, B y C (rojo) y tiempo de llegada de cada álabe (negro). Se ha representado la señal filtrada para cada sensor (azul) como referencia.

Una vez determinados los instantes de llegada reales, el programa calcula los teóricos conocidos el número total de álabes y la velocidad de rotación (señal OPR), halla la diferencia entre ellos y usando la Ecuación 8 obtiene la deflexión para cada álabe en las posiciones de los sensores. En la Figura 55 se han representado estos valores para 50 revoluciones cuando la turbina está girando a 7047 rpm. Calculando la FFT de los mismos se obtiene el espectro de onda viajera representado en la Figura 56. Tal como se ha comentado previamente, se puede realizar una monitorización de la salud estructural de los álabes tanto en el dominio temporal como en el frecuencial mediante la definición de valores de alarma. Para ello, es necesario eliminar el post-procesado de las señales diseñando un programa que entregue estos datos en tiempo real (o bien adquiriendo uno comercial).

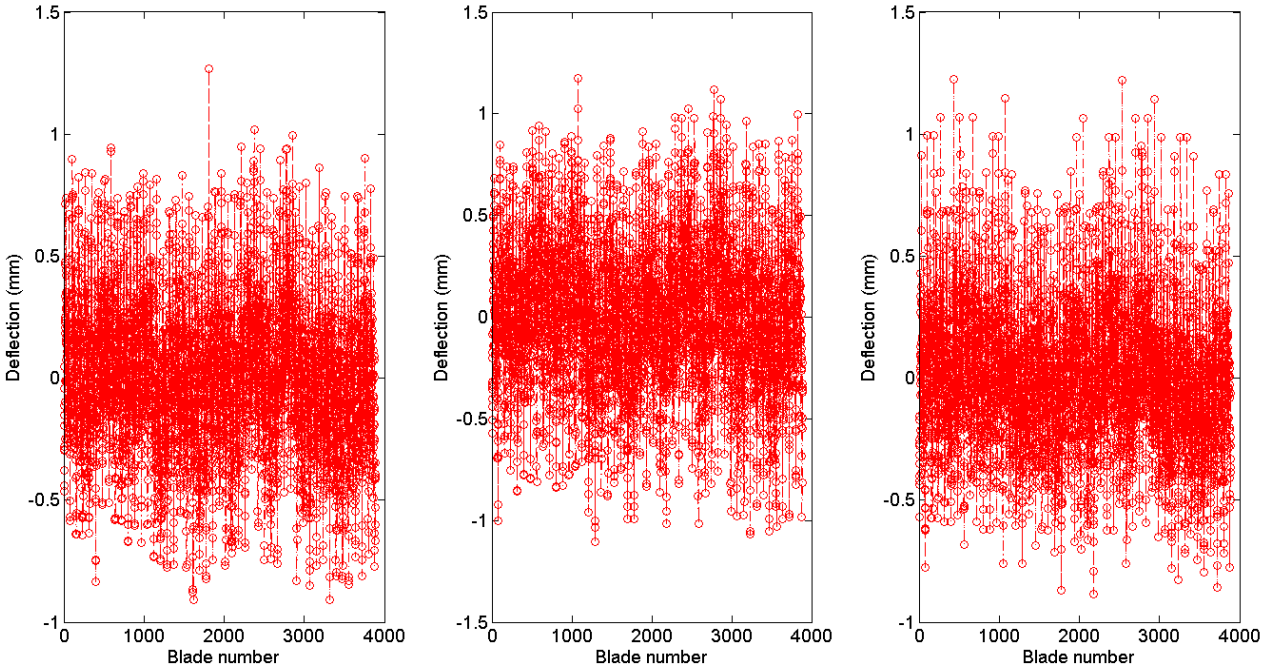

Figura 55. Amplitudes de vibración de los álabes proporcionadas por los tres sensores A, B y C, respectivamente, cuando la turbina gira a 7047 rpm. Se muestran 50 vueltas consecutivas.

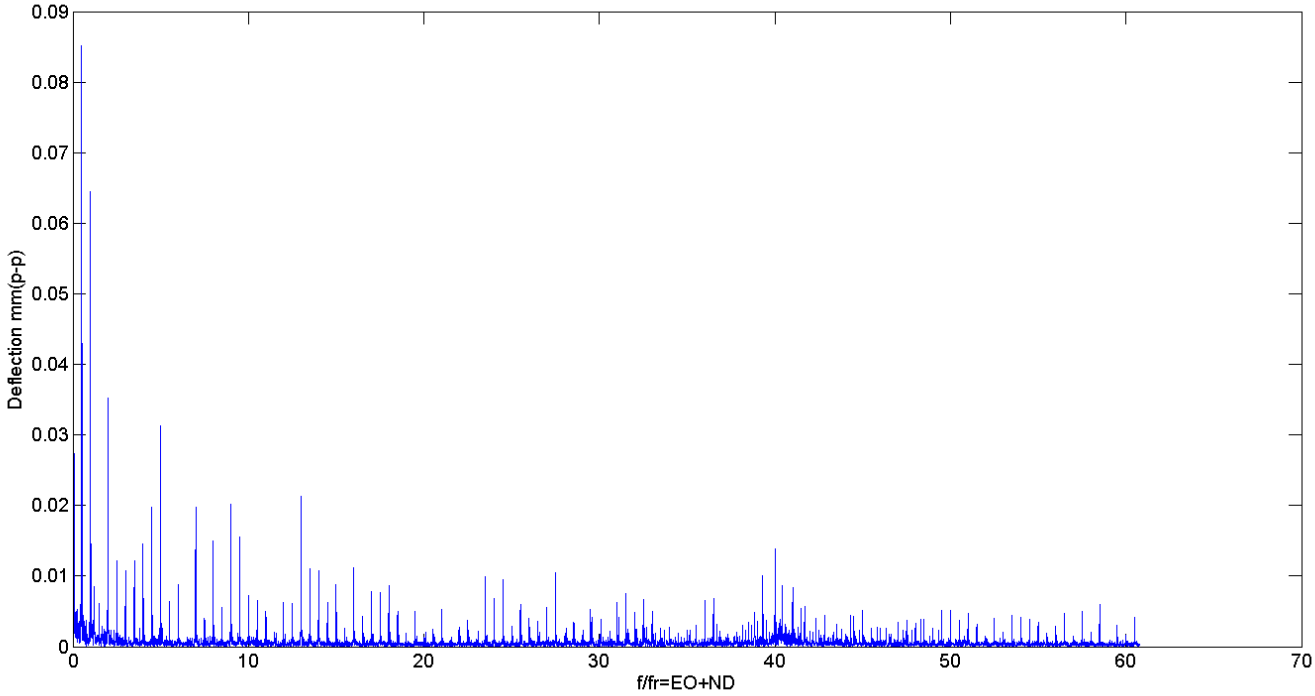

Figura 56. Espectro de onda viajera obtenido a 7047 rpm.

Incluso aunque el túnel de viento está preparado para mantener una velocidad de rotación constante, se detectaron algunas inestabilidades consistentes en pequeños cambios de la velocidad de rotación pero en

instantes muy pequeños de tiempo. Estos cambios abruptos provocaban vibraciones de una amplitud inusualmente elevada (ver Figura 57) que sin embargo no provocaron ningún daño en los álabes, ya que una vez finalizada la inestabilidad todos los álabes volvían a valores normales en sus amplitudes de vibración. En la Figura 58 se ha representado el espectro de onda viajera para una adquisición durante la cual se produjo una inestabilidad. En ella, se puede apreciar claramente un pico que surge para EO+ND = 40.

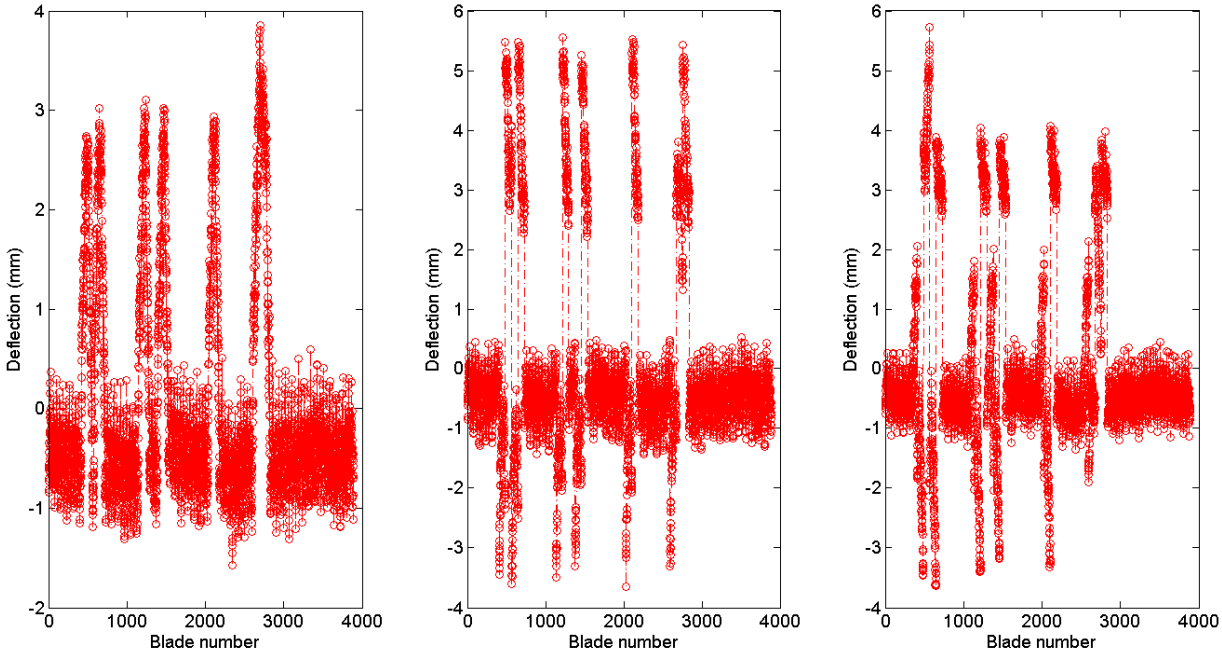

Figura 57. Amplitudes de vibración de los álabes proporcionadas por los tres sensores A, B y C, respectivamente, cuando la turbina gira a 7047 rpm y se producen inestabilidades en la frecuencia de rotación. Se muestran 50 vueltas consecutivas.

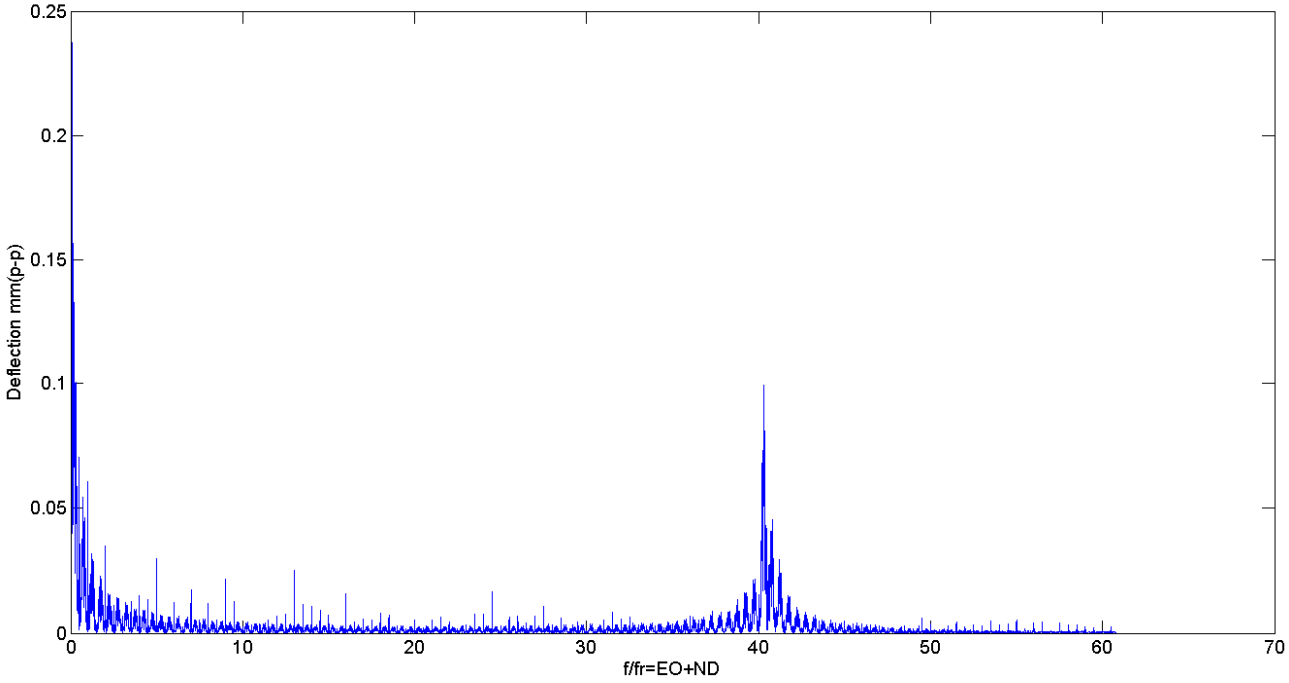

Figura 58. Espectro de onda viajera obtenido a 7047 rpm con presencia de inestabilidades en la frecuencia de rotación.

Durante estos ensayos se trató de caracterizar las vibraciones de los álabes durante el apagado del túnel de viento. Dos fueron los factores que limitaron una caracterización completa del mismo. Por un lado el apagado del túnel debe hacerse de una manera progresiva, de forma que todos los parámetros estén dentro de unos ciertos límites y no se produzca una caída del sistema. Esto implica que el apagado va a tardar varios minutos. Por otro lado, la memoria del osciloscopio solo nos permitió hacer adquisiciones de un minuto de duración como máximo (además hay que tener en cuenta que tarda otro minuto en guardar las adquisiciones). Por lo tanto, solamente se pudieron adquirir ciertos intervalos de este régimen de apagado. En la Figura 59 se muestra uno de ellos y en la 60 todos los intervalos obtenidos con el sensor A. Para el resto de sensores se obtienen resultados similares.

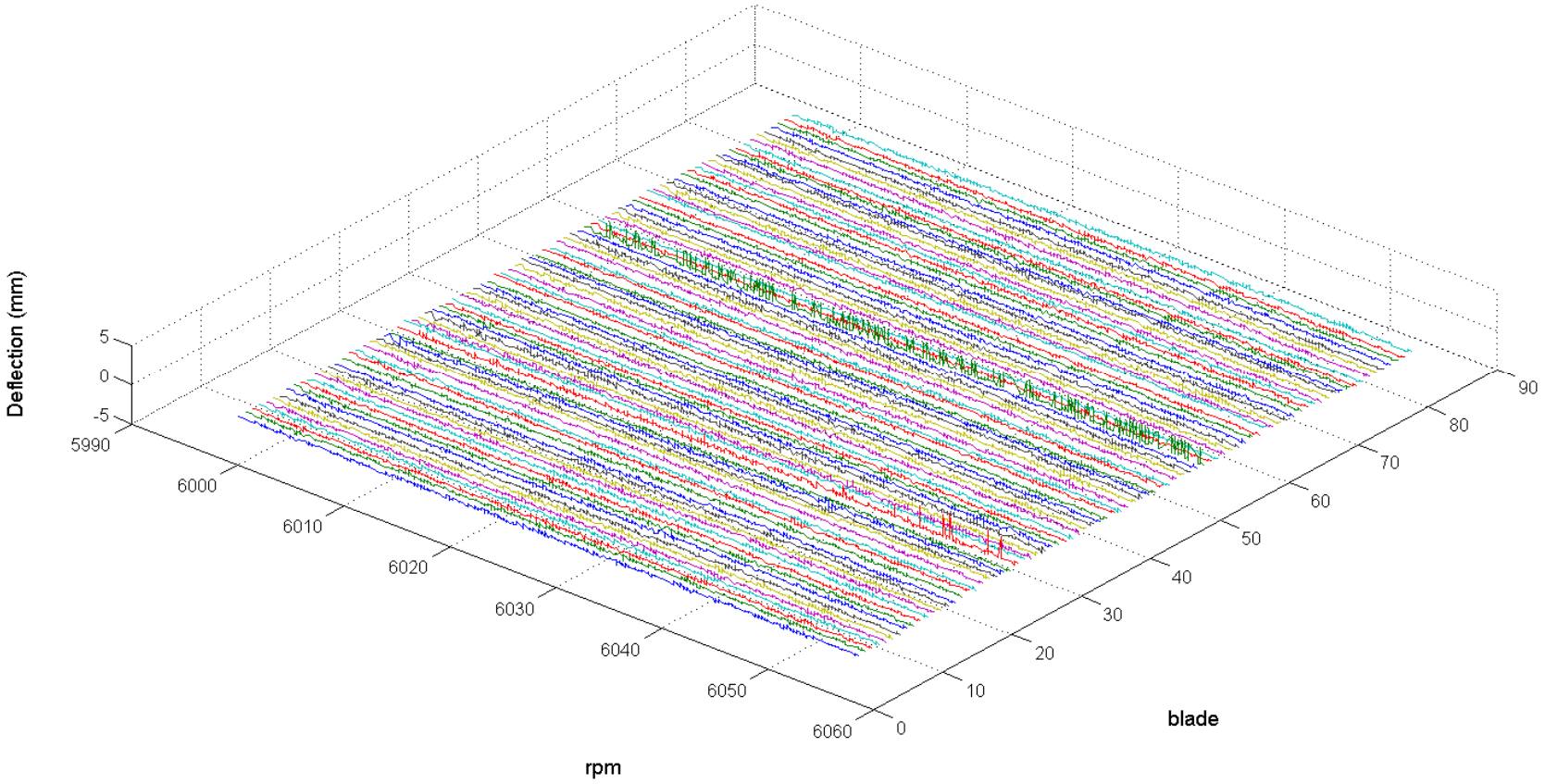

Figura 59. Amplitudes de vibración para los 81 álabes durante un intervalo del régimen de apagado obtenidas con el sensor A.

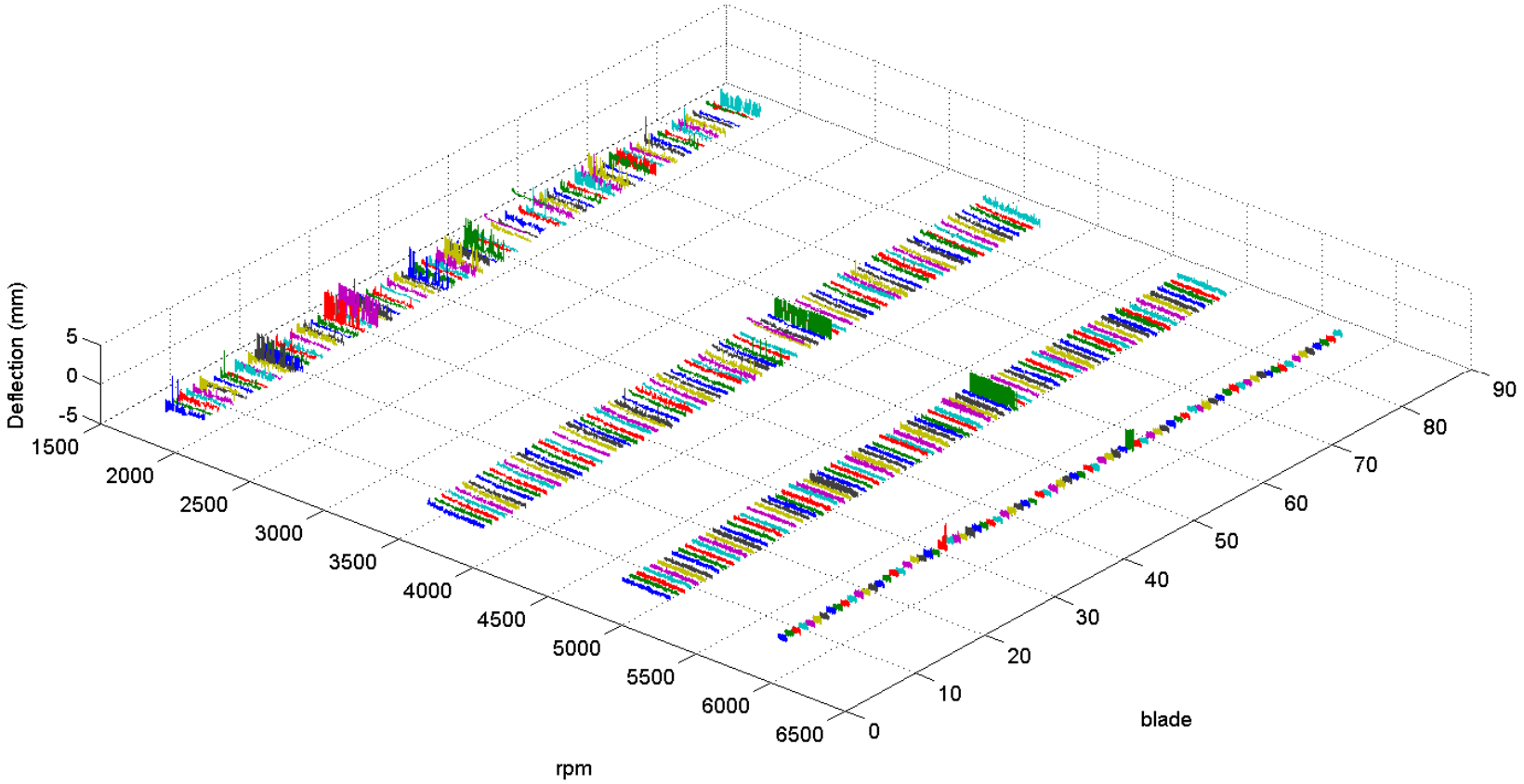

Figura 60. Amplitudes de vibración para los 81 álabes durante los intervalos adquiridos del régimen de apagado obtenidas con el sensor A.

Capítulo 4

Conclusiones

En este capítulo se presentan las conclusiones de la tesis, así como las posibles líneas futuras de investigación que se pueden derivar de ella con el objetivo de evolucionar en las prestaciones ofrecidas por el sensor de fibra óptica. También se exponen las publicaciones y conferencias que han surgido como consecuencia del trabajo realizado durante la tesis.

4.1- Conclusiones

En la presente tesis se ha desarrollado un sensor basado en fibra óptica para la medida del tip clearance y de las vibraciones de los álabes por medio de la técnica del tip timing. El funcionamiento de este sensor está basado en la modulación de la luz reflejada en función de la distancia de los álabes. Después de adquirir ciertos conocimientos en cuanto al funcionamiento de un motor aeronáutico y del comportamiento de los álabes que componen sus diferentes blisks, se diseñaron varios prototipos del sensor, mejorando sucesivamente sus prestaciones hasta conseguir cumplir con los requisitos iniciales en cuanto a:

a) Medida sin contacto de manera que no se afecte el comportamiento mecánico de los álabes.

b) Precisión en la medida del tip clearance. El requisito inicial de 30 μm se ha visto ampliamente mejorado ya que la última versión del sensor aportó una precisión de 12 μm en un entorno real.

c) Rango de medida del tip clearance de 2 mm. En el caso de usar la región II este rango es superado ampliamente sin ningún problema. Para el caso de medir la región I, el último prototipo cumple justo este valor. Sin embargo, siguiendo los criterios de diseño dados en el capítulo 2, este rango puede aumentarse fácilmente en caso de ser necesario.

d) Ancho de banda. Se cumplió con un mínimo de 200 kHz para la medida del tip timing, aunque este requisito tiene un carácter general. Para cada aplicación concreta va a depender de la velocidad de rotación máxima del blisk así como de su número de álabes. Como hemos visto en la última aplicación, para el túnel de viento este puede ser reducido al girar a una velocidad máxima de 7000 rpm aproximadamente.

e) Facilidad de instalación. Este punto fue uno de los que más gustó a los técnicos del ITWL y del Centro de Tecnologías Aeronáuticas, ya que una vez diseñado el acoplador, el sensor proporciona un importante ahorro de tiempo en su instalación respecto a otros métodos como las galgas.

f) Robustez. Este requisito ha quedado demostrado con el empleo del sensor en el motor real.

g) Diseño económico que pueda tener una viabilidad comercial. Este requisito también se ha cumplido y entre otras compañías se han interesado por el sensor fabricantes de motores como ITP o General Electric, y aerolíneas como Delta Air Lines.

Además de la caracterización de los prototipos tanto en el laboratorio como en aplicaciones reales, se ha desarrollado un sistema automatizado de calibración, así como una serie de programas para el procesado de las señales del sensor en las diferentes aplicaciones para las que se ha utilizado. También se ha desarrollado un programa para la simulación de la curva de calibración resultante para un sensor en función de los parámetros de diseño, que va a facilitar en gran medida el desarrollo de sensores de este tipo para nuevas aplicaciones.

El último prototipo del sensor permite la realización de ambas medidas de una forma simultánea y una configuración totalmente independiente para cada una de ellas. Respecto a la medida del tip clearance, además de poder ser utilizado en el desarrollo y caracterización de motores con ensayos en tierra, satisface los requisitos iniciales para el desarrollo de sistemas de control activos del tip clearance, ya que la precisión obtenida para el último prototipo fue de 12 μm. Por ello, podría ser incluso embarcado en un motor en vuelo para comprobar su rendimiento en esas condiciones, y comprobar así su utilidad en ese tipo de sistemas. También se ha comprobado su utilidad en la caracterización y optimización de otros elementos rotativos como discos, y su validez para otro tipo de medidas como el cálculo de la excentricidad. Si se analizan los resultados para la medida del tip timing, se ha validado el funcionamiento del sensor en un motor aeronáutico usando como referencia un sistema basado en sensores inductivos. Este sistema lleva más de dos décadas siendo empleado por las fuerzas aéreas polacas. Se ha demostrado

su utilidad como sistema para monitorizar la integridad de los álabes tanto en un dominio temporal como frecuencial. Además se han realizado los primeros ensayos con varios sensores en la misma etapa, lo cual va a permitir la caracterización completa de los blisks.

En resumen, el sensor desarrollado no solo ha cumplido con los requisitos iniciales, si no que en muchos casos los ha mejorado. Además, ha proporcionado soluciones para medidas y aplicaciones que inicialmente no estaban previstas, demostrando su versatilidad. Por todo ello, su comportamiento ha superado las expectativas iniciales demostrando su aptitud para este tipo de medidas en motores aeronáuticos.

4.2- Líneas futuras

Los resultados obtenidos durante el desarrollo de la presente tesis muestran el potencial del sensor para aplicaciones relacionadas con la medida del tip clearance y tip timing en blisks. Sin embargo, hay diferentes aspectos que harían evolucionar sus prestaciones y que mejorarían sus capacidades como son:

a) Desarrollo de un software que proporcione resultados en tiempo real para ambas medidas. Para el caso del tip clearance este software ya ha sido desarrollado, y se está a la espera de poder disponer de unos ensayos en el túnel de viento para comenzar a comprobar su funcionamiento. Para el caso del tip timing va a ser necesario evaluar si merece la pena su desarrollo de forma que se forme un paquete software con el programa del tip clearance, o si es más interesante la adquisición de un programa comercial.

b) Con el sensor se han caracterizado las vibraciones radiales (tip clearance) y tangenciales (tip timing). También sería muy interesante hacerlo con la vibraciones axiales ya que actualmente nadie ha proporcionado un solución efectiva para realizarlo.

c) Realización de medidas en partes de mayor temperatura del motor, como puede ser la turbina de baja presión funcionando en condiciones reales. Las temperaturas en esta parte del motor estarán entre 700 y 1000 °C, por lo que el diseño del haz de fibras tendrá que ser modificado ya que actualmente soporta 350 °C como máximo. Otro problema importante a solucionar será el de la contaminación debido a las partículas procedentes de la cámara de combustión.

d) Realización de medidas en turbinas de baja presión de alta velocidad. Todos los fabricantes de motores están potenciando una tecnología en la que por medio de un engranaje directo entre el ventilador y la turbina de baja presión se consigue un ahorro de combustible del 15% aproximadamente. Para ello, es necesario que la turbina gire a velocidades tres veces superiores a las actuales. El Centro de Tecnologías Aeronáuticas está adecuando sus instalaciones para poder ensayar este tipo de turbinas, y para ello, van a necesitar nueva instrumentación entre la que se encuentra una versión avanzada del sensor de fibra óptica.

e) Caracterización de las vibraciones síncronas del blisk mediante el empleo de varios sensores y la técnica del tip timing. Normalmente se suelen emplear hasta 8 sensores por cada etapa del motor en la que se quieren caracterizar completamente todos los tipos de vibraciones tangenciales. En esta tesis se han empleado un máximo de 3 sensores y el objetivo para el futuro sería ampliarlo para poder obtener datos de todos los tipos de vibración presentes en el blisk.

4.3- Publicación de resultados

4.3-1. Contribuciones de la tesis

Durante la realización de la tesis se han publicado los siguientes artículos en revistas internacionales:

[Artículo 1] **García, I.,** Zubia, J., Durana, G., Aldabaldetreku, G., Illarramendi, M. A., & Villatoro, J. (2015). Optical Fiber Sensors for Aircraft Structural Health Monitoring. *Sensors*, *15*(7), 15494-15519 (Q1 Instruments & Instrumentation).

[Artículo 2] **García, I.,** Beloki, J., Zubia, J., Aldabaldetreku, G., Illarramendi, M. A., & Jiménez, F. (2013). An optical fiber bundle sensor for tip clearance and tip timing measurements in a turbine rig. *Sensors*, *13*(6), 7385-7398 (Q1 Instruments & Instrumentation).

[Artículo 3] **García, I.,** Zubia, J., Berganza, A., Beloki, J., Arrue, J., Illarramendi, M. A., Mateo, J., & Vázquez, C. (2015). Different configurations of a reflective intensity-modulated optical sensor to avoid modal noise in tip-clearance measurements. *IEEE Journal of Lightwave Technology*, *33*(12), 2663-2669 (Q1 Optics)

[Artículo 4] **García, I.,** Zubia, J., Beloki, J., Arrue, J., Durana, G., & Aldabaldetreku, G. (2017). Optical Tip Clearance Measurements as Tool for Rotating Disk Characterization. *Sensors*, *17*(1), 165 (Q1 Instruments & Instrumentation).

[Artículo 5] **García, I.,** Przysowa, R., Amorebieta, J., & Zubia, J. (2016). Tip-Clearance Measurement in the First Stage of the Compressor of an Aircraft Engine. *Sensors*, *16*(11), 1897 (Q1 Instruments & Instrumentation).

4.3-2. Otras publicaciones

[Capitulo 1] Arrospide, E., Bikandi, I., **García, I.,** Durana, G., Aldabaldetreku, G., Zubia, J., "Mechanical properties of polymer-optical fibres", in Polymer Optical Fibres: Fibre Types, Materials, Fabrication, Characterisation and Applications, 1st edition, Woodhead Publishing, 2016, pp. 201-215.

4.3-3. Conferencias

[Conf 1] Zubia, J., **García, I**., Durana, G., Villatoro, J., Illaramendi, M.A., Mateo, J., Vázquez, C. "Polymer optical fiber sensors for aircraft structural and engine monitoring". International Workshop on Photonics Polymer for Innovation (IWPPI), Nasu Highland, Japan, October 12, 2016 **(Invitada)**.

[Conf 2] **García, I.,** Przysowa, R., Zubia, J. "Tip-clearance measurement in a legacy turbojet with the use of an optical fiber sensor". GTI Conference, Berlin, Germany, September 28, 2016.

[Conf 3] **García, I.,** Przysowa, R., Zubia, J., Mateo, J., Vázquez, C. "Tip timing measurements for structural health monitoring in the first stage of the compressor of an aircraft engine". 18th International Conference on Transparent Optical Networks (ICTON), Trento, Italy, July 10, 2016 **(Invitada)**.

[Conf 4] **García, I.,** Zubia, J., Beloki, J., Ayesta, I., Aldabaldetreku, G. "Tip timing measurements for Structural Health Monitoring in a low-pressure turbine using three optical sensors". 8th European Workshop On Structural Health Monitoring (EWSHM), Bilbao, Spain, July 5, 2016.

[Conf 5] **García, I.,** Zubia, J., Villatoro, J., Illaramendi, M.A., Mateo, J., Vázquez, C. "POF Sensors for Aircraft Structures and Engine Monitoring". 2016 Optical Fiber Communication Conference and Exhibition (OFC2016), Anaheim, USA, March 20, 2016 **(Invitada)**.

[Conf 6] Zubia, J., **García, I.,** Villatoro, J., Illaramendi, M.A., Mateo, J., Vázquez, C. "POF sensors for aeronautical engine monitoring". 24rd International Conference on Plastic Optical Fibers (POF2015), Nuremberg, Germany, September 22, 2015 **(Invitada)**.

[Conf 7] Gil-García, J.M.; **García, I.;** Zubia, J.; Aranguren G. "Measurement of blade tip clearance and time of arrival in turbines using an optic sensor". 2015 International Conference on Applied Electronics (AE), Pilsen, Czech Republic, September 8, 2015.

[Conf 8] **García, I.,** Zubia, J., Beloki, J., Aldabaldetreku, G., Durana, G. and Illaramendi, M.A. "Optical tip clearance measurements for rotating disk characterization". 17th International Conference on Transparent Optical Networks (ICTON), Budapest, Hungary, July 5, 2015 **(Invitada)**.

[Conf 9] **García, I.,** Zubia, J., Beloki, J., Arrue, J., Villatoro, J. "Evaluation of the vibrational behaviour of a rotating disk by optical tip-clearance measurements". SPIE Optical Metrology, Munich, Germany, June 22, 2015.

[Conf 10] Gil-García, J.M., **García, I.,** Zubia, J., Aranguren G. "Blade tip clearance and time of arrival immediate measurement method using an optic probe". 2nd IEEE International Workshop on Metrology for Aerospace, Benevento, Italy, June 4, 2015.

[Conf 11] **García, I.,** Zubia, J., Berganza, A., Arrospide E., Casado, L., Vázquez, C., Mateo, J. "Performance characterization of a low-cost optical current sensor against temperature fluctuations". 23rd International Conference on Plastic Optical Fibers (POF 2014), Yokohama, Japan, October 8, 2014.

[Conf 12] Zubia, J., **Garcia, I.,** Berganza, A., Beloki, J., Arrue, J., Mateo, J. "Improvements in the design of an optical sensor for tip-clearance measurements in turbines". 16th International Conference on Transparent Optical Networks (ICTON), Graz, Austria, June 6, 2014 **(Invitada)**.

[Conf 13] **García, I.,** Zubia, J., Berganza, A., Beloki, J., Mateo, J., Vázquez, C. (2014). "Comparison of three different configurations of an optical sensor for tip-clearance measurements in

turbines". 23rd International Conference on Optical Fibre Sensors, Santander, Spain, June 2, 2014.

[Conf 14] Zubia, J., **García, I.,** Beloki, J., Durana, G., Aldabaldetreku, G., Illarramendi, M. A., Berganza, A. "Low-cost current, tip timing and tip clearance measurement sensors based on plastic optical fibers". 22nd Internacional Conference on Plastic Optical Fibers, Armaçao dos Buzios, Brazil, September 11, 2013 **(Invitada)**.

[Conf 15] **García, I.,** Berganza, A., Aldabaldetreku, G., Durana, G., Arrospide, E., Zubia, J. "Sensor basado en un haz de fibras ópticas para la medida del tip timing y tip clearance de los álabes de una turbina". 8ª Reunión Española de Optoelectrónica, Alcalá de Henares, Spain, July 10, 2013.

[Conf 16] **García, I.,** Beloki, J., Zubia, J., Durana, G., Aldabaldetreku, G. "Turbine-blade tip clearance and tip timing measurements using an optical fiber bundle sensor". SPIE Optical Metrology, Munich, Germany, May 13, 2013.

Referencias

[1] Fidanboylu, K. A., & Efendioglu, H. S. (2009, May). Fiber optic sensors and their applications. In *5th International Advanced Technologies Symposium (IATS'09)* (Vol. 6).

[2] López-Higuera, J. M. (Ed.). (2002). *Handbook of optical fibre sensing technology*. Wiley.

[3] Grattan, K. T. V., & Sun, T. (2000). Fiber optic sensor technology: an overview. *Sensors and Actuators A: Physical*, *82*(1), 40-61.

[4] Sabri, N., Aljunid, S. A., Salim, M. S., Ahmad, R. B., & Kamaruddin, R. (2013). Toward optical sensors: Review and applications. In *Journal of Physics: Conference Series* (Vol. 423, No. 1, p. 012064). IOP Publishing.

[5] Anwar Zawawi, M., O'Keffe, S., & Lewis, E. (2013). Intensity-modulated fiber optic sensor for health monitoring applications: a comparative review. *Sensor Review*, *33*(1), 57-67.

[6] Krohn, D. A. (1987, April). Intensity modulated fiber optic sensors overview. In *Cambridge Symposium-Fiber/LASE'86* (pp. 2-11). International Society for Optics and Photonics.

[7] Rantala, J., Hännikäinen, J., & Vanhala, J. (2011). Fiber optic sensors for wearable applications. *Personal and Ubiquitous Computing*, *15*(1), 85-96.

[8] Wild, G., & Hinckley, S. (2008). Acousto-ultrasonic optical fiber sensors: overview and state-of-the-art. *IEEE Sensors Journal*, *8*(7), 1184-1193.

[9] Krohn, D. A. Fiber Optic Sensors, fundamentals and applications, 2000. *Instrument Society of America*.

[10] Boller, C., & Meyendorf, N. (2008, December). State-of-the-art in Structural Health monitoring for aeronautics. In *Proc. of Internat. Symposium on NDT in Aerospace*.

[11] Wild, G. (2013, February). Optical fiber Bragg grating sensors applied to gas turbine engine instrumentation and monitoring. In *Sensors Applications Symposium (SAS), 2013 IEEE* (pp. 188-192). IEEE.

[12] Heath, S., & Imregun, M. (1998). A survey of blade tip-timing measurement techniques for turbomachinery vibration. *Journal of Engineering for Gas Turbines and Power*, *120*(4), 784-791.

[13] Wisler, D. C. (1985). Loss reduction in axial-flow compressors through low-speed model testing. *Journal of engineering for gas turbines and power*, *107*(2), 354-363.

[14] Wiseman, M. W., & Guo, T. H. (2001). An investigation of life extending control techniques for gas turbine engines. In *American Control Conference, 2001. Proceedings of the 2001* (Vol. 5, pp. 3706-3707). IEEE.

[15] Airline Fuel Cost and Consumption. Disponible en http://www.transtats.bts.gov/fuel.asp (accedido el 26 de octubre de 2016).

[16] Geisheimer, J. L., & Holst, T. A. (2007, April). Metrology considerations for calibrating turbine tip clearance sensors. In *JL Geisheimer, TA Holst–Rhode-St-Genèse, Belgium: XIX Biannual Symposium on Measuring Techniques in Turbomachinery*.

[17] Kempe, A., Schlamp, S., Rösgen, T., & Haffner, K. (2006, June). Spatial and temporal high-resolution optical tip-clearance probe for harsh environments. In *13th Int Symp on Applications of Laser Techniques to Fluid Mechanics*.

[18] Guo, O. A.. Active Turbine Tip Clearance Control Research. Available online: http://www.grc.nasa.gov/WWW/cdtb/aboutus/workshop2015/ACC_2_Guo.pdf (accessed on 8 August 2016).

[19] Sheard, A. G. (2011). Blade by blade tip clearance measurement. *International Journal of Rotating Machinery*, *2011*.

[20] Haase, W. C.; Haase, Z. S. High-Speed, capacitance-based tip clearance sensing. In Proceedings of Aerospace Conference, Big Sky, MT, USA, 2013.

[21] Haase, W. C., & Haase, Z. S. (2013, March). High-Speed, capacitance-based tip clearance sensing. In *Aerospace Conference, 2013 IEEE* (pp. 1-8). IEEE.

[22] Cao, S. Z., Duan, F. J., & Zhang, Y. G. (2006). Measurement of rotating blade tip clearance with fibre-optic probe. In *Journal of Physics: Conference Series*(Vol. 48, No. 1, p. 873). IOP Publishing.

[23] Schicht, A., Schwarzer, S., & Schmidt, L. P. (2012). Tip clearance measurement technique for stationary gas turbines using an autofocusing millimeter-wave synthetic aperture radar. *IEEE Transactions on Instrumentation and Measurement*, *61*(6), 1778-1785.

[24] Violetti, M., Skrivervik, A. K., Xu, Q., & Hafner, M. (2012, October). New microwave sensing system for blade tip clearance measurement in gas turbines. In *Sensors, 2012 IEEE* (pp. 1-4). IEEE.

[25] Pfister, T., Büttner, L., Czarske, J., Krain, H., & Schodl, R. (2006). Turbo machine tip clearance and vibration measurements using a fibre optic laser Doppler position sensor. *Measurement Science and Technology*, *17*(7), 1693.

[26] Kempe, A., Schlamp, S., Rösgen, T., & Haffner, K. (2003). Low-coherence interferometric tip-clearance probe. *Optics letters*, *28*(15), 1323-1325.

[27] Georgiev, V., Holík, M., Kraus, V., Krutina, A., Kubín, Z., Liška, J., & Poupa, M. (2011, July). The blade flutter measurement based on the blade tip timing method. In *Proceedings of the 15th WSEAS International Conference on Systems, Corfu Island, Greece* (pp. 14-16).

[28] Zablotskii, I. E., Korostelev, Y. A., & Sviblov, L. B. (1974). *Contactless measuring of vibrations in the rotor blades of turbines* (No. FTD-HT-23-673-74). FOREIGN TECHNOLOGY DIV WRIGHT-PATTERSON AFB OH.

[29] Nieberding, W. C., & Pollack, J. L. (1977, March). Optical detection of blade flutter. In *ASME 1977 International Gas Turbine Conference and Products Show* (pp. V001T01A064-V001T01A064). American Society of Mechanical Engineers.

[30] Roth, H. (1980). Vibration measurements on turbomachine rotor blades with optical probes. In *Measurement Methods in Rotating Components of Turbomachinery* (Vol. 1, pp. 215-224).

[31] McCarty, P. E., & Thompsonk Jr, J. W. (1980). *Development of a Noninterference Technique for Measurement of Turbine Engine Compressor Blade Stress* (No. AEDC-TR-79-78). ARNOLD ENGINEERING DEVELOPMENT CENTER ARNOLD AFB TN.

[32] Watkins, W. B., Robinson, W. W., & Chi, R. M. (1985). Noncontact engine blade vibration measurements and analysis. In *AIAA, SAE, ASME, and ASEE, Joint Propulsion Conference, 21 st, Monterey, CA*.

[33] Watkins, W. B., & Chi, R. M. (1989). Noninterference blade-vibration measurement system for gas turbine engines. *Journal of Propulsion and Power*, *5*(6), 727-730.

[34] Kawashima, T., Iinuma, H., Wakatsuki, T., & Minagawa, N. (1992, June). Turbine blade vibration monitoring system. In *ASME 1992 International Gas Turbine and Aeroengine Congress and Exposition* (pp. V005T14A016-V005T14A016). American Society of Mechanical Engineers.

[35] Fuehrer, K., Bloemers, D., Zuefle, E., & Wuethrich, C. (1993). Optische Überwachung von Turbinenschaufelschwingungen im Betrieb. *VGB Kraftwerkstechnik*, *73*(1), 29-33.

[36] Kramer, E., & Plan, E. (1997). Optical vibration measuring system for long, free-standing LP rotor blades. *ABB REV*, (5), 4-9.

[37] Heath, S., & Imregun, M. (1998). A survey of blade tip-timing measurement techniques for turbomachinery vibration. *Journal of Engineering for Gas Turbines and Power*, *120*(4), 784-791.

[38] Baumgartner, M., Kameier, F., & Hourmouziadis, J. (1995). Non-engine order blade vibration in a high pressure compressor. In *ISABE- International Symposium on Air Breathing Engines, 12 th, Melbourne, Australia* (pp. 1019-1030).

[39] Freund, O., Montgomery, M., Mittelbach, M., & Seume, J. R. (2014). Non-contact test set-up for aeroelasticity in a rotating turbomachine combining a novel acoustic excitation system with tip-timing. *Measurement Science and Technology*, *25*(3), 035008.

[40] Dello, J. (1987). Frequency evaluation of a steam turbine bladed disk. *Turbomachinery International (January/February 1987)*.

[41] Washburn, R., & Kim, N. (2007). Hardware transmitted excitation sources and the associated blade responses using tip timing instrumentation. *LECTURE SERIES-VON KARMAN INSTITUTE FOR FLUID DYNAMICS*, *3*, 10.

[42] Kameier, F., & Neise, W. (1997). Rotating blade flow instability as a source of noise in axial turbomachines. *Journal of Sound and Vibration*, *203*(5), 833-853.

[43] Srinivasan, A. V. (1997). Flutter and resonant vibration characteristics of engine blades. *Journal of Engineering for Gas Turbines and Power*, *119*(4), 742-775.

[44] Janicki, G., Pezouvanis, A., Mason, B., & Ebrahimi, M. K. (2014). Turbine blade vibration measurement methods for turbocharges. *American Journal of Sensor Technology*, *2*(2), 13-19.

[45] Zielinski, M., & Ziller, G. (2000). Noncontact vibration measurements on compressor rotor blades. *Measurement Science and Technology*, *11*(7), 847.

[46] Zielinski, M., & Ziller, G. (1998). Optical blade vibration measurement at MTU. In *AGARD conference proceedings* (pp. 31-1). AGARD.

[47] Frischbier, J., Schulze, G., Zielinski, M., Ziller, G., Blaha, C., & Hennecke, D. K. (1996, June). Blade Vibrations of a High Speed Compressor Blisk-Rotor: Numerical Resonance Tuning and Optical Measurements. In *ASME 1996 International Gas Turbine and Aeroengine Congress and Exhibition* (pp. V005T14A007-V005T14A007). American Society of Mechanical Engineers.

[48] Allport, J. M., Jupp, M. L., Pezouvanis, A., Janicki, G. W., Pierończyk, A. I., Day, A. J., ... & Ebrahimi, M. K. (2012, May). Turbocharger blade vibration: Measurement and validation through laser tip-timing. In *10th International Conference on Turbochargers and Turbocharging* (pp. 173-181). Elsevier.

[49] Chen, Z., Yang, Y., Xie, Y., Guo, B., & Hu, Z. (2013). Non-contact crack detection of high-speed blades based on principal component analysis and Euclidian angles using optical-fiber sensors. *Sensors and Actuators A: Physical*, *201*, 66-72.

[50] Zielinski, M. and Ziller, G., Noncontact blade vibration measurement system for aero engine application, Proceedings of 17th International Symposium on Airbreathing Engines, Munich, Germany, Paper No. ISABE-2005-1220, September, 2005.

[51] Przysowa, R., Rokicki, E., & Majewski, P. (2014, June). Optimized magnetic sensors to measure speed and position in adverse environments. In *Instrumentation Symposium 2014, IET & ISA 60th International* (pp. 1-4). IET.

[52] Szczepanik, R., Rokicki, E., Spychała, J., Kaźmierczak, K., Majewski, P., & Przysowa, R. (2012). *Application of blade-tip sensors to blade-vibration monitoring in gas turbines*. INTECH Open Access Publisher.

[53] Faria, J. B. (1998). A theoretical analysis of the bifurcated fiber bundle displacement sensor. *IEEE Transactions on instrumentation and measurement*, *47*(3), 742-747.

[54] Yasin, M., Harun, S. W., Abdul-Rashid, H. A., & Zaidan, A. H. (2007). Performance of optical displacement sensor using a pair type bundled fiber from a theoretical and experimental perspective. *Optoelectronics and Advanced Materials-Rapid Communications*, *1*(11), 549-553.

[55] Huang, H., & Tata, U. (2008). Simulation, implementation, and analysis of an optical fiber bundle distance sensor with single mode illumination. *Applied optics*, *47*(9), 1302-1309.

[56] Bergougnoux, L., Misguich-Ripault, J., & Firpo, J. L. (1998). Characterization of an optical fiber bundle sensor. *Review of scientific instruments*, *69*(5), 1985-1990.

[57] Suganuma, F., Shimamoto, A., & Tanaka, K. (1999). Development of a differential optical-fiber displacement sensor. *Applied optics*, *38*(7), 1103-1109.

[58] Cao, S., Duan, F., Fang, Z., & Ma, Y. (2006, June). Research on optical fiber bundle displacement sensor with multi-grouped receiving fibers. In *Advanced Laser Technologies 2005* (pp. 63442Y-63442Y). International Society for Optics and Photonics.

[59] Binu, S., & George, J. (2013). Displacement sensing with polymer fibre optic probe. *Frontiers in Sensors (FS) Vol*, *1*.
[60] Cook, R. O., & Hamm, C. W. (1979). Fiber optic lever displacement transducer. *Applied Optics*, *18*(19), 3230-3241.
[61] Shimamoto, A., & Tanaka, K. (1995). Optical fiber bundle displacement sensor using an ac-modulated light source with subnanometer resolution and low thermal drift. *Applied optics*, *34*(25), 5854-5860.
[62] Qing-Bin, T., Hui-Ping, M., Li-Hua, L., Xiao-Dong, Z., & Gui-Bin, L. (2011). Measurements of radiation vibrations of turbomachine blades using an optical-fiber displacement-sensing system. *Journal of Russian Laser Research*, *32*(3), 216-229.
[63] Guo, H., Duan, F., Wu, G., & Zhang, J. (2014). Blade tip clearance measurement of the turbine engines based on a multi-mode fiber coupled laser ranging system. *Review of Scientific Instruments*, *85*(11), 115105.
[64] Ye, D. C., Duan, F. J., Guo, H. T., Li, Y., & Wang, K. (2012). Turbine blade tip clearance measurement using a skewed dual-beam fiber optic sensor. *Optical Engineering*, *51*(8), 081514-1.
[65] Binghui, J., & Xiaodong, Z. (2011). An optical fiber blade tip clearance sensor for active clearance control applications. *Procedia Engineering*, *15*, 984-988.
[66] Cao, H., Chen, Y., Zhou, Z., & Zhang, G. (2007). Theoretical and experimental study on the optical fiber bundle displacement sensors. *Sensors and Actuators A: Physical*, *136*(2), 580-587.
[67] Yu-zhen, M., Yong-kui, Z., Guo-ping, L., & Hua-guan, L. (2011, January). Tip clearance optical measurement for rotating blades. In *Management Science and Industrial Engineering (MSIE), 2011 International Conference on* (pp. 1206-1208). IEEE.
[68] Vázquez, R., Iturregui, J. J., Arsuaga, M., & Armananzas, L. (2003). A New Transonic Test Turbine Facility. In *XVI International Symposium on Air Breathing Engines (ISABE), Cleveland, OH, August*.
[69] Hill, K. O., Tremblay, Y., & Kawasaki, B. S. (1980). Modal noise in multimode fiber links: theory and experiment. *Optics letters*, *5*(6), 270-272.
[70] Petermann, K. (1980). Nonlinear distortions and noise in optical communication systems due to fiber connectors. *IEEE Journal of Quantum Electronics*, *16*(7), 761-770.
[71] Couch, P., & Epworth, R. (1983). Reproducible modal noise measurements in system design and analysis. *Journal of Lightwave Technology*, *1*(4), 591-596.
[72] Daino, B., De Marchis, G., & Piazzolla, S. (1979). Analysis and measurement of modal noise in an optical fibre. *Electronics Letters*, *15*, 755.
[73] Attia, R., & Marcou, J. (2000). Mode scrambler for polymer optical fibers. *Optical Engineering*, *39*(1), 299-303.
[74] Savović, S., & Djordjevich, A. (2009). Calculation of the coupling coefficient in step index glass optical fibers. *Applied optics*, *48*(22), 4496-4500.
[75] Test Methods for Attenuation of All Plastic Multimode Optical Fibers, Japanese Industrial Standard, JIS C 6863, 1990.
[76] Jiang, G., Shi, R. F., & Garito, A. F. (1997). Mode coupling and equilibrium mode distribution conditions in plastic optical fibers. *IEEE Photonics Technology Letters*, *9*(8), 1128-1130.
[77] Zubia, J., & Arrue, J. (2001). Plastic optical fibers: An introduction to their technological processes and applications. *Optical Fiber Technology*, *7*(2), 101-140.
[78] Peterman, K., & Arnold, G. (1982). Noise and distortion characteristics of semiconductor lasers in optical fiber communication systems. *IEEE Transactions on Microwave Theory and Techniques*, *30*(4), 389-401.
[79] Shimamoto, A., & Tanaka, K. (1996). Geometrical analysis of an optical fiber bundle displacement sensor. *Applied optics*, *35*(34), 6767-6774.

[80] Harun, S. W., Yang, H. Z., Yasin, M., & Ahmad, H. (2010). Theoretical and experimental study on the fiber optic displacement sensor with two receiving fibers. *Microwave and Optical Technology Letters*, *52*(2), 373-375.

[81] Judge, J., Pierre, C., & Mehmed, O. (2000, May). Experimental investigation of mode localization and forced response amplitude magnification for a mistuned bladed disk. In *ASME Turbo Expo 2000: Power for Land, Sea, and Air* (pp. V004T03A004-V004T03A004). American Society of Mechanical Engineers.

[82] Szczepanik, R., & Witoś, M. (2000). Turbine Engine Health/Maintenance Status Monitoring with Use of Phase-Discrete Method of Blade Vibration Monitoring. *Proceedings of RTO-M8-AVT-121*.

[83] Przysowa, R., & Rokicki, E. (2015). Inductive sensors for blade tip-timing in gas turbines. *Test Cell and Controls Instrumentation and EHM Technologies for Military Air, Land and Sea Turbine Engines, MP-AVT-229-10, Rzeszów*.

[84] Tappert, P., von Flotow, A., & Mercadal, M. (2001). Autonomous PHM with blade-tip-sensors: algorithms and seeded fault experience. In *Aerospace Conference, 2001, IEEE Proceedings.* (Vol. 7, pp. 7-3295). IEEE.

Apéndice: Contribuciones de la tesis

Artículo 1

Optical Fiber Sensors for Aircraft Structural Health Monitoring

García, I., Zubia, J., Durana, G., Aldabaldetreku, G., Illarramendi, M. A., & Villatoro, J.

Sensors, *15*(7), 15494-15519 (2015).

Sensors **2015**, *15*, 15494-15519; doi:10.3390/s150715494

OPEN ACCESS

sensors

ISSN 1424-8220

www.mdpi.com/journal/sensors

Review

Optical Fiber Sensors for Aircraft Structural Health Monitoring

Iker García [1,*], Joseba Zubia [1], Gaizka Durana [1], Gotzon Aldabaldetreku [1], María Asunción Illarramendi [2] and Joel Villatoro [1,3]

[1] Department of Communications Engineering, E.T.S.I. of Bilbao, University of the Basque Country UPV/EHU, Alda. Urquijo s/n Bilbao 48013, Spain; E-Mails: joseba.zubia@ehu.eus (J.Z.); gaizka.durana@ehu.eus (G.D.); gotzon.aldabaldetreku@ehu.eus (G.A.); agustinjoel.villatoro@ehu.eus (J.V.)

[2] Department of Applied Physics I, E.T.S.I. of Bilbao, University of the Basque Country UPV/EHU, Alda. Urquijo s/n Bilbao 48013, Spain; E-Mail: ma.illarramendi@ehu.eus

[3] IKERBASQUE—Basque Foundation for Science, E-48011 Bilbao, Spain

***** Author to whom correspondence should be addressed; E-Mail: iker.garciae@ehu.eus; Tel.: +34-946-017-305; Fax: +34-946-014-259.

Academic Editor: Vittorio M.N. Passaro

Received: 8 May 2015 / Accepted: 19 June 2015 / Published: 30 June 2015

Abstract: Aircraft structures require periodic and scheduled inspection and maintenance operations due to their special operating conditions and the principles of design employed to develop them. Therefore, structural health monitoring has a great potential to reduce the costs related to these operations. Optical fiber sensors applied to the monitoring of aircraft structures provide some advantages over traditional sensors. Several practical applications for structures and engines we have been working on are reported in this article. Fiber Bragg gratings have been analyzed in detail, because they have proved to constitute the most promising technology in this field, and two different alternatives for strain measurements are also described. With regard to engine condition evaluation, we present some results obtained with a reflected intensity-modulated optical fiber sensor for tip clearance and tip timing measurements in a turbine assembled in a wind tunnel.

Keywords: structural health monitoring; optical fiber sensors; fiber Bragg grating; long period grating; turbine condition monitoring

1. Introduction

All kinds of engineering infrastructures undergo aging, and damage appears as a consequence of the loads applied to them, so inspection and maintenance actions are required to predict and lengthen their lifetime thus avoiding catastrophic failures. Among these infrastructures, those related to aviation demand the highest levels of damage detection, since most of them are designed according to a damage-tolerant principle [1]. In order to get lighter structures, these are designed to withstand damages with certain characteristics. Nevertheless, damage-tolerant design involves a considerable amount of time and effort for structure inspection, because there are a wide variety of factors that can cause damage in aircraft structures, most of which are summarized in [2]. Due to the harsh conditions suffered by aircraft structures, periodic and scheduled inspection and maintenance tasks are essential for safe and efficient operation. The cost for the personnel needed to carry out these procedures is high, but the cost due to aircraft downtime during these time-consuming inspections is significantly greater [3]. Hence, automation of the inspection process is a point of capital importance to reduce inspection efforts. In this context, a structural health monitoring (SHM) system can be defined as a set of devices that provides information that allows us to locate, evaluate and predict the loading and damage conditions of a structure. SHM of aircraft structures can perform real time inspection, reducing costs and improving the reliability and performance of these structures [4]. The successful application of SHM to aircraft requires two conditions: it must provide reliable and accurate information about the condition of the structure, increasing the security of critical components and avoiding disasters, and it must be a profitable process for the airline operators by reducing economic losses caused by unproductive downtimes. Therefore, there is a great interest from industry and academia in developing SHM systems that meet both conditions. A wide range of potential SHM technologies is being developed to fulfill these conditions [1], and the most promising options are: electrical strain gauges and crack wires, acoustic emission methods, optical-based technologies, comparative vacuum monitoring [5] and MEMS.

Their intrinsic capabilities, such as insensitivity to electromagnetic radiation, light weight, small size, great sensitivity and resolution, and, above all, their suitability to be embedded into structures [6], make optical fiber sensors (OFSs) very appropriate to perform SHM [7]. There are three possible approaches in order to deploy a SHM system based on optical sensors [8]. The first one uses single-point sensors [9], which is the way in which most of the pressure or temperature sensors operate. The second one employs distributed sensing [10], where the measurand can be obtained at any point of an optical fiber. Finally, there are quasi-distributed systems that use a number of single-point sensors, allowing the sensing of large structures [11]. In this review article we summarize some of the results we have obtained in relation to aircraft SHM projects during the last few years. In Section 2.1, the basic principles of fiber Bragg gratings (FBG) and a quasi-distributed system for impact detection are presented. In Section 2.2, we describe the measurement of strain along a helicopter tail boom by using an elongation sensor, and also the determination of strain in a steel plate by means of a long period grating (LPG). Whereas the LPG is a single-point sensor, the elongation sensor is a distributed one. The performances of both sensors are compared with the results obtained using FBGs. Finally, in Section 3 the design and results of an optical sensor that has been used to carry out the SHM of an aircraft turbine are reported.

2. SHM in Aircraft Structures

OFSs for monitoring the strain in aircraft structures can be classified into the following categories [12]: intensity-based OFSs [13], interferometric OFSs [14], grating-based sensors and distributed OFSs [15]. Intensity-based OFSs were the first optical sensors employed to measure the strain, and they are the simplest and least expensive optical sensors for SHM. Interferometers work on the principle of the interference caused by a reflected monocromatic light with its original source. Several interferometer configurations have been proposed, being Fabry-Perot the most widely utilized. There are different techniques for implementing a distributed OFS; optical time domain reflectometry (OTDR) based on Rayleigh scattering, Raman optical time domain reflectometry (ROTDR) or Brillouin optical time domain reflectometry (BOTDR), based on Raman and Brillouin scattering, respectively. BOTDR resolution and acquisition time has been improved by Brillouin optical time domain analysis (BOTDA) using the phenomenon know as Stimulated Brillouin Scatter. Among grating-based sensors, FBGs are probably the most mature and widely employed optical sensors for SHM of engineering structures, due to their fast development achieved in recent years [16,17]. For the particular case of aircraft structures, even though FBGs have demonstrated to be a promising technology to monitor strain [18], strain gauges still remain being the most used method to perform strain measurements in operational aircraft structures. FBGs have important advantages over conventional strain sensors, namely:

(a) Intrinsic benefits of optical fiber sensors such as light weight and small size, absence of electromagnetic interference, high sensitivity and resolution, *etc.* [19].
(b) Suitability for being attached to a structure or embedded in composite materials [20].
(c) Wavelength-encoded sensing in a way that is totally independent of the optical intensity [21], which confers them long-term stability without the need of recalibrating.
(d) High multiplexing capability: since each FBG has a narrow-wavelength operating band, it is possible to multiplex several sensors in the same fiber, thus allowing for simultaneous multi-point measurements [22].
(e) Different magnitudes can be measured using FBGs, such as strain, temperature, vibration or humidity.

Regarding strain measurement, FBGs show a similar behavior to strain gauges. However, even though strain gauges are robust, low cost and well known, they present important disadvantages such as their long-term signal drift or time-consuming and complex wiring [23], since two leads per sensor are required. The multiplexing capability of the FBGs overcomes the complex wiring drawback. This characteristic has been reported in several works [11,24], in which the multiplexing capability of the FBGs provides a size optimization for the practical implementation of a quasi-distributed SHM system. The additional possibility of being embedded in the structures allows the use of FBGs to identify damage in composite structures [20], as well as the monitoring of composite cure during its manufacture [25].

2.1. Fiber Bragg Gratings

An optical fiber grating can be defined as a periodic perturbation pattern in the refractive index of the fiber core, in such a way that certain wavelengths of the guided mode are diffracted either into other

radiation modes or into cladding modes [26]. In the former case, the device is known as a short-period fiber grating or fiber Bragg grating. Such gratings have a sub-micron period and a total length ranging from 1 mm to 10 mm. A Bragg grating allows most of the power (P_o) to propagate forward. However, when the guided mode in a single-mode fiber reaches the grating, a certain portion of its incident power (P_i) is reflected at each grating plane. The electric fields are added up only if the Bragg condition given by Equation (1) is satisfied:

$$\lambda_B = 2 \cdot n_{eff} \cdot \Lambda \tag{1}$$

where λ_B is the resonant wavelength or Bragg wavelength, n_{eff} is the effective index of the mode and Λ is the grating period. The working principle of the FBGs is illustrated in Figure 1.

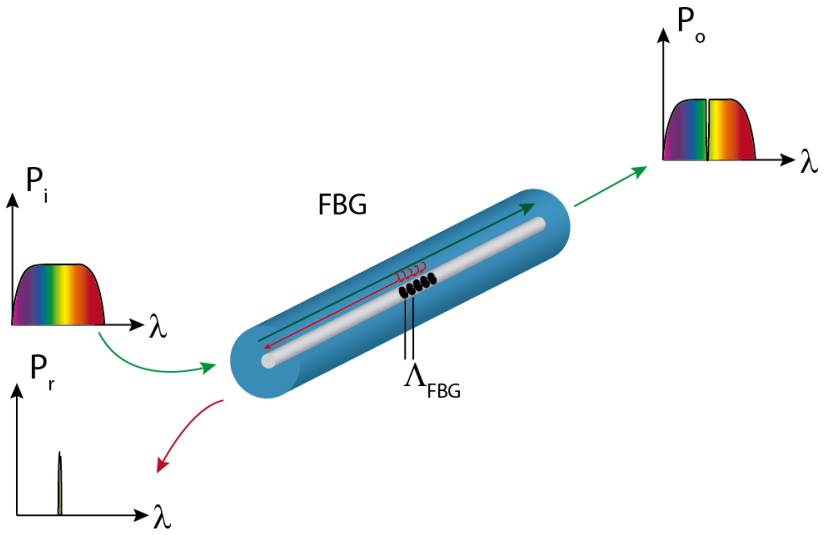

Figure 1. FBG concept and working principle.

There are two basic techniques to inscribe Bragg gratings in fibers. The first one uses ultraviolet light to change the refractive index of photosensitized fibers. The photosensitivity process typically consists in doping the fiber core with germanium, so that the fiber becomes receptive to UV-induced refractive index changes. Several methods have been employed to enhance the photosensitivity, such as high temperature treatment of hydrogen preforms, B-Ge co-doping, flame brushing, and high-pressure hydrogen loading of fibers [27]. The second fabrication technique makes use of a femtosecond laser to write a grating in non-photosensitive single-mode commercial fibers [28]. The main advantages of this technique are the shortening of the processing time, the reduced requirements for the fabrication process and the mechanical strength of the gratings. Currently, the most employed methods to inscribe the gratings are holographic techniques [29] and phased mask methods [30]. The point-by-point technique is usually employed when femtosecond lasers are used to inscribe the gratings [31].

As mentioned before, the measurand is encoded in the variations of the Bragg wavelength. Any change in the temperature or in the strain of the fiber causes a change in the grating period and/or in the effective index, shifting the central wavelength reflected by the grating. When the FBG is subjected to a tension, the change in the Bragg wavelength is given by Equation (2):

$$\frac{\Delta\lambda_B}{\lambda_B} = (1 - P_e) \cdot \Delta\varepsilon \tag{2}$$

where ε is the longitudinal strain in the FBG and P_e is the effective photo-elastic constant of the fiber core material. In Equation (2), P_e can be calculated as:

$$P_e = \frac{n_{eff}}{2}\left[p_{12} - \upsilon\left(p_{11} + p_{12} \right)\right] \tag{3}$$

where p_{11} and p_{12} are the elasto-optic coefficients, which represent the change in the refractive index due to the applied strain, and υ is the Poison ratio. The temperature changes affect the Bragg wavelength in two ways. On the one hand, the expansion coefficient of the fiber material (α) characterizes the thermal expansion of the grating, and, on the other, the variations in the refractive index are determined by the thermo-optic coefficient (ζ). Therefore, the change in the Bragg wavelength with temperature can be expressed as:

$$\frac{\Delta\lambda_B}{\lambda_B} = (\alpha + \zeta)\cdot\Delta T \tag{4}$$

Combining Equations (2) and (4) we get that the total Bragg-wavelength variation can be calculated as:

$$\frac{\Delta\lambda_B}{\lambda_B} = (\alpha + \zeta)\cdot\Delta T + (1 - P_e)\cdot\Delta\varepsilon \tag{5}$$

Thus, it is clearly seen that the Bragg wavelength presents a cross-sensitivity phenomenon (it is sensitive to both temperature and strain). For strain measurements, the effect of temperature has to be compensated. Different configurations have been reported for this purpose [32–44]. However, when temperature gradients in the structure are not excessive, the use of a single FBG insulated from the effect of the strain is enough to compensate the effect of temperature in the rest of the FBGs, thus allowing us to discriminate the variations in the Bragg wavelength that appear as a consequence of strain. FBGs are excellent strain sensors when the load is applied in the axial direction of the sensor. In this situation, the FBG only undergoes contraction or elongation. If there is a transverse stress applied, the fiber presents birefringence due to the variation experienced by the effective refraction index on each propagation axis [45]. As a consequence, the grating exhibits two different Bragg conditions, and the approximately Gaussian-shaped reflected spectrum of the FBG splits into two peaks, as represented in Figure 2 [46]. Another similar phenomenon appears when there is a non-uniform strain field, because, in this case, the spectrum is broadened and even split into several peaks [20], which makes it difficult to track the Bragg wavelength. Both problems can arise when the FBG is embedded in composite materials. In conclusion, FBGs constitute a mature technology and compared to strain gauges, provide multiple benefits and attractive properties, such as multiplexing capability, the possibility of being embedded in the structure, long term stability and a competitive cost per channel. Nevertheless, some issues, like non-uniform or multidirectional complex strain conditions and the lack of aircraft certification must be solved, so that FBGs can be used in SHM systems for aircraft structures.

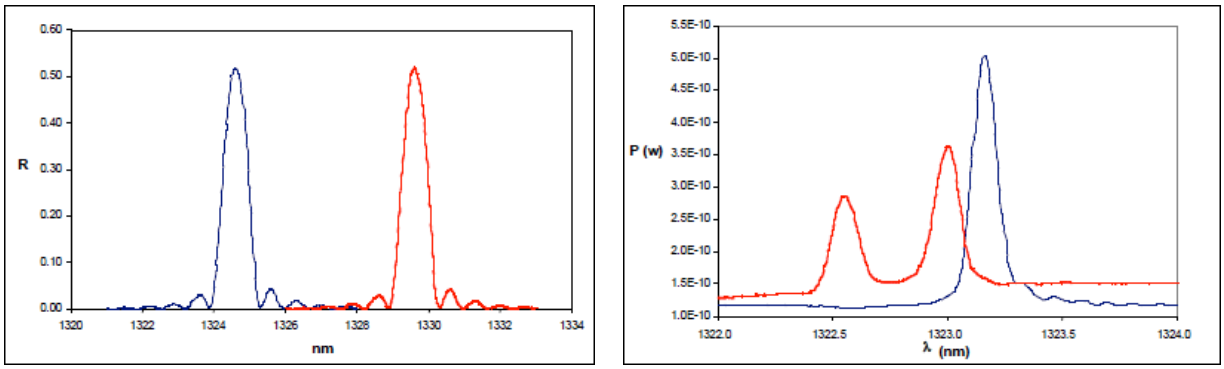

(**a**) (**b**)

Figure 2. (**a**) Ideal behavior of the reflected spectrum of an FBG subjected to a longitudinal strain; (**b**) Effect of a transverse stress on the reflected spectrum of the FBG. In all figures the blue line represents the non-perturbed spectrum of the FBG and the red one is the spectrum after the application of the load.

Another important concern is the effect of aging on the response of the FBGs under extreme conditions. In [47] an analysis of the influence of aging FBGs is presented. FBGs were bonded on three specimens using different adhesives to evaluate their performance against aging. In order to reproduce aging under real conditions, two of them were stored in a climate chamber at 70 ℃ and 90% relative humidity for one and two months, respectively. The damage produced in the specimen aged for two months can be observed in Figure 3.

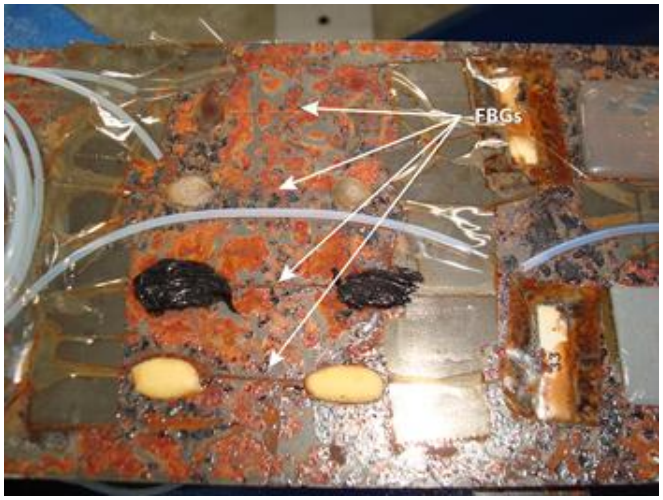

Figure 3. Photograph of four FBGs bonded with different adhesives to the F114 steel specimen after being aged for two months in a climate chamber.

The results of the tests on the specimens previously aged for one and two months are very similar and, unexpectedly, they show that the readings of the FBGs are about 50% higher than those obtained before the aging. Since the maximum working temperature of the FBG was never exceeded, this discrepancy in the readings must be caused by the effect of humidity. Its influence can make the refractive index vary, shifting the Bragg wavelength and yielding much higher strain values than expected, so in order to avoid this problem, it is necessary to properly insulate the FBG from humidity. The results for two FBGs of the specimen aged for one month for 200 kN traction stress tests are displayed in Figure 4. The traction

stress was applied in steps of 20 kN. In most cases, FBGs are employed in SHM applications to detect strain or temperature variations in a quasi-static way. However, if FBGs are used to detect impacts in aircraft structures, vibrations at higher frequencies must be analyzed [48]. We developed a proof-of-concept system for impact detection in composites using FBGs [49]. The objective was to obtain the arrival times of the surface mechanical waves produced by an impact in different points of the structure. Using these times, the impact location could be determined by triangulation. Two arrays of five FBGs were instrumented on a piece of Carbon Fiber Reinforced Polymer (CFRP). In order to detect the mechanical waves due to the impacts in as many directions as possible, nine of the FBGs were placed following the arrangement given in [50]. The remaining FBG was insulated from the vibrations and employed to compensate the effect of the temperature. The final layout can be observed in Figure 5. The test procedure included five different impact points; each impact was repeated three times with increasing energies from 0.245 J to 29.4 J.

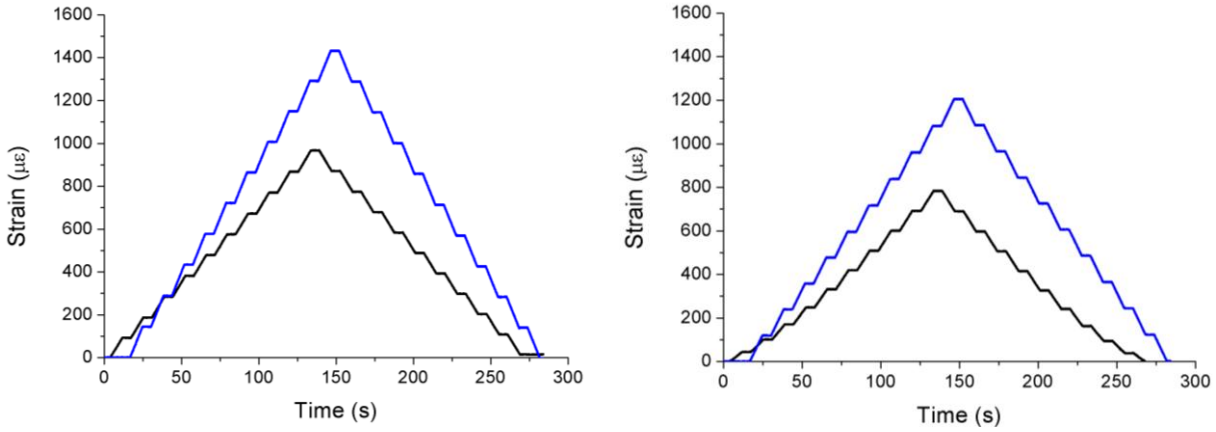

Figure 4. Spectra of two FBGs bonded on the specimen before (**black line**) and after (**blue line**) aging for one month in a climate chamber.

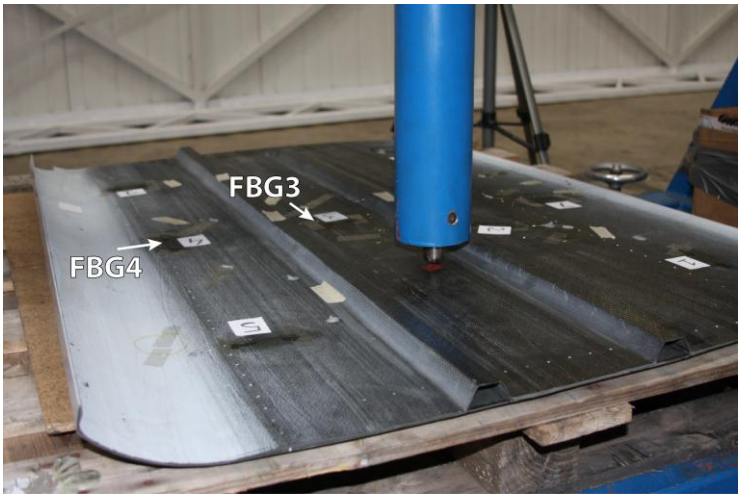

Figure 5. Instrumented specimen for impact detection and certified impact machine used in the tests.

A 20 kHz interrogator was employed to obtain the response of the FBGs and Figure 6 shows the difference between the arrival times of the wavefronts generated by the impact for two FBGs.

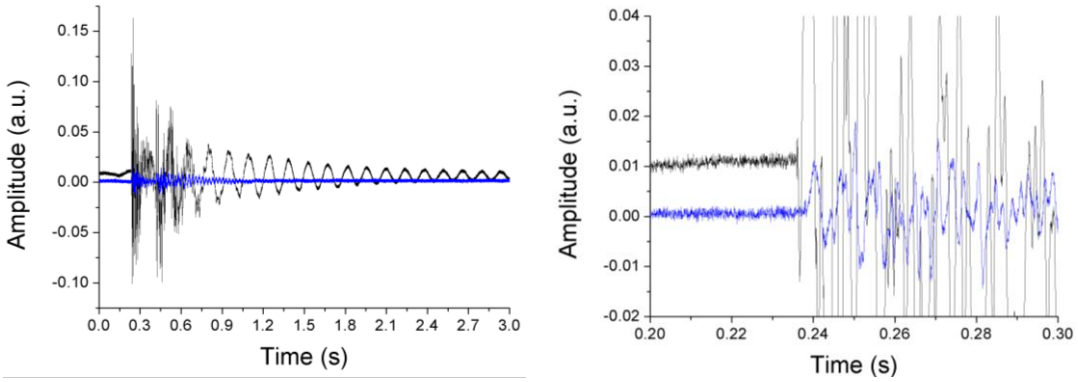

(**a**) (**b**)

Figure 6. (**a**) Response of two different FBGs (FBG3 and FBG4 shown in Figure 5) to the mechanical waves produced by an impact; (**b**) Detailed view of the arrival of the mechanical waves to the FBGs.

2.2. Alternatives to Fiber Bragg Gratings

FBGs are probably the most well-known, developed and widely used OFSs for SHM in aeronautical structures. Their characteristics make them the most promising technique to evaluate the condition of these structures, but in order to have a broad vision of the possibilities that OFSs offer, it is necessary to consider different alternatives to FBGs that can provide suitable solutions to specific cases. In this section we present two different sensors as possible alternatives to FBGs. Their performances are analyzed and compared to those of the FBGs working in the same conditions.

2.2.1. Plastic Optical Fiber Elongation Sensor

In this section we present a plastic optical fiber (POF) elongation sensor as a possible alternative to FBGs for the measurement of strain and vibrations in aircraft structures. The sensor's operating principle relies on the measurement of the phase shift between two sinusoidally-modulated optical signals. These signals travel in two different POFs, one used as reference and the other one bonded to the surface of the aircraft structure under test [51].

The main advantage of this sensor is the use of low-cost components. Conventional POFs are used as the sensitive component of the sensor. Due to the multimode nature of these fibers, the phase and the polarization state are not maintained along the fiber, so the only possible transduction technique must be based on intensity modulation [52]. In Figure 7 a schematic representation of the sensor is depicted. The output of the voltage-controlled oscillator (VCO) is a sinusoidal voltage with an adjustable frequency (f_m). This VCO signal is applied to the transmitter, which is basically a light-emitting diode at 650 nm. The Y coupler divides the optical signal in two identical ones that will be transmitted by the reference fiber and the measuring fiber, respectively. The receiver, essentially a photodiode, transforms into voltages the optical signals coming out from the fibers as:

$$V_{R1} = \sin\left(2\pi f_m t\right) \tag{6}$$

$$V_{R2} = \sin\left(2\pi f_m t + \Delta\phi\right) \tag{7}$$

When the measuring fiber is elongated or shortened due to the strain applied to the aircraft structure, the phase difference between the signals ($\Delta\phi$) given by Equations (6) and (7) changes. In order to capture the phase difference, the outputs of both receivers are connected to a phase comparator from which the elongation of the fiber (Δl) can be estimated as [53]:

$$\Delta l = \frac{c}{n_{core}} \cdot \frac{1}{360^{\circ}} \cdot \frac{\Delta\phi}{f_m} \tag{8}$$

where c is the speed of light in vacuum and n_{core} is the refractive index of the fiber core. Once the phase comparator signal is acquired by a data acquisition module (NI-USB3210 from National Instruments), a Labview program processes the signal to obtain the elongation of the fiber.

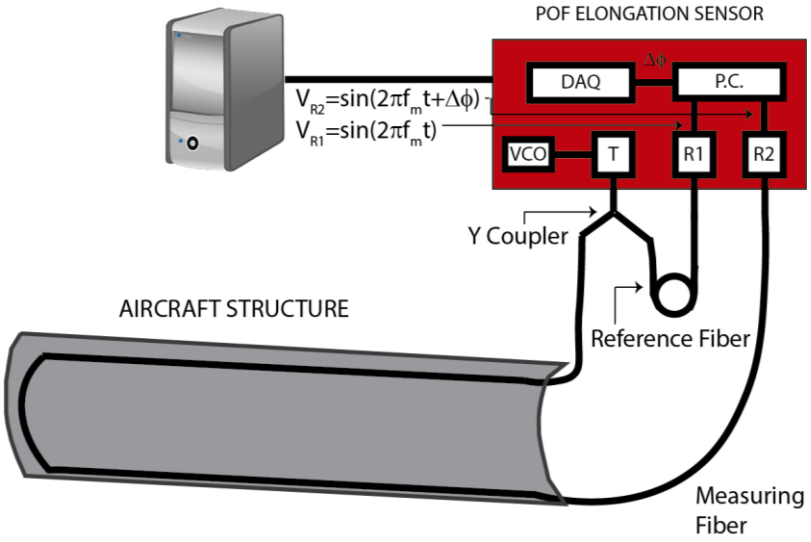

Figure 7. POF elongation sensor components and set-up. VCO: Voltage-controlled oscillator; T: Transmitter; R1: Receiver 1; R2: Receiver 2; P.C.: Phase comparator; DAQ: Data acquisition module.

In contrast to the discrete-point measurement obtained using FBGs, the POF elongation sensor provides a distributed measurement of the strain in the structure, since the overall fiber elongation is taken into account. In previous works [54,55], the sensor was employed to characterize the response of a wing flap to flexural-type loading conditions. We compared the results of the POF elongation sensor to those provided by FBGs. For these tests, the structure to be assessed was a helicopter (Eurocopter EC 135) tail boom which can be observed in Figure 8. The assembly is composed of a rigid metal structure on one end of the tail boom and a hydraulic actuator on the other one. The load applied by the actuator produces bending of the tail boom and, therefore, stress in the structure. Three different fatigue cycles were applied to the tail boom and each load cycle lasted for 16 s. The forces applied in the fatigue cycles were 0.25, 0.50 and 0.75 kN.

Besides the POF elongation sensor, ten FBGs in two different fibers were instrumented on the surface of the tail boom for the sake of comparison. In the first fiber, four FBGs were installed in the longitudinal direction of the tail boom and the last one in a perpendicular direction. For the second

fiber, four FBGs were placed longitudinally and one was used for temperature compensation. The response of the FBGs was measured using the SM130-200 interrogator from MicronOptics.

(**a**) (**b**)

Figure 8. (**a**) Experimental set-up for the tests performed on the tail boom; (**b**) Prototype of the electronics for the POF elongation sensor.

The results obtained by the POF elongation sensor for several load cycles can be observed in Figure 9. When a force of 0.75 kN or 0.5 kN is applied, the cycles are clearly detected by the sensor. However, for the case of 0.25 kN the noise makes it impossible to distinguish the stress cycles in the post-processed signal. The goal of these tests was to demonstrate the capability of the POF elongation sensor to detect the load cycles on the tail boom. Although this goal was achieved, more tests should be carried out to ensure the reliability of the sensor, and the quality of the output signal must be improved. The offset variations in the displacement signals are due to the drift of the modulation frequency provided by the VCO, which is interpreted by the phase comparator as a change in the phase of the received signals. Hence, the VCO performance must be optimized to stabilize the modulation frequency and avoid changes in the offset of the output signal. Another way to improve the POF elongation sensor would be to bond the reference fiber on the outer surface of the tail boom, so that the phase difference between the two optical signals would increase. Thus, increasing the sensitivity of the sensor. For the sake of comparison, the results obtained for one of the FBGs are plotted on Figure 10. The signals are obviously less noisy than those of the POF elongation sensor. The strain in the structure is represented by the changes of the reflected wavelength in the FBG for the three applied forces. As expected, the strain given by the FBG placed in the perpendicular direction of the tail boom is noticeably smaller than the ones provided by the FBG placed longitudinally.

The FBGs are much more sensitive than the POF elongation sensor and offer an excellent performance for a single-point measurement. On the other hand, the POF elongation sensor provides a distributed measurement of the strain in the whole structure and it is a cost-effective option when the required measurement resolution is not so high.

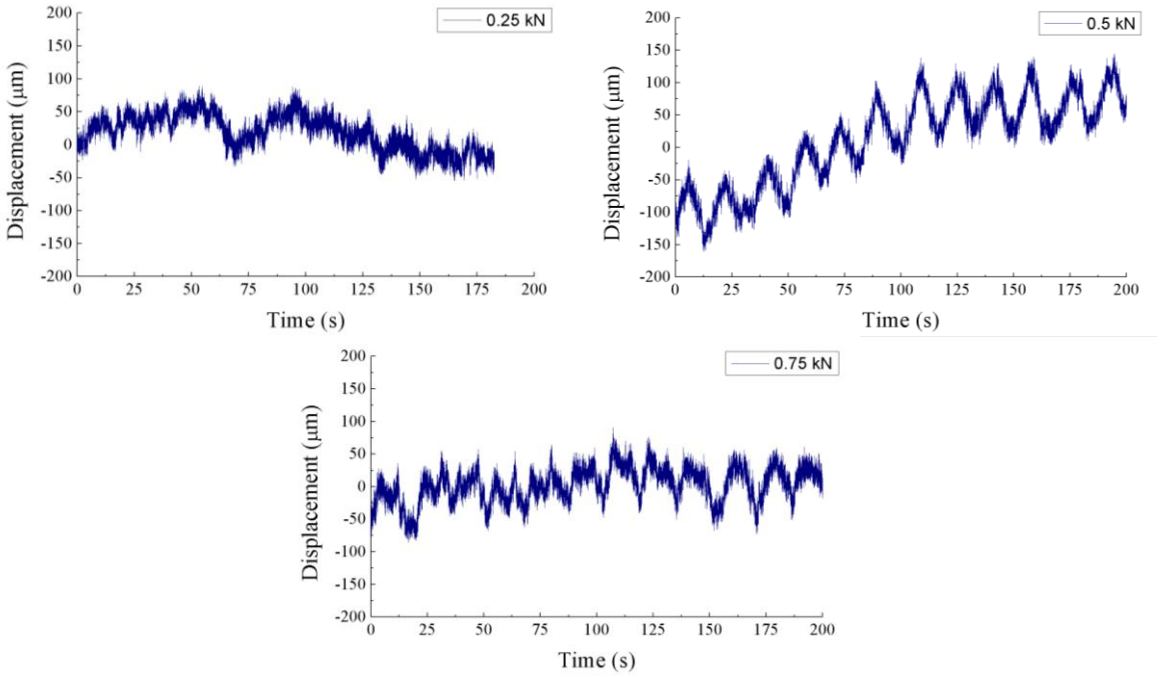

Figure 9. POF elongation corresponding to the three fatigue cycles of 0.25 kN, 0.5 kN and 0.75 kN.

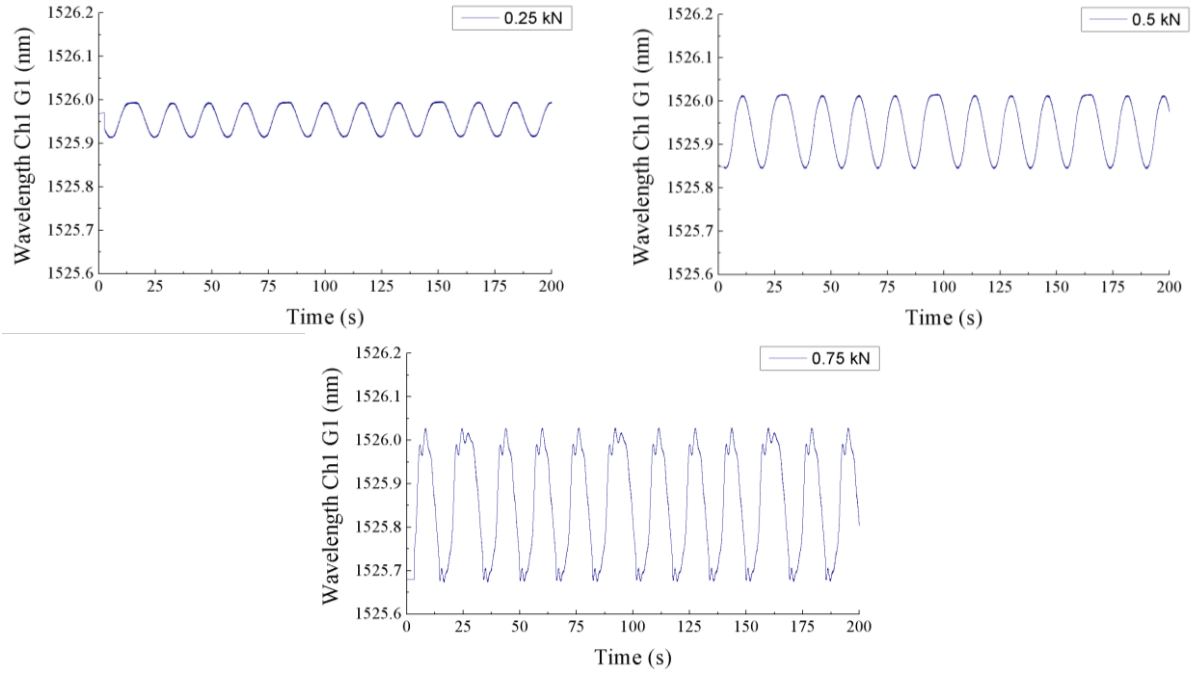

Figure 10. Wavelength variations due to the strain in the tail boom provided by the first FBG during the three fatigue cycles.

2.2.2. Long Period Gratings in Microstructured POF

In this section we present the use of long period gratings in microstructured POFs (mPOFs) as an option to measure strain in aircraft structures instead of FBGs. mPOFs are the counterpart version of the photonic crystal fibers using polymer fibers instead of glass fibers. In the mPOFs a pattern of air

channels along the POF guides the light and confers unique properties to the fiber [56]. Among these properties, the single-mode and polarization-maintaining behavior, combined with the intrinsic flexibility and ease of connection of the POF are particularly interesting for sensing purposes. In order to obtain an LPG in an mPOF, a periodic modification of the cladding structure of the mPOF is written along the direction of light propagation [57], so that the core mode is coupled to cladding modes, which are rapidly attenuated, resulting in depressions in the transmission spectrum at wavelengths where the Equation (9) is satisfied [58]:

$$m\lambda = (n_{core}(\lambda) - n_{cl}(\lambda))\Lambda_{LPG} \quad (9)$$

where m is the order of the interaction, n_{core} and n_{cl} are the effective indices of the core and the cladding, and Λ_{LPG} is the period of the grating. Unlike FBGs, this period is much larger than the wavelength of the light propagating along the mPOF, so LPGs are easier to fabricate. In the case of LPGs, the length of the structure is in the order of 30 mm, whereas the grating period range is typically from 100 μm to 1 mm [59]. The LPG causes the coupling between the core-guided mode and the forward-propagating cladding modes at certain wavelengths, which causes "notches" in its transmission spectrum. The working principle of the LPG is depicted in Figure 11.

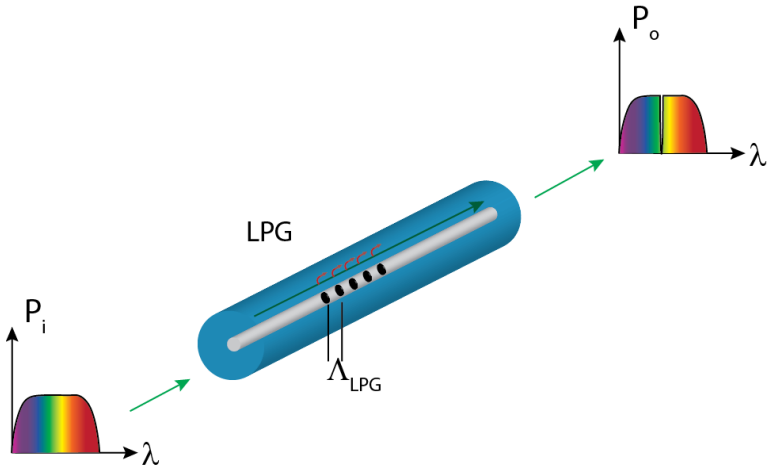

Figure 11. LPG concept and working principle.

Figure 12 shows the mPOF employed to inscribe the LPG that we used in the tests and its normalized transmission spectrum. Since changes in the strain of the mPOF can modify the period of the LPG, the wavelength that matches the phase condition changes. As a result, the depression at 620 nm in the spectrum is sensitive to strain and its wavelength changes accordingly.

In order to detect the changes of the resonant wavelength in the LPG, light from a white source is launched into the fiber and the spectrum of the output light is obtained by using the USB4000 miniature fiber optic spectrometer from Ocean Optics. The experimental set-up is represented in Figure 13 [60].

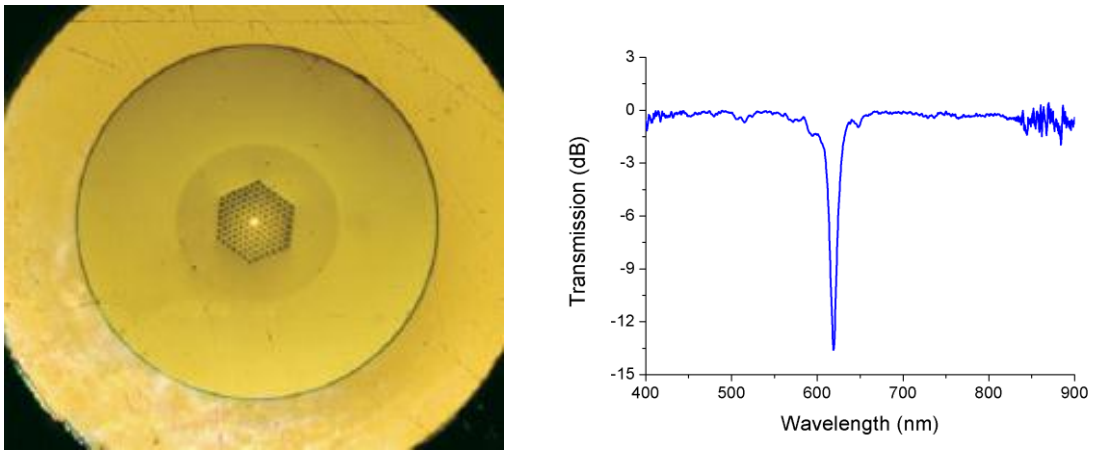

(**a**) (**b**)

Figure 12. (**a**) Cross section of the mPOF used to inscribe an LPG; (**b**) Normalized transmission spectrum of the LPG used in the tests.

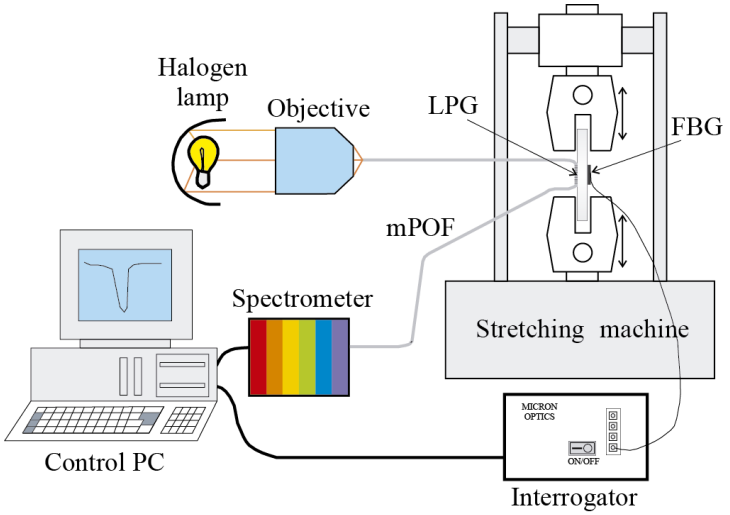

Figure 13. Experimental set-up for the traction-compression tests in a steel plate specimen.

The LPG mPOF with a total grating length of 60 mm was bonded to the surface of a one-meter-length steel plate, whereas on the other surface of the plate an FBG was instrumented as a reference sensor (see Figure 14). The SM130-200 interrogator was employed to capture the response of the FBG. The plate was subjected to a triangular-like tension cycle at a frequency of 0.2 Hz by means of a servo-hydraulic actuator.

As can be observed in Figure 15a, the responses of the sensors are 180 °out of phase because of the opposite variation of the wavelength with respect to the strain for FBGs and LPGs. In the case of the LPG, the fluctuations in the signal are due to the resolution of the spectrometer employed in these tests. To smooth these fluctuations a spectrometer with higher resolution can be used, or low-pass filtering can be applied to the signal. The spectrum corresponding to the LPG signal is represented in Figure 15b; the peak corresponding to the fundamental frequency (0.2 Hz) is clearly identified.

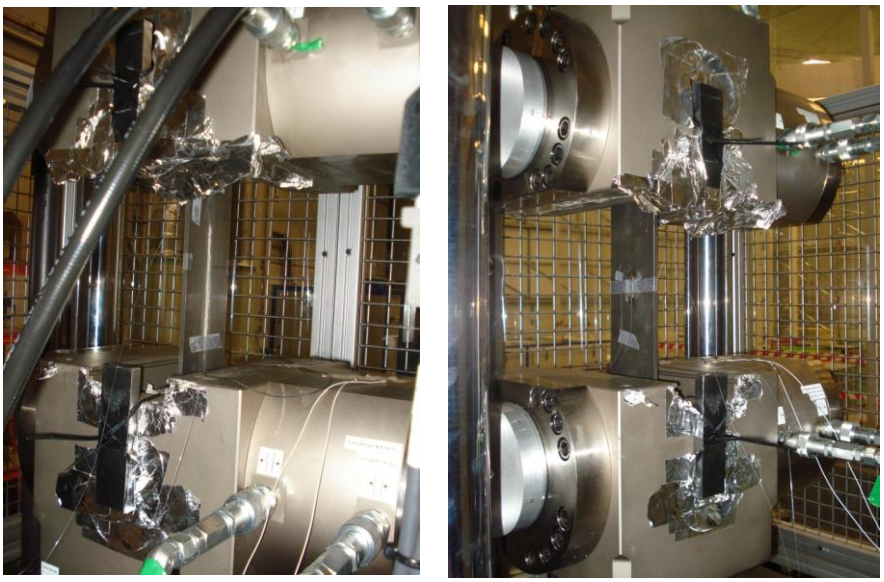

(**a**) (**b**)

Figure 14. (**a**) Plate specimen assembled on the stretching machine with the LPG; (**b**) The FBG instrumented on the other side of the plate.

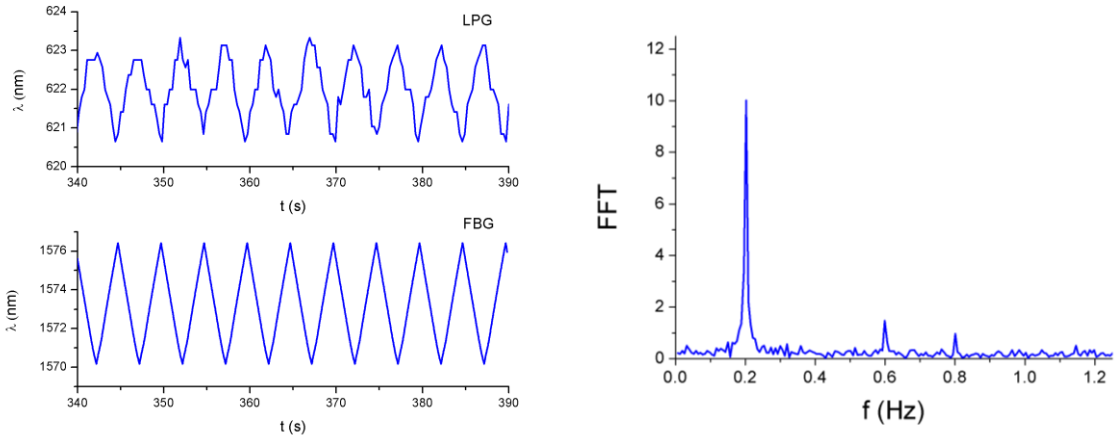

(**a**) (**b**)

Figure 15. (**a**) Responses of the LPG and the FBG to a triangular-like tension cycle at a frequency of 0.2 Hz; (**b**) FFT of the LPG response.

3. SHM in Aircraft Engines

In addition to monitoring the integrity of the aircraft structures it is also essential to ensure the condition of the engines. Optical methods can be employed to monitor different engine parameters such as vibration, temperature, pressure or rotational speed of the engine [61]. They are commonly based on FBGs or interferometric technology but we have developed a reflective intensity-modulated method to assess the performance and SHM of aircraft engines. Several prototypes of this optical sensor are being successfully employed to characterize turbines of aircraft engines in a wind tunnel installation. Other systems based on microwave [62], eddy current [63], or capacitive [64] probes have been developed and in [65] are compared to different optical techniques.

There are three different types of blade vibrations that can be analyzed, namely, radial, tangential and axial (see Figure 16). Currently, the sensor is being used to quantify the radial and tangential vibrations.

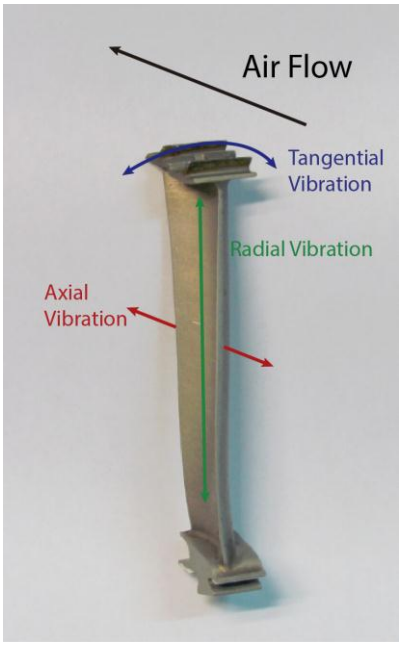

Figure 16. Possible vibrations of the blade during turbine operation: radial (green), axial (red) and tangential (blue). The turbine blade is courtesy of the Aeronautical Technologies Center.

The distance between the tip of the blades of an aircraft engine and its casing is known as tip clearance (TC). The measurement of this distance is equivalent to evaluating the radial vibrations of the blades. This measurement is interesting since it is possible to get a more efficient engine by reducing its TC [66]. Several kinds of sensors, such as capacitive or discharge probe sensors, can be used to carry out these measurements. In Section 3.1 we compile the improvements in the design of an optical sensor for TC measurements of turbine rigs and present another practical application of this optical sensor.

Tip timing is a well-known [67] technique to compute the amplitude of blade vibrations using the differences between the theoretical and the real arrival times of the blades. Since our sensor is placed in a radial position, the tangential vibrations of the turbine blades are also assessed. These vibration amplitudes provide useful information about the turbine operation and the SHM of the blades, since it is possible to detect cracks in the blades or flutter. In Section 3.2 we present a set of tip timing tests for a turbine with 146 blades.

3.1. Tip Clearance Measurements

The main component of the optical sensor is a trifurcated bundle of optical fibers with a common leg on one side and three legs on the other. In Figure 17, the bundle and a cross section view of the common leg are depicted.

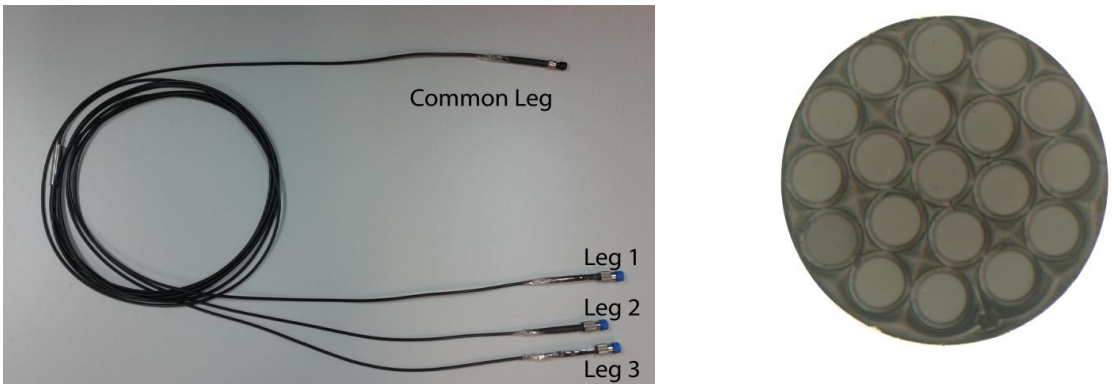

(**a**) (**b**)

Figure 17. (**a**) Trifurcated bundle of optical fibers; (**b**) Microscope view of the cross section of the bundle common leg.

The central fiber guides the light from a laser module connected at leg 1 to the probe end, so that the blades of the turbine are illuminated. This fiber is surrounded by two rings of receiving fibers which collect the reflected light from the blades. The set of receiving fibers corresponding to the first ring (6 fibers) and the second ring (12 fibers) are gathered in bundle legs 2 and 3, respectively. At the end of these legs two photodetectors are connected to convert the optical signals into voltage. The distance from the sensor tip to the blade is calculated from the quotient of these voltages to minimize the effects of fluctuations of the light source or variations in the reflectivity of the surface [68,69]. Detailed information about the configuration of the sensor and the set-up to perform the measurements is provided in [70]. The calibration curve of the sensor is depicted in Figure 18. Previous works carried out the measurements using the front-slope region (region I), whereas our sensor operates in the back-slope region (region II). In this region, there is a trade-off between the sensitivity of the sensor and its linear range, so that the TC can be measured for larger distances but with lower sensitivity.

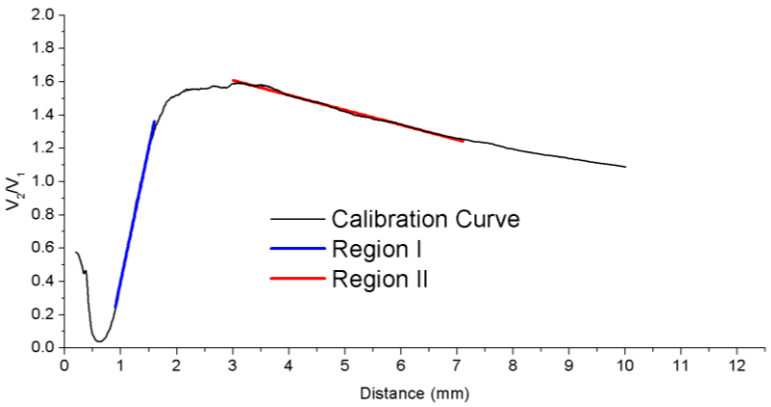

Figure 18. Calibration curve of the sensor showing the two possible regions of measurement: region I (front-slope) in blue and region II (back-slope) in red.

Several configurations have been tested to improve the sensitivity of the sensor. The two main changes have been the reduction of the modal noise at the output of the optical probe and the employment of asymmetric gain for the photodetectors [71]. The evolution of the sensor is summarized in Table 1. Although the third configuration shows the best precision, its maximum operating

temperature is 60 ℃, which restricts the measurements to low temperatures. In contrast, the bundles of glass fibers can work at temperatures up to 350 ℃. Therefore, we decided to use the fourth configuration for future measurements.

The sensor can be used for other purposes beyond the measurement of the TC in the turbines. For instance, three sensors have been used to assess the vibrational behavior of a rotating disk that separates two chambers of different pressures in a real aircraft engine. This disk fluttered under certain circumstances and three sensors were installed to detect these vibrations during some tests carried out in a wind tunnel. The sensors were placed at 120 ° with respect to each other, as shown in Figure 19. The three ends of the probes were placed 4.8 mm away from the rotating disk.

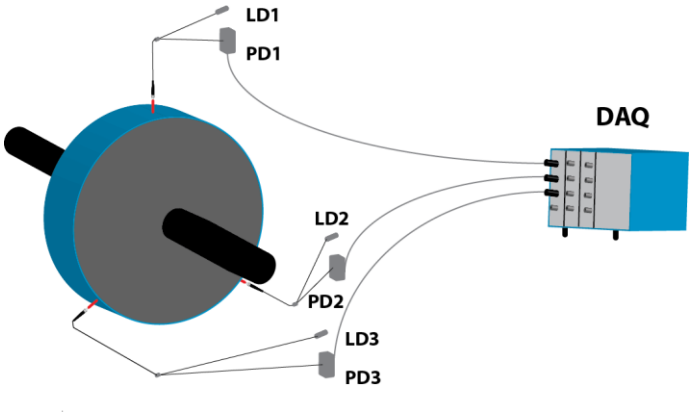

Figure 19. Set-up of the three sensors to evaluate the vibrations in the rotating disk. LDx: Laser diode x; PDx: Photodetector x; DAQ: Data acquisition system.

The disk vibrated even when it was not rotating due to the air flow between the edges of the disk and the casing, so measurements for several rotational speeds from 0 to 3000 revolutions per minute (rpm) and multiple pressure differences at both sides of the disk were carried out. In Figure 20 the signal obtained from one of the sensors and its FFT when the disk is static with a pressure difference of 2.75 bar are shown. The FFT presents a clear peak at 2236 Hz that indicates the frequency of the radial vibration of the disk.

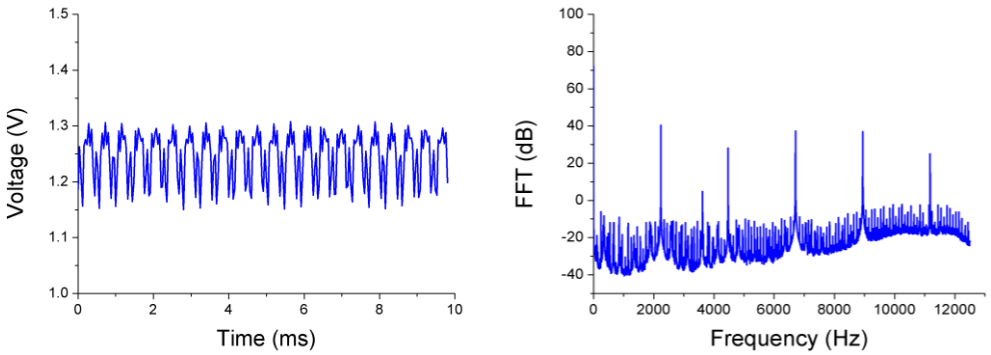

Figure 20. (**a**) Voltage output from one of the sensors when the disk is static and the pressure difference is 2.75 bar; (**b**) FFT of the signal.

Table 1. Characteristics of the different configurations of the TC sensor.

Config.	1st Sensor Configuration	2nd Sensor Configuration	3rd Sensor Configuration	4th Sensor Configuration
Light source (Laser)	7 mW 650 nm	30 mW 650 nm	30 mW 650 nm	20 mW 650 nm
Optical fibers bundle	Multimode $Ø_{core}$ = 100 µm NA = 0.22	Scrambler + Multimode $Ø_{core}$ = 100 µm NA = 0.22	POF $Ø_{core}$ = 240 µm NA = 0.5	Single-mode illuminating fiber $Ø_{core}$ = 4.3 µm NA = 0.12 Multimode receiving fibers $Ø_{core}$ = 100 µm NA = 0.22
Photodetectors gain	Symmetric gain $G_1 = G_2 = 0.75 \times 10^4$ V/A	Asymmetric gain $G_1 = 0.75 \times 10^5$ V/A $G_2 = 2.38 \times 10^5$ V/A	Asymmetric gain $G_1 = 0.75 \times 10^5$ V/A $G_2 = 2.38 \times 10^5$ V/A	Asymmetric gain $G_1 = 0.75 \times 10^5$ V/A $G_2 = 2.38 \times 10^5$ V/A
Calibration curve	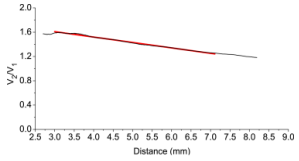 $V_2/V_1 = -0.089d + 1.8783$	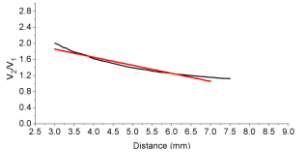 $V_2/V_1 = -0.2002d + 2.4578$	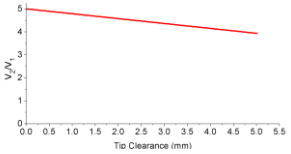 $V_2/V_1 = -0.213d + 5.0064$	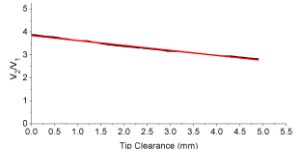 $V_2/V_1 = -0.2167d + 3.8448$
Cross section of the common leg	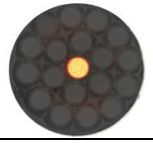		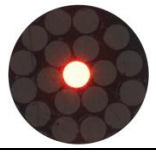	
Laboratory precision	141 µm	51 µm	33 µm	24 µm
Wind tunnel precision	24 µm	-	25 µm	28 µm

Figure 21 shows how the amplitude of the vibration changes when the pressure difference varies. The maximum amplitude of the vibrations is achieved at a pressure difference of 2.7 bar. In Table 2 the amplitude, expressed in dB with respect to one micrometer, and the frequency of the disk vibration for all measured pressure differences are listed. The uncertainty in the frequency measurements is 2 Hz, it could be improved employing a higher number of points to perform the FFT. The obtained frequency values match exactly with those given by one strain gauge instrumented on the surface of the disk.

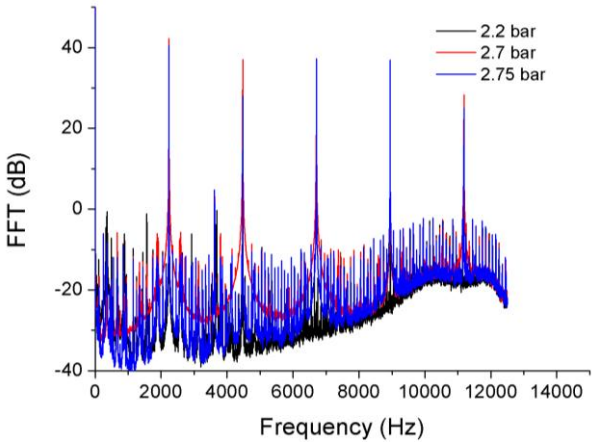

Figure 21. FFTs of the sensor signal obtained at pressure differences of 2.2, 2.7 and 2.75 bar.

Table 2. Amplitude and frequency of the disk vibrations at several pressure differences when the disk is static.

Pressure Difference (bar)	Amplitude (dB)	Frequency (Hz)
2.2	14.3	2238
2.3	19.5	2238
2.4	31.6	2238
2.5	38.5	2238
2.6	32	2236
2.7	42.2	2236
2.75	40.5	2236

3.2. Tip Timing Measurements

As we mentioned before, tip timing is a technique used for the evaluation of the amplitude of tangential vibrations of the blades. Taking into account the difference between the theoretical and the real blade arrival times, the amplitude of the blade deflection is obtained. The entire signal processing to get the deflection of each blade is extensively explained in [70]. The travelling wave spectrum is calculated as the FFT of the deflection values for the blades, and represents the average amplitude of the vibration of the blades at a certain nodal diameter. Figure 22 depicts the deviations of every blade of a 146-blade turbine turning at different rotational speeds. These deviations provide useful information to monitor the turbine blades, since they allow the detection of cracks or flutter when the amplitude of the blade vibration exceeds a predefined alarm value.

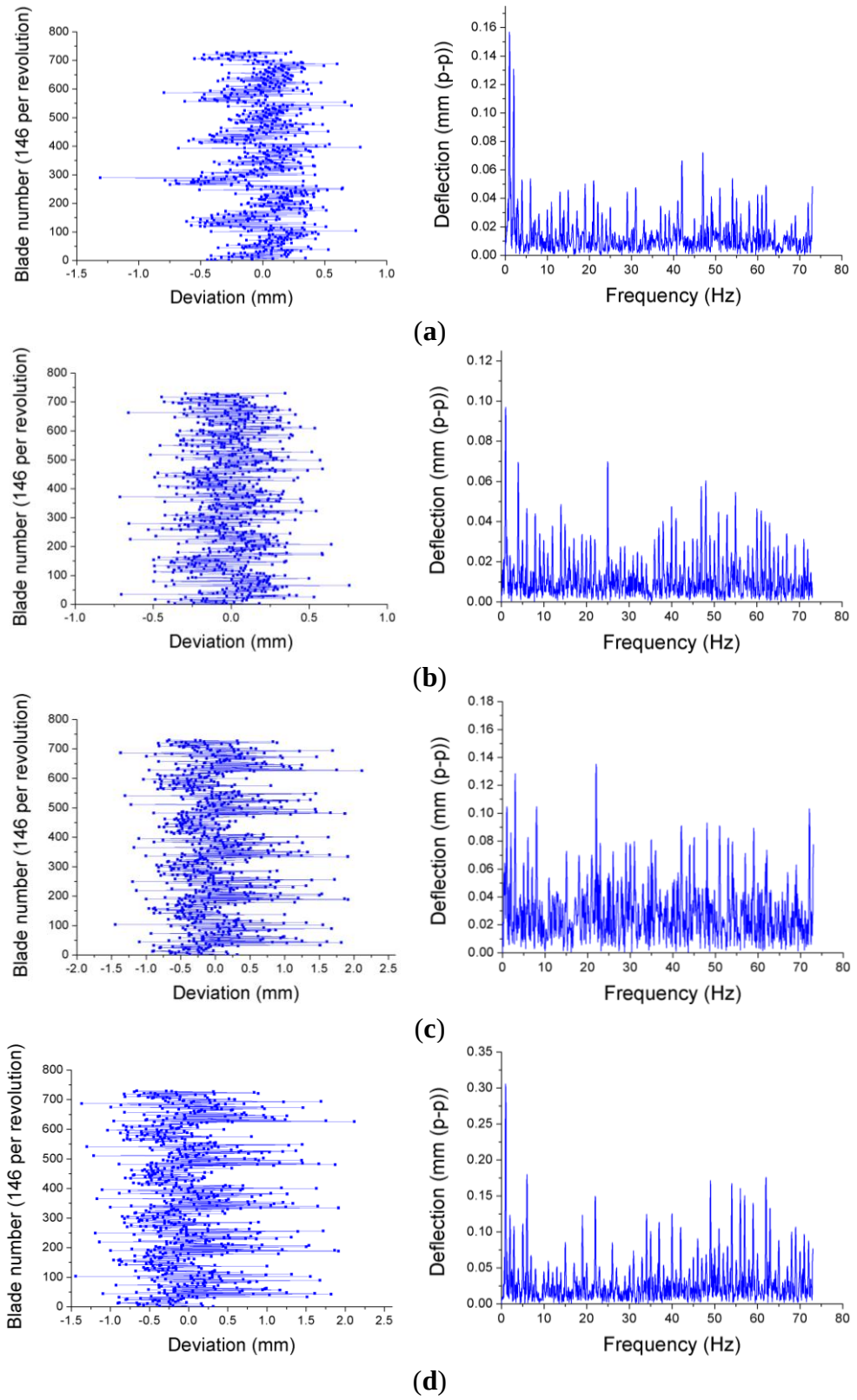

Figure 22. Deviations of each blade form the equilibrium position and travelling wave spectrum of a 146-blade turbine working at 2422 rpm (**a**); 3390 rpm (**b**); 4360 rpm (**c**) and 5570 rpm (**d**).

Although there are some exceptions, the results show a trend towards increasing the amplitude of the blade vibrations as the rotational speed gets higher. The tests were repeated again four days later.

In Figure 23 the results obtained at 3390 and 5570 rpm in this second test campaign are shown. As can be observed, the amplitudes of the vibrations are quite similar for both cases. This fact indicates that the blades of the turbine did not suffer any significant damage between both tests.

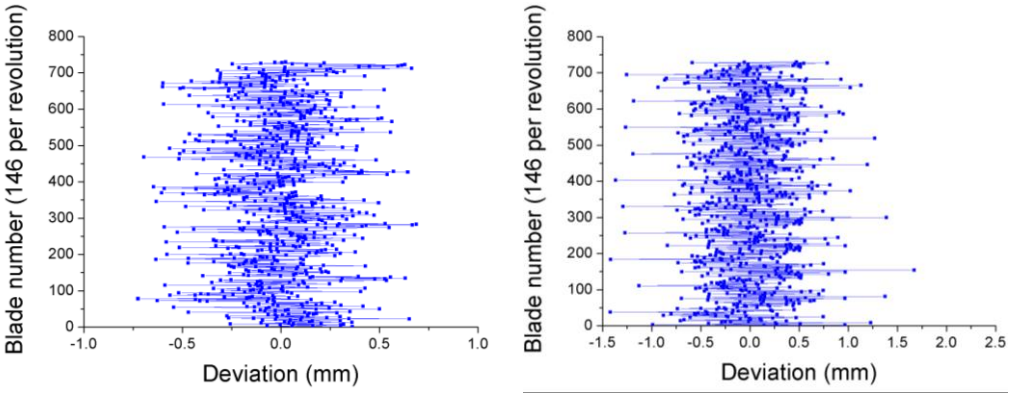

(**a**) (**b**)

Figure 23. Deviation of each blade form the equilibrium position obtained four days later at 3390 rpm (**a**) and 5570 rpm (**b**).

4. Conclusions

Aircraft structures, due to their operating conditions and design principles, require intense inspection and maintenance operations. SHM based on optical sensors could play an important role in these operations provided that two issues can be overcome. The potential economic and life-safety benefits of optical sensors for SHM should be clearly demonstrated to the aviation companies, so that the industry takes decisions towards the extensive use of these devices. The other aspect to be considered is the lack of agreed standards and certification of optical sensors for SHM in aircraft structures, which is an essential condition for the application of optical sensors for SHM on a large scale. FBGs represent the most mature and promising technology for this purpose and, even though they can be employed for other applications, they are mainly used for strain measurements. For this purpose, they present several advantages with respect to strain gauges, like their long-term stability, high multiplexing capability and suitability for being embedded into composite materials. Two other early-stage alternatives for strain measurement in aircraft structures are mentioned in this article. Regarding engines, optical sensors have provided excellent results for the evaluation of aeronautical turbines in ground tests, so the next challenge will be to apply them to aircraft engines in flight.

Acknowledgments

The authors would like to thank Professor A. Güemes for the permission to use the FBG responses shown in Figure 2. This work has been sponsored by the Ministerio de Economía y Competitividad (Spain) and FEDER funds under project TEC2012-37983-C03-01, the Gobierno Vasco/Eusko Jaurlaritza under projects IT664-13, ETORTEK14/13 and by the University of the Basque Country (UPV/EHU) through programs UFI11/16, US13/09 and EUSKAMPUS.

Conflicts of Interest

The authors declare no conflict of interest.

References

1. Boller, C.; Meyendorf, N. State-of-the-art in Structural Health monitoring for aeronautics. In Proceedings of the International Symposium on NDT in Aerospace 2008, Fürth, Germany, 3–5 December 2008.
2. Boller, C. Why SHM? A Motivation; NATO Lecture Series AVT-220. Available online: https://www.researchgate.net/profile/Christian_Boller/publication/268151300_Why_SHM_A_Motivation/links/5463efc80cf2837efdb347cf.pdf (accessed on 30 June 2015).
3. Kapoor, H.; Braun, C.; Boller, C. Modelling and optimisation of maintenance intervals to realise Structural Health Monitoring applications on aircraft. In Proceedings of the 5th European Workshop on Structural Health Monitoring, Sorrento, Italy, 28 June–4 July 2010.
4. Farrar, C.R.; Worden, K. An introduction to structural health monitoring. *Philos. Trans. R. Soc. A Math. Phys. Eng. Sci.* **2007**, *365*, 303–315.
5. Roach, D. Real time crack detection using mountable comparative vacuum monitoring sensors. *Smart Struct. Syst.* **2009**, *5*, 317–328.
6. Zhou, G.; Sim, L.M. Damage detection and assessment in fibre-reinforced composite structures with embedded fibre optic sensors—A review. *Smart Mater. Struct.* **2002**, *11*, 925–939.
7. Güemes, A. SHM Technologies and Applications in Aircraft Structures. In Proceedings of the 5th International Symposium on NDT in Aerospace, Singapore, 13–15 November 2013.
8. Grattan, K.T.V.; Sun, T. Fiber optic sensor technology: An overview. *Sens. Actuators A Phys.* **2000**, *82*, 40–61.
9. Claus, R.O.; Gunther, M.F.; Wang, A.; Murphy, K.A. Extrinsic Fabry-Perot sensor for strain and crack opening displacement measurements from −200 to 900 degrees C. *Smart Mater. Struct.* **1992**, *1*, doi:10.1088/0964-1726/1/3/008.
10. Güemes, A; Fernandez-Lopez, A.; Fernandez, P. Damage Detection in Composite Structures from Fibre Optic Distributed Strain Measurements. In Proceedings of the 7th European Workshop on Structural Health Monitoring, Nantes, France, 8–11 July 2014.
11. Mrad, N.; Xiao, G.Z. Multiplexed fiber Bragg gratings for potential aerospace applications. In Proceedings of the International Conference on MEMS, NANO and Smart Systems, Banff, AL, Canada, 24–27 July 2005.
12. Takeda, N. Fiber optic sensor-based SHM technologies for aerospace applications in Japan. In Proceedings of the 15th International Symposium on: Smart Structures and Materials & Nondestructive Evaluation and Health Monitoring, San Diego, CA, USA, 14–18 March 2008.
13. Nishino, Z.T.; Chen, K.; Gupta, N. Power modulation-based optical sensor for high-sensitivity vibration measurements. *IEEE Sens. J.* **2014**, *14*, 2153–2158.
14. Read, I.; Foote, P.; Murray, S. Optical fibre acoustic emission sensor for damage detection in carbon fibre composite structures. *Meas. Sci. Technol.* **2002**, *13*, doi:10.1088/0957-0233/13/1/402.

15. Yari, T.; Nagai, K.; Hotate, K. Monitoring aircraft structural health using optical fiber sensors. *Mitsubishi Heavy Ind. Tech. Rev.* **2008**, *45*, 5–8.
16. Majumder, M.; Gangopadhyay, T.K.; Chakraborty, A.K.; Dasgupta, K.; Bhattacharya, D.K. Fibre Bragg gratings in structural health monitoring—Present status and applications. *Sens. Actuators A Phys.* **2008**, *147*, 150–164.
17. Guo, H.; Xiao, G.; Mrad, N.; Yao, J. Fiber Optic Sensors for Structural Health Monitoring of Air Platforms. *Sensors* **2011**, *11*, 3687–3705.
18. Mrad, N.; Guo, H.; Xiao, G.; Rocha, B.; Sun, Z. On the use of a compact optical fiber sensor system in aircraft structural health monitoring. In Proceedings of the Photonic Applications for Aerospace, Transportation, and Harsh Environment III, Baltimore, MD, USA, 1 May 2012.
19. Gholamzadeh, B.; Nabovati, H. Fiber optic sensors. *World Acad. Sci. Eng. Technol.* **2008**, *42*, 335–340.
20. Kahandawa, G.C.; Epaarachchi, J.; Wang, H.; Lau, K.T. Use of FBG sensors for SHM in aerospace structures. *Photon. Sens.* **2012**, *2*, 203–214.
21. Hill, K.O.; Meltz, G. Fiber Bragg grating technology fundamentals and overview. *J. Lightw. Technol.* **1997**, *15*, 1263–1276.
22. Frövel, M.; Pintado, J.M.; Güemes, A.; del Olmo, E.; Obst, A. Multiplexable fiber Bragg grating temperature sensors embedded in CFRP structures for cryogenic applications. In Proceedings of the 3rd European Workshop on Structural Health Monitoring, Granada, Spain, 5–7 July 2006.
23. Davis, C.; Tejedor, S.; Grabovac, I.; Kopczyk, J.; Nuyens, T. High-strain fiber bragg gratings for structural fatigue testing of military aircraft. *Photon. Sens.* **2012**, *2*, 215–224.
24. Ecke, W.; Latka, I.; Willsch, R.; Reutlinger, A.; Graue, R. Fibre optic sensor network for spacecraft health monitoring. *Meas. Sci. Technol.* **2001**, *12*, doi:10.1088/0957-0233/12/7/339.
25. Wood, K.; Brown, T.; Rogowski, R.; Jensen, B. Fiber optic sensors for health monitoring of morphing airframes: II. Chemical sensing using optical fibers with Bragg gratings. *Smart Mater. Struct.* **2000**, *9*, 170–174.
26. López-Higuera, J.M. *Handbook of Optical Fibre Sensing Technology*; Wiley and Sons: Chichester, West Sussex, UK, 2002.
27. Lemaire, P.J.; Atkins, R.M.; Mizrahi, V.; Reed, W.A. High pressure H_2 loading as a technique for achieving ultrahigh UV photosensitivity and thermal sensitivity in GeO_2 doped optical fibres. *Electron. Lett.* **1993**, *29*, 1191–1193.
28. Martinez, A.; Khrushchev, I.Y.; Bennion, I. Direct inscription of Bragg gratings in coated fibers by an infrared femtosecond laser. *Opt. Lett.* **2006**, *31*, 1603–1605.
29. Meltz, G.; Morey, W.; Glenn, W.H. Formation of Bragg gratings in optical fibers by a transverse holographic method. *Opt. Lett.* **1989**, *14*, 823–825.
30. Hill, K.O.; Malo, B.; Bilodeau, F.; Johnson, D.C.; Albert, J. Bragg gratings fabricated in monomode photosensitive optical fiber by UV exposure through a phase mask. *Appl. Phys. Lett.* **1993**, *62*, 1035–1037.
31. Malo, B.; Hill, K.O.; Bilodeau, F.; Johnson, D.C.; Albert, J. Point-by-point fabrication of micro-Bragg gratings in photosensitive fibre using single excimer pulse refractive index modification techniques. *Electron. Lett.* **1993**, *29*, 1668–1669.

32. Xu, M.G.; Archmbault, J.L.; Reekie, L.; Dakin, J.P. Thermally-compensated bending gauge using surface-mounted fibre gratings. *Int. J. Optoelectron.* **1994**, *9*, 281–283.
33. Haran, F.M.; Rew, J.K.; Foote, P.D. A strain isolated fibre Bragg grating sensor for temperature compensation of fibre Bragg grating strain sensors. *Meas. Sci. Technol.* **1998**, *9*, 1163–1166.
34. Song, M.; Lee, S.B.; Choi, S.S.; Lee, B. Simultaneous measurement of temperature and strain using two fibre Bragg gratings embedded in a glass tube. *Opt. Fibre Technol.* **1997**, *3*, 194–196.
35. Patrick, H.J.; Williams, G.M.; Kersey, A.D.; Pedrazini, J.R. Hybrid fibre Bragg grating/long period fibre grating sensor for strain/temperature discrimination. *Photon. Technol. Lett.* **1996**, *8*, 1223–1225.
36. Xu, M.G.; Archmbault, J.L.; Reekie, L.; Dakin, J.P. Discrimination between strain and temperature effects using dual-wavelength fibre grating sensors. *Electron. Lett.* **1994**, *30*, 1085–1087.
37. James, S.W.; Dockney, M.L.; Tatam, R.P. Simultaneous independent temperature and strain measurement using in-fibre Bragg grating sensors. *Electron. Lett.* **1996**, *32*, 1133–1134.
38. Song, M.; Lee, B.; Lee, S.B.; Choi, S.S. Interferometric temperature-insensitive strain measurement with different diameter fibre Bragg gratings. *Opt. Lett.* **1997**, *22*, 790–792.
39. Jung, J.; Nam, H.; Lee, J.H.; Park, N.; Lee, B. Simultaneous measurement of strain and temperature by use of a single Bragg grating and an erbium-doped fibre amplifier. *Appl. Opt.* **1999**, *38*, 2749–2751.
40. Jung, J.; Park, N.; Lee, B. Simultaneous measurement of strain and temperature by use of a single fiber Bragg grating written in an erbium:ytterbium-doped fiber. *Appl. Opt.* **2000**, *39*, 1118–1120.
41. Dunphy, J.R.; Meltz, G.; Varasi, M.; Vannucci, A.; Signorazzi, M.; Ferraro, P.; Voto, C. Embedded Optical Sensor Capable of Strain and Temperature Measurement using A Single Diffraction Grating. U.S. Patent No. 5, 399,854, 21 March 1995.
42. Ferreira, L.A.; Farahi, F.; Arau, F.M. Simultaneous measurement of strain and temperature using interferometrically interrogated fiber Bragg grating sensors. *Opt. Eng.* **2000**, *39*, 2226–2234.
43. Lo, Y.L.; Kuo, C.P. Packaging a fiber Bragg grating with metal coating for an athermal design. *J. Lightw. Technol.* **2003**, *21*, 1377–1383.
44. Tian, K.; Liu, Y.; Wang, Q. Temperature-independent fiber Bragg grating strain sensor using bimetal cantilever. *Opt. Fiber Technol.* **2005**, *11*, 370–377.
45. Viegas, D.; Pinto, N.M.P.; Romero, R.; Fraz ão, O.; Costa, A. Birefringence effect in uniform fibre bragg gratings. Available online: https://www.researchgate.net/profile/Diana_Viegas/publication/228903206_Birefringence_effect_in_uniform_fibre_Bragg_gratings/links/0fcfd50a529adefaea000000.pdf (accessed on 30 June 2015).
46. Güemes, A. Fiber Optics Strain Sensors; NATO Lecture Series AVT-220. Available online: http://ftp.rta.nato.int/public/PubFullText/RTO/EN/STO-EN-AVT-220/EN-AVT-220-03.pdf (accessed on 30 June 2015).
47. Montero, A.; Saez de Ocariz, I.; Lopez, I.; Venegas, P.; Gomez, J.; Zubia, J. Fiber Bragg Gratings, IT Techniques and Strain Gauge Validation for Strain Calculation on Aged Metal Specimens. *Sensors* **2011**, *11*, 1088–1104.
48. Frieden, J.; Cugnoni, J.; Botsis, J.; Gmür, T. Low energy impact damage monitoring of composites using dynamic strain signals from FBG sensors–Part I: Impact detection and localization. *Compos. Struct.* **2012**, *94*, 438–445.

49. Gomez, J.; Jorge, I.; Durana, G.; Arrue, J.; Zubia, J.; Aranguren, G.; Montero, A.; López, I. Proof of Concept of Impact Detection in Composites Using Fiber Bragg Grating Arrays. *Sensors* **2013**, *13*, 11998–12011.
50. Vella, T.; Chadderdon, S.; Selfridge, R.; Schultz, S.; Webb, S.; Park, C.; Peters, K.; Zikry, M. Full-spectrum interrogation of fiber Bragg gratings at 100 kHz for detection of impact loading. *Meas. Sci. Technol.* **2010**, *21*, doi:10.1088/0957-0233/21/9/094009.
51. Luber, M.; Poisel, H.; Loquai, S.; Neuner, C.; Bachmann, A.; Ziemann, O.; Hartl, E. POF strain sensor using phase measurement techniques. In Proceedings of the 16th International Plastic Optical Fibres Conference, Torino, Italy, 10–12 September 2007.
52. Kalymnios, D.; Scully, P.; Zubia, J.; Poisel, H. POF sensors overview. In Proceedings of the 13th International Plastic Optical Fibres Conference, Nürnberg, Germany, 27–30 September 2004.
53. Neuner, C. Faseroptischer Längensensor Basierend auf Laufzeitmessung, Master's Thesis, Georg Simon Ohm University of Applied Science Nuremberg, Nuremberg, Germany, 2007.
54. Durana, G.; Kirchhof, M.; Luber, M.; de Ocáriz, I.S.; Poisel, H.; Zubia, J.; Vázquez, C. Use of a novel fiber optical strain sensor for monitoring the vertical deflection of an aircraft flap. *Sens. J.* **2009**, *9*, 1219–1225.
55. Gomez, J.; Zubia, J.; Aranguren, G.; Arrue, J.; Poisel, H.; Saez, I. Comparing polymer optical fiber, fiber Bragg grating, and traditional strain gauge for aircraft structural health monitoring. *Appl. Opt.* **2009**, *48*, 1436–1443.
56. Van Eijkelenborg, M.; Large, M.C.J.; Argyros, A.; Zagari, J.; Manos, S.; Issa, N.A.; Bassett, I.; Fleming, S.; McPhedran, R.C.; Sterke, M.; *et al.* Microstructured polymer optical fibre. *Opt. Express* **2001**, *9*, 319–327.
57. Van Eijkelenborg, M.; Padden, W.; Besley J.A. Mechanically induced long-period gratings in microstructured polymer fibre. *Opt. Commun.* **2004**, *236*, 75–78.
58. Hiscocks, M.P.; Van Eijkelenborg, M.; Argyros, A.; Large, M.C.J. Stable imprinting of long-period gratings in microstructured polymer optical fibre. *Opt. Express* **2006**, *14*, 4644–4649.
59. James, S.W.; Tatam, R.P. Optical fibre long-period grating sensors: Characteristics and application. *Meas. Sci. Technol.* **2003**, *14*, 49–61.
60. Durana, G.; Gomez, J.; Aldabaldetreku, G.; Zubia, J.; Montero, A.; de Ocdriz, I.S. Assessment of an LPG mPOF for strain sensing. *IEEE Sens. J.* **2012**, *12*, 2668–2673.
61. Wild, G. Optical fiber Bragg grating sensors applied to gas turbine engine instrumentation and monitoring. In Proceedings of the Sensors Applications Symposium, Galveston, TX, USA, 19–21 February 2013.
62. Violetti, M.; Skrivervik, A.K.; Xu, Q.; Hafner, M. New microwave sensing system for blade tip clearance measurement in gas turbines. In Proceedings of the IEEE Sensors, Taipei, Taiwan, 28–31 October 2012; pp. 1–4.
63. Dowell, M.; Sylvester, G. Turbomachinery prognostics and health management via eddy current sensing: Current developments. In Proceedings of the Aerospace Conference, Aspen, CO, USA, 6–13 March 1999.
64. Sheard, A.G. Blade by blade tip clearance measurement. *Int. J. Rotat. Mach.* **2011**, *2011*, doi:10.1155/2011/516128.

65. Russhard, P. The use of blade tip timing technologies to assess and monitor rotor blade health from design to production. In Proceedings of the Test Cell and Controls Instrumentation and EHM Technologies for Military Air, Land and Sea Turbine Engines, Rzeszow, Poland, 20–23 April 2015.
66. Wiseman, M.W.; Guo, T.H. An Investigation of Life Extending Control Techniques for Gas Turbine Engines. In Proceedings of the American Control Conference, Arlington, VA, USA, 25–27 July 2001.
67. Heath, S.; Imregun, M. A survey of blade tip-timing measurement techniques for turbomachinery vibration. *J. Eng. Gas Turbines Power* **1998**, *120*, 784–791.
68. Cao, S.Z.; Duan, F.J.; Zhang, Y.G. Measurement of rotating blade tip clearance with fibre-optic probe. *J. Phys. Conf. Ser.* **2006**, *48*, 873–877.
69. Ma, Y.; Li, G.; Zhang, Y.; Liu, H. Tip Clearance Optical Measurement for Rotating Blades. In Proceedings of the International Conference on Management Science and Industrial Engineering (MSIE), Harbin, China, 6–11 January 2011.
70. Garcá, I.; Beloki, J.; Zubia, J.; Aldabaldetreku, G.; Illarramendi, M.A.; Jiménez, F. An Optical Fiber Bundle Sensor for Tip Clearance and Tip Timing Measurements in a Turbine Rig. *Sensors* **2013**, *13*, 7385–7398.
71. Garcá, I.; Zubia, J.; Berganza, A.; Beloki, J.; Arrue, J.; Illarramendi, M.A.; Mateo, J.; Vazquez, C. Different configurations of a reflective intensity-modulated optical sensor to avoid modal noise in tip-clearance measurements. *J. Lightw. Technol.* **2015**, *12*, 2663–2669.

Artículo 2

An optical fiber bundle sensor for tip clearance and tip timing measurements in a turbine rig

García, I., Beloki, J., Zubia, J., Aldabaldetreku, G., Illarramendi, M. A., & Jiménez, F.

Sensors, *13*(6), 7385-7398 (2013).

Sensors **2013**, *13*, 7385-7398; doi:10.3390/s130607385

OPEN ACCESS

sensors

ISSN 1424-8220

www.mdpi.com/journal/sensors

Article

An Optical Fiber Bundle Sensor for Tip Clearance and Tip Timing Measurements in a Turbine Rig

Iker García [1,*], Josu Beloki [2], Joseba Zubia [1], Gotzon Aldabaldetreku [1], María Asunción Illarramendi [3] and Felipe Jiménez [4]

[1] Department of Communications Engineering, University of the Basque Country, Alda. Urquijo s/n Bilbao 48013, Spain; E-Mails: joseba.zubia@ehu.es (J.Z.); gotzon.aldabaldetreku@ehu.es (G.A.)

[2] CTA, Centro de Tecnologías Aeronáuticas, Parque tecnológico de Bizkaia, Edif. 303, Zamudio 48170, Spain; E-Mail: josu.beloki@ctabef.com

[3] Department of Applied Physics I, University of the Basque Country, Alda. Urquijo s/n Bilbao 48013, Spain; E-Mail: ma.illarramendi@ehu.es

[4] Department of Applied Mathematics, University of the Basque Country, Alda. Urquijo s/n Bilbao 48013, Spain; E-Mail: felipe.jimenez@ehu.es

***** Author to whom correspondence should be addressed; E-Mail: iker.garciae@ehu.es; Tel.: +34-946-017-305; Fax: +34-946-014-259.

Received: 9 April 2013; in revised form: 16 May 2013 / Accepted: 29 May 2013 / Published: 5 June 2013

Abstract: When it comes to measuring blade-tip clearance or blade-tip timing in turbines, reflective intensity-modulated optical fiber sensors overcome several traditional limitations of capacitive, inductive or discharging probe sensors. This paper presents the signals and results corresponding to the third stage of a multistage turbine rig, obtained from a transonic wind-tunnel test. The probe is based on a trifurcated bundle of optical fibers that is mounted on the turbine casing. To eliminate the influence of light source intensity variations and blade surface reflectivity, the sensing principle is based on the quotient of the voltages obtained from the two receiving bundle legs. A discrepancy lower than 3% with respect to a commercial sensor was observed in tip clearance measurements. Regarding tip timing measurements, the travel wave spectrum was obtained, which provides the average vibration amplitude for all blades at a particular nodal diameter. With this approach, both blade-tip timing and tip clearance measurements can be carried out simultaneously. The results obtained on the test turbine rig demonstrate the suitability and reliability of the type of sensor used, and suggest the possibility of performing these measurements in real turbines under real working conditions.

Keywords: optical fiber bundle; real operating conditions measurement; tip clearance; tip timing; turbine

1. Introduction

Blade-tip timing (BTT) and tip clearance (TC) are two critical parameters for turbine engineering, since their measurement and optimization lead to more effective, secure and reliable engines [1]. BTT is a technique for blade vibration measurements that uses the differences between real and theoretical blade arrival times to calculate the vibration amplitude of the blade. Pioneering works in the BTT technique were performed in the 70 s and during the last forty years ample research has been developed and published related to this technique. Some examples of these works, chronologically ordered, can be found in References [2–11]. Blade vibration measurements are crucial to assess turbine operation and predict blade failures due to fatigue [12]. Blade vibrations can occur due to different causes. For instance, combustors or stators can produce synchronous responses in the rotor blades, or even irregularities in the casing or in the intake geometry can produce non-regular pressure distributions that lead to synchronous responses in the rotor blades. In contrast, rotating stall or adverse flow-blade interaction with negative aero-damping can cause non-synchronous responses, such as flutter, which consists of a self-sustained aerodynamic instability. In order to predict the lifetime of blades and to prevent damages that can lead to huge repairing costs or even to engine destruction, a low-cost and effective blade vibration system is needed. The BTT technique fulfils both requirements detecting all blade vibrations.

Blade vibrations are usually measured with strain gauges. These devices can be used provided that the influence of their mass is negligible. Results are provided only for the blades on which gauges are mounted and the signals from the gauges have to be transmitted by telemetry or a slip ring. Despite their proven suitability, strain gauges require considerable instrumentation, their use is restricted to a few blades of the turbine and they are in physical contact with the blades. A second standard method is the frequency modulated grid system [13]. This method is based on small permanent magnets attached to the tips of some blades that induce an electromagnetic voltage in a wire installed in the casing. Its disadvantages are similar to those of the strain gauges [14].

As to the TC, it is defined as the distance between the blade-tip and the engine casing, and its usual values are 2–3 mm. This distance is one of the factors on which engine efficiency depends, as the latter increases as TC decreases. A high TC allows an amount of air to flow without generating a useful work, whereas a lack of clearance can put engine integrity at risk. A 0.25-mm-TC reduction is equivalent to a reduction of 1% in specific fuel consumption, and of 10 °C in exhaust gas temperature [15]. As a consequence, the engine works at lower temperatures and the life cycle of its components is increased. In addition to the economical benefit, aircraft noise and emissions are also reduced, implying additional environmental advantages.

For the measurement of TC, traditional methods make use of capacitive, eddy current and discharging probe sensors. Capacitive sensors are simple and inexpensive but they have a poor frequency response and require iron blades. Eddy current sensors provide non-contact measurements,

but the magnetic disturbance of the turbine engine can interfere with their output. In addition, they need to be calibrated in advance, because they are highly dependent on the tip shape and temperature [16]. Finally, discharging probes, in the same way as eddy current sensors, require conducting blades and they only measure the shortest clearance. On the contrary, optical fiber sensors provide small size and simplicity, non-contact measurements and simple instrumentation, high sensitivity, resolution and bandwidth, insensitivity to electromagnetic interference and measurement of every blade [17]. In this paper we will show the results obtained for the BTT and TC measurement using an optical fiber bundle sensor.

2. Experimental Section

All tests and measurements took place in the Aeronautical Technologies Center (CTA) facilities and were performed in a turbine rig with a rotor of 146 blades. The main component of the sensor is a trifurcated optical fiber bundle (manufactured *ad-hoc* by Fiberguide Industries, Stirling, NJ, USA, according to our requirements). The bundle structure is depicted in Figure 1: its length is 3 m and it consists of multimode glass optical fibers. Optical fibers temperature operating range goes from −190 to 350 °C, whereas the maximum temperature reached during the measurements is 88.1 °C.

Figure 1. Trifurcated optical fiber bundle and legs cross-section.

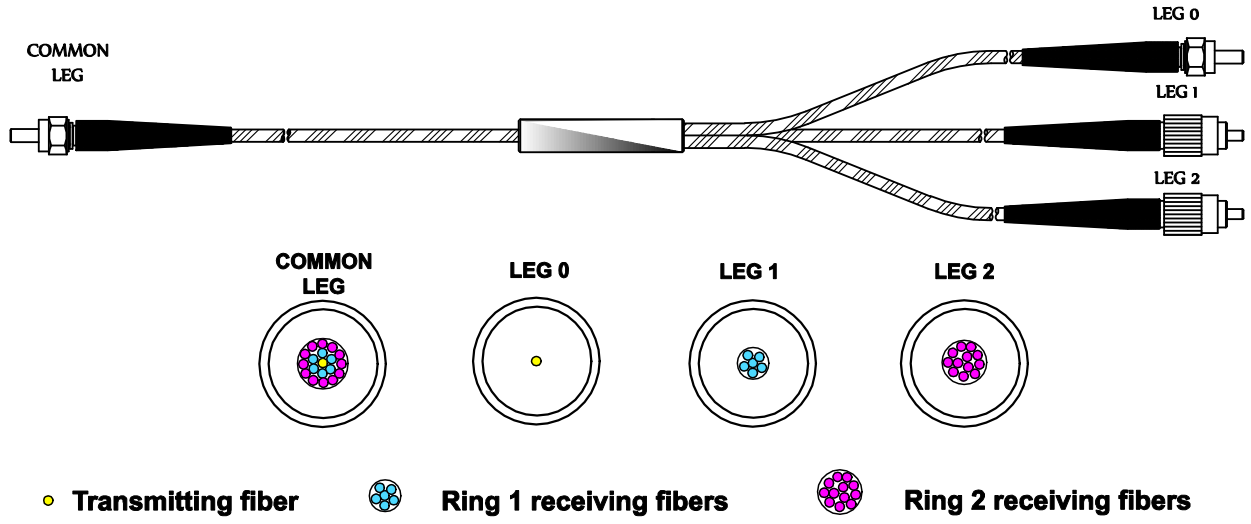

Figure 2. Microscope image of the cross-section of the common leg.

Figure 2 shows a microscope image of the cross-section of the common leg. The central fiber is the transmitting fiber which guides the light from the laser to the probe end in order to illuminate the blade. The reflected light is collected by two receiving fiber rings around the transmitting fiber. The inner ring is formed by six fibers that are gathered in leg 1 and the outer ring is composed of twelve fibers gathered in leg 2.

A trifurcated bundle is chosen to eliminate the effects of variations in the light source, reflectivity of the blade surface, and optical losses and misalignments between the probe and the target surface [16,18]. This is possible because the distance to the target is obtained as a function of the quotient of two photodetector voltages (V_1 and V_2), so the influence of any previous disturbance is cancelled. To evaluate the reflected light irradiance collected by each ring of receiving fibers, let us call I_0 the light irradiance leaving the transmitting fiber in the common leg of the bundle. Then the optical irradiance at the end of legs 1 and 2 can be expressed as:

$$I_1 = K_0 R I_0 K_1 F_1(d) \tag{1}$$

$$I_2 = K_0 R I_0 K_2 F_2(d) \tag{2}$$

where R represents the reflectivity of the blade, the coefficients K_1 and K_2 account for the losses in the corresponding receiving fibers, each function $F_1(d)$ and $F_2(d)$ represents the relationship between the collected irradiance and the target distance for each group of fibers considered as a bifurcated bundle [19–24], and K_0 is a factor that accounts for laser fluctuations.

Dividing both equations we obtain:

$$I_2 / I_1 = K_2 F_2(d) / K_1 F_1(d) = K F(d) \tag{3}$$

Therefore, the quotient of the irradiances only depends on a constant related to the losses in the optical fibers and it is a function of the distance to the illuminated blade.

We employ a 655-nm-wavelength laser (FP-65 7FE-SMA, Laser Components, Olching, Germany) as the light source with a typical power of 7 mW. The laser is coupled to leg 0. Two identical photodetectors (PDA100A-EC, Thorlabs, Dachau, Germany) are connected to the end of legs 1 and 2, which convert the reflected light collected by each ring into a voltage signal. The photodetectors consist of a reverse-biased PIN photodiode and a switchable gain transimpedance amplifier. The adjustable gain range goes from 0 to 70 dB, and the bandwidth decreases from 1.5 MHz to 2 kHz as the gain increases. The maximum output signal amplitude for a 50 Ω load is 5 V through a BNC connector. To acquire the output signal an Agilent Technologies (Santa Clara, CA, USA) Infinium MSO9104A oscilloscope was used. It has four analog channels of 1 GHz and a maximum sample rate of 20 Gsa/s. All these components are depicted in Figure 3(a) with the exception of the oscilloscope, which was placed at the control room due to the high temperatures reached. In order to carry the signal from the photodetectors to the oscilloscope and reduce the noise of the engine, two 25 m long double-shielded coaxial cables were used.

The first problem we encountered during the assembly was how to couple the common leg SMA connector to the casing of the turbine. It was solved using a threaded tip in order to fix the SMA connector to a coupler which was inserted in a probe hole, shown in Figure 3(b), that placed the bundle tip at a distance of 0.45 mm from the inner face of the casing.

Figure 3. (**a**) Experimental setup for the tip clearance and tip timing measurements in the turbine rig at the CTA facilities. (**b**) Coupler to fix the bundle tip to the turbine casing.

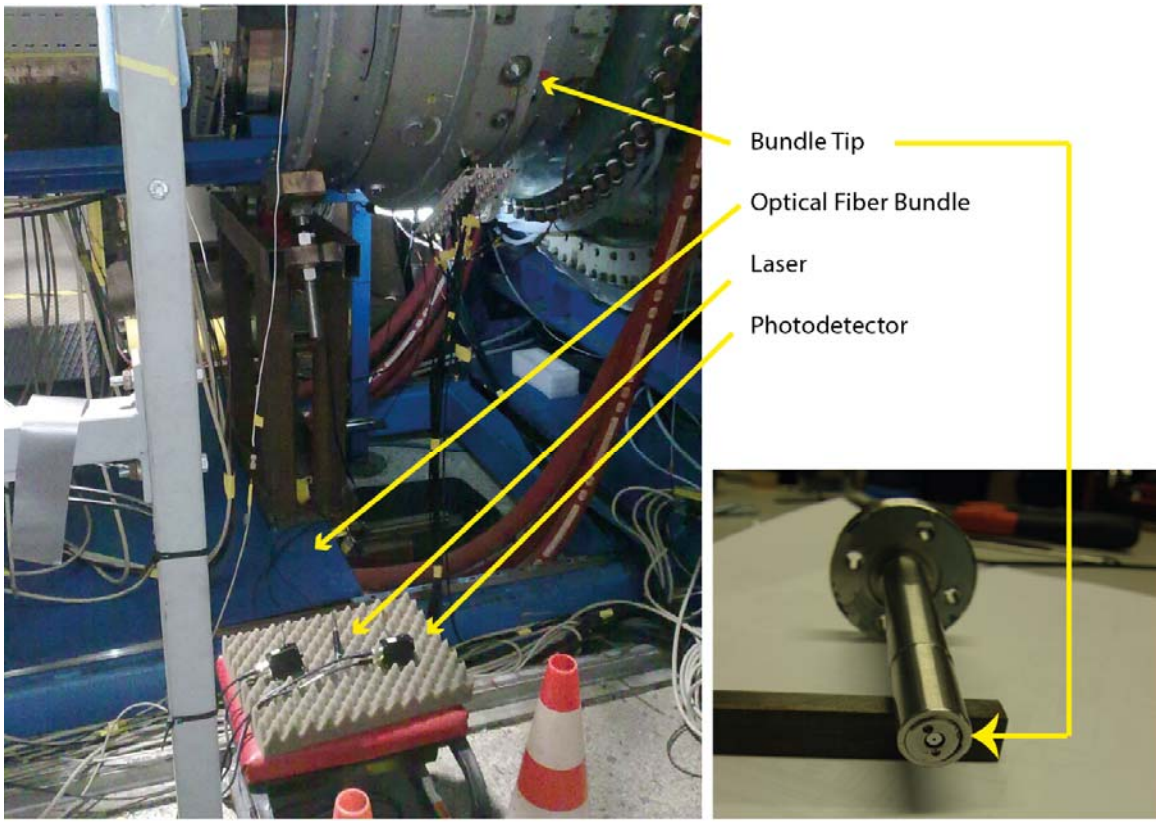

(**a**) (**b**)

In Figure 4 the blade shape can be observed. We decided to illuminate the flat platform of the blade, so that the whole laser spot illuminates a flat surface and, therefore, most of the reflected light returns to the bundle. Since the difference between the flat platform and the nearest part of the blade to the casing is 1.3 mm, 1.75 mm should be subtracted from the measured distance to obtain the real TC.

Figure 4. Blade profile image.

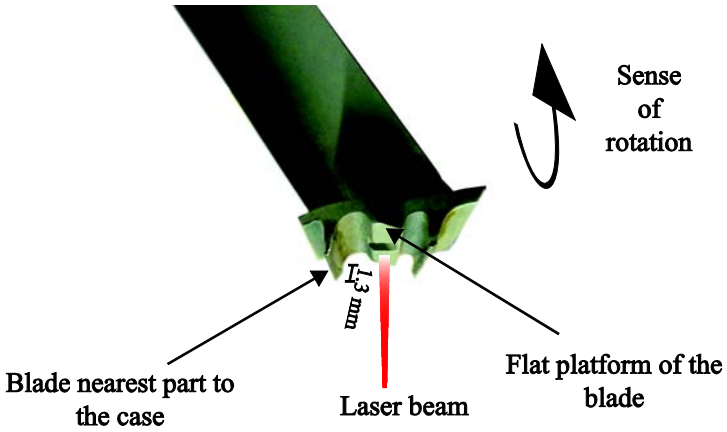

The experimental set-up is depicted in Figure 5. In addition to the sensor components, the inset shows the operational principle of the sensor. The light from the illuminating fiber is reflected by the blade and collected by the two rings of receiving fibers. Afterwards, the photodetectors connecting to

each receiving leg of the optical fiber bundle carry out the photoelectric conversion. Finally, the oscilloscope acquires and saves the signals from both photodetectors. Additionally, the inset clarifies the tip timing and TC parameters.

Figure 5. Experimental set-up and operational principle. Legend: DO: Digital Oscilloscope; PD1: Photodetector 1; PD2: Photodetector 2; OFB: Optical Fiber Bundle; LD: Laser Diode; TC: Tip Clearance; BTT: Blade Tip Timing; RB: Rotor Blade; L0: Leg 0; L1: Leg 1; L2: Leg 2; CL: Common Leg.

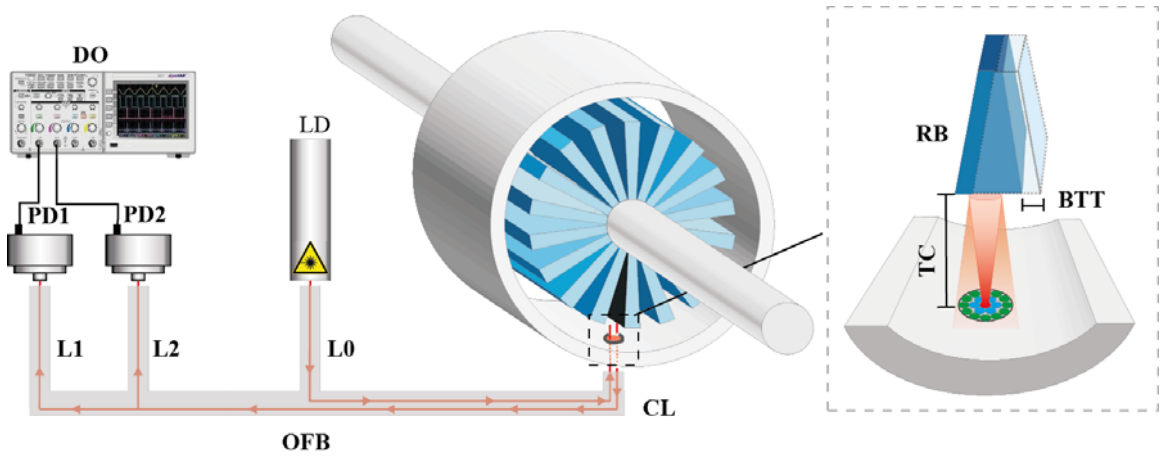

During the calibration we used the same components except for the oscilloscope, which was replaced by two digital multimeters (notice that during the calibration process a high acquisition rate is not necessary and that multimeters are much easier to automate). The bundle tip was fixed to a self-made SMA adapter. The blade was installed on a linear stage and it was longitudinally moved away from the common leg of the bundle in 10-μm steps. Using this procedure we obtained the calibration curve of the sensor. This calibration was carried out both in darkness and in the presence of light, and the differences between them were found negligible. The calibration curve is shown in Figure 6.

Figure 6. Calibration curve of the optical fiber sensor: quotient of photodetector voltages (V_2/V_1) as a function of the blade distance (d). The red line represents the fit to the calibration curve of a straight line in the range 3–7 mm. The shaded area corresponds to usual values of the TC (without correction).

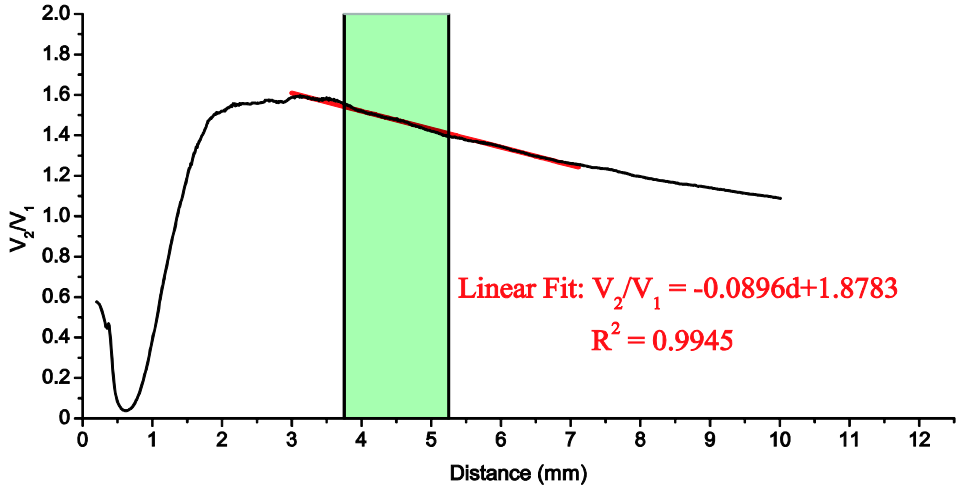

Taking into account that typical TC values for our turbine range between 2 and 3.5 mm, and that we have to add the 1.75 mm offset distance, the measurement range should be between 3.75 mm and 5.25 mm (represented by the shaded area). A straight line has been fitted to the calibration curve, as shown in Figure 6, by the least-square method for the 3–7 mm interval, with a coefficient of determination $R^2 = 0.9945$.

3. Results and Discussion

An important restriction of our acquisition system is that the oscilloscope has only 8 bits for vertical resolution. Therefore, we performed an oversampled acquisition to obtain a better-detailed waveform. For the case of TC measurements the sampling frequency was 250 Msa/s, and the oscilloscope memory depth allowed a maximum acquisition time of 82 ms from both photodetectors. In BTT measurements the accuracy in the amplitude of the signals is not as critical as in the former case, so the sampling frequency was set to 250 Ksa/s, obtaining 82 s of acquisition time. Both measurements were performed for 84 different working conditions (working points) of the engine. To identify each revolution, a blade with a particular reflection pattern has been used. The data from the sensor are post-processed after a low-pass filtering (cut-off frequency 50 KHz). Once the sensing principle is validated, a real time implementation will be possible. In Figure 7(a), we can observe the post-filtering signal from photodetector 2 for a specific working point where the turbine rotates at 2,400 rpm.

Figure 7. (**a**) Raw signal of photodetector 2. (**b**) Second derivative of the raw signal. (**c**) Detected blade events.

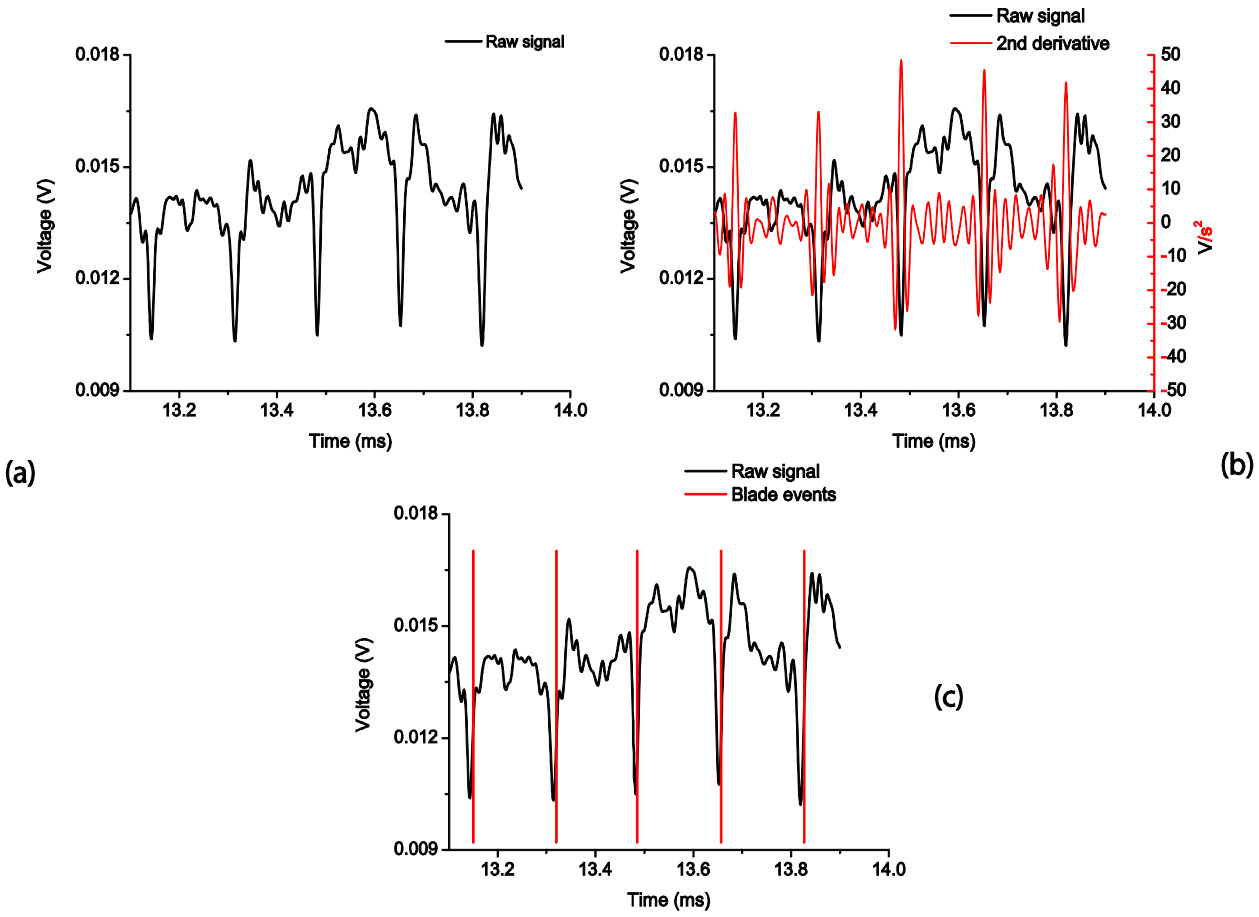

3.1. Tip Timing Measurements

The BTT technique is based on the measurement of the arrival times of all the blades. If the blades do not vibrate, the theoretical arrival times are obtained from a simple relationship involving the number of blades, the rotation frequency and the blade radius. However, if the blades do vibrate, their arrival times precede or succeed the theoretical non-vibrating arrival times. The difference between the theoretical and the real arrival time is related to blade deflections and it is used in the post-processing section of the system [25].

Furthermore, by placing probes at different circumferential positions, a sine wave model can be fitted to the blade deflections measured at each position. From these sinusoidal fits, we will be able to obtain the frequencies and amplitudes of the vibrations.

In our tests, a single probe was used to measure the blade arrival times. With this single probe application it is not possible to carry out an appropriate model fitting and a complete modal analysis cannot be achieved. Nevertheless, it is still possible to perform a travelling wave analysis in order to obtain the average amplitude of the blade tips at a particular nodal diameter (*ND*) (note that the minimum value of *ND* is 0, which is obtained when all the blades vibrate with the same phase, whereas *ND* reaches its maximum value (half of the number of blades) when each blade is out of phase with its neighbour). This travelling wave analysis can be used for monitoring the integrity of the blades against flutter, crack propagation or foreign object damage (*FOD*).

The travelling wave mode is the vibration condition of the blades. In a bladed disk system, the blades vibrate at the same amplitude but with a phase lag between them. This is known as the inter blade phase angle (*Ibpa*). This phase lag between the blades is related to the nodal diameter (*ND*) of the bladed disk mode according to:

$$ND = \frac{2\pi n}{Ibpa} \tag{4}$$

where n is the number of blades.

As a consequence the frequency detected by the probe (f_{probe}) is the frequency of the blade (f_{blade}) plus the nodal diameter multiplied by the rotation frequency (ω), *i.e.*, [26]:

$$f_{probe} = f_{blade} + \omega ND \tag{5}$$

Let us define the engine order (*EO*) as:

$$EO = \frac{f_{blade}}{\omega} \tag{6}$$

Dividing Equation (5) by the rotation frequency and substituting Equation (6):

$$f_{probe} / \omega = f_{blade} / \omega + ND = EO + ND \tag{7}$$

Therefore, a probe placed in the casing that measures the frequency of a rotating part detects not only the frequency of the blade, but also the phase lag that a blade has with its neighbour, so that it is not possible to discriminate *EO* from *ND,* because the probe detects the arrival time of each blade as a superposition of both terms.

The travelling wave analysis is mainly used for non-synchronous responses, such as flutter, where $EO + ND$ has non-zero values. For synchronous responses it turns out that $EO + ND = 0$, since the

excitation and the response are in phase and, therefore, synchronous responses are more difficult to detect with the travelling wave analysis.

Finally, the working point of the turbine is defined by two parameters: the rotational velocity *N* and the work per unit mass flow *Ws*. The specific work is defined as [27]:

$$Ws = C_p * \Delta T_0 \tag{8}$$

where C_p is the air specific heat capacity at a constant pressure and ΔT_0 is the total temperature drop within the stage.

Figure 7(a) shows the raw signal obtained with the optical probe for a test performed at nominal working conditions (2,400 rpm). Notice that we can estimate the arrival time of each blade by calculating the second derivative of the signal. This derivative gives the change in concavity/convexity of the raw signal as can be seen in Figure 7(b). Choosing a threshold value for the second derivative of the raw signal, the blade arrival event can be obtained for every blade. In Figure 7(c), the raw signal together with the blade arrival events can be observed.

From the arrival times we can obtain the deflection or deviation of each blade from its theoretical equilibrium position. The deviations from the theoretical equilibrium position in one revolution for every blade are shown in Figure 8. This deviation provides us with useful information for health monitoring to predict possible damages in blades. By plotting the deviations in real time, flutter or crack propagations can be detected as the deviation of a certain blade increases in time and gets close to predefined pre-alarm values.

Figure 8. Deviation of each blade from the equilibrium position in a complete revolution.

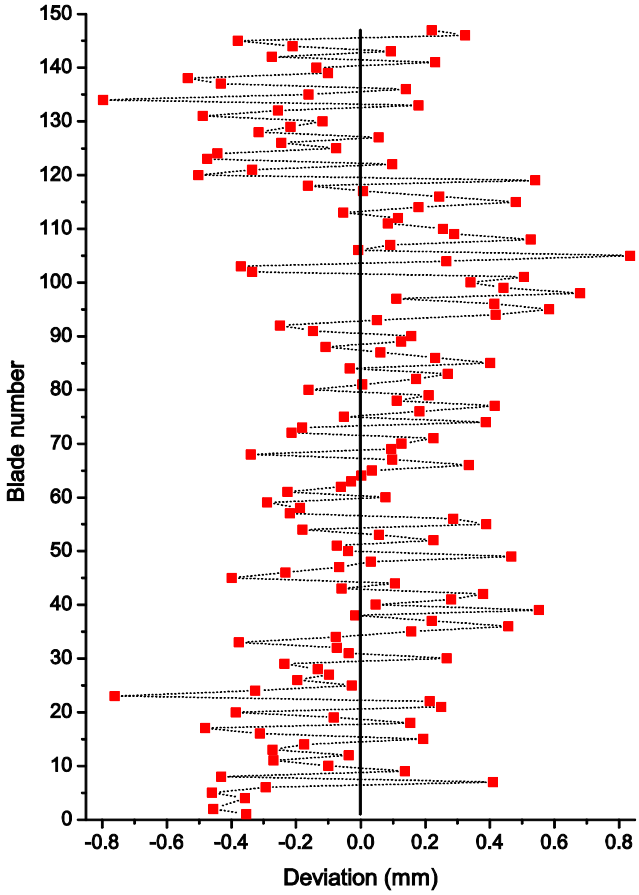

With the deflection values of the blades a fast Fourier transform can be performed to obtain the travelling wave spectrum of the system, which gives the average tip amplitude of all the blades, as shown in Figure 9. The travelling wave spectrum gives an average value of all the blade vibration amplitudes at a certain nodal diameter and it can also be used to monitor the system in real time, in order to check that the average blade tip amplitude does not exceed a predefined maximum value.

Figure 9. Travelling wave frequency spectrum of the system.

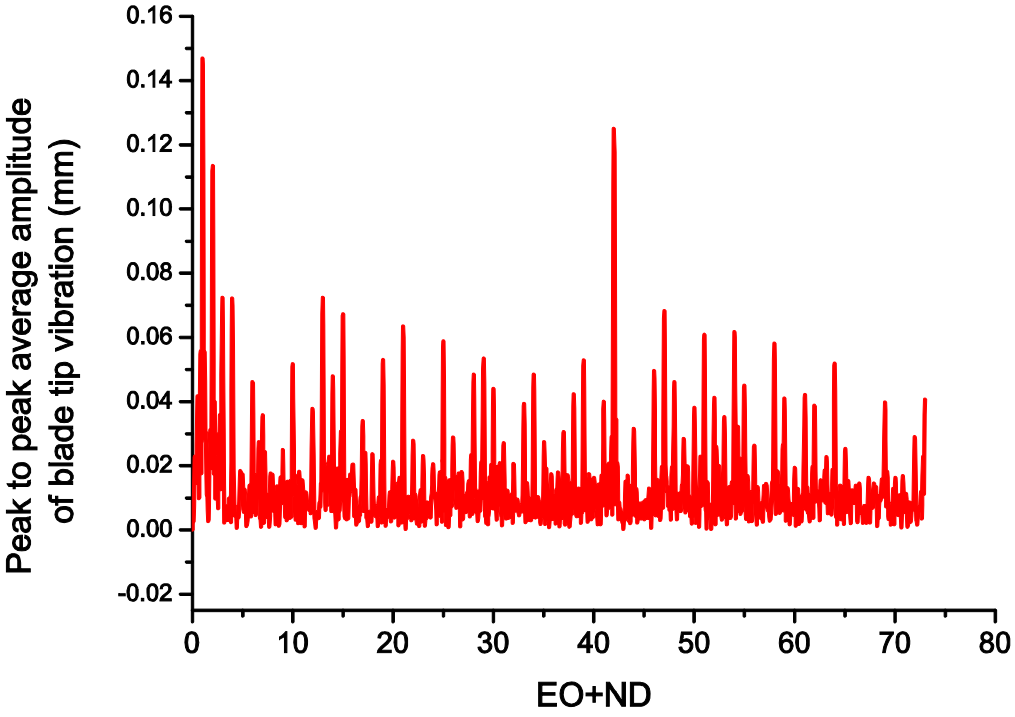

Figure 9 depicts the peak to peak average amplitude of blade tip vibration. There is a dominant peak of 0.15 mm at $EO + ND = 1$. This is probably a solid rigid rotation ($EO = 1$, $ND = 0$) due to some unbalancing of the rotor or the facility instead of a blade vibration mode.

There is another important peak at $EO + ND = 42$ of 0.13 mm that could be due to a low amplitude non-synchronous response, such as a flutter. When a blade starts moving, the surrounding flow exerts an aerodynamic force on it, and the direction and phase of this force can dampen or speed up the motion of the blade, leading to flutter. The *Ibpa* determines the phase between the local unsteady flow and local blade motion and this phase affects the unsteady aerodynamic work done on the blades. Unfavorable phase angles can lead to positive work being performed on the blades, which results in flutter.

All in all, the vibration amplitudes are always below 0.2 mm in the frequency spectrum of Figure 9 which is indicative of the stability of the rotor. More tests were performed for different rotation frequencies, leading to similar conclusions.

In order to discriminate the frequency of the blade and the nodal diameter, more probes should be placed in the casing in other circumferential positions. In the future, more probes are planned to be mounted in order to perform more detailed modal analysis of the rotors.

3.2. Tip Clearance Measurements

As we have already mentioned, TC represents the gap between the blade tip and the engine casing. This distance is obtained as a function of the quotient of two photodetector voltages, and the calibration curve of Figure 6 is used to relate both quantities. Figure 10 shows the two filtered photodetector signals and its quotient during the acquisition of a working point at 3,148 rpm. In this figure, 15 blades can be observed. If we pay attention to the minimum values that limit each blade, we can notice that each minimum has a different level (dashed line in Figure 10). This offset is probably due to the vibrations of the rotor-shaft assembly, so the first step in the signal processing, after the low pass filtering, is to remove this offset so that the signals start at the same level for all blades. Afterwards V_2 and V_1 are divided and its maximum value is found for a complete revolution. By definition, the TC is the distance corresponding to the maximum value of the quotient.

Figure 10. Filtered signals from the photodetectors and their quotient at a working point of 3,148 rpm.

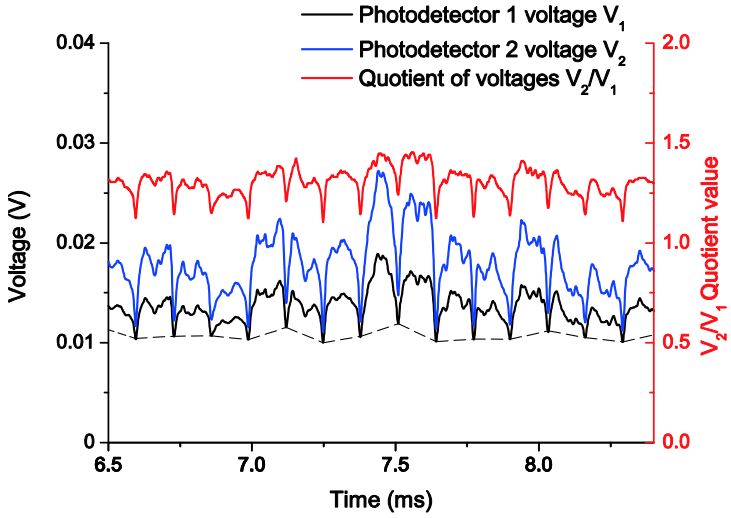

As we have already mentioned, 84 different working points were acquired during turbine assessment. Since the TC value depends mainly on the number of rpm, for a first evaluation of the sensor operation, all working points with the same rpm were averaged to obtain a TC for each turning speed. The optical sensor response was compared with a discharging probe sensor (Rotatip RCSM4 from Rotadata, Derby, UK) used by CTA. After appropriate data processing, the results for both sensors are shown in Table 1.

Whereas the optical sensor can obtain the distance to the casing for each blade at any instant, the discharging probe sensor gets only the smallest clearance of all the blades in an unknown revolution. The measurement instant is, therefore, not the same for both sensors, and even though measurements are taken in a steady state, they are measuring different distances (different vibration modes of the blades in different revolutions). It must be also taken into account that the standard deviation in the data from the sensor before speckle correction was about 150 μm. However, since our aim is to compare the behaviour of both sensors, we believe it is useful to show the obtained results. The latest statement is demonstrated by the fact that the differences between the two sensors are on the order of some tens of microns and the relative difference is less than 3%, as it can be observed in Table 1.

Table 1. Tip clearance measurements obtained during turbine tests.

Working Point (rpm)	Discharging Probe Tip Clearance (mm)	Optical Sensor Tip Clearance (mm)	Difference (%)
3148.52	2.890	2.954	2.22
3390.71	2.919	2.961	1.42
3632.91	2.893	2.843	1.72
3875.10	2.851	2.840	0.38

4. Conclusions

An optical sensor based on a trifurcated optical fiber bundle has been used to carry out BTT and TC measurements using a reflected intensity-modulation technique. Despite the limitation of using a unique probe for BTT measurements, the travelling wave spectrum has been obtained and with it the average vibration amplitude for all blades. With respect to TC measurements, a good approximation to a commercial sensor has been achieved, with differences lower than 3% for average TC values at each turning speed.

The great potential of optical fiber bundles for this kind of measurements has been demonstrated. The main novelties of this work with respect the previous ones are the possibility to simultaneously carry out both BTT and TC measurements with the same probe, and the reporting of these results as obtained from a real test of a turbine rig. In addition, the measurement system is a non-contact one, which allows to obtain information from all the blades with very short instrumentation times and relatively low cost. In future tests, several probes will be installed in the casing to make the most of the BTT measurements.

Acknowledgments

This work has been sponsored by the institutions Ministerio de Economía y Competitividad under projects TEC2009-14718-C03-01, TEC2012-37983-C03-01, Gobierno Vasco/Eusko Jaurlaritza under projects AIRHEM-II, S-PE12CA001, IT664-13 and by the University of the Basque Country (UPV/EHU) through program UFI11/16.

Conflict of Interest

The authors declare no conflict of interest.

References

1. Ye, D.C.; Duan, F.J.; Guo, H.T.; Li, Y.; Wang, K. Turbine blade tip clearance measurement using a skewed dual-beam fiber optic sensor. *Opt. Eng.* **2012**, doi:10.1117/1.OE.51.8.081514.
2. Zablotskii, I.E.; Korostelev, Y.A.; Sviblov, L.B. *Contactless Measuring of Vibrations in the Rotor Blades of Turbines*; Defense Technical Information Center: Fort Belvoir, VA, USA, 1974.
3. Nieberding, W.C.; Pollack, J.L. Optical Detection of Blade Flutter. In Proceedings of the Gas Turbine Conference and Products Show, Philadelphia, PA, USA, 27–31 March 1977.

4. Roth, H. Vibration Measurements on Turbomachine Rotor Blades with Optical Probes. In *Measurement Methods in Rotating Components of Turbomachinery*, Proceedings of the Joint Fluids Engineering Gas Turbine Conference and Products Show, New Orleans, LA, USA, 10–13 March 1980; pp. 215–224.
5. McCarthy, P.E.; Thompson, J.W., Jr. Development of a Noninterference Technique for Measurement of Turbine Engine Compressor Blade Stress; Arnold Engineering Development Center, US Air Force: Arnold AFB, TN, USA, 1980.
6. Watkins, W.B.; Robinson, W.W.; Chi, R.M. Noncontact engine blade vibration measurements and analysis. In Proceedings of the AIAA/SAE/ASME/ASEE 21st Joint Propulsion Conference, Monterey, CA, USA, 8–10 July 1985.
7. Watkins, W.B.; Chi, R.M. Noninterference blade-vibration measurement system for gas turbine engines. *J. Propul. Power* **1989**, *5*, 727–730.
8. Kawashima, T.; Iinuma, H.; Wakatsuki, T.; Minagawa, N. Turbine Blade Vibration Monitoring System. In Proceedings of the 37th International Gas Turbine and Aeroengine Congress and Exposition, Cologne, Germany, 1–4 June 1992; p. 6.
9. Bloemers, D.; Heinen, M.; Krämer, E.; Wüthrich, C. Optische Überwachung von Turbinenschaufelschwingungen in Bettrieb. *VGB Kraftwerkstechnik*, **1993**, *73*, 29–33 (in German).
10. Krämer, E.; Plan, E. Optical vibration measuring system for long, free-standing LP rotor blades. *ABB Rev.* **1997**, *5*, 4–9.
11. Heath, S.; Imregun, M. A survey of blade tip-timing measurement techniques for turbomachinery vibration. *J. Eng. Gas Turbines Power* **1998**, *120*, 784–791.
12. Georgiev, V.; Holík, M.; Kraus, V.; Krutina, A.; Kubín, Z.; Liška, J.; Poupa, M. The Blade Flutter Measurement Based on the Blade Tip Timing Method. In Proceedings of the 15th WSEAS International Conference on Systems, Corfu Island, Greece, 14–16 July 2011; pp. 270–275.
13. Zielinski, M.; Ziller, G. Optical Blade Vibration Measurement at MTU. In Proceedings of the AGARD conference, Brussels, Belgium, 20–24 October 1998.
14. Zielinski, M.; Ziller, G. Noncontact vibration measurements on compressor rotor blades. *Meas. Sci. Technol.* **2000**, *11*, 847–859.
15. Wiseman, M.W.; Guo, T.-H. An Investigation of Life Extending Control Techniques for Gas Turbine Engines. In Proceedings of the American Control Conference, Arlington, VA, USA, 25–27 June 2001; pp. 3706–3707.
16. Cao, S.Z.; Duan, F.J.; Zhang, Y.G. Measurement of rotating blade tip clearance with fibre-optic probe. *J. Phys. Confer. Ser.* **2006**, *48*, 873–877.
17. López-Higuera, J.M. *Handbook of Optical Fibre Sensing Technology*; Wiley: New York, NY, USA, 2002.
18. Ma, Y.; Li, G.; Zhang, Y.; Liu, H. Tip Clearance Optical Measurement for Rotating Blades. In Proceedings of the International Conference on Management Science and Industrial Engineering (MSIE), Harbin, China, 8–11 January 2011; pp. 1206–1208.
19. Dhadwal, H.S.; Kurkov, A.P. Dual-laser probe measurement of blade-tip clearance. *J. Turbomach.* **1999**, *121*, 481–485.
20. Jia, B.; Zhang, X. An optical fiber blade tip clearance sensor for active clearance control applications. *Procedia Eng*. **2011**, *15*, 984–988.

21. Tong, Q.; Ma, H.; Liu, L.; Zhang, X.; Li, G. Measurements of radiation vibrations of turbomachine blades using an optical-fiber displacement-sensing system. *J. Russ. Laser Res.* **2011**, *32*, 216–229.
22. Faria, J.B. A theoretical analysis of the bifurcated fiber bundle displacement sensor. *IEEE Trans. Instrum. Meas.* **1998**, *47*, 742–747.
23. Cao, H.; Chen, Y.; Zhou, Z.; Zhang, G. Theoretical and experimental study on the optical fiber bundle displacement sensors. *Sens. Actuators A Phys*. **2007**, *136*, 580–587.
24. Cook, R.O.; Hamm, C.W. Fiber optic lever displacement transducer. *Appl. Opt.* **1979**, *18*, 3230–3241.
25. Non-Intrusive Stress Measurement Systems. Available online: http://agilis.com/documents/NSMS.pdf (accessed on 11 March 2013).
26. Washburn, R.; Kim N.-E.; Brouckaert, J.-F. Hardware transmitted excitation sources and the associated blade responses using tip timing instrumentation. In *VKI Lecture Series*; von Karman Institute: Rhode-Saint-Genése, Belgium, 2007.
27. Cohen, H.; Rodgers, G.F.C.; Saravanamuttoo, H.I.H. *Gas Turbine Theory*, 4th ed.; Pearson Education Limited: Essex, UK, 1996; p. 273.

Artículo 3

Different configurations of a reflective intensity-modulated optical sensor to avoid modal noise in tip-clearance measurements

García, I., Zubia, J., Berganza, A., Beloki, J., Arrue, J., Illarramendi, M. A., Mateo, J., & Vázquez, C.

Journal of Lightwave Technology, *33*(12), 2663-2669 (2015).

Different Configurations of a Reflective Intensity-Modulated Optical Sensor to Avoid Modal Noise in Tip-Clearance Measurements

Iker García, Joseba Zubia, Amaia Berganza, Josu Beloki, Jon Arrue, María Asunción Illarramendi, Javier Mateo, and Carmen Vázquez, *Senior Member, IEEE*

***Abstract*—Tip clearance is critical to the performance of rotating turbomachinery. The objective of this paper is to develop a non-contact sensor with a precision of 30 μm to measure tip clearance in a turbine rig assembled in a wind tunnel. To carry out the measurements, an optical sensor whose main component is a bundle of optical fibers is employed. We use four different configurations of this sensor, which are tested in two distinct turbines with the aim of minimizing the effect of the noise on the repeatability of the measurements. Each configuration serves to increase the precision until the required performance is achieved for the measurement of the tip clearance. Our results may be helpful to develop applications related to structural health monitoring or active clearance-control systems.**

***Index Terms*—Active clearance-control system, bundle of optical fibers, optical sensor, structural health monitoring, tip clearance, turbine.**

I. Introduction

THE gap existing between the blade tip and the casing of a turbine allows an air flow to pass through the turbine without generating any useful work [1]. This distance is known as tip clearance (TC) and it changes as a function of the revolutions of the turbine, becoming smaller as the rotational speed increases. TC also varies during the engine start-up and shutdown, so it is important to maintain a security interval. TC must be as short as possible to optimize the fuel consumption of the engine [2], minimizing leakage flow through this gap. Consequently, there is a growing interest in techniques that provide an accurate measurement of the TC. There are various kinds of non-optical sensors that could be used to measure TC, such as capacitive ones, eddy-current sensors and discharging probes. However, optical sensors can provide higher sensitivity, bandwidth and resolution, smaller size, non-contact measurements, easy acquisition of data for every blade of the turbine and, of course, immunity to electromagnetic interference. During the last few years, in collaboration with the *Aeronautical Technologies Center*, we have performed several TC measurements in turbine rigs using optical fiber sensors [3], [4]. The performance of all these sensors was evaluated firstly in our laboratory, taking measurements of a single blade, and later in a wind tunnel, taking measurements of the same blade in a turbine rig.

During the development of the first prototype of our reflective intensity-modulated optical sensor, the main problem that initially arose was the limited spatial precision of the measurement, which was due to the modal noise at the end of the bundle [5]. This noise appears when a light source of narrow bandwidth is used in combination with a multimode fiber [6]. The coherent light excites various modes that are guided in the fiber. Since the length of the fiber of the sensor is very short (3 meters), the equilibrium mode distribution (EMD) is not accomplished and the different propagation modes are not mixed [7]. As a consequence, the interference of these multiple propagating modes produces a random intensity distribution at the endface of the fiber, which is similar to a speckle noise pattern [8]. This pattern depends on the laser wavelength and bandwidth, on the fiber type (refractive index profile) and on its length.

The total intensity at the output of the fiber would be independent of the distribution given by the random interference pattern if the whole pattern were measured at the detector [9]. However, in practice, the elements of the sensor only gather a part of the total spot of light, so random changes in the collected interference pattern generate modal noise. These changes can be due to different causes, such as vibrations or a mechanical disturbance of the fiber or frequency instability of the source [10]. As a consequence, the intensity collected by the sensor fluctuates in spite of keeping the same distance to the target. This fact leads to repeatability problems in the measurement. The second source of noise is the speckle noise produced in the light reflected by the target surface and it also must be taken into account.

Manuscript received August 25, 2014; revised December 11, 2014; accepted January 23, 2015. Date of publication January 27, 2015; date of current version April 29, 2015. This work has been sponsored by the Ministerio de Economía y Competitividad (Spain) and FEDER funds under project TEC2012–37983-C03–01, the Gobierno Vasco/Eusko Jaurlaritza under projects IT664-13, ETORTEK14/13 and by the University of the Basque Country (UPV/EHU) through programs UFI11/16, US13/09 and EUSKAMPUS.

I. García, J. Zubia, and J. Arrue are with the Department of Communications Engineering, E.T.S.I. of Bilbao, University of the Basque Country (UPV/EHU), Bilbao 48013, Spain (e-mail: iker.garciae@ehu.es; joseba.zubia@ehu.es; jon.arrue@ehu.es).

A. Berganza is with the Department of Applied Mathematics, E.U.I.T.I. of Bilbao, University of the Basque Country (UPV/EHU), Bilbao 48013, Spain (e-mail: amaia.berganza@ehu.es).

J. Beloki is with the CTA, Aeronautical Technologies Center, Bizkaia Technological Park, Zamudio 48170 Spain and also with the Department of Nuclear Engineering and Fluid Mechanics, E.T.S.I. of Bilbao, University of the Basque Country (UPV/EHU), Bilbao 48013, Spain (e-mail: josu.beloki@ctabef.com).

M. A. Illarramendi is with the Department of Applied Physics I, E.T.S.I. of Bilbao, University of the Basque Country (UPV/EHU), Bilbao 48013, Spain (e-mail: ma.illarramendi@ehu.es).

J. Mateo is with the Department of Electronic Engineering, Aragon Institute of Engineering Research, University of Zaragoza, Zaragoza E-50018, Spain (e-mail: jmateo@unizar.es).

C. Vázquez is with the Electronics Technology Department, Carlos III University of Madrid, Leganés 28911, Spain (e-mail: cvazquez@ing.uc3m.es).

Color versions of one or more of the figures in this paper are available online at http://ieeexplore.ieee.org.

Digital Object Identifier 10.1109/JLT.2015.2397473

The objective of this work is to design and develop an optical sensor for TC measurements with a precision of at least 30 μm. This is the worst acceptable resolution required by the *Aeronautical Technologies Center* for their tip-clearance measurements. In order to achieve this goal, the effect of both kinds of noises must be reduced.

The first step to reduce noise was the attainment of a uniform intensity distribution at the output of the fiber to avoid random intensity patterns. For this purpose, three alternatives were tried. The first one was the employment of scramblers to mix and filter the modes [11], thereby shortening the necessary fiber length for EMD. The second one was the use of plastic optical fibers (POFs) whose coupling length is shorter than that of glass fibers [12], [13]. The last alternative was to use a single-mode glass fiber to illuminate the blades of the turbine [14]. Unlike previous works using a single-mode illuminating fiber [15], which use a mirror as target, in this paper we employ a turbine blade instead of the mirror, which gives an idea of the robustness of the sensor. We study the performance of a trifurcated bundle of optical fibers working in the back-slope region (region II, of negative slope). This region allows us to extend the linear range of our sensor to 4–5 mm, instead of the maximum of 1 mm achieved in previous works working in the front-slope region (region I, of positive slope). As we employ a trifurcated bundle instead of a bifurcated one, we can determine the distance to the target as the ratio of the optical intensities obtained in the receiving legs of the bundle, thus avoiding problems derived from fluctuations of the source or from changes in the reflectivity of the blades. Another novelty of the sensor is the use of asymmetric gain for the photodetectors to increase the sensor sensitivity, as explained in Section III.

The second step to reduce noise was the development of a new processing method of the TC measurements. Specifically, the results obtained at consecutive revolutions in a period of time of a minute were averaged to get a measurement with minimal noise.

In this paper, four different configurations of the optical sensor for measuring tip clearance are presented and evaluated. The general structure of the sensor and the specific characteristics of each configuration are explained in Section II. In Section III, measurements carried out on a wind tunnel for each configuration are presented and discussed. Finally, the conclusions are summarized in Section IV.

II. Methods

Even though sensors based on other techniques such as interferometry [16], [17] can achieve better accuracy, our reflective intensity optical sensor presents several advantages, such as simplicity, robustness, low cost and higher bandwidth. The main component of the sensor is a trifurcated bundle of optical fibers composed of one illuminating fiber and two rings of receiving fibers. The intensity of the reflected optical signal is collected by each ring as shown in Fig. 1. The distance is obtained as a quotient of the intensities of each of the rings in order to avoid the influence of the reflectivity of the blade surface or variations of the light source power [18], [19].

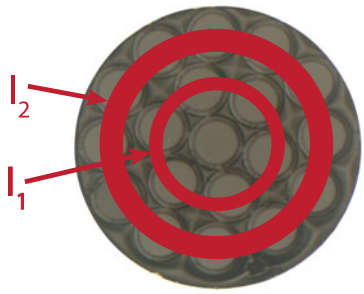

Fig. 1. Microscope view of the cross section of the common leg of the bundle. I_1 and I_2 represent the reflected intensities collected by the two rings of receiving fibers. The photodetectors produce the corresponding voltages V_1 and V_2 from these intensities.

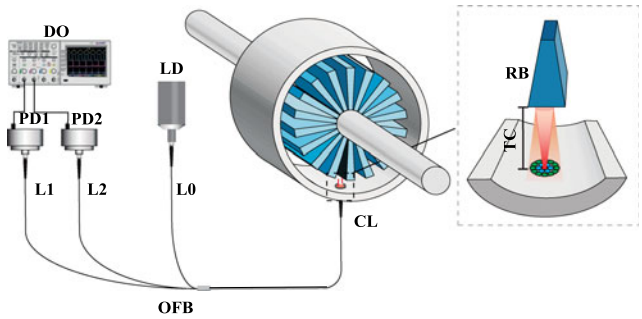

Fig. 2. DO: Digital Oscilloscope; PD1: Photodetector 1; PD2: Photodetector 2; OFB: Optical Fiber Bundle; LD: Laser Diode; TC: Tip Clearance; RB: Rotor Blade; L0: Leg 0; L1: Leg 1; L2: Leg 2; CL: Common Leg.

A laser module is utilized to couple light into the illuminating fiber. Its wavelength is 650 nm and it is manufactured with an SMA or an FC connector for easy coupling to the bundle. Two photodetectors convert the optical signals in each ring into voltages, which are acquired by an Agilent Technologies Infinium MSO9104A oscilloscope for post-processing. The sampling frequency for the acquisition is 250 ksamples/s. The arrangement of the sensor elements and the operation principle of the sensor are displayed in Fig. 2.

To perform the measurements were used two different turbines because the first one was available only for a short time. The following four configurations of the sensor were tested: bundle of glass fibers, bundle of glass fibers plus scrambler, bundle of POFs, and bundle of glass fibers with single-mode illuminating fiber. The results obtained employing the first alternative correspond to the third stage of a multistage turbine rig with 146 blades. Since it is the platform of the blade that is illuminated instead of the tip of the blade, the measured distance for this turbine was about 4–5 mm, or, equivalently, values of the TC between 2–3 mm (see Fig. 4).

To test the rest of configurations a one-stage rotor with 106 blades was used (see Fig. 3). As can be observed in Fig. 4, the blades of this rotor are completely different from those of the first rotor. In this case, the measurement requirements are much more demanding because the distance from the end of the probe to the platform is about 17–18 mm, corresponding to TC values of about 4–5 mm. Besides, the illuminated platform presents a steeper surface.

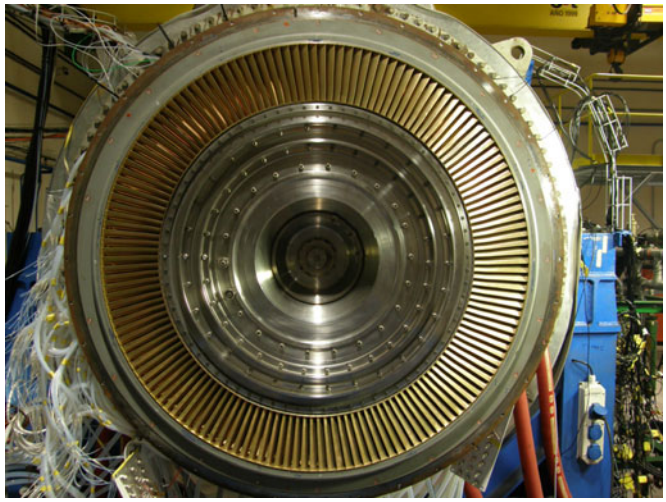

Fig. 3. Turbine rotor that was used to test the third and fourth sensor configurations, assembled in the wind tunnel.

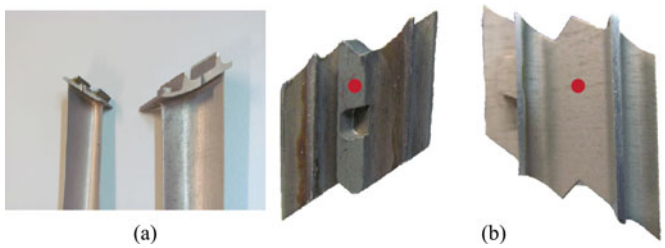

Fig. 4. (a) On the left, a blade profile corresponding to the first turbine of 146 blades, and on the right, the one corresponding to the second turbine of 106 blades. (b) Top view of both blades displaying the light spot for each blade.

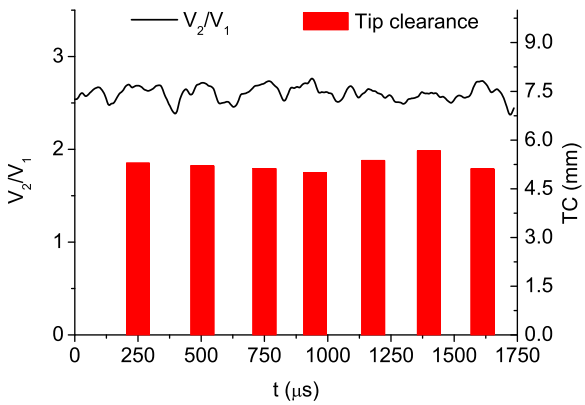

Fig. 5. Signal obtained at 2458 rpm as the quotient of the voltages V_1 and V_2 of the first and second photodetectors, respectively, by using a single-mode illuminating fiber. The value of the TC for each blade is represented by the amplitude of the bars.

When the turbine is rotating, the expected variations in the angle between the tip of the sensor and the blades are lower than 1°. According to the laboratory tests, if the changes in this angle are smaller than ±5°, the obtained differences in the tip clearance are smaller than 2%. Since the angular changes during our tests were lower than 1°, their effect was considered negligible.

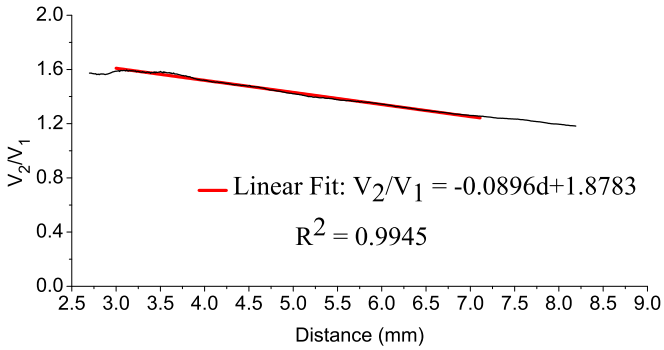

Fig. 6. Calibration curve for the first configuration of the sensor. The red line represents the fit of the calibration curve to a straight line in the range 3–7 mm.

Fig. 5 shows the signal obtained from the quotient of the voltages of the two photodetectors, together with the corresponding TC values for each blade, which are calculated at the corresponding peaks of the signal. The displayed results are obtained when the turbine is rotating at 2458 revolutions per minute (rpm), by using a single-mode illuminating fiber.

A. First Sensor Configuration

For the first configuration the FP-65 7FE-SMA laser module from *Laser Components* was used as source of light. The typical output power of this laser is 7 mW. The trifurcated bundle was manufactured by *Fiberguide Industries* using multimode glass optical fibers with a core diameter of 100 μm and a numerical aperture (NA) of 0.22. Two adjustable-gain photodetectors were chosen (PDA 100A-EC from *Thorlabs*). The gain of the transimpedance amplifier for both photodetectors was set at 0.75×10^4 V/A. Fig. 6 shows the calibration curve obtained in our laboratory for this configuration in a measurement range from 3 to 7 mm.

B. Second Sensor Configuration

The bundle in this second configuration is the same as the previous one, but a scrambler was placed between the laser module and the bundle to achieve a more uniform intensity distribution at the output of the fiber. The scrambler design consisted of two mandrels with a diameter of 42 mm separated by 3 mm from each other. A POF is wound around them following the instructions given in [20]. The mode scrambler is shown in Fig. 7.

The insertion losses of the scrambler are compensated by using a laser module of greater power (30 mW), namely the FP-SMA-650–30P from the same manufacturer as the one employed in the first configuration. The same photodetectors are used, but their gains are 0.75×10^5 V/A (first photodetector) and 2.38×10^5 V/A (second photodetector). This asymmetric gain of the photodetectors increases four times the sensitivity of the sensor with respect to a symmetric gain, as will be demonstrated in the next section. The calibration curve for the first turbine and for the same distance range as in the first configuration has been plotted in Fig. 8.

The improvement in the performance of the second sensor configuration is clearly seen in Table I. To characterize the

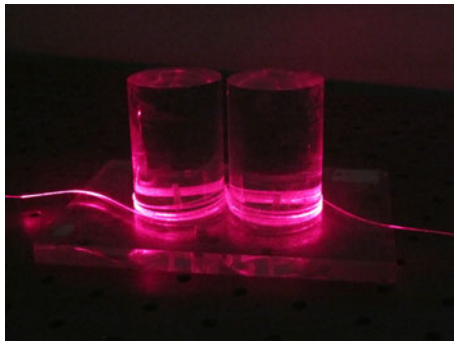

Fig. 7. Mode scrambler used in the second configuration of the tip clearance sensor.

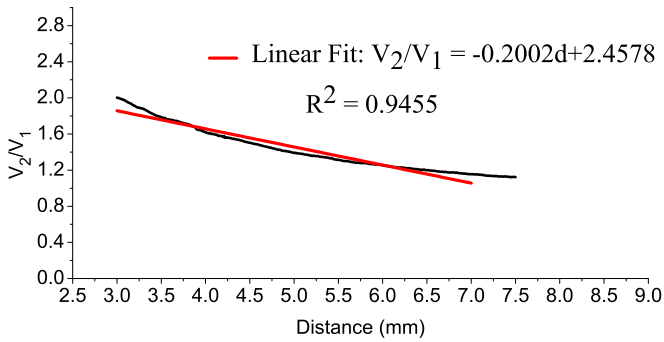

Fig. 8. Calibration curve and its linear fit for the second sensor configuration.

TABLE I
SENSITIVITY AND PRECISION OBTAINED IN OUR LABORATORY FOR THE FIRST AND SECOND SENSOR CONFIGURATION

Configuration	Sensitivity (mm^{-1})	Precision (μm)
1st Sensor Configuration	0.0896	141
2nd Sensor Configuration	0.2002	51

sensor performance we use two parameters: the sensitivity and the precision of the sensor. The sensitivity is defined as the derivative of the quotient of the voltage of each ring of receiving fibers with respect to the distance to the target, or, equivalently, the slope of the calibration curve. The precision in each sensor configuration is calculated by repeating three times a set of measurements increasing the displacement in steps of 25 μm in the whole range. The M-ILS250CC Linear Stage from Newport is used for this purpose. The minimum possible step (minimum incremental motion) using this stage would be 1 μm. The precision in the whole range is estimated as the average of the standard deviations of a set of three measurements carried out for each displacement. Due to the asymmetric gain of the photodetectors, for the second configuration, the sensitivity is more than twice the sensitivity of the first configuration. Besides, the precision is almost three times better, because of the mode mixing achieved by the scrambler. Unfortunately, we could not test this configuration on the turbines because they were not available for the time this configuration was ready.

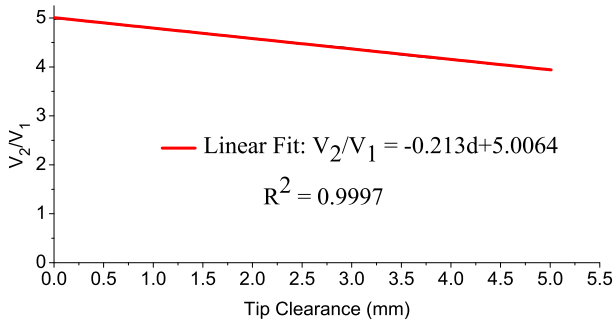

Fig. 9. Calibration curve and its linear fit for the third sensor configuration.

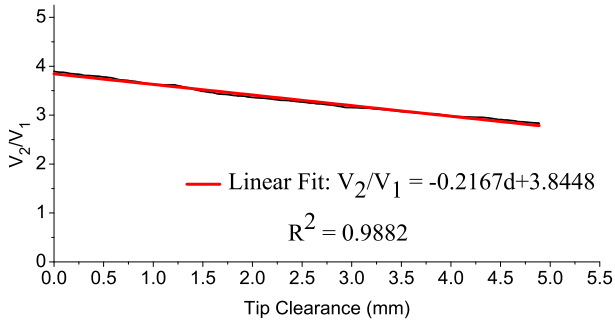

Fig. 10. Calibration curve and its linear fit for the fourth sensor configuration

C. Third Sensor Configuration

Since the profile of blades of the second turbine imposes a different calibration set-up with respect to the first and second configurations, now we will change the format of the calibration curves. Specifically, in the third and fourth configurations the x axis will represent the TC value instead of the total measured distance.

For the third configuration, the employed laser module and the asymmetric-gain photodetectors are the same ones as those described in the second configuration, but the bundle was manufactured by *FiberTech Optica* using POFs of 240 μm of core diameter and $\mathrm{NA} = 0.5$. The calibration curve is shown in Fig. 9 for a TC range from 0 to 5 mm.The disadvantage of this configuration is the much lower operating temperature of POFs as compared to glass fibers. The bundle of POFs has a maximum operating temperature of 60 °C, whereas our bundles of glass fibers can work at temperatures up to 350 °C. The reason for that low operating temperature is not the POF itself, but it is related to the glue used to assemble the bundle. This temperature constraint will be solved in a future prototype using an adhesive that can stand higher temperatures.

D. Fourth Sensor Configuration

In this configuration the bundle is also manufactured using glass fibers from *Fiberguide Industries*, but now a single-mode fiber is used as illuminating fiber to eliminate the modal noise. The receiving fibers are the same as in the first configuration. The single-mode fiber has a core diameter of 4.3 μm and $\mathrm{NA} = 0.12$. A pigtailed laser module with an output power of 20 mW (HSML-0660–20-FC from *Frankfurt Laser Company*) was used

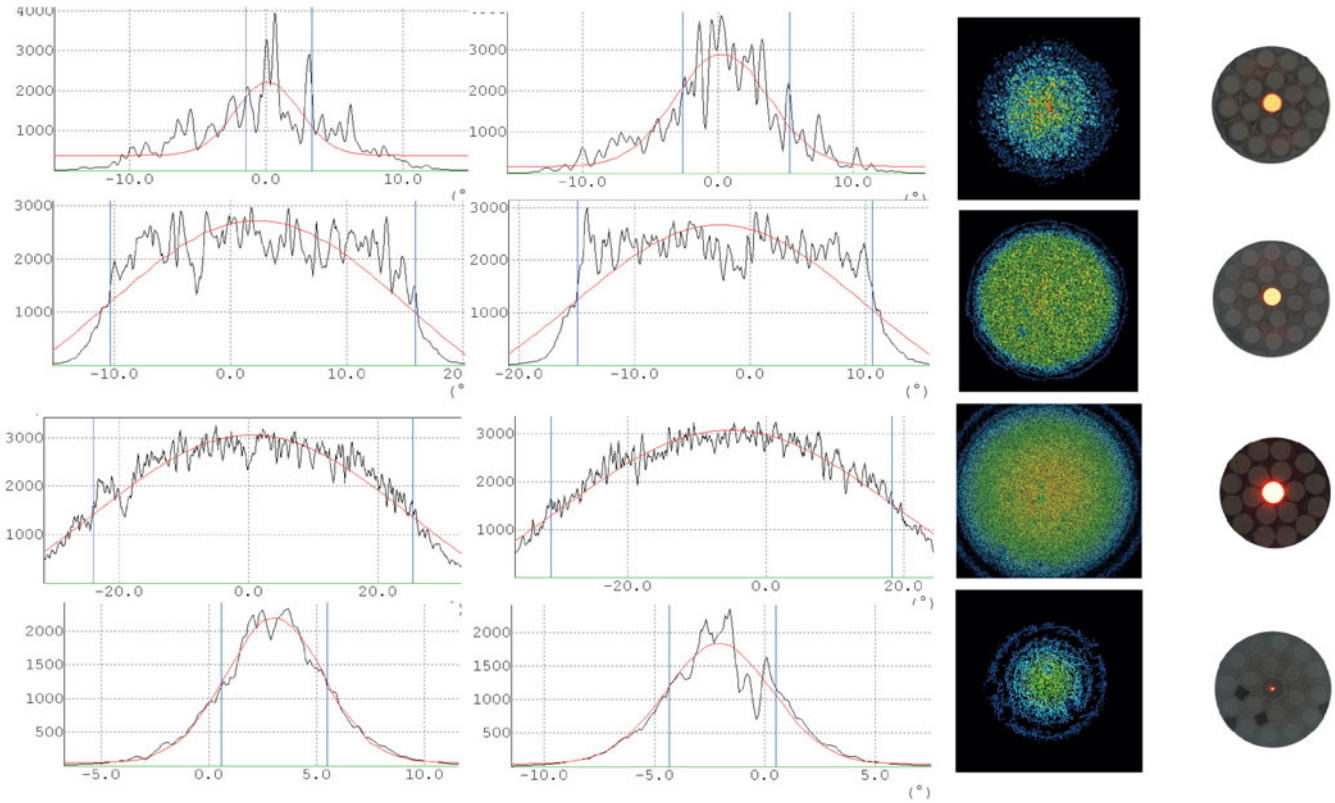

Fig. 11. Output power distribution in two perpendicular planes and 2D representations for the first, second, third and fourth sensor configurations, respectively. The common leg of the bundles is also shown. The total diameter of the bundles for all configurations is 660 μm, except for the POF bundle whose diameter is 1280 μm.

to couple light into the illuminating fiber. Asymmetric-gain photodetectors were adopted again, obtaining the calibration curve shown in Fig. 10 for the same range of TC values as in the third sensor configuration.

The output power distributions of all the configurations can be observed in Fig. 11. The power distributions are measured in the far field using the laser beam profiler LEPAS-12 from *Hamamatsu*. In this figure, a significant reduction in modal noise with respect to the first configuration can be observed, due to a greater uniformity of the output power pattern.

TABLE II
COMPARISON OF THE SENSITIVITY AND PRECISION FOR THE THIRD AND FOURTH SENSOR CONFIGURATIONS WITH SYMMETRIC AND ASYMMETRIC GAINS IN THE PHOTODETECTORS

Configuration	Sensitivity (mm^{-1})	Precision (μm)
3rd Symmetric Gain	0.0526	59
3rd Asymmetric Gain	0.213	36
4th Symmetric Gain	0.0448	61
4th Asymmetric Gain	0.2167	15

III. RESULTS

Prior to the analysis of the results for each configuration, it is important to underline the improvement on the performance of the sensor owing to the asymmetric gain of the photodetectors. The increase in the gain of the second photodetector serves to obtain a quotient V_2/V_1 that is much higher than in a symmetrical configuration. This higher quotient yields a steeper calibration curve, so the sensitivity of the sensor is increased. To assess this improvement, the experimentally obtained sensitivities and precisions of the third and fourth sensor configurations are compared for the two cases of using symmetric and asymmetric gains. As can be observed in Table II, the asymmetric gain provides values of the sensitivity more than four times higher than in the case of symmetric gain. Regarding the precision of the sensor, it is also clearly improved with the use of asymmetric gain.

The way in which the signals are acquired and processed to determine the TC values in each rotor revolution were explained in our previous works [3]. The only difference is that, to obtain the TC for each working point during these tests, the acquisition lasts for one minute and the final value is calculated averaging the minimum clearance for each revolution in this interval. This averaging cancels the effect of noises, thus increasing the performance of the sensor.

For the first sensor configuration, although many points were tested, only five different working points will be compared. This is because only five of them correspond to the same revolutions per minute, so this set of five working points will allow us to assess the sensor performance. Since the duration of each working point of the turbine was very short, the corresponding TC measurement could not be repeated more than once in each test session. However, we carried out a second TC measurement

TABLE III
FIRST SENSOR CONFIGURATION RESULTS

rpm	TC (mm)		σ (μm)
3148	2.89	2.832	41
3390	2.896	2.844	37
4359	2.829	2.811	13
4601	2.812	2.805	5
4843	2.831	2.799	22
σ_{lab}		σ_{TC}	
141 μm		24 μm	

TABLE IV
THIRD SENSOR CONFIGURATION RESULTS

rpm	TC (mm)		σ (μm)
1664	4.594	4.564	22
1898	4.539	4.498	29
1898	4.545	4.52	18
2242	4.506	4.485	15
2811	4.500	4.476	18
3059	4.498	4.429	48
σ_{lab}		σ_{TC}	
33 μm		25 μm	

in another session several days later. The TC values obtained for each working point are shown in Table III. The precision achieved in the laboratory (σ_{lab}) was 141 μm. To calculate the precision for the TC measurements of the turbine (σ_{TC}), the standard deviation (σ) of our two measurements for each working point was evaluated. The precision of the sensor was calculated from the average of all deviations, and the value obtained was 24 μm. This value is much lower than the aforementioned σ_{lab} thanks to the high number of TC values averaged in the processing of the acquired signals to avoid the influence of the noise. Even though the advancement is significant, the processing cannot completely remove the effect of noise. It is interesting to remark that the results indicate that there are some wrong values in the measurements. As was mentioned before, TC values decrease when the rpm of the turbine increases. However, the second and fifth working points for the first set of measurements do not fulfill this requirement, so these must be incorrect values. In the third column of Table III, corresponding to the second set of measurements, the second value from the top also must be wrong, for the same reason, i.e. the effect of the noise was not completely canceled.

Regarding the third configuration, six working points were analyzed. Identical working points were measured in two different sessions separated by three days, and the corresponding TC values are shown in Table IV.

The precision obtained in the wind tunnel for this configuration of the sensor was 25 μm, improving the one obtained in our laboratory. Although the measurement conditions in the second turbine are much more complicated than in the first one, the results confirm that the performance of the third configuration of the sensor is satisfactory anyway, since all working points exhibit a correct behavior and the sensor satisfies the required precision of 30 μm.

TABLE V
FOURTH SENSOR CONFIGURATION RESULTS

rpm	Session 1		Session 2		σ (μm)
	TC1 (mm)	TC2 (mm)	TC1 (mm)	TC2 (mm)	
2458	4.552	4.552	4.542	4.551	5
2730	4.495	4.498	4.472	4.476	13
3054	4.433	4.441	4.382	4.392	3
3475	4.369	4.375	4.307	4.315	35
3749	4.338	4.324	4.257	4.252	45
4310	4.282	4.277	4.210	4.201	43
	σ_{lab}			σ_{TC}	
	24 μm			28 μm	

In the case of the fourth configuration, six working points were used again to assess the performance of the sensor. The points were acquired in two different sessions separated by five days. In these tests, the working points were stable for longer time than in the rest of the measurements carried out for the other configurations. Therefore, it was possible to carry out two measurements separated by five minutes in the time that the working point was stable (TC1 and TC2). The results obtained for the fourth configuration are presented in Table V.

The precision obtained for this configuration was 28 μm, i.e. very similar to the laboratory value (24 μm). As in the previous configuration, the measurements of all working points present a correct behavior. The precision is a bit worse than the precision of the third configuration, but it must be due to the fact that the rpm of this measurements are higher, which induce greater amplitudes in blade vibrations leading to larger deviations in the measurements.

IV. CONCLUSION

Four different configurations of the sensor to measure TC in turbines have been tested and evaluated. Except for the second configuration that could not be tested on the wind tunnel, all of them show a measurement uncertainty that fulfills the initial requirement of 30 μm. The first sensor configuration has proved to be less satisfactory than the other ones, since several working points yielded incorrect behavior. The third configuration presents the best precision. However, its important disadvantage is that the POF bundle has a maximum operating temperature of 60 °C, restricting the possibilities of the measurements. The fourth configuration shows good results in all working points and the maximum operating temperature is 350 °C, so this is the configuration that has the best characteristics for TC measurements. This sensor has a great potential not only to perform TC measurements, but also to satisfy the requirements of active clearance control systems. It can also serve to develop applications in the field of structural health monitoring, by evaluating the vibration amplitude of the turbine blades using tip-timing methods in order to detect any damage on them. For instance, the *Aeronautical Technologies Center* will use three sensors circumferentially equidistributed to obtain the TC of a rotating disk of a real aircraft engine. The objective is to assess its behavior at different rotational speeds. The sensors will provide useful

information about the vibration of the disk and the eccentricity of the shaft, which will allow to improve the design of the disk.

REFERENCES

[1] D. C. Wisler, "Loss reduction in axial-flow compressors through low-speed model testing," *J. Eng. Gas Turbines Power*, vol. 107, no. 2, pp. 354–363, 1985.

[2] M. W. Wiseman, "An investigation of life extending control techniques for gas turbine engines," in *Proc. Amer. Control Conf.*, 2001, vol. 5, pp. 3706–3707.

[3] I. García, J. Beloki, J. Zubia, G. Aldabaldetreku, M.A. Illarramendi, and F. Jiménez, "An optical fiber bundle sensor for tip clearance and tip timing measurements in a turbine rig," *Sensors*, vol. 13, no. 6, pp. 7385–7398, Jun. 2013.

[4] I. García, J. Zubia, A. Berganza, J. Beloki, J. Mateo, and C. Vázquez, "Comparison of three different configurations of an optical sensor for tip-clearance measurements in turbines," presented at the 23rd Int. Conf. Opt. Fiber Sens., Santander, Spain, Jun. 2014, vol. 9157A5.

[5] K. O. Hill, Y. Tremblay, and B. S. Kawasaki, "Modal noise in multimode fiber links: Theory and experiment," *Opt. Lett.*, vol. 5, no. 6, pp. 270–272, Jun. 1980.

[6] K. Petermann, "Nonlinear distortions and noise in optical communication systems due to fiber connectors," *IEEE J. Quantum Electron.*, vol. 16, no. 7, pp. 761–770, Jul. 1980.

[7] S. Savovic and A. Djordjevich, " Calculation of the coupling coefficient in step index glass optical fibers," *Appl. Opt.*, vol. 48, no. 22, pp. 4496–4500, 2009.

[8] M. Imai, "Statistical properties of optical fiber speckles," *Bulletin Faculty Eng.*, vol. 130, pp. 89–104, 1986.

[9] P. Couch and R. Epworth, "Reproducible modal noise measurements in system design and analysis," *J. Lightw. Technol*, vol LT-1, no. 4, pp. 591–596, Dec. 1983.

[10] B. Daino, G. De Marchis, and S. Piazzolla, "Analysis and measurement of modal noise in an optical fibre," *Electron. Lett.*, vol. 15, no. 23, pp. 755–756, 1979.

[11] R. Attia and J. Marcou, "Mode scrambler for polymer optical fibers," *Opt. Eng.*, vol. 39, no. 1, pp. 299–303, Jan. 2000.

[12] G. Jiang, R. F. Shi, and A. F. Garito, "Mode coupling and equilibrium mode distribution conditions in plastic optical fibers," *IEEE Photon. Technol. Lett.*, vol. 9, no. 8, pp. 1128–1130, Aug. 1997.

[13] J. Zubia and J. Arrue, "Plastic optical fibers: An introduction to their technological processes and applications," *Opt. Fiber Technol.*, vol. 7, no. 2, pp. 101–140, 2001.

[14] K. Peterman and G. Arnold, "Noise and distortion characteristics of semiconductor lasers in optical fiber communication systems," *IEEE Trans. Microw. Theory Tech.*, vol. MTT-30, no. 4, pp. 389–401, Apr. 1982.

[15] H. Huang and U. Tata, "Simulation, implementation, and analysis of an optical fiber bundle distance sensor with single mode illumination," *Appl. Opt.*, vol. 47, no. 9, pp. 1302–1309, 2008.

[16] A. Mehta, W. Mohammed, and E. G. Johnson, "Multimode interference-based fiber-optic displacement sensor," *IEEE. Photon. Technol. Lett.*, vol. 15, no. 8, pp. 1129–1131, Aug. 2003.

[17] A. M. R. Pinto, J. M. Baptista, J. L. Santos, M. Lopez-Amo, and O. Frazão, "Micro-displacement sensor based on a hollow-core photonic crystal fiber," *Sensors*, vol. 12, no. 12, pp. 17497–17503, 2012.

[18] S. Z. Cao, F. J. Duan, and Y. G. Zhang, "Measurement of rotating blade tip clearance with fibre-optic probe," *J. Phys. Conf. Series*, vol. 48, no. 1, pp. 873–877, Oct. 2006.

[19] M. Yu-zhen, L. Guo-ping, Z. Yong-kui, and L. Hua-guan, "Tip clearance optical measurement for rotating blades," in *Proc. Int. Conf. Manage. Sci. Ind. Eng.*, Jan. 2011, pp. 1206–1208.

[20] *Test Methods for Attenuation of all Plastic Multimode Optical Fibers*, Japanese Industrial Standard JIS C 6863, 1990.

Iker García received the M.Sc. degree in telecommunications engineering from the University of the Basque Country, Bilbao, Spain, in 2006. He is currently working toward the Ph.D. degree with the Applied Photonics Group, University of the Basque Country. He has been researching optical sensors at the School of Engineering of Bilbao, University of the Basque Country since 2012. His main research interests include optical fiber sensors and their industrial applications.

Joseba Zubia received the M.Sc. degree in solid-state physics and the Ph.D. degree in physics from the University of the Basque Country, Bilbao, Spain, in 1988 and 1993, respectively. His Ph.D. work focused on the optical properties of ferroelectric liquid crystals.

Currently, he is a Full Professor in the Department of Communications Engineering, University of the Basque Country. He has more than 20 years of experience doing basic research in the field of polymer optical fibers and is currently involved in research projects in collaboration with universities and companies from Spain and other countries in the field of polymer optical fibers, fiber-optic sensors, and applied photonics.

Amaia Berganza received the M.Sc. degree in telecommunications engineering from the University of the Basque Country, Bilbao, Spain, in 2004. In 2014, she received the Ph.D. degree for her thesis "Estudio y caracterización de fibras ópticas de plástico multinúcleo." From 2007 to 2011, she was a Ph.D. scholar with the Department of Electronics and Telecommunications, Faculty of Engineering of Bilbao, University of the Basque Country, working on optical fibres. Since 2011, she has been serving as an Assistant Professor with the Department of Applied Mathematics, Faculty of Technical Engineering of Bilbao, University of the Basque Country, spending her time teaching in undergraduate degrees and researching on Applied Photonics. Her current main scientific interests include the analysis of light propagation properties in plastic optical fibres, fabrication of plastic optical fibres, and Raman spectroscopy.

Josu Beloki received the M.Sc. degree in industrial engineering from the University of the Basque Country, Bilbao, Spain, in 2003. He received the M.Sc. degree in engineering mechanics from the KTH, Royal Institute of Technology, Stockholm, Sweden, in 2007, and also received a Research Master (former Diploma Course) from The Von Karman Institute for Fluid Dynamics, Sint-Genesius-Rode, Belgium, in 2007. From 2008–2014, he was with the Centro Tecnologías Aeronáuticas, as a Research and Test Engineer. Since 2014, he has been with the University of the Basque Country, as an Associate Lecturer in fluid dynamics.

Jon Arrue was born in Bilbao, Biskay, Spain. He was a Lecturer at the University of the Basque Country, Bilbao, Spain, from 1996–2001, where he currently a Professor. He has been researching on polymer optical fibers since 1993. His main research interests include new types and applications of polymer optical fibers, and POF amplifiers and lasers.

María Asunción Illarramendi, biography not available at the time of publication.

Javier Mateo received the M.Sc. degree in electrical engineering from the Polytechnic University of Madrid, Madrid, Spain, and the Ph.D. degree from the University of Zaragoza, Zaragoza, Spain, in 1989 and 2000, respectively. From 1989 to 1993, he was with Cables de Comunicaciones S. A., Zaragoza, where he worked on fiber optic sensors and optical communications. In 1993, he joined the Electronic Engineering and Communications Department, University of Zaragoza, where he is currently an Associate Professor of optical fiber communications. His professional research interests include signal processing, in particular, applied to biomedical signals, fiber optic sensors, and optical communication systems. He is part of the Aragon Institute of Engineering Research.

Carmen Vázquez (M'99–SM'05) received the M.Sc. degree in Physics (electronics) from the Complutense University of Madrid, Madrid, Spain, in 1991, and the Ph.D. degree in photonics from the Telecommunications Engineering School, Universidad Politécnica of Madrid, Madrid, in 1995. From 1992 to October 1995, she was with the Optoelectronics Division of Telefónica Investigación y Desarrollo, Madrid. In October 1995, she joined the University Carlos III of Madrid, Madrid, where she is currently a Full Professor at Electronics Technology Department and the Head of the Displays and Photonic Applications Group. She was a Visiting Scientist at the Research Laboratory of Electronics, Massachusetts Institute of Technology from August 2012 to July 2013, working on silicon photonics. She was also the Head of Department for three years and Vice Chancellor for four years. Her research interests include integrated optics, optical communications, and instrumentation including, plastic optical fibers, broadband access networks and monitoring techniques, RoF systems, filters, switches, fiber optic sensors, and WDM networks.

Artículo 4

Optical Tip Clearance Measurements as Tool for Rotating Disk Characterization

García, I., Zubia, J., Beloki, J., Arrue, J., Durana, G., & Aldabaldetreku, G.

Sensors, 17(1), 165 (2017).

sensors

MDPI

Technical Note

Optical Tip Clearance Measurements as a Tool for Rotating Disk Characterization

Iker García [1,*], Joseba Zubia [1], Josu Beloki [2,3], Jon Arrue [1], Gaizka Durana [1] and Gotzon Aldabaldetreku [1]

[1] Department of Communications Engineering, E.T.S.I. of Bilbao, University of the Basque Country UPV/EHU, Alda. Urquijo s/n Bilbao 48013, Spain; joseba.zubia@ehu.eus (J.Z.); jon.arrue@ehu.eus (J.A.); gaizka.durana@ehu.eus (G.D.); gotzon.aldabaldetreku@ehu.eus (G.A.)

[2] CTA, Aeronautical Technologies Center, Bizkaia Technological Park, Zamudio 48170, Spain; josu.beloki@ctabef.com

[3] Department of Nuclear Engineering and Fluid Mechanics, E.T.S.I. of Bilbao, University of the Basque Country (UPV/EHU), Bilbao 48013, Spain

* Correspondence: iker.garciae@ehu.eus; Tel.: +34-946-017-305

Academic Editors: Thierry Bosch, Aleksandar D. Rakić and Santiago Royo
Received: 22 November 2016; Accepted: 10 January 2017; Published: 15 January 2017

Abstract: An experimental investigation on the vibrational behavior of a rotating disk by means of three optical fiber sensors is presented. The disk, which is a scale model of the real disk of an aircraft engine, was assembled in a wind tunnel in order to simulate real operation conditions. The pressure difference between the upstream and downstream sides of the disk causes an airflow that might force the disk to vibrate. To characterize this vibration, a set of parameters was determined by measuring the tip clearance of the disk: the amplitude, the frequency and the number of nodal diameters in the disk. All this information allowed the design of an upgraded prototype of the disk, whose performance was also characterized by the same method. An optical system was employed for the measurements, in combination with a strain gauge mounted on the disk surface, which served to confirm the results obtained. The data of the strain gauge coincided closely with those provided by the optical fiber sensors, thus demonstrating the suitability of this innovative technique to evaluate the vibrational behavior of rotating disks.

Keywords: optical fiber sensor; rotating disk; tip clearance; vibration measurement; nodal diameter

1. Introduction

The operation of multiple devices, such as computer hard disks or circular saws, is based on rotating disks [1]. During operation, these rotating disks may experience vibrations that reduce their performance and service lives. Such vibrations could be due to several reasons, e.g., tolerances in the manufacturing process, aging, or some asymmetry in the disk. Vibrations of critical amplitudes cause a reduction in the reliability of the devices, which may undergo failures due to fatigue [2]. Therefore, there is a great interest in exploring techniques that allow the monitorization and characterization of the vibrational behavior of rotating disks [3–5].

In this paper, we report on our evaluation works related to the vibrational behavior of a rotating disk that is a scale model of a real disk of an aircraft engine. Such evaluation was carried out by means of a non-contact method employing three optical fiber sensors (OFSs) [6,7]. Its interest lies in the fact that reliability of aircraft components is of capital importance, since a failure in one of them could lead to a catastrophic situation. Although it is completely unfeasible to totally avoid the chance of disk failures, nowadays the number of disk flaws has been considerably reduced by means of melting-process controls and non-destructive-inspection techniques [8]. Up to now, these have usually been carried out employing strain gauges, which still constitute the most common sensors

for the characterization of the strain and vibrations of aircraft components. However, they present several drawbacks, such as the need of a telemetry system to transmit the signals, or their complex and time-consuming wiring. In comparison, OFSs present intrinsic benefits [9–11], so they are being more and more used to evaluate the structural health of aeronautical components [12]. One of them is the engine. In previous works, we developed a sensor for it that was based on a bundle of optical fibers, which served to carry out tip-clearance (TC) measurements in low pressure turbines [13] and compressors [14] of aircraft engines. The TC is the gap between the tip of the turbine/compressor blades and the casing of the engine, and it is a crucial parameter related to the efficiency of the engine [15]. This parameter has also been employed to evaluate other phenomena, such as cracks in the blades [16]. To characterize the vibrational behavior of our special rotating disk, we decided to employ three OFSs, because, as a matter of fact, the distance from the edges of a rotating disk to the casing of a wind tunnel can be interpreted as a clearance that varies as a result of disk vibrations. This method based on three OFSs provided a great reduction in the time needed to get the system ready to start the tests in comparison to a system based only on strain gauges. In addition, as only one strain gauge is required, there is a lower influence in the mechanical behaviour of the disk with respect to a measuring system based on multiple strain gauges.

The disk was assembled in a wind tunnel to assess its vibrational behavior. In order to simulate real operation conditions, a pressure difference was set between the upstream and downstream sides of the disk. This, in turn, creates an air flow through the gap between the casing of the wind tunnel and the disk edge. Under particular conditions, the air flow can force the disk to vibrate. This aerolastic instability, known as flutter, is self-initiated and also self-maintained, because the vibrations return energy to the disk in a way that their amplitudes increase dramatically if the damping is not able to dissipate that energy [17]. All details about the assembly of the disk in the wind tunnel and the OFSs configuration are described in Section 2. In Section 3, the results obtained for the two prototypes of the disk tested in the wind tunnel are presented and discussed. Finally, the conclusions of the work are summarized in Section 4.

2. Experimental Set-Up

The experiments were carried out in the transonic wind tunnel at Aeronautical Technologies Center (CTA). The CTA's rotating-turbine-test facility is a continuous transonic-flow-test bed with an atmospheric inlet/outlet. The level of pressure/vacuum, the temperature and the mass flow are individually regulated, so that Mach and Reynolds numbers can be independently modified.

The supply and exit air conditions in the test section are achieved by employing two centrifugal compressor and vacuum groups, which are run, respectively, by electrical motors of 3.7 MW and 5 MW. The compressors are able to supply a maximum mass flow of 18 kg/s, with a maximum supply pressure up to 4.5 bar, a minimum exit pressure of 0.3 bar, and a temperature regulation from atmospheric temperature up to 160 °C. The turbine power is transmitted by a single shaft (up to 7800 rpm) to a dynamometer (up to 11,000 rpm 3.3 MW). The test section has a diameter of 1 m. A schematic of the facility is included in Figure 1.

The data acquisition system is able to acquire up to 800 pressure channels, 200 temperature channels and 28 vibration signals. It can also acquire 20 rotating signals and it incorporates high accuracy torque machines and duplicated rpm and mass flow measurements. More information regarding the tunnel can be found in [18].

As mentioned before, the main objective of the tests was to characterize the vibrational behavior of the rotating disk under test. Specifically, we needed to know the vibration frequencies and the number of nodal diameters (NDs) of the disk at those frequencies. A nodal diameter can be defined as the line of stationary points that separates parts of the disk vibrating out of phase with respect to each other. The concept of nodal diameter is represented in Figure 2, where we can see a disk vibrating with one, two and three nodal diameters.

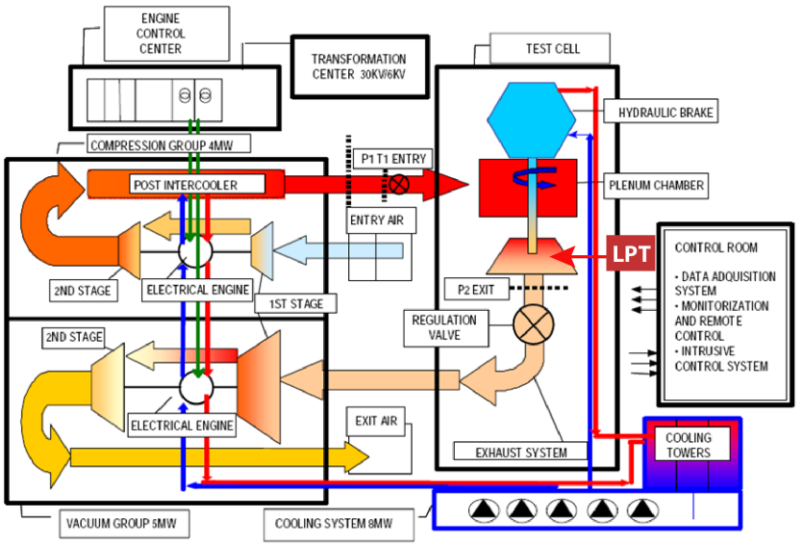

Figure 1. Scheme of the transonic test turbine facility. The disk under test was assembled in the position where the low-pressure turbine (LPT) is usually placed.

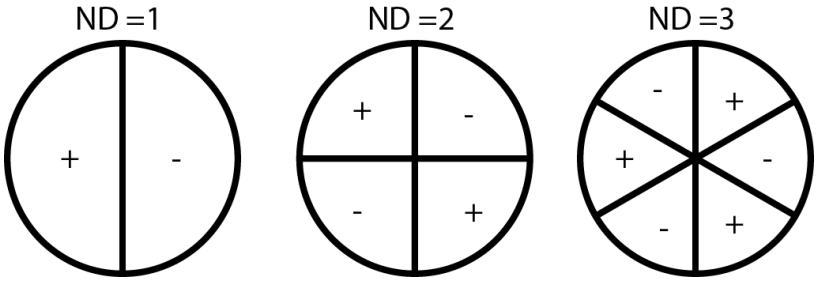

Figure 2. Disks vibrating with one, two and three nodal diameters, respectively.

This information enabled the design of an improved second prototype with damped vibrations. In order to obtain results from the disk that correspond to real working conditions, this was assembled in a wind tunnel where a pressure difference was established between both sides of the disk, ranging from 2 to 3 bar. As well as evaluating the case when the disk is not rotating, the disk's performance was analyzed at its nominal rotating speed ($RPM_{nominal}$), and at 1.5 and 2 times $RPM_{nominal}$. In order to get these rotating speeds, the shaft was driven by a 100 kW electric motor and it was controlled by means of a hydraulic brake.

Three OFSs were installed in the wind tunnel to carry out TC measurements. They were arranged at an angle of 120 °between them and separated by 4.75 mm from the disk edge (see Figure 3). These reflective intensity-modulated OFSs were originally developed to perform TC measurements in turbines [19]. Their main component is a trifurcated bundle of optical fibers whose particular design allows us to transmit the light from a laser to the target, and to collect the reflected light which is employed to calculate the distance from the bundle tip to the target. All the components and the performance characteristics of the sensors have been described in [20]. Each of the three sensors provides two output signals, whose quotient serves us to obtain the distance to the target according to a calibration curve. This method provides immunity to the fluctuations of the light source, to changes in the reflectivity of the target surface, and to losses or misalignments between the sensor probe and the target [21]. Due to the high number of sensors and transducers needed to measure the temperature and pressure in multiple points of the wind tunnel, only three inputs of the acquisition system were available. In this situation, we have two options: (a) one sensor with two output signals; or (b) three sensors, each one with a single output, (see Figure 3). We chose the latter option because it implied a loss of accuracy of only about ±8% in the measured amplitude with respect to the first option. This loss of accuracy does not affect the detection of the vibration frequency, which was the

main goal of the tests, since both options would yield the same frequency, although with different amplitudes. Besides, the use of three sensors allows us to calculate the eccentricity of the disk.

The probe fixed to the casing (Figure 3) does not detect the real vibration frequency of the disk when it is rotating, but a modulated frequency instead. The reason is that the measured frequency is modulated by the rotational speed and by the set of NDs excited in the disk, according to the following equation [22]:

$$f_{os} = f_{disk} \pm f_r \cdot ND \quad (1)$$

where f_{os} is the frequency detected by the OFS, f_{disk} is the vibration frequency of the disk, f_r is the rotational frequency, and ND is the number of nodal diameters. In order to check the ability of the sensors to detect the vibration frequency and to obtain the NDs of the disk, a strain gauge was instrumented on the disk surface.

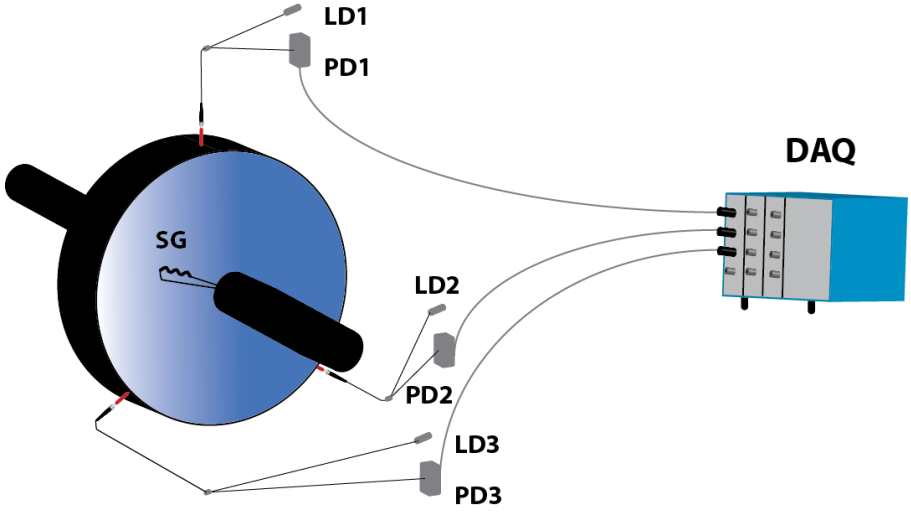

Figure 3. Experimental set-up for the TC measurements in the wind tunnel. LD x stands for Laser Diode x, PD x for Photodetector x, SG for Strain Gauge, and DAQ for Data Acquisition System.

The calibration process of the OFSs is illustrated in Figure 4. It is the flattest part of the disk that is illuminated, so as to get the most stable signal, taking into account that the disk will flutter. To obtain the calibration curve of each sensor, the values of the voltage of the photodetector were successively stored as the tip of the probe was separated from the disk surface in steps of 10 μm. This procedure was repeated three times to obtain a calibration curve in a range of distances up to 10 mm, and the results were averaged to obtain a more accurate calibration. Since the expected amplitude of the vibration was 0.25 mm, the resulting curve was linearized in the interval 4.5–5 mm to obtain the following calibration curves (represented in Figure 5):

$$d = -1.78 \cdot V + 7.11 \quad (2)$$

$$d = -1.28 \cdot V + 7.46 \quad (3)$$

$$d = -1.79 \cdot V + 7.34 \quad (4)$$

where d is the distance to the disk (in mm) and V is the voltage of the photodetector (in V).

As can be seen in Figure 4b, the disk incorporates a flange whose depth is 4.57 mm. Therefore, to obtain the real TC of the disk, this distance must be subtracted from the value provided by Equations (2)–(4).

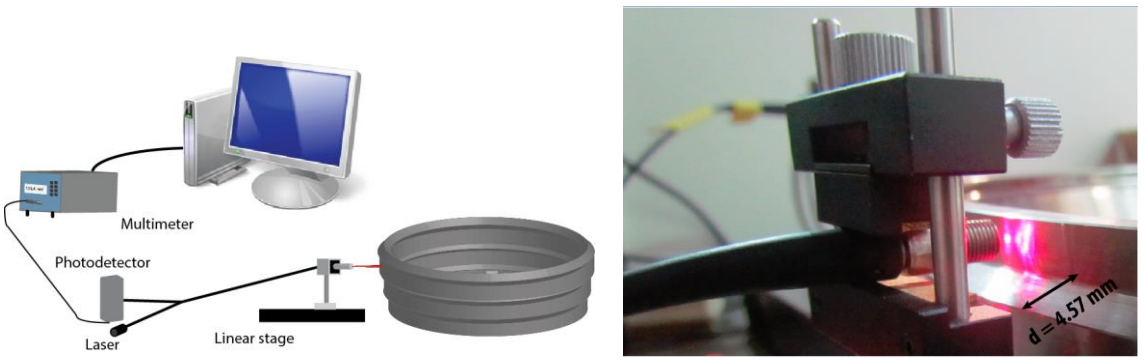

(**a**) (**b**)

Figure 4. Sensor calibration process (**a**) and detail of the tip of the OFS illuminating the rotating disk during the calibration process (**b**).

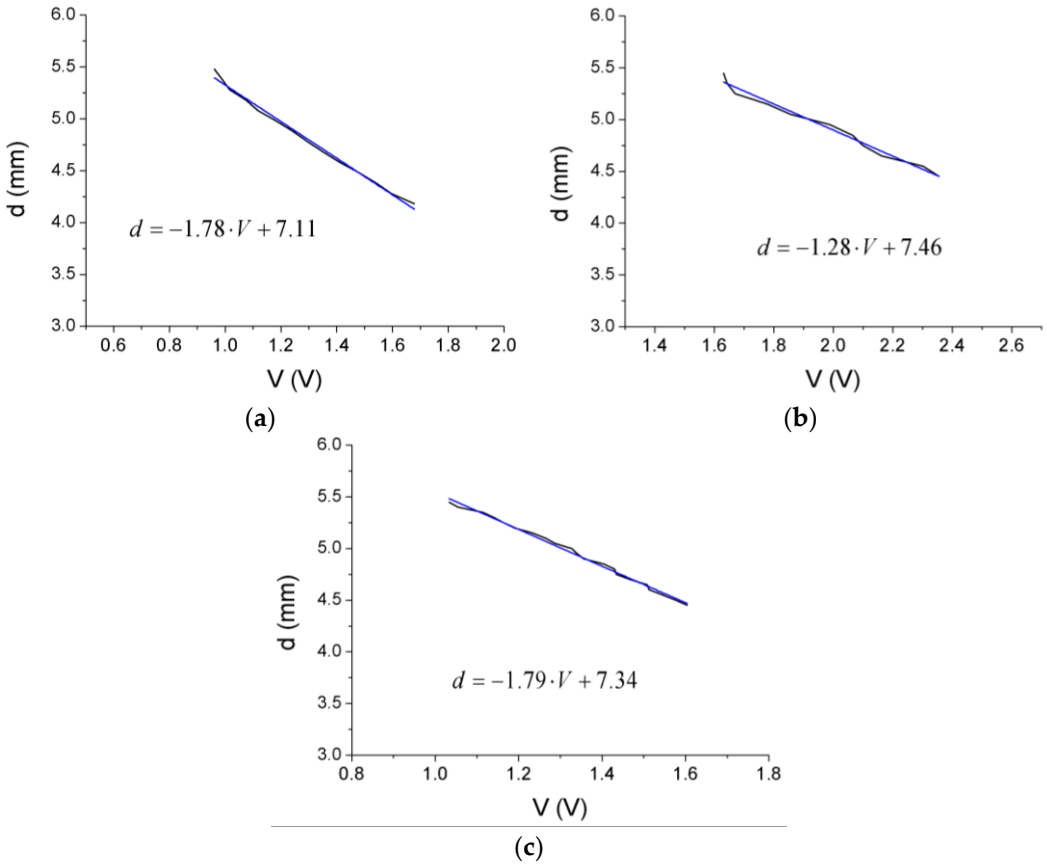

(**a**) (**b**) (**c**)

Figure 5. Calibration curve (black) and its linear fit (blue) for OFS 1 (**a**), OFS 2 (**b**) and OFS 3 (**c**) for the measuring interval.

The signals of all the sensors involved in the tests were acquired using the dynamic-signal-acquisition module PXI-4472 from National Instruments. They were sampled at 25 k samples/s and the complete signal-acquisition process for each signal lasted for 5 s (125,000 samples). For the OFS, Matlab was used to obtain the Fast Fourier Transform (FFT) of each signal with a frequency resolution of 0.2 Hz. However, the FFT of the signal from the strain gauge was provided by the acquisition program employed in CTA with a frequency resolution of 2 Hz.

To determine the uncertainty of the measurements of the three OFSs, some tests were carried out in our laboratory. The tip of the probe was placed 4.5 mm away from the disk edge and it was moved outwards along 1 mm in 25-μm steps using a linear stage. In each step, the voltage of the photodetector was recorded. This procedure was repeated three times for each distance, and the

standard deviation of the three measurements was calculated. The final uncertainty of each sensor (see Table 1) was obtained as the average of all the standard deviations for each distance.

Table 1. Uncertainty for each sensor obtained in laboratory tests.

Sensor	Uncertainty (μm)
1	7
2	7
3	10

3. Results

As mentioned in the previous section, the objective of the tests is to experimentally characterize the vibrational behavior of a rotating disk (first prototype) in a realistic operation condition. In this way, the manufacturer could optimize some parameters of the disk to reduce the vibrations in an upgraded design (second prototype).

Figure 6 shows the signals and their FFTs obtained for the case of the first prototype of the disk. The signals were obtained from OFS 1, which was placed on the upper part of the wind tunnel, in the direction of an imaginary vertical axis that passes by the center of the disk. OFS 2 and OFS 3 were placed forming angles of 120 ° and −120 ° with the direction of OFS 1, respectively. The graphs correspond to a pressure difference of 2.5 bar when the disk is rotating at nominal speed (c and d), and when it is not rotating (a and b). Notice that the airflow forces the disk to flutter even when it is static. Even in such a case, the TC varies substantially with the vibration of the disk, and the vibration frequency is easily identified by the peak in the FFT of the signal. The signal in the time domain becomes more complex when the disk is rotating, and its FFT shows that more vibration frequencies than in the static condition are detected.

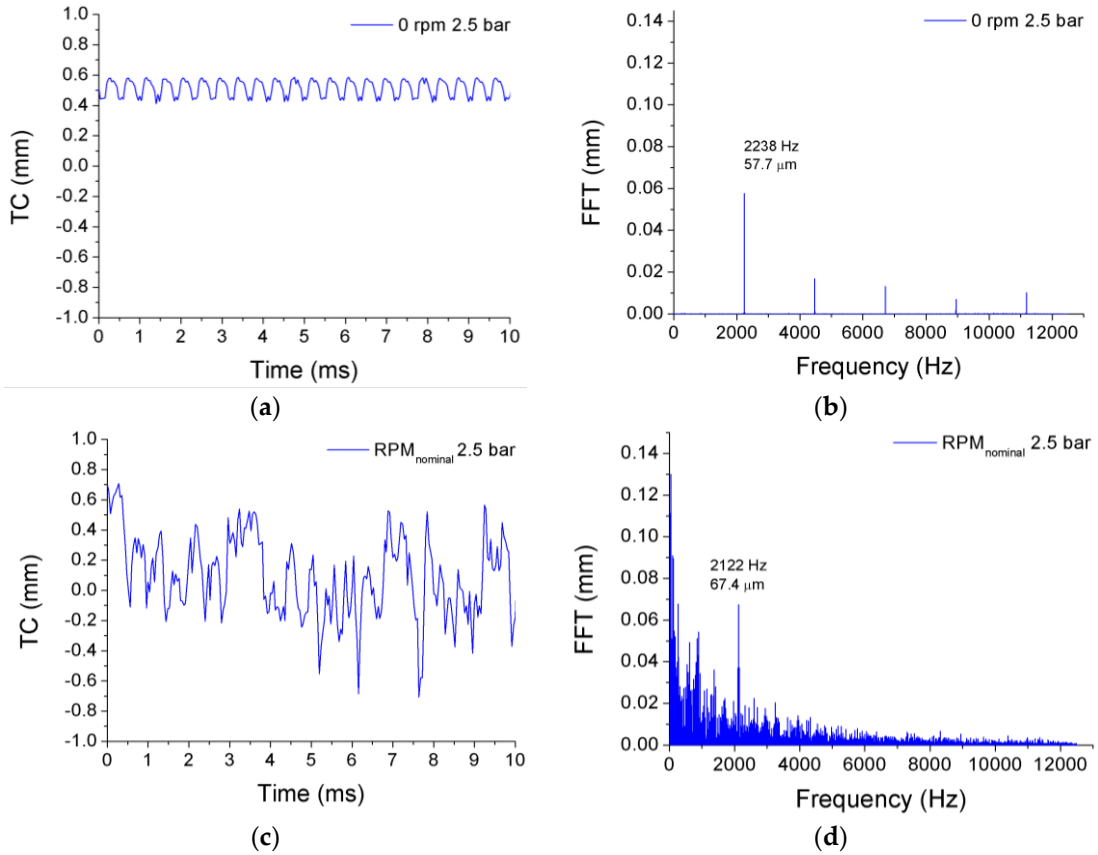

Figure 6. Time domain signals and their FFTs for OFS 1 when the disk is not rotating (**a**,**b**) and when it is turning at its nominal speed (**c**,**d**). Clear peaks appear at f_{os} = 2238 Hz and f_{os} = 2122 Hz, respectively.

The results obtained for the first prototype at various rotational speeds are summarized in Tables 2–5. To calculate the amplitude of the vibrations, the TC of the disk is expressed in terms of its change, hence the negative values shown in Figure 6c. While the frequency of the strain gauge installed on the disk surface represents the real vibration frequency of the disk in every case, the frequency of the OFSs (f_{os}) is modulated by the rotational speed of the disk and by the NDs. Thus, the vibration frequency of the disk provided by the OFS (f_{disk}) has to be obtained by demodulating f_{os} using Equation (1). The only exception is the case in which the disk is not rotating, since the frequencies of the signals from the strain gauge and from the OFSs coincide. All vibration frequencies provided by the OFSs match one another, and they also match those given by the strain gauge. The corresponding amplitudes are not correlated, since they correspond to vibrations measured at different points of the disk. For a fixed rotational speed, the amplitude of each vibration increases as the pressure difference between both sides of the disk becomes higher (see Figure 7). A situation that is worthy of study can be seen in Figure 7, in the case when the pressure difference is 2.6 bar and the disk is turning at $RPM_{nominal}$. In such a case, the vibration frequency of the disk is markedly different, because it passes from 2247 Hz to 1574 Hz (2122 Hz to 1474 Hz for the frequency detected by the OFS). This is due to a change in the way this disk vibrates: for the lower pressure differences, the disk vibrates with five nodal diameters whereas at 2.6 bar the disk vibrates with ND = 4. The value of ND can be obtained from Equation (1), since f_{disk} only matches the correct vibration frequency, which is given by the strain gauge, when the correct value of ND is used to demodulate f_{os}. A similar behavior can be observed when the disk is rotating at 1.5 × $RPM_{nominal}$, and at 2 × $RPM_{nominal}$, with the peculiarity that it happens at lower pressure difference: 2.4 bar for 1.5 × $RPM_{nominal}$ and 2.2 bar for 2 × $RPM_{nominal}$.

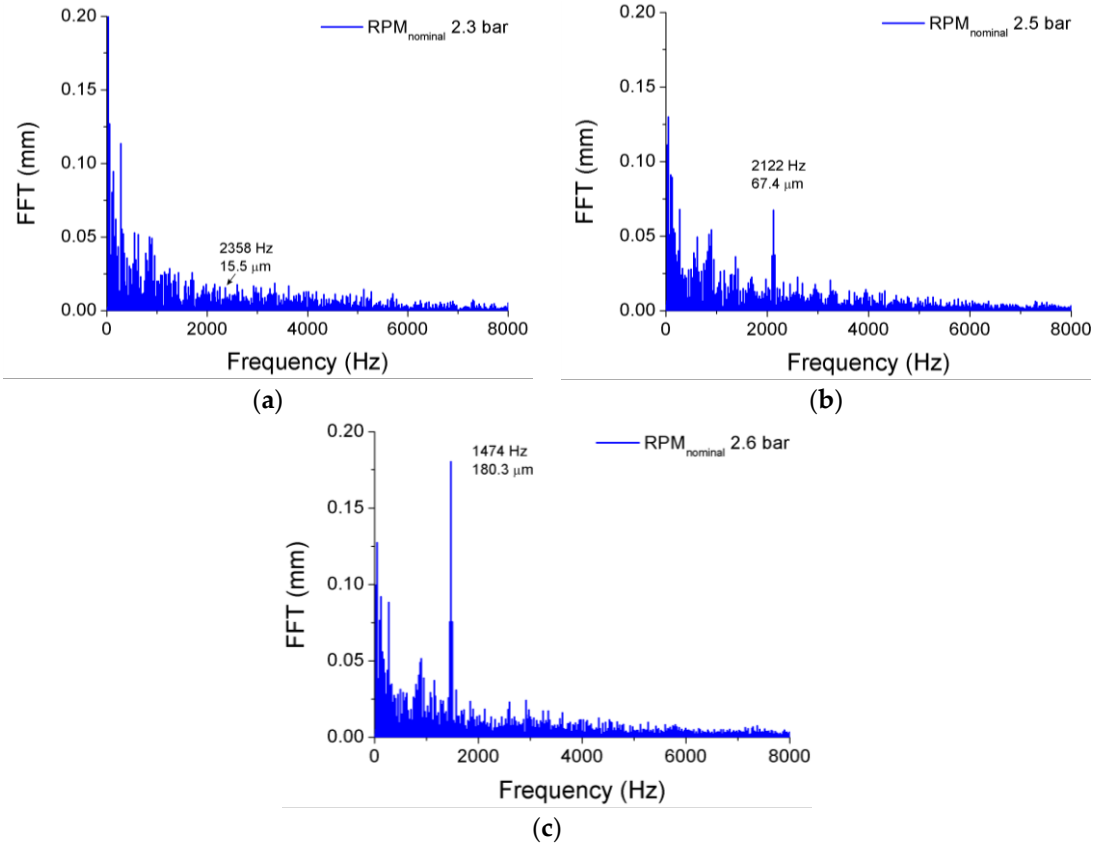

Figure 7. Evolution with the pressure difference of the vibration signal for the OFS 1 when the disk is rotating at $RPM_{nominal}$.

Table 2. Results for the first prototype at 0 rpm.

Pressure Difference (bar)	ND	Sensor 1			Sensor 2			Sensor 3		
		Amplitude (μm)	f_{os} (Hz)	f_{disk} (Hz)	Amplitude (μm)	f_{os} (Hz)	f_{disk} (Hz)	Amplitude (μm)	f_{os} (Hz)	f_{disk} (Hz)
2.3	5	2.5	2238	2238	0.2	2238	2238	0.6	2238	2238
2.4	5	20.1	2238	2238	19.3	2238	2238	46.2	2238	2238
2.5	5	57.7	2238	2238	19.7	2238	2238	22.9	2238	2238
2.6	5	87.8	2236	2236	201.4	2236	2236	194.3	2236	2236
2.7	5	79.2	2236	2236	624	2236	2236	171.2	2236	2236

Table 3. Results for the first prototype at $RPM_{nominal}$.

Pressure Difference (bar)	ND	Sensor 1			Sensor 2			Sensor 3		
		Amplitude (μm)	f_{os} (Hz)	f_{disk} (Hz)	Amplitude (μm)	f_{os} (Hz)	f_{disk} (Hz)	Amplitude (μm)	f_{os} (Hz)	f_{disk} (Hz)
2.2	5	4	2358	2233	2.2	2358	2233	5.2	2358	2233
2.3	5	15.5	2358	2233	2.2	2358	2233	45.1	2358	2233
2.4	5	33	2357	2232	3.5	2357	2232	32.7	2357	2232
2.5	5	67.4	2122	2247	41.4	2122	2247	58	2122	2247
2.6	4	180.3	1474	1574	105.8	1474	1574	185.7	1474	1574

Table 4. Results for the first prototype at 1.5 × $RPM_{nominal}$.

Pressure Difference (bar)	ND	Sensor 1			Sensor 2			Sensor 3		
		Amplitude (μm)	f_{os} (Hz)	f_{disk} (Hz)	Amplitude (μm))	f_{os} (Hz)	f_{disk} (Hz)	Amplitude (μm)	f_{os} (Hz)	f_{disk} (Hz)
2.1	5	0.1	2413	2230	0.1	2413	2230	0.2	2414	2230
2.2	5	28.7	2415	2232	3.7	2415	2232	28.8	2415	2232
2.3	5	42.4	2414	2231	23.9	2414	2231	42.7	2414	2231
2.4	4	100.9	1434	1580	84.1	1434	1580	124	1434	1580
2.5	4	128.7	1433	1579	77.1	1433	1579	136.6	1433	1579

Table 5. Results for the first prototype at 2 × $RPM_{nominal}$.

Pressure Difference (bar)	ND	Sensor 1			Sensor 2			Sensor 3		
		Amplitude (μm)	f_{os} (Hz)	f_{disk} (Hz)	Amplitude (μm)	f_{os} (Hz)	f_{disk} (Hz)	Amplitude (μm)	f_{os} (Hz)	f_{disk} (Hz)
1.9	5	0.2	2472	2230	0.2	2472	2230	2.8	2473	2231
2	5	0.3	2472	2230	0.2	2472	2230	0.3	2472	2230
2.1	5	25.5	2473	2231	11.1	2473	2231	19.2	2473	2231
2.2	4	44.8	1394	1588	49	1394	1588	67.2	1394	1588
2.3	4	120.4	1394	1588	89.1	1394	1588	125.2	1394	1588

All this information was employed to manufacture an improved design of the disk in a second prototype, which was also tested in the wind tunnel in order to evaluate the improvements in its vibrational behavior. The results of the tests for the second prototype are shown in Tables 6 to 9. Again, all the frequencies provided by the OFSs and the strain gauge match each other for each rotational speed. The optimization of the design of the disk has allowed the achievement of a significant reduction in both the amplitude and the frequency of the vibration. The results for all the sensors can be seen in Table 10. When the disk is not rotating, there is a reduction of about 99% in the vibration amplitude and of 9.5% in its frequency. As the rotational speed increases, the vibration-amplitude reduction decreases down to 20% of the amplitude corresponding to the first prototype, whereas the frequency reduction remains constant at around 24%. In this table, the amplitude reduction for OFS 2 at 2 × $RPM_{nominal}$ and 2.3 bar is negative, because, unexpectedly, an increase in the vibration amplitude for this sensor was measured under those conditions.

Table 6. Results for the second prototype at 0 rpm.

Pressure Difference (bar)	ND	Sensor 1			Sensor 2			Sensor 3		
		Amplitude (μm)	f_{os} (Hz)	f_{disk} (Hz)	Amplitude (μm)	f_{os} (Hz)	f_{disk} (Hz)	Amplitude (μm)	f_{os} (Hz)	f_{disk} (Hz)
2.7	3	1.1	2024	2024	2.5	2024	2024	0.3	2024	2024
2.75	3	0.8	2024	2024	0.6	2024	2024	1.2	2024	2024
2.8	3	4.6	2025	2025	3	2025	2025	4.1	2025	2025
2.85	3	16.1	2025	2025	16.1	2025	2025	83	2025	2025
2.9	3	55	2025	2025	184	2025	2025	31.6	2025	2025

Table 7. Results for the second prototype at $RPM_{nominal}$.

Pressure Difference (bar)	ND	Sensor 1			Sensor 2			Sensor 3		
		Amplitude (μm)	f_{os} (Hz)	f_{disk} (Hz)	Amplitude (μm)	f_{os} (Hz)	f_{disk} (Hz)	Amplitude (μm)	f_{os} (Hz)	f_{disk} (Hz)
2.7	3	83.6	1116	1191	63	1116	1191	67.8	1116	1191
2.75	3	294.6	1114	1189	176.1	1114	1189	248.3	1114	1189
2.9	3	119.3	1118	1193	73.8	1118	1193	81.2	1118	1193
2.95	3	151	1118	1193	98.2	1118	1193	110.1	1118	1193
3	3	179.6	1117	1192	90.5	1117	1192	126.6	1117	1192

Table 8. Results for the second prototype at 1.5 × $RPM_{nominal}$.

Pressure Difference (bar)	ND	Sensor 1			Sensor 2			Sensor 3		
		Amplitude (μm)	f_{os} (Hz)	f_{disk} (Hz)	Amplitude (μm)	f_{os} (Hz)	f_{disk} (Hz)	Amplitude (μm)	f_{os} (Hz)	f_{disk} (Hz)
2.5	3	97.1	1085	1195	49.5	1085	1195	80.6	1085	1195
2.6	3	201	1084	1194	122.3	1084	1194	138.9	1084	1194
2.8	3	138	1088	1198	83.5	1088	1198	94.3	1088	1198
2.9	3	272	1086	1196	193.5	1086	1196	175.6	1086	1196

Table 9. Results for the second prototype at 2 × $RPM_{nominal}$.

Pressure Difference (bar)	ND	Sensor 1			Sensor 2			Sensor 3		
		Amplitude (μm)	f_{os} (Hz)	f_{disk} (Hz)	Amplitude (μm)	f_{os} (Hz)	f_{disk} (Hz)	Amplitude (μm)	f_{os} (Hz)	f_{disk} (Hz)
2.3	3	95.5	1064	1208	131.5	1063	1207	116.5	1063	1207
2.4	3	162.9	1055	1199	114	1063	1207	117.1	1063	1207
2.6	3	96.1	1059	1203	91	1063	1207	83.6	1063	1207
2.7	3	256.6	1057	1201	206.5	1057	1201	151.2	1057	1201

Table 10. Reduction in amplitude and frequency vibration in the second prototype for each optical sensor.

Working Point	Sensor 1		Sensor 2		Sensor 3	
	Amplitude (%)	Frequency (%)	Amplitude (%)	Frequency (%)	Amplitude (%)	Frequency (%)
0 rpm 2.7 bar	98.6	9.48	99.6	9.48	99.8	9.48
$RPM_{nominal}$ 2.6 bar	53.6	24.3	40.4	24.3	63.5	24.3
1.5 × $RPM_{nominal}$ 2.5 bar	24.5	24.3	35.8	24.3	41	24.3
2 × $RPM_{nominal}$ 2.3 bar	20.7	23.9	-47.6	24	6.95	24

To better appreciate the improvement in the second prototype, the amplitude and frequency of the most similar working points for both prototypes have been depicted in Figure 8a,b. The results shown in both figures correspond to the OFS 1.

Another important improvement detected in the second prototype is the absence of changes in the way the disk was vibrating. There was no change in the number of nodal diameters of the disk. The second prototype vibrates with ND = 5 when the disk is not rotating and with ND = 3 for the rest of

rotational speeds, independently of the rotational speed. Therefore, a more uniform and less complex vibrational behavior was achieved for this prototype.

The fact that three OFSs were employed allows us to determine the eccentricity of the disk. The circumference corresponding to the disk was calculated from the three TC measurements provided by each OFS when the disk is static. The lowest pressure difference (2.3 bar) was used to measure the eccentricity, so that the influence of the vibration in the measurement was minimum. The TC value was obtained as the mean value of the signal for an acquisition time of five seconds. The three TC points define a unique circumference, whose equation is easily calculated by solving the following system of equations to find A, B and C. Where x_{OFSi} and y_{OFSi} are the values obtained by subtracting the TC variation measurement of each sensor from the initial distance of the disk.

$$x_{OFS1}^2 + y_{OFS1}^2 + Ax_{OFS1} + By_{OFS1} + C = 0 \quad (5)$$

$$x_{OFS2}^2 + y_{OFS2}^2 + Ax_{OFS2} + By_{OFS2} + C = 0 \quad (6)$$

$$x_{OFS3}^2 + y_{OFS3}^2 + Ax_{OFS3} + By_{OFS3} + C = 0 \quad (7)$$

The eccentricity of the disk was determined in three different positions: the TC measurements were acquired with the disk in an initial position of 0 °and with the disk rotated 90 °and 202.5 °with respect to this initial position. Figure 9a depicts the results for the three positions of the disk. As expected, the differences between the circumferences are very small. Their corresponding centers differ from the theoretical one in less than 0.65 mm, as can be seen in Figure 9b. This distance means a shift of the center of about 0.2% of the circumference radius, which makes it quite difficult to distinguish each circumference in Figure 9a.

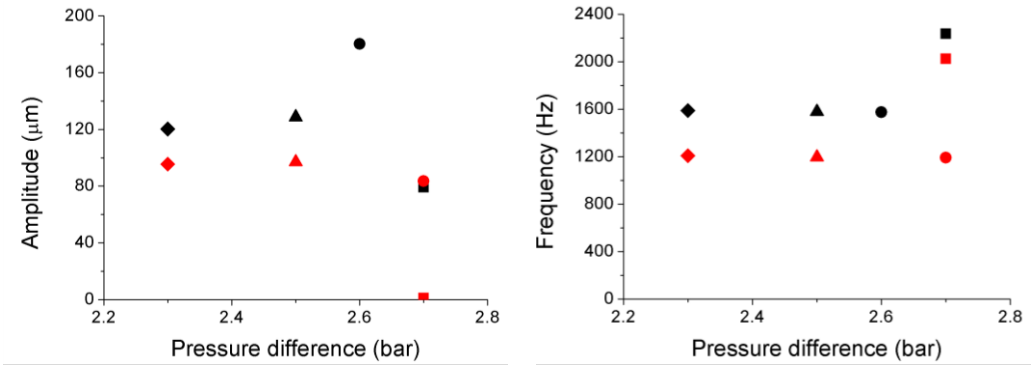

Figure 8. Vibration amplitude (**a**) and frequency (**b**) for the first Prototype (black) and the second Prototype (red) obtained by OFS 1 for the most similar working points (squares correspond to 0 rpm, circles to $RPM_{nominal}$, triangles to 1.5 × $RPM_{nominal}$ and diamonds to 2 × $RPM_{nominal}$).

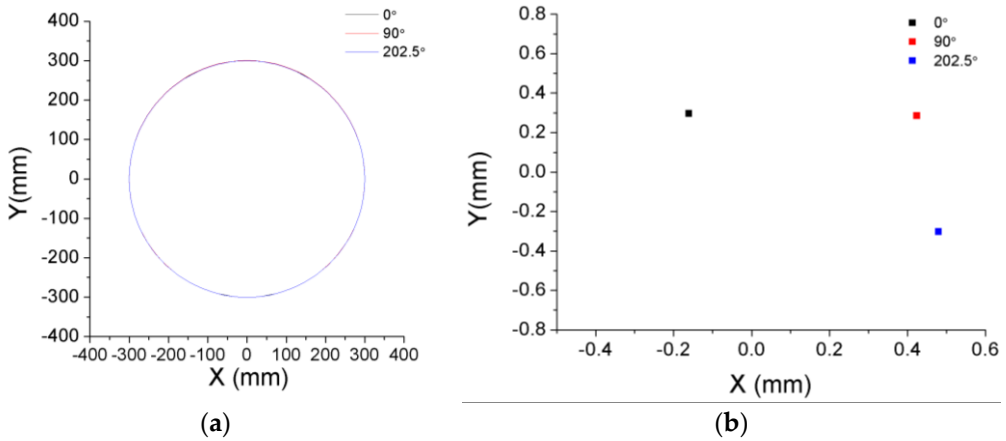

Figure 9. Disk circumferences calculated from the TC measurements of the three OFSs at three different turning positions: 0 °, 90 °, 202.5 °(**a**); Positions of the centers of the circumferences (**b**).

4. Conclusions

The vibrational behavior of a rotating disk has been studied from the tip-clearance measurements provided by three optical fiber sensors. This disk is a model of a real aircraft engine component. It was installed in a wind tunnel, where real working conditions were simulated. Although the sensors were initially designed to perform the TC measurements in low pressure turbines, the configuration was adapted to successfully perform these measurements in the rotating disk. A first prototype of the disk was completely characterized by identifying not only the amplitude and frequency of the vibration, but also the number of nodal diameters of the disk and its variations during the tests. All this valuable information allowed the disk manufacturer to design an upgraded prototype of the disk. This, in turn, was also characterized by examining its vibrational behavior in order to assess the improvements in performance. The obtained results have confirmed a clear improvement in the design of the component. Therefore, the suitability of this innovative optical system both to characterize and to improve rotating disks has also been demonstrated.

Acknowledgments: This work has been funded in part by the Fondo Europeo de Desarrollo Regional (FEDER); by the Ministerio de Economía y Competitividad under project TEC2015-638263-C03-1-R; by the Gobierno Vasco/Eusko Jaurlaritza under projects IT933-16 and ELKARTEK (KK-2016/0030 and KK-2016/0059) and by the University of the Basque Country UPV/EHU under program UFI11/16.

Author Contributions: Iker García, Gaizka Durana, Josu Beloki, and Joseba Zubia conceived and designed the experiments; Iker García, Gotzon Aldabaldetreku and Josu Beloki performed the experiments; Iker García, and Jon Arrue performed the sensor calibration, Iker García, Gaizka Durana, and Josu Beloki analyzed the data; Iker García, Gotzon Aldabaldetreku and Jon Arrue wrote the paper. Joseba Zubia supervised the whole project.

Conflicts of Interest: The authors declare no conflict of interest.

References

1. Huang, X.Y.; Hoque, M.E.; Wang, X. An experimental study on feedback control of rotating disk flutter. *J. Fluids Struct.* **2005**, *20*, 71–80.
2. Judge, J.; Pierre, C.; Mehmed, O. Experimental investigation of mode localization and forced response amplitude magnification for a mistuned bladed disk. *J. Eng. Gas Turbines Power* **2001**, *123*, 940–950.
3. Castellini, P.; Paone, N. Development of the tracking laser vibrometer: Performance and uncertainty analysis. *Rev. Sci. Instrum.* **2000**, *71*, 4639–4647.
4. Kuschmierz, R.; Filippatos, A.; Günther, P.; Langkamp, A.; Hufenbach, W.; Czarske, J.; Fischer, A. In-process, non-destructive, dynamic testing of high-speed polymer composite rotors. *Mech. Syst. Signal Proces.* **2015**, *54*, 325–335.
5. Clem, M.M.; Woike, M.R.; Abdul-Aziz, A. Investigation of a cross-correlation based optical strain measurement technique for detecting radial growth on a rotating disk. In Proceedings of the SPIE Smart Structures and Materials + Nondestructive Evaluation and Health Monitoring, San Diego, CA, USA, 11–14 March 2013.
6. García, I.; Zubia, J.; Beloki, J.; Arrue, J.; Villatoro, J. Evaluation of the vibrational behaviour of a rotating disk by optical tip-clearance measurements. In Proceedings of the SPIE Optical Metrology, Munich, Germany, 22–25 June 2015.
7. García, I.; Zubia, J.; Beloki, J.; Aldabaldetreku, G.; Durana, G.; Illaramendi, M.A. Optical tip clearance measurements for rotating disk characterization. In Proceedings of the 17th International Conference on Transparent Optical Networks (ICTON), Budapest, Hungary, 5–9 July 2015.
8. Heermann, K.F.; Kriksson, R.H.; McClure, K.R. *Study to Improve Turbine Engine Rotor Blade Containment*; Pratt and Whitney Aircraft Group: East Hartford, CT, USA, 1977.
9. Zhou, G.; Sim, L.M. Damage detection and assessment in fibre-reinforced composite structures with embedded fibre optic sensors-review. *Smart Mater. Struct.* **2002**, *11*, 925–939.
10. Güemes, A. SHM technologies and applications in aircraft structures. In Proceedings of the 5th International Symposium on NDT in Aerospace, Singapore, 13–15 November 2013.
11. Gholamzadeh, B.; Nabovati, H. Fiber optic sensors. *World Acad. Sci. Eng. Technol.* **2008**, *42*, 335–340.
12. García, I.; Zubia, J.; Durana, G.; Aldabaldetreku, G.; Illarramendi, M.A.; Villatoro, J. Optical Fiber Sensors for Aircraft Structural Health Monitoring. *Sensors* **2015**, *15*, 15494–15519.

13. García, I.; Beloki, J.; Zubia, J.; Aldabaldetreku, G.; Illarramendi, M.A.; Jiménez, F. An Optical Fiber Bundle Sensor for Tip Clearance and Tip Timing Measurements in a Turbine Rig. *Sensors* **2013**, *13*, 7385–7398.
14. García, I.; Przysowa, R.; Amorebieta, J.; Zubia, J. Tip-Clearance Measurement in the First Stage of the Compressor of an Aircraft Engine. *Sensors* **2016**, *16*, 1897.
15. Wiseman, M.W.; Guo, T.-H. An Investigation of Life Extending Control Techniques for Gas Turbine Engines. In Proceedings of the American Control Conference, Arlington, VA, USA, 25–27 June 2001.
16. Gyekenyesi, A.L.; Sawicki, J.T.; Martin, R.E.; Haase W.C.; Baaklini, G. Vibration Based Crack Detection in a Rotating Disk. Part 2; Experimental Results. Available online: http://ntrs.nasa.gov/search.jsp?R=20130013094 (accessed on 15 August 2015).
17. Shubov, M.A. Flutter phenomenon in aero elasticity and its mathematical analysis. *J. Aerosp. Eng.* **2006**, *19*, 1–12.
18. Vázquez, R.; Iturregui, J.J.; Arsuaga, M.; Armañanzas, L. A New Transonic Test Turbine Facility. In Proceedings of the XVI International Symposium on Air Breathing Engines (ISABE), Cleveland, OH, USA, 31 August–5 September 2003.
19. García, I.; Beloki, J.; Zubia, J.; Durana, G.; Aldabaldetreku, G. Turbine-blade tip clearance and tip timing measurements using an optical fiber bundle sensor. In Proceedings of the SPIE Optical Metrology, Munich, Germany, 13–16 May 2013.
20. García, I.; Zubia, J.; Berganza, A.; Beloki, J.; Arrue, J.; Illarramendi, M.A.; Mateo, J.; Vazquez, C. Different configurations of a reflective intensity-modulated optical sensor to avoid modal noise in tip-clearance measurements. *J. Lightwave Technol.* **2015**, in press.
21. Ma, Y.; Li, G.; Zhang, Y.; Liu, H. Tip Clearance Optical Measurement for Rotating Blades. In Proceedings of the International Conference on Management Science and Industrial Engineering (MSIE), Harbin, China, 8–9 January 2011.
22. Non-Intrusive Stress Measurement Systems. Available online: http://agilis.com/documents/NSMS.pdf (accessed on 3 June 2015).

Artículo 5

Tip-Clearance Measurement in the First Stage of the Compressor of an Aircraft Engine.

García, I., Przysowa, R., Amorebieta, J., & Zubia, J.

Sensors, *16*(11), 1897 (2016).

sensors

MDPI

Article

Tip-Clearance Measurement in the First Stage of the Compressor of an Aircraft Engine

Iker García [1,*], Radosław Przysowa [2], Josu Amorebieta [1] and Joseba Zubia [1]

[1] Department of Communications Engineering, Engineering School of Bilbao, University of the Basque Country UPV/EHU, Alda. Urquijo s/n E-48013 Bilbao, Spain; jamorebieta001@ikasle.ehu.eus (J.A.); joseba.zubia@ehu.eus (J.Z.)

[2] Air Force Institute of Technology (Instytut Techniczny Wojsk Lotniczych), ul. Ksiecia Boleslawa 6 01-494 Warszawa, Poland; radoslaw.przysowa@itwl.pl

* Correspondence: iker.garciae@ehu.eus; Tel.: +34-946-017-305

Academic Editor: Jose Miguel López Higuera

Received: 30 September 2016; Accepted: 4 November 2016; Published: 11 November 2016

Abstract: In this article, we report the design of a reflective intensity-modulated optical fiber sensor for blade tip-clearance measurement, and the experimental results for the first stage of a compressor of an aircraft engine operating in real conditions. The tests were performed in a ground test cell, where the engine completed four cycles from idling state to takeoff and back to idling state. During these tests, the rotational speed of the compressor ranged between 7000 and 15,600 rpm. The main component of the sensor is a tetrafurcated bundle of optical fibers, with which the resulting precision of the experimental measurements was 12 μm for a measurement range from 2 to 4 mm. To get this precision the effect of temperature on the optoelectronic components of the sensor was compensated by calibrating the sensor in a climate chamber. A custom-designed MATLAB program was employed to simulate the behavior of the sensor prior to its manufacture.

Keywords: tip clearance; optical fiber sensor; aircraft engine; optical fiber bundle; compressor

1. Introduction

The development of more and more efficient aircraft engines is a continuous challenge that provides several benefits. In addition to monetary profit, carbon-emission reductions, longer service lives, and flight-range capabilities of the aeroplanes are improved, thanks to the reduction of fuel burnt [1]. The performance of the engine can be significantly improved by minimizing the leak flows through the gap between the blade tip and the casing of the compressor or the turbine. Therefore, this distance, known as tip clearance (TC), plays a major role in the aerodynamic efficiency of axial compressors and turbines [2]. The TC value varies with the operation condition of the engine (ground idle, takeoff, cruise, and landing) [3], as well as with the engine aging [4]. These fluctuations of the TC are due to two types of loads, namely engine and flight loads. The first kind of load encompasses centrifugal, thermal, internal engine pressure, and thrust loads, whereas flight loads are comprised by inertial (gravitational), aerodynamic (external pressure), and gyroscopic loads [5].

An accurate and real-time TC measurement is necessary to prevent any blade contacting with the casing and to lessen the leak flows in the fan, compressor, and turbine sections of the engines, which serves to optimize the engine performance. That is, precisely, the purpose of active-clearance control systems, in which the TC is limited by directing air to the casing by means of valves to control the thermal expansion of the casing, and to keep the TC to a minimum so that the engine efficiency increases. In contrast with power-system turbines where TC common values range from 2 to 8 mm, in aircraft turbines TC values are usually lower than 3 mm [6], so a resolution better than 25 μm is required for the whole measurement interval [7]. Currently, several kinds of sensors are employed to

carry out TC measurements. The most common method is the employment of capacitive sensors [8,9]. These sensors are robust, small, and low-cost, but their accuracy is limited to 30 μm [10]. Microwave sensors have also been employed for TC measurements [11,12]. Since their signal depends on several variables, they require a complex calibration and advanced processing of signals. Besides, they provide a limited spatial resolution as compared to optical sensors, and it is not an economical technology [13]. Another option are eddy-current (inductive) sensors, which have the advantage of not requiring a direct view of the blade tip, so the sensor is not exposed to the harsh conditions of the engine [14], but their calibration is highly dependent on the tip shape and temperature [15]. Finally, optical sensors offer multiple inherent advantages [16] and that is the reason why they are being more and more employed in the aircraft industry [17–19]. Regarding TC measurement, optical sensors yield the best resolution. On the contrary, they are seriously affected by contamination and debris, thus being suitable only for the clean parts of the engine such as the fan and the compressor, or for the testing of rigs during the engine-development phase [20].

Optical sensors for TC measurements have been developed by using diverse techniques such as Doppler positioning [21] or interferometry [22]. Nevertheless, the simplest and most affordable devices to obtain high accuracy [23] and bandwidth are intensity-based sensors [24,25]. Several configurations of intensity-modulated sensors using trifurcated bundles for TC measurements have been previously proposed by other authors [15,26,27]. However, their performances were demonstrated only in laboratory conditions and using a rig instead of a real engine. In addition to this, their measurement ranges and stand-off distances are not suitable for measurements in real engines. In this paper, we present the results obtained for an intensity-based sensor whose principal component is a tetrafurcated bundle of optical fibers. It was specifically designed to carry out tip clearance and tip timing measurements in a compressor of a real engine in a simultaneous and independent way. In Section 2, the experimental set-up and the sensor design are explained. In Section 3, the results obtained in the compressor of a real aircraft engine are presented and discussed. The conclusions of the work are summarized in Section 4.

2. Materials and Methods

2.1. Sensor Design

In previous works, we developed a reflective intensity-modulated optical fiber sensor to carry out TC measurements in turbines [20] and rotating components of aircraft engines [28]. The essential component of this sensor was a bundle of optical fibers. We used to employ trifurcated bundles, with one common leg on one side and three independent legs on the other. One of these legs was connected to a light source (illuminating fiber), and the other two legs were connected to their respective photodetectors (receiving fibers). The illuminating fiber was located in the center of the common leg and the light emitted by this fiber was reflected by the target and collected by two rings of receiving fibers surrounding the illuminating fiber. Each ring of receiving fibers was gathered into a leg on the other end of the bundle, which was connected to a photodetector in order to convert the optical signals into an electrical one. Finally, the quotient of these two voltage signals (V_1 and V_2) was related to the distance of the target by a linearized calibration curve as the one shown in Figure 1 (for a more detailed explanation of the sensor operation see [20,29]).

With respect to the works of other groups, we introduced two important improvements in the sensor design [29]. Firstly, we used a single-mode fiber as illuminating fiber to reduce the modal noise at the output of the bundle. The second improvement was the employment of asymmetric gain for the photodetectors, which increases the sensitivity of the sensor. The resulting sensitivity was more than the double of the sensitivity obtained using a configuration of symmetric gain as it is shown in [29]. In the calibration curve depicted in Figure 1, two different regions can be distinguished. The region I (front-slope region) provides more sensitivity than the region II (back-slope region). In addition, the region I is less sensitive to noise since the amplitudes of V1 and V2 have higher values than those

of the region II. On the other hand, the measurement range from 1 to 1.6 mm may be too short and it requires placing the bundle tip very close to the blades. In previous tests, we employed the region II due to these constraints. However, in this occasion we decided to make some changes in the bundle design so that the most sensitive region I could be used for the tests.

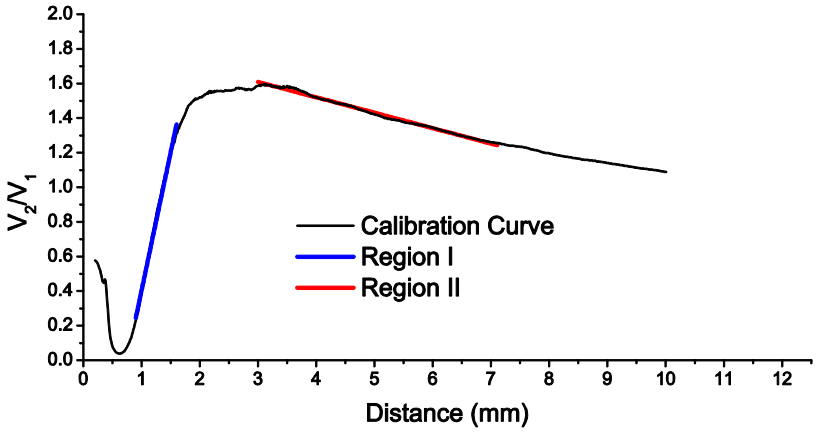

Figure 1. Typical calibration curve for a sensor using a trifurcated bundle of optical fibers.

Once the sensor was assembled in the casing of the engine, the required measurement range for the TC was estimated to be the interval from 2 to 4 mm. Therefore, the first necessary variation in the bundle design consists in shifting the measurement range so that it starts at 2 mm. The beginning of region I is determined by the target distance in which the reflected light starts to enter the second ring of receiving fibers, so the distance between the center of the illuminating fiber and the fibers of the second ring of receiving fibers was increased in the new design. To take this ring away, we could have chosen the option of inserting a considerable number of needles between the first and second rings of receiving fibers until achieving the required distance, but we decided to insert fewer needles and to introduce another ring of receiving fibers. The fibers of this ring were gathered in another independent leg, so what we have is a tetrafurcated bundle (see Figure 2). This leg allows carrying out tip-timing measurements with another photodetector whose gain, and therefore whose bandwidth, is not dependent on the gain of the photodetectors used for the TC configuration [30]. The common leg of the bundle has a threaded head to facilitate its coupling to the casing of the engine, whereas the legs on the other side have conventional FC connectors.

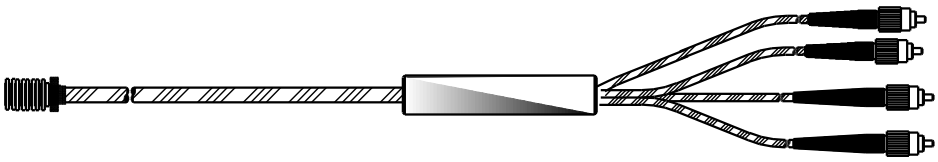

Figure 2. Tetrafurcated bundle employed in the TC optical sensor.

The second necessary variation in the bundle design consists in widening the measurement range of the region I. We could modify two characteristics of the optical fibers in order to get this objective. The first option is to use an illuminating fiber with a lower numerical aperture. The upper limit of the measurement range for the region I is determined by the distance of the target in which the reflected-light cone completely covers the second ring of receiving fibers. Thus, the measurement range becomes higher as the numerical aperture of the illuminating fiber becomes smaller, as illustrated in Figure 3. Since a single-mode fiber with a numerical aperture of 0.12 is employed as illuminating fiber, there is little margin to reduce it. The other option to extend the range is to increment the diameter of the receiving fibers so that the target distance can be greater before the second ring is completely

covered by the reflected light. The effect of increasing the diameter of the receiving fibers is depicted in Figure 4.

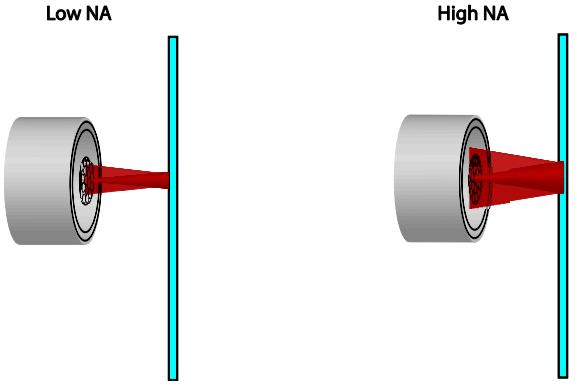

Figure 3. Effect of the variation of the numerical aperture of the illuminating fibers over the reflected-light cone.

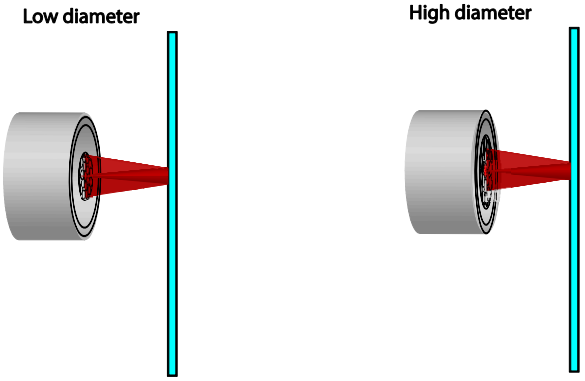

Figure 4. Effect of the variation of the diameter of the receiving fibers.

Based on our previous experience, we finally decided to employ the fibers of the manufacturer Fiberguide Industries shown in Figure 5, where R1 = 300 µm, R2 = 700 µm, and R3 = 1070 µm. In the same figure, a microscope picture of the cross section of the manufactured bundle is also depicted. The final distances in our manufactured bundle were R1 = 324 µm, R2 = 686 µm, and R3 = 1125 µm, somewhat different from the design radius.

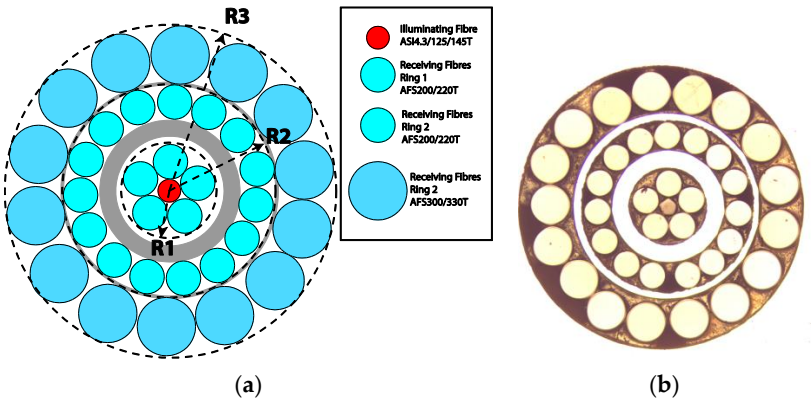

(**a**) (**b**)

Figure 5. Initial design (**a**) of the bundle of optical fibers and a microscope picture (**b**) of the cross section of the common leg in the manufactured bundle.

Before manufacturing the bundle, we developed a MATLAB program in order to verify the behavior of the sensor. This software was developed according to the theoretical models described in literature [23,31–33]. As all these papers assume that the target is a mirror instead of a blade, we adjusted the parameters of the reflected light in order to get more realistic results. This parameter optimization was achieved by performing several experimental measurements using the trifurcated bundles we have in our laboratory. Figure 6 depicts the experimentally obtained calibration curve for the sensor employing the tetrafurcated bundle in the region I, together with the simulation. Table 1 shows the distance differences between the two curves for the same values of V_2/V_1 obtained along the measurement range. We can see that the simulation provides good results except for the last part of the measurement range, where the distance difference increases significantly.

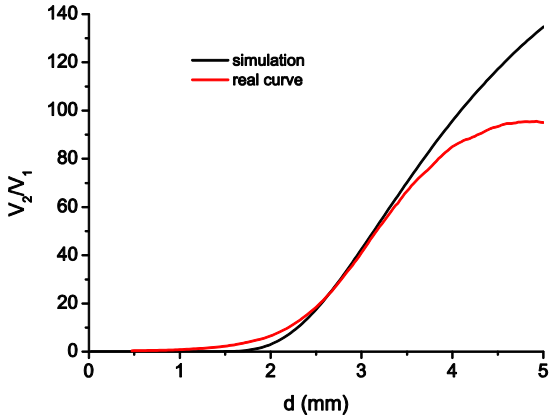

Figure 6. Simulated calibration curve and real calibration curve for the sensor using the tetrafurcated bundle.

Table 1. Comparison between distances obtained using the real and simulated calibration curve.

V_2/V_1	Simulation Distance (mm)	Experimental Distance (mm)	Difference (mm)
20	2.575	2.55	0.025 (1%)
30	2.775	2.78	−0.005 (−0.2%)
40	2.97	3	−0.03 (−1%)
50	3.15	3.175	−0.025 (−1.1)
60	3.325	3.375	−0.05 (−1.5%)
70	3.5	3.6	−0.1 (−2.8%)
80	3.7	3.875	−0.175 (−4.37%)
90	3.9	4.325	−0.425 (−10.9%)

The rest of the components of the sensor are depicted in Figure 7. A laser module from Frankfurt Components (HSML-0660-20-FC, Frankfurt Laser Company, Friedrichsdorf, Germany) was employed as source of light. It has a nominal output power of 20 mW at 660 nm. An optical isolator (IO-F-660 from Thorlabs, Newton, NJ, US) was placed between the laser and the bundle in order to avoid any possible reflection that could destabilize the light source. Finally, the photodetectors employed were PDA100A-EC ones from Thorlabs. Photodetectors 1 and 2 were employed for TC measurements with transimpedance gains of 1.51×10^3 V/A (BW = 1.5 MHz) and 1.51×10^5 V/A (BW = 60 kHz), respectively. Photodetector 3 was used for tip timing measurements and its gain was 4.75×10^4 V/A (BW = 200 kHz).

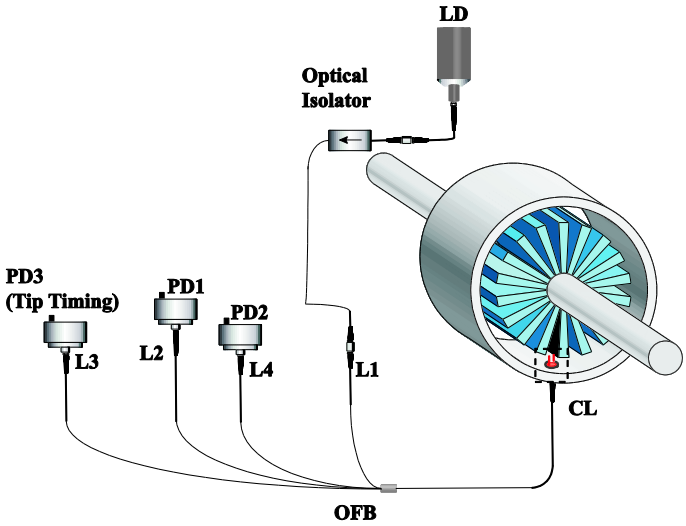

Figure 7. Components of the optical fiber sensor for TC measurements. LD stands for Laser Diode, PDx for Photodetector x, Lx for Leg x, CL for Common Leg and OFB for optical fiber bundle.

Regarding the calibration of the sensor, we employed a linear translation stage and we followed a procedure similar to our previous works [20]. Since it was impossible to use a compressor blade for the calibration process, the most similar blade available in our laboratory was employed. The ambient temperature of the test cell was expected to be quite low (5–10 °C), so we checked the effect of the temperature on the calibration curve of the sensor. We introduced all the sensor components in a climate chamber and we carried out two calibrations at 20 °C and 10 °C. The resulting curves and their linearization for the measurement range are depicted in Figure 8. Even though the distance difference to the linearized calibration curve was quite small at the beginning of the measurement range, it reached 100 µm in the last part of the measurement range, so we employed the calibration obtained at 10 °C for the tests.

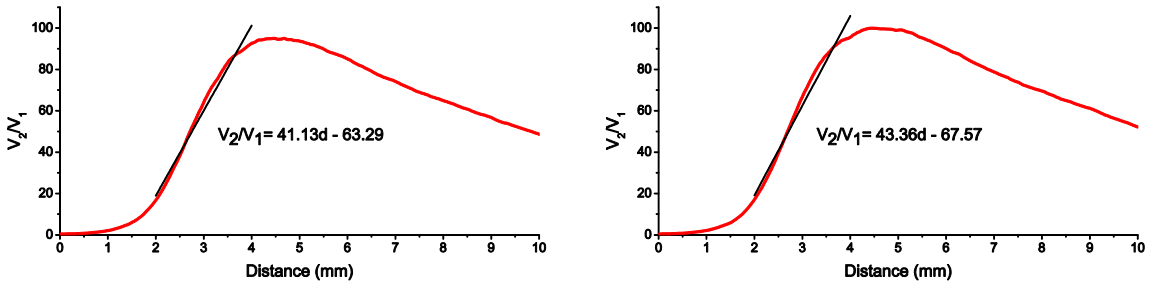

Figure 8. Calibration curves for 20 °C (**Left**) and 10 °C (**Right**).

2.2. Experimental Set-up

The performance of the optical sensor was tested in the SO-3 engine that is employed to power the TS-11 "Iskra" combat jet trainer. Its compressor is composed of seven stages and the optical sensor was installed in the first one. This stage has 28 blades made of 18H2N4WA steel, with a length of 100 mm, a chord of 37 mm, and a maximum width of 1.5 mm. The surface of the blade is rough and it usually presents some corrosion which makes the measuring more difficult. The tests were performed on the test cell that the Air Force Institute of Technology has in Warsaw. Figure 9 depicts the upper view of the blade and the engine in the test cell.

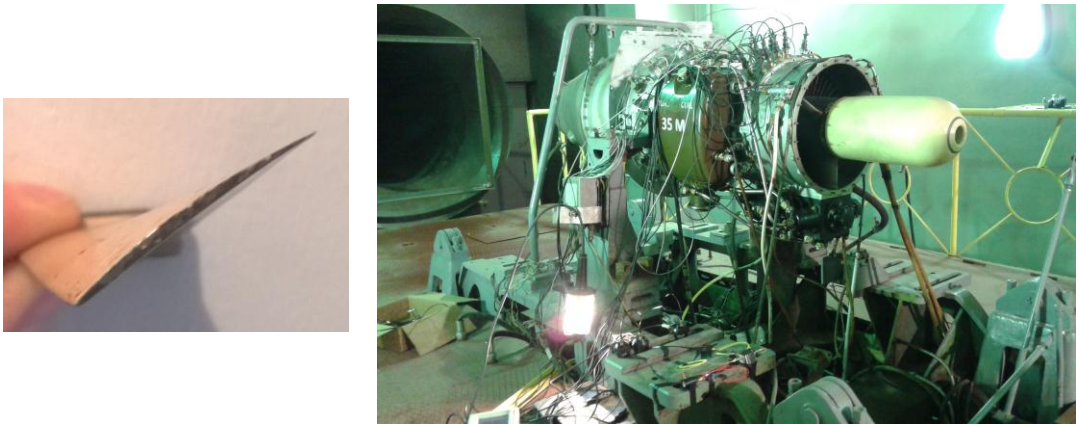

(**a**) (**b**)

Figure 9. (**a**) Upper view of a blade of the first stage of the compressor; (**b**) SO-3 engine in the test cell with the optical sensor installed in its casing.

A special bracket was designed to fix the tip of the bundle in the casing of the engine. The tip of the bundle was placed at an approximated distance of 3 mm from the blade tip. Both the bracket and the final arrangement of the bundle in the area of the casing corresponding to the first stage of the compressor can be observed in Figure 10. At this part of the engine the gas temperature is approximately the same as the ambient temperature. The rotational speed of the engine is dependent on the operation condition of the engine, and the revolutions per minute (rpm) of the rotor range from 6900 rpm in idling condition to a maximum of 15,600 rpm during the takeoff.

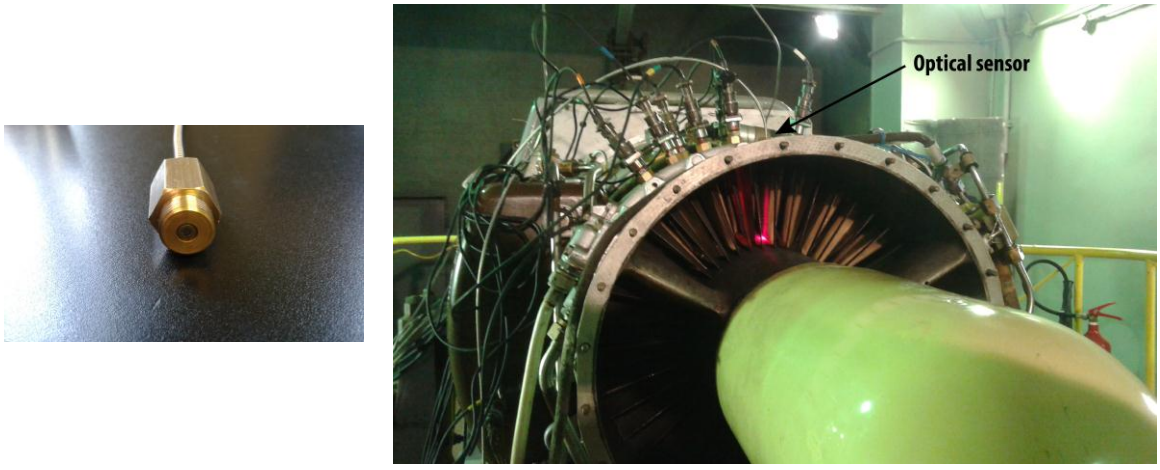

(**a**) (**b**)

Figure 10. (**a**) Bracket employed to fix the bundle to the casing of the engine; (**b**) Bundle of optical fibers installed in the casing. Several inductive sensors for tip-timing measurements were also installed in the casing.

The signals provided by the photodetectors are very sharp due to the small thickness of the blades, and their amplitudes are quite different for each of the blades, as can be seen in Figure 11. Whereas V_1 is around 100 mV, certain blades produce peaks of several volts in V_2. Therefore, we had to use two different PXIe-6358 data-acquisition modules (from National Instruments, Austin, TX, United States) in order to take advantage of the 16-bit resolution of each module. The sampling frequency for the signal acquisition was 500 kS/s.

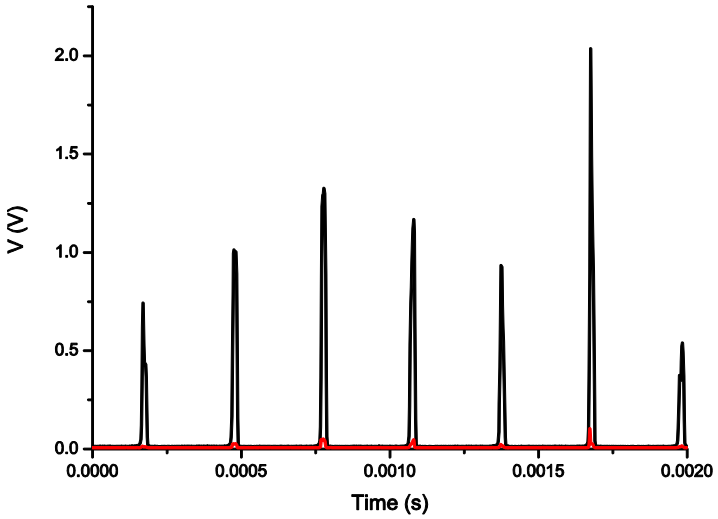

Figure 11. Signals obtained from both photodetectors, V_1 (**Red**) and V_2 (**Black**), when the engine was in idling state.

3. Results

The tests consisted of four complete cycles in which the engine ran from idling operational state to takeoff and back to idling state again. The starting and final rotational speed was approximately 7000 rpm and the maximum speed reached during takeoff was 15,600 rpm. In our first and the third cycle the engine acceleration and deceleration were linear, the rotational speed increased continuously up to 15,600 rpm and then decreased back to idling state. In our second and fourth cycle the rotational speed increased in steps of about 1000 rpm (see Figure 12b), whereas the deceleration was linear as in the other cycles. The flight profile for the cycles 1 and 2 are shown in Figure 12.

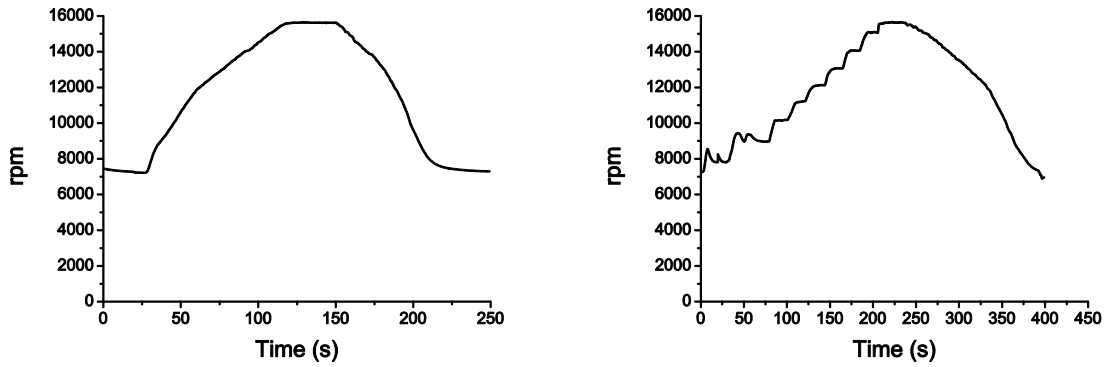

Figure 12. Flight profile for the cycles 1 (**a**) and 2 (**b**).

During each cycle, three signals were acquired: the OPR (Once Per Revolution) signal and the signals corresponding to the outputs of the photodetectors, V_1 and V_2. These signals were stored and post-processed off-line using a LabVIEW program designed specifically for the analysis of TC measurements using the sensor. The program divides the whole acquisition in individual revolutions making use of the OPR signal. In this way, it can evaluate the quotient V_2/V_1 during one revolution and find the TC values for each of the 28 blades of the compressor. The minimum of such values is considered as the TC for that revolution. To calculate the TC value for each blade, the calibration curve in Figure 8 is employed to convert the value of the quotient V_2/V_1 into distance. In Figure 13 the three signals (OPR, V_1 and V_2) are depicted at 7600 rpm and at 15,600 rpm. For the sake of clarity,

the amplitude of the signal V_1 has been magnified by a factor of 10. In this figure, it is clearly seen that the amplitude of the signals becomes higher as the rotational speed increases. This is due to the fact that the faster the engine is turning, the closer the blades are to the casing and the higher is the reflected light intensity that reaches the bundle of optical fibers.

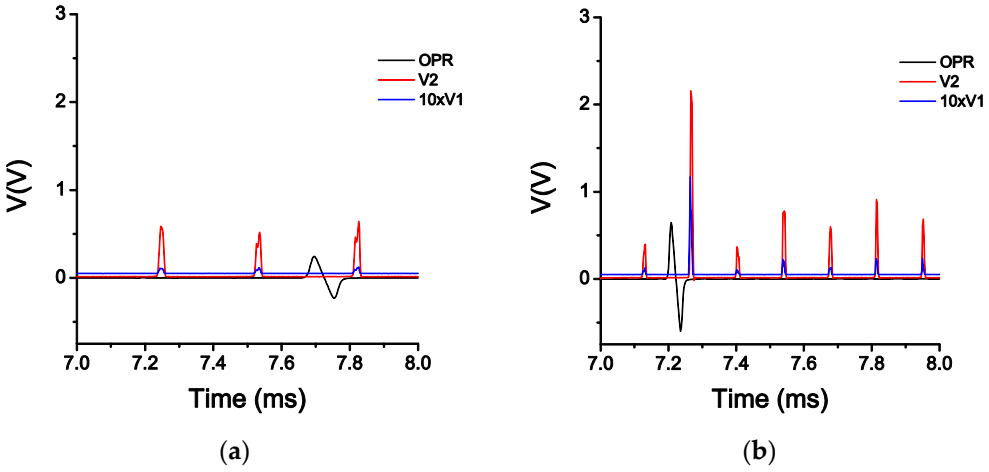

Figure 13. OPR, V_1 ($\times$10) and V_2 signal during the Cycle 1 at 7600 rpm (**a**) and at 15,600 rpm (**b**).

In Table 2 the TC measurements during the acceleration of the cycles 1 and 3 are shown. In order to calculate the TC at each rotational speed, an interval of 0.2 s (100,000 samples) was considered as a "constant-speed" interval. The rotational speed in each measurement is the average of the interval. In both cycles, the TC decreases as the rotational speed increases showing a reasonable behavior. The results for the TC values are quite similar during both acceleration cycles, being the most significant differences between 12,000 and 15,000 rpm. In the case of 15,000 rpm, the sensor shows a maximum difference of 96 µm.

Table 2. TC values during the acceleration of the cycles 1 and 3.

rpm	TC Cycle 1 (mm)	rpm	TC Cycle 3 (mm)
7226	2.355	7126	2.359
7960	2.332	8060	2.339
9003	2.327	9072	2.331
10,025	2.317	10,025	2.320
11,229	2.308	11,078	2.290
12,041	2.285	12,089	2.253
13,064	2.249	13,080	2.213
14,112	2.232	14,059	2.163
15,321	2.216	15,098	2.120
15,603	2.115	15,567	2.114

In Table 3, we can observe the results during the acceleration of the cycles 2 and 4. In these cases the transition from idling state to takeoff is accomplished in steps of 1000 rpm approximately. These cases yield longer intervals in which the rotational speed is constant, so we decided to employ 0.6-s intervals (300,000 samples) to determine the TC at each speed. The behavior of the sensor is correct during both cycles, and the maximum TC difference between the cycles is 24 µm. In Figure 14, the measurements during the four cycles have been plotted. Except for the case of the first cycle in the range from 12,000 to 15,000 rpm, the TC measurement exhibits the same evolution in all cycles and the sensor provides similar TC values for all the speeds of each cycle.

Table 3. TC values during the acceleration of the cycles 2 and 4.

rpm	TC Cycle 2 (mm)	rpm	TC Cycle 4 (mm)
7265	2.343	7124	2.341
8533	2.341	8051	2.325
9406	2.323	9293	2.311
10,147	2.316	10,284	2.306
11,174	2.288	11,259	2.280
12,092	2.265	11,980	2.245
13,068	2.225	12,997	2.209
14,055	2.183	14,006	2.159
15,096	2.128	15,047	2.117
15,635	2.106	15,617	2.103

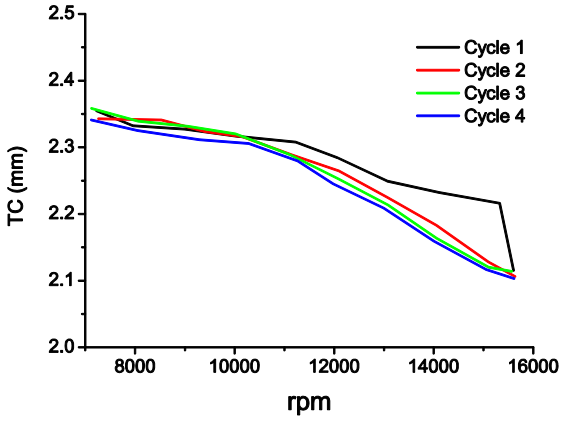

Figure 14. TC measurements in the four cycles during acceleration from idling state to takeoff.

In Table 4, the TC values obtained during the engine deceleration in every cycle are depicted. For all cases, the deceleration is linear, and the evolution of the measurement is shown in Figure 15. As can be seen in the graph, the four cycles behave in a highly analogous way, yielding a maximum difference of 23 µm among the measurements, which is very similar to the previous case.

Table 4. TC values during the deceleration.

rpm	TC Cycle 1 (mm)	rpm	TC Cycle 2 (mm)
14,998	2.139	15,049	2.116
14,001	2.171	14,039	2.152
13,030	2.207	13,028	2.203
12,050	2.253	12,009	2.256
10,941	2.293	10,996	2.283
10,028	2.317	10,006	2.315
9006	2.331	9024	2.342
8069	2.347	8004	2.354
7281	2.359	7226	2.358
rpm	**TC Cycle 3 (mm)**	**rpm**	**TC Cycle 4 (mm)**
15,055	2.117	15,039	2.117
14,007	2.151	14,028	2.151
13,022	2.192	13,043	2.202
11,997	2.245	11,997	2.240
11,014	2.274	10,980	2.273
10,006	2.317	10,006	2.315
9005	2.323	8942	2.321
8019	2.340	7962	2.336
6990	2.357	7011	2.351

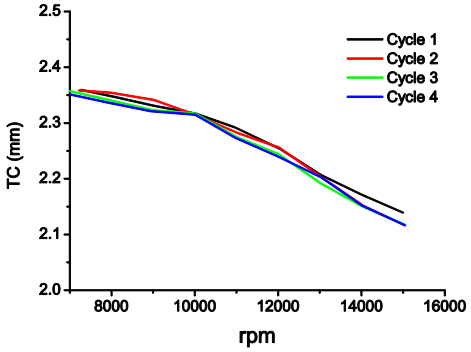

Figure 15. TC measurements in the four cycles during the deceleration from takeoff to idling state.

In Figure 16, the TC values for each revolution of the acceleration in the Cycle 3 have been plotted. In order to help to visualize the TC evolution during the engine acceleration, a smoothed representation of the results is also shown. In Figure 17, the TC measurements of each cycle of acceleration and deceleration are depicted. These charts allow us to verify that there are no apparent signs of hysteresis in the performance of the sensor.

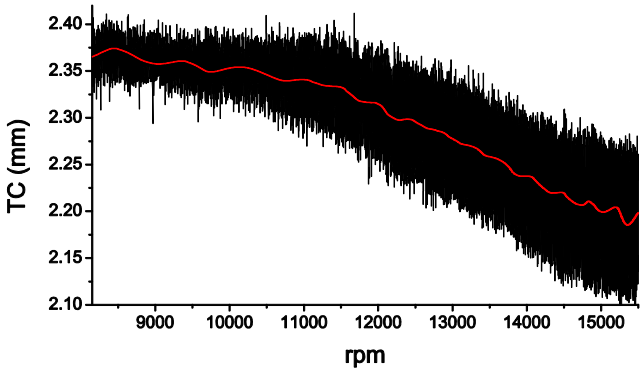

Figure 16. TC measurements for each revolution during the acceleration in the Cycle 3, and a smoothed representation of the results (**red line**).

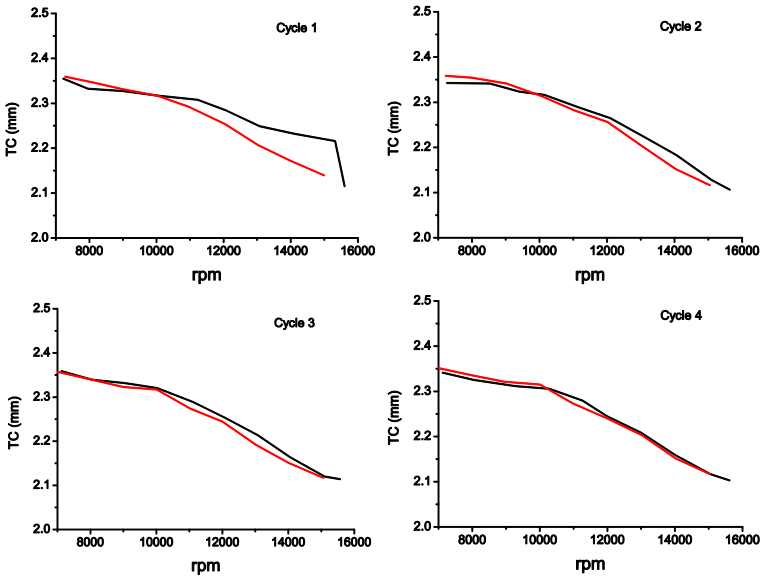

Figure 17. Acceleration (**Black**) and deceleration (**Red**) for each cycle of the engine operation.

Regarding the accuracy of the results, unfortunately no other sensor could be installed to measure TC during the tests. The amplitude of the signals provided by the inductive sensors installed for tip timing measurement depended on speed, and they were not calibrated for tip clearance measurement. Consequently, there is not any reference with which the results can be compared. However, it is worth noting that the laboratory tests carried out prior to the measurements in the test cell with the real engine provided errors lower than 1% in the range of the measurement with a minimum resolution of 1 μm. With respect to the sensor precision, these preliminary tests give us a standard deviation in the laboratory measurements of 2 μm. In order to compare this value with the measurements in the real engine, the TC for each rotational speed has been assigned to nearest value of the rotational speed shown Table 5, in such a way that we have eight values for each rotational speed (except for 15,600 rpm, in which we have only four). As can be observed in Table 5, the maximum value for the standard deviation of all cycles is 34 μm. The Cycle 1 contributes significantly to heighten this value due to the strange behavior of the measurements during the acceleration of this cycle. If we discard this cycle, the maximum standard deviation drops to 12 μm, which is an excellent value if we take into account that the measurements were taken at slightly different rotational speeds.

Table 5. Mean and standard deviations for all the measurements.

rpm	Mean TC (mm)	Mean TC (mm) *	Standard Deviation (μm)	Standard Deviation (μm) *
7000	2.353	2.351	7	8
8000	2.339	2.339	9	9
9000	2.326	2.325	9	10
10,000	2.315	2.315	4	5
11,000	2.286	2.281	11	7
12,000	2.255	2.251	14	9
13,000	2.212	2.207	18	11
14,000	2.170	2.160	27	12
15,000	2.134	2.119	34	5
15,600	2.110	2.108	6	6

* Discarding Cycle 1.

4. Conclusions

The TC measurement for the first stage of a compressor of an aircraft engine was carried out using an optical fiber sensor. The engine in the test cell worked in real conditions. The tests consisted of four cycles from idling state to takeoff and back to idling state. Even though it was no possible to install a reference sensor to compare the accuracy of the results, the sensor showed a correct behavior as regards the variation of the rotational speed. The standard deviation of the measurements, if we discard the Cycle 1 due to its strange behavior in the last part of the acceleration, was 12 μm. This is a notable value if we take into account that the measurements were taken at slightly different speeds and that the conditions were adverse due to the corrosion present on the blades. It is also worth noting the short time needed to calibrate and to install the sensor in the engine, and the feasibility of performing independent tip-timing measurements using the leg three of the optical fiber bundle. In conclusion, a correct behavior of the sensor was demonstrated for the first stage of the compressor in such a way that we can expect similar results in harsher environments as the turbine. In order to get satisfactory results, the high temperature and contamination issues must be correctly tackled with the necessary modifications in the bundle design.

Acknowledgments: This work has been funded in part by the Fondo Europeo de Desarrollo Regional (FEDER); by the Ministerio de Economía y Competitividad under project TEC2015-638263-C03-1-R; by the Gobierno Vasco/Eusko Jaurlaritza under projects IT933-16 and ELKARTEK; and by the University of the Basque Country UPV/EHU under programmes UFI11/16 and Euskampus.

Author Contributions: Iker García, Radosław Przysowa, and Joseba Zubia conceived and designed the experiments; Iker García and Radosław Przysowa performed the experiments; Josu Amorebieta performed the sensor calibration and developed the software to simulate the sensor performance; Iker García and Radosław Przysowa analyzed the data; Iker García and Josu Amorebieta wrote the paper. Joseba Zubia supervised the whole project.

Conflicts of Interest: The authors declare no conflict of interest.

References

1. Vakhtin, A.B.; Chen, S.J.; Massick, S.M. Optical probe for monitoring blade tip clearance. In Proceedings of the 47th AIAA Aerospace Sciences Meeting Including The New Horizons Forum and Aerospace Exposition, Orlando, FL, USA, 5–8 January 2009.
2. Wisler, D.C. Loss reduction in axial-flow compressors through low-speed model testing. *J. Eng. Gas Turbines Power* **1985**, *107*, 354–363. [CrossRef]
3. Kempe, A.; Schlamp, S.; Rösgen, T.; Haffner, K. Spatial and temporal high-resolution optical tip-clearance probe for harsh environments. In Proceedings of the 13th International Symposium on Applications of Laser Techniques to Fluid Mechanics, Lisbon, Portugal, 26–29 June 2006.
4. Guo, O.A. Active Turbine Tip Clearance Control Research. Available online: http://www.grc.nasa.gov/WWW/cdtb/aboutus/workshop2015/ACC_2_Guo.pdf (accessed on 8 August 2016).
5. Lattime, S.B.; Steinetz, B.M.; Robbie, M.G. Test rig for evaluating active turbine blade tip clearance control concepts. *J. Propuls. Power* **2005**, *21*, 552–563. [CrossRef]
6. Geisheimer, J.L.; Holst, T.A. Metrology considerations for calibrating turbine tip clearance sensors. In Proceedings of the XIX Biannual Symposium on Measuring Techniques in Turbomachinery Transonic and Supersonic Flow in Cascades and Turbomachines, Rhodes-St-Genèse, Belgium, 7–8 April 2007.
7. Guo, H.; Duan, F.; Wu, G.; Zhang, J. Blade tip clearance measurement of the turbine engines based on a multi-mode fiber coupled laser ranging system. *Rev. Sci. Instrum.* **2014**, *85*, 115105. [CrossRef] [PubMed]
8. Sheard, A.G. Blade by blade tip clearance measurement. *Int. J. Rotating Mach.* **2011**, *2011*, 516128. [CrossRef]
9. Haase, W.C.; Haase, Z.S. High-Speed, capacitance-based tip clearance sensing. In Proceedings of the Aerospace Conference, Big Sky, MT, USA, 2–9 March 2013.
10. Ye, D.C.; Duan, F.J.; Guo, H.T.; Li, Y.; Wang, K. Turbine blade tip clearance measurement using a skewed dual-beam fiber optic sensor. *Opt. Eng.* **2012**, *51*, 081514. [CrossRef]
11. Schicht, A.; Schwarzer, S.; Schmidt, L.P. Tip clearance measurement technique for stationary gas turbines using an autofocusing millimeter-wave synthetic aperture radar. *IEEE Trans. Instrum. Meas.* **2012**, *61*, 1778–1785. [CrossRef]
12. Violetti, M.; Skrivervik, A.K.; Xu, Q.; Hafner, M. New microwave sensing system for blade tip clearance measurement in gas turbines. In Proceedings of the 2012 IEEE Sensors, Taipei, Taiwan, 28–31 October 2012.
13. Szczepanik, R.; Przysowa, R.; Spychała, J.; Rokicki, E.; Kaźmierczak, K.; Majewski, P. *Application of Blade-Tip Sensors to Blade-Vibration Monitoring in Gas Turbines*; INTECH Open Access Publisher: Rijeka, Croatia, 2012.
14. Du, L.; Zhu, X.; Zhe, J. A high sensitivity inductive sensor for blade tip clearance measurement. *Smart Mater. Struct.* **2014**, *23*, 065018. [CrossRef]
15. Cao, S.Z.; Duan, F.J.; Zhang, Y.G. Measurement of rotating blade tip clearance with fiber-optic probe. *J. Phys. Confer. Ser.* **2006**, *48*, 873–877. [CrossRef]
16. López-Higuera, J.M. *Handbook of Optical Fiber Sensing Technology*; Wiley and Sons: Chichester, West Sussex, UK, 2002.
17. García, I.; Zubia, J.; Durana, G.; Aldabaldetreku, G.; Illarramendi, M.A.; Villatoro, J. Optical Fiber Sensors for Aircraft Structural Health Monitoring. *Sensors* **2015**, *15*, 15494–15519. [CrossRef] [PubMed]
18. Davinson, I. Use of optical sensors and signal processing in gas turbine engines. In Proceedings of the SPIE 1374, Integrated Optics and Optoloelectronics II, San José, CA, USA, 17–19 September 1990.
19. Durana, G.; Kirchhof, M.; Luber, M.; de Ocáriz, I.S.; Poisel, H.; Zubia, J.; Vázquez, C. Use of a novel fiber optical strain sensor for monitoring the vertical deflection of an aircraft flap. *IEEE Sens. J.* **2009**, *9*, 1219–1225. [CrossRef]
20. García, I.; Beloki, J.; Zubia, J.; Aldabaldetreku, G.; Illarramendi, M.A.; Jiménez, F. An Optical Fiber Bundle Sensor for Tip Clearance and Tip Timing Measurements in a Turbine Rig. *Sensors* **2013**, *13*, 7385–7398. [CrossRef] [PubMed]

21. Pfister, T.; Büttner, L.; Czarske, J.; Krain, H.; Schodl, R. Turbo machine tip clearance and vibration measurements using a fiber optic laser Doppler position sensor. *Meas. Sci. Technol.* **2006**, *17*, 1693. [CrossRef]
22. Kempe, A.; Schlamp, S.; Rösgen, T.; Haffner, K. Low-coherence interferometric tip-clearance probe. *Opt. Lett.* **2003**, *28*, 1323–1325. [CrossRef] [PubMed]
23. Suganuma, F.; Shimamoto, A.; Tanaka, K. Development of a differential optical-fiber displacement sensor. *Appl. Opt.* **1999**, *38*, 1103–1109. [CrossRef] [PubMed]
24. Trudel, V.; St-Amant, Y. One-dimensional single-mode fiber-optic displacement sensors for submillimeter measurements. *Appl. Opt.* **2009**, *48*, 4851–4857. [CrossRef] [PubMed]
25. Cook, R.O.; Hamm, C.W. Fiber optic lever displacement transducer. *Appl. Opt.* **1979**, *18*, 3230–3241. [CrossRef] [PubMed]
26. Qing-Bin, T.; Hui-Ping, M.; Li-Hua, L.; Xiao-Dong, Z.; Gui-Bin, L. Measurements of radiation vibrations of turbomachine blades using an optical-fiber displacement-sensing system. *J. Russ. Laser Res.* **2011**, *32*, 216–229. [CrossRef]
27. Yu-zhen, M.; Yong-kui, Z.; Guo-ping, L.; Hua-guan, L. Tip clearance optical measurement for rotating blades. In Proceedings of the 2011 International Conference on Management Science and Industrial Engineering (MSIE), Harbin, China, 8–11 January 2011; IEEE: New York, NY, USA, 2011; pp. 1206–1208.
28. García, I.; Zubia, J.; Beloki, J.; Aldabaldetreku, G.; Durana, G.; Illaramendi, M.A. Optical tip clearance measurements for rotating disk characterization. In Proceedings of the 17th International Conference on Transparent Optical Networks (ICTON), Budapest, Hungary, 5–9 July 2015.
29. García, I.; Zubia, J.; Berganza, A.; Beloki, J.; Arrue, J.; Illarramendi, M.A.; Mateo, J.; Vázquez, C. Different configurations of a reflective intensity-modulated optical sensor to avoid modal noise in tip-clearance measurements. *J. Lightwave Technol.* **2015**, *33*, 2663–2669. [CrossRef]
30. García, I.; Przysowa, R.; Zubia, J.; Mateo, J.; Vázquez, C. Tip timing measurements for structural health monitoring in the first stage of the compressor of an aircraft engine. In Proceedings of the 18th International Conference on Transparent Optical Networks (ICTON), Trento, Italy, 10–14 July 2016.
31. Cao, H.; Chen, Y.; Zhou, Z.; Zhang, G. Theoretical and experimental study on the optical fiber bundle displacement sensors. *Sens. Actuators A Phys.* **2007**, *136*, 580–587. [CrossRef]
32. Shimamoto, A.; Tanaka, K. Geometrical analysis of an optical fiber bundle displacement sensor. *Appl. Opt.* **1996**, *35*, 6767–6774. [CrossRef] [PubMed]
33. Harun, S.W.; Yang, H.Z.; Yasin, M.; Ahmad, H. Theoretical and experimental study on the fiber optic displacement sensor with two receiving fibers. *Microw. Opt. Technol. Lett.* **2010**, *52*, 373–375. [CrossRef]